

**VIBRATION-BASED STRUCTURAL DAMAGE
DETECTION AND SYSTEM IDENTIFICATION USING
WAVELET MULTIREOLUTION ANALYSIS**

SEYED ALIREZA RAVANFAR

**THESIS SUBMITTED IN FULFILMENT OF THE
REQUIREMENTS FOR THE DEGREE OF DOCTOR OF
PHILOSOPHY**

**FACULTY OF ENGINEERING
UNIVERSITY OF MALAYA
KUALA LUMPUR**

2017

UNIVERSITY OF MALAYA
ORIGINAL LITERARY WORK DECLARATION

Name of Candidate: **SEYED ALIREZA RAVANFAR**

Registration/Matric No: **KHA100100**

Name of Degree: **DOCTOR OF PHILOSOPHY**

Title of Project Paper/Research Report/Dissertation/Thesis (“this Work”):

VIBRATION-BASED STRUCTURAL DAMAGE DETECTION AND SYSTEM IDENTIFICATION USING WAVELET MULTIREOLUTION ANALYSIS

Field of Study: **STRUCTURAL ENGINEERING & MATERIALS**

I do solemnly and sincerely declare that:

- (1) I am the sole author/writer of this Work;
- (2) This Work is original;
- (3) Any use of any work in which copyright exists was done by way of fair dealing and for permitted purposes and any excerpt or extract from, or reference to or reproduction of any copyright work has been disclosed expressly and sufficiently and the title of the Work and its authorship have been acknowledged in this Work;
- (4) I do not have any actual knowledge nor do I ought reasonably to know that the making of this work constitutes an infringement of any copyright work;
- (5) I hereby assign all and every rights in the copyright to this Work to the University of Malaya (“UM”), who henceforth shall be owner of the copyright in this Work and that any reproduction or use in any form or by any means whatsoever is prohibited without the written consent of UM having been first had and obtained;
- (6) I am fully aware that if in the course of making this Work I have infringed any copyright whether intentionally or otherwise, I may be subject to legal action or any other action as may be determined by UM.

Candidate’s Signature

Date:

Subscribed and solemnly declared before,

Witness’s Signature

Date:

Name:

Designation:

ABSTRACT

During the service life of various civil, mechanical and aerospace structures, damage can nucleate, accumulate and propagate leading to out-of-service conditions which are dangerous and can sometimes collapse. Therefore, Structural Health Monitoring (SHM) is a crucial tool for identifying the presence and the evolution of possible damage. This thesis, investigates rigorously two paramount concerns of the SHM: damage detection and parametric system identification.

The first proposed method is applied to detect crack damage in a structure. The location of the crack is identified by defining the damage index called relative wavelet packet entropy (RWPE). Then, the damage severities at the identified locations are assessed using genetic algorithm (GA), through defining a database to reveal the relationships between the energies obtained and damage severities. However, most of existing damage detection methods requires reference data which are not always available. Meanwhile, there has also been a pressing need for real-time monitoring to avoid sudden catastrophic disasters. Therefore, a new reference-free damage detection algorithm is proposed. The RWPE measurements of different sensor-to-sensor pairs are applied for defining the reference-free damage index (RDI) of each sensor location. To improve the proposed algorithm, GA was utilized to identify the best choice for “mother wavelet function” and “decomposition level” of the signals by means of the fundamental fitness function. This resulted in the high accuracy of the damage detection algorithm.

The second proposed method seeks to identify damage in the structural parameters of linear and nonlinear systems. Initially, the connection coefficients for the scaling function of the proper selection of Daubechies wavelets are developed to derive the velocity and displacement from the measured acceleration responses. Then, the next step is to define the dominant components according to the relative energy distributions of wavelet packet transform (WPT) components of the acceleration responses, and transforming the

equations of motion of the system in the time-domain to a reduced representation of the equations of motion based on the WPT. Finally, the least square error minimization method is implemented across the dominant components to determine the structural parameters of a linear system. Moreover, wavelet multiresolution analysis is applied to identify the tangent stiffness matrix and the hysteresis-restoring force of nonlinear structural systems without prior assumptions about the nonlinear characteristics of the systems.

To demonstrate the validity and accuracy of the methods, numerical and experimental studies are conducted on a beam element and subsequently on a three-story building model. Results indicate that the wavelet-based damage detection method precisely identified the location and severity of damages even without reference data. In addition, the structural parameters of a system can be accurately estimated through the proposed system identification methods for both cases of linear and nonlinear conditions. Moreover, the accuracy and reliability of the proposed methods are investigated on various damage scenarios with different levels of severity, and noise levels.

ABSTRAK

Semasa jangka hayat sesebuah struktur awam, struktur mekanikal dan struktur angkasa, kerosakan boleh menyebabkan kelumpuhan pada tahap rekabentukperkhidmatan dan merbahaya sehingga boleh menyebabkan kepada kerosakan menyeluruh sesebuah struktur. Maka Pemantauan Kesihatan Struktur (SHM) adalah mekanisme yang penting untuk mengenalpasti sebarang perubahan dan keberangkalian kerosakan dalam sesebuah struktur. Dalam kajian tesis ini, tumpuan diberikan kepada dua aspek iaitu; mengenalpasti kerosakan dan sistem parametrik.

Kaedah pertama dalam kajian adalah untuk mengenalpasti jenis kerosakan dalam struktur. Lokasi retak dapat dikenalpasti dengan indeks kerosakan yang dipanggil entropi paket wavelet relatif (RWPE). Kemudian tahap kerosakan yang teruk di lokasi dapat dinilai menggunakan kaedah algoritma genetik (GA) dengan menggunakan pengkalan data untuk melihat hubungkait antara tenaga dan juga tahap kerosakan. Secara amnya, kaedah yang sedia ada memerlukan data rujukan yang pada kebiasaannya tidak mudah diperolehi. Sementara itu, keperluan yang kritikal dalam pemantauan secara langsung adalah penting untuk mengelakkan bencana yang datang secara tiba-tiba. Maka, sebuah kaedah yang tidak menggunakan data rujukan diperkenalkan dalam kajian ini. Ukuran RWPE dalam sensor yang berlainan digunakan dalam menilai indeks kerosakan tanpa data rujukan (RDI) untuk setiap lokasi sensor. Untuk menaiktaraf algoritma, GA digunakan untuk mengenalpasti fungsi wavelet induk dan tahap penguraian isyarat yang terbaik menggunakan fungsi kecergasan asas. Ini menerbitkan ketepatan yang tinggi dalam mengenalpasti kerosakan dalam algoritma.

Kaedah kedua yang diperkenalkan dalam kajian adalah untuk mengenalpasti kerosakan dalam parameter struktur sistem linear dan juga tidak linear. Pada awalnya, pemalar penghubung untuk fungsi skalar untuk pemilihan wavelet Daubechies dihasilkan untuk menilai kelajuan dan anjakan daripada tindakbalas pecutan yang direkodkan daripada

sensor. Langkah berikutnya adalah mengenalpasti komponen dominan berdasarkan penyebaran tenaga relatif daripada komponen paket transformasi wavelet (WPT) untuk tindakbalas pecutan dan membuat perubahan dalam persamaan pergerakan sistem dalam domain masa untuk mengurangkan gerakan persamaan dengan menggunakan WPT. Akhir sekali, kaedah ralat kurang persegi digunakan ke atas dominan komponen untuk mengenalpasti parameter struktur dalam sistem linear. Seterusnya, analisa wavelet resolusi kepelbagaian digunakan untuk mengenalpasti matrik kekakuan tangen dan kuasa ulangan kembali dalam sistem tidak linear tanpa beranggapan tentang sifat tidak linear di dalam sistem.

Untuk memastikan kaedah adalah jitu dan tepat, kajian simulasi dan eksperimen dijalankan ke atas struktur rasuk dan model bangunan tiga tingkat. Keputusan menunjukkan kaedah wavelet adalah amat tepat untuk mengenalpasti lokasi kerosakan dan tahap kerosakan tanpa menggunakan data rujukan. Tambahan lagi, parameter struktur sesebuah sistem dapat dianggar secara jitu dengan menggunakan kaedah yang diperkenalkan untuk kes keadaan linear dan juga keadaan tidak linear. Ketepatan dan kesesuaian kaedah yang diperkenalkan juga disiasat dengan kepelbagaian keadaan kerosakan dengan tahap kerosakan dan tahap bising yang pelbagai.

ACKNOWLEDGEMENTS / DEDICATION

First and foremost, praises and thanks to the God, the Almighty, for His showers of blessing throughout my research work to complete the research successfully.

I would like to express my sincerest appreciation to my supervisor Prof. Hashim Abdul Razak for his generosity, supports, guidance, expert instruction and giving me the opportunity to be involved in such interesting research. His patience and encouragement have led me through the hard time of my study, which will never be forgotten. It was a great experience to work and collaborate with him for completing my Ph.D. Without his support, this present thesis would never exist and I would never have been able to complete this study. I would like to present my wholehearted appreciation to him.

I would like to express my sincere gratitude to my second supervisor Prof. Zubaidah Ismail for guidance, advice, and support throughout my doctoral studies. Her continuous availability along with many open-minded discussions is greatly appreciated.

I am deeply grateful to my parents. My Mom and Dad are a constant source of love, support, motivation and strength all these years. It was under their watchful eyes that I gained so much drive, strength and an ability to tackle challenges head on.

Finally, it's a great opportunity to express my gratefulness and love to my wife, Neda Rezaei. She is always there standing by me with her support, encouragement, patience and love through the good times and bad.

TABLE OF CONTENTS

ORIGINAL LITERARY WORK DECLARATION	ii
ABSTRACT	iii
<i>ABSTRAK</i>	v
ACKNOWLEDGEMENTS / DEDICATION	vii
LIST OF FIGURES	xiv
LIST OF TABLES	xx
LIST OF SYMBOLS AND ABBREVIATION	xxii
CHAPTER 1: INTRODUCTION	1
1.1 Background	1
1.2 Motivation of research	4
1.3 Objectives of research	6
1.4 Scope of research	7
CHAPTER 2: LITERATURE REVIEW	9
2.1 Introduction	9
2.2 Vibration-based damage detection techniques	9
2.2.1 Frequency change	9
2.2.2 Mode shape change	11
2.2.3 Mode shape curvature/strain mode shape	12
2.2.4 Modal flexibility change	13
2.2.5 Modal strain energy change	14
2.2.6 Model Updating Methods	16
2.2.7 Neural network and genetic algorithm	18
2.3 Advanced damage detection methods based on wavelet transform	20
2.3.1 Continuous wavelet transform	21
2.3.2 Discrete wavelet transform	26
2.3.3 Wavelet packet transform	27
2.3.4 Combining wavelet transform with other techniques	29

2.4	System identification based on the wavelet transform	33
2.4.1	Continuous wavelet transform	34
2.4.2	Discrete wavelet transform	37
2.5	Summary	39
	CHAPTER 3: THE WAVELET THEORY	41
3.1	Introduction	41
3.2	Development of wavelet theory	41
3.3	Continuous wavelet transform	42
3.4	Discrete wavelet transform	45
3.5	Wavelet multiresolution analysis	46
3.5.1	The Daubechies wavelets	50
3.5.2	Fast wavelet transformation	52
3.5.3	Wavelet decomposition of signals through filters	55
3.6	Wavelet packet transform	57
3.7	Summary	59
	CHAPTER 4: DAMAGE DETECTION AND SYSTEM IDENTIFICATION ALGORITHMS	61
4.1	Introduction	61
4.2	Damage detection algorithms based on wavelet multiresolution and GA	62
4.2.1	Wavelet packet component energies	62
4.2.2	Relative wavelet packet entropy (RWPE)	63
4.2.3	Damage severity evaluation using RWPE and GA	66
4.2.3.1	The genetic algorithm method	66
4.2.3.2	Damage severity assessment	68
4.2.4	RWPE-based Reference-free damage identification algorithm	70
4.2.4.1	Choice of wavelet using GA	72
4.3	Parameter identification using wavelet multiresolution analysis	75

4.3.1	Equation of motion according to the scaling function	75
4.3.2	Wavelet connection coefficients	78
4.3.3	Definition of dominant component	86
4.3.3.1	Equations of motion according to the WPT	86
4.3.4	Least square error minimization procedure	89
4.3.5	Nonlinear parameter estimation using wavelet multiresolution	90
4.3.5.1	Procedure for nonlinear system	90
4.4	Summary	94
CHAPTER 5: EXPERIMENTAL WORK		96
5.1	Introduction	96
5.2	Illustrative models for damage detection	96
5.2.1	I-Beams	96
5.2.1.1	Numerical study	96
5.2.1.2	Experimental study	99
5.2.2	Three-story building model	100
5.2.2.1	Model test building	100
5.3	Illustrative models for system identification	106
5.3.1	Beam structure under flexural vibration	106
5.3.1.1	Numerical study	106
5.3.1.2	Experimental study	107
5.3.2	Three-story building model	109
5.3.2.1	Numerical study	109
5.3.2.2	Experimental study	111
5.4	Instrumentation	115
5.4.1	Excitation	115
5.4.1.1	Source of excitation	116

5.4.2 Data Acquisition system	116
5.4.3 Accelerometers	117
5.4.4 Force transducer	118
5.5 Summary	119
CHAPTER 6: VERIFICATION OF PROPOSED ALGORITHMS	120
6.1 Introduction	120
6.2 Damage identification in beam structures	120
6.2.1 Two-step damage identification approach	120
6.2.2 Numerical investigation	121
6.2.2.1 Damage location identification	121
6.2.2.2 Effect of measurement noise	125
6.2.2.3 Damage severity evaluation	127
6.2.3 Experimental investigation	130
6.2.3.1 Experimental results	130
6.3 Reference-free damage identification in beam structures	132
6.3.1 Reference-free damage identification approach	132
6.3.2 Numerical investigation	133
6.3.2.1 Tested damage scenarios	133
6.3.2.2 Damage location identification	134
6.3.2.3 Identification of progressive damage	138
6.3.3 Experimental investigation	143
6.3.3.1 Experimental results	144
6.4 Damage identification algorithms for three-story building model	146
6.4.1 RWPE-based damage identification	146
6.4.1.1 Damage location identification	146
6.4.1.2 Damage severity evaluation	148

6.4.2 RWPE-based reference-free damage identification	151
6.4.2.1 Damage location identification	151
6.4.2.2 Identification of progressive damage	154
6.5 Wavelet-based system identification in a beam structure under flexural vibration	157
6.5.1 Wavelet-based system identification approach	157
6.5.2 Numerical investigation	158
6.5.2.1 Evaluation of damage severity in terms of the stiffness parameter	158
6.5.3 Experimental investigation	164
6.5.3.1 Experimental Results	164
6.6 Wavelet-based system identification algorithm for three-story building model	167
6.6.1 Numerical results	167
6.6.1.1 Evaluation of original numerical model	168
6.6.1.2 Case1: Damage in first story (linear model)	175
6.6.1.3 Case2: Damage in first and second stories (linear model)	177
6.6.1.4 Case3: Damage in third story (bilinear model)	179
6.6.1.5 Effect of measurement noise	181
6.6.2 Experimental results	186
6.6.2.1 Evaluation of original experimental model	186
6.6.2.2 Case1: Damage in first story (linear model)	189
6.6.2.3 Case2: Damage in second story (linear model)	191
6.6.2.4 Case3: Damage in first story (piecewise linear model)	193
6.7 Summary	195
CHAPTER 7: CONCLUSION AND RECOMMENDATIONS	197
7.1 Introduction	197
7.2 Conclusions	197

7.3 Recommendations for future work	200
REFERENCES	201

University of Malaya

LIST OF FIGURES

Figure 3.1: The Daubechies wavelet functions for DB1, DB2, DB4 and DB5	51
Figure 3.2: The Daubechies scaling functions for DB1, DB2, DB4 and DB5	51
Figure 3.3: The fast and inverse wavelet transform from a digital filter point of view ..	55
Figure 3.4: A schematic diagram of the DWT at decomposition level 3	57
Figure 3.5: A Schematic diagram of the WPT at decomposition level 3	58
Figure 4.1: Probability distribution and entropy comparison	64
Figure 4.2: Proposed chromosome for GA for two damage location and severities	69
Figure 4.3: Flowchart of the proposed identification algorithm.....	70
Figure 4.4: Calculation of reference-free damage index (RDI_{RWPE})	71
Figure 4.5: Order of Daubechies wavelet function	73
Figure 4.6: Proposed chromosome for GA for the optimal search of DB order and decomposition level.....	74
Figure 4.7: Entire proposed reference-free damage identification algorithm	75
Figure 4.8: The location of $\phi_{0,q}(t)$ in terms of time in the first case, $q \leq -(L - 1)$	81
Figure 4.9: The location of $\phi_{0,q}(t)$ in terms of time in the second case, $-(L - 1) < q < 0$	81
Figure 4.10: The location of $\phi_{0,q}(t)$ in terms of time in the third case, $0 \leq q < (L - 1)$	82
Figure 4.11: The location of $\phi_{0,q}(t)$ in terms of time in the fourth case, $q \geq (L - 1)$..	83
Figure 4.12: Block diagram of the proposed system identification method	94
Figure 5.1: I-section specimen. (a) Dimension and damage depth of beams, (b) damage location of beams.....	98
Figure 5.2: Dynamic test in laboratory. (a) Tested beams, (b) experimental setup and data acquisition system	99
Figure 5.3: Three-story test building model	101

Figure 5.4: Slab and flat bar connection	102
Figure 5.5: Columns and floors numbers of three-story building model.....	103
Figure 5.6: Double damage scenarios of thee-story building model. (a) DS1, (b) DS2 and (c) DS3	104
Figure 5.7: Triple damage scenarios of thee-story building model. (a) DS4, (b) DS5 .	105
Figure 5.8: Different levels of cuts in steel flat bars	106
Figure 5.9: Dimensions and damage locations of beams under flexural vibration. (a) Case 1, (b) Case2	107
Figure 5.10: Experimental setup using beam under flexural vibration. (a) Data acquisition system, (b) damage locations of tested beam	108
Figure 5.11: The model of a three-story frame structure	109
Figure 5.12: (a) Experimental setup of three-story building model, (b) data acquisition system.....	111
Figure 5.13: Frequency domain response of acceleration response signal in building model.....	112
Figure 5.14: Schematic diagram of the hydraulic cylinder-piston system	113
Figure 5.15: A three story building model equipped with VSD.....	113
Figure 5.16: ET-132-2 Electrodynamic shaker	115
Figure 5.17: APS-125 Power amplifier.....	116
Figure 5.18: OROS38 with 32 channels	117
Figure 5.19: The setup of analyzer and NVGate	117
Figure 5.20: K-shear accelerometer	118
Figure 5.21: Force transducer	118
Figure 6.1: The values of RWPE for each depth of damage. (a) Beam1, (b) beam 2, (c) beam3	122

Figure 6.2: Damage identification results using different wavelet function. (a) Beam1, (b) beam2, (c) beam3	123
Figure 6.3: Histograms of RWPE in beam 2 with different orders of Daubechies wavelets.....	124
Figure 6.4: Different levels of noise contamination in the measured signal at location 8 for the undamaged case.....	126
Figure 6.5: Damage identification results in beam 3 after adding different levels of noise. (a) SNR= 2 dB, (b) SNR= 5 dB, (c) SNR= 10 dB	127
Figure 6.6: The damage severity evaluation results by using GA. (a) Beam1, (b) beam2, (c) beam3	129
Figure 6.7: RWPE for different damage cases. (a) Beam 1, (b) beam 2, (c) beam 3....	131
Figure 6.8: Encoded damage severity result for beam3 with different levels of severity	132
Figure 6.9: Damage identification in beam1. (a) Histogram of RDI_{RWPE} , (b) histogram of RDI_{RWPE}^{UL} after consider damage threshold, (c) comparison of RDI_{RWPE} before and after damage.....	135
Figure 6.10: Damage identification in multiple damage scenarios with different sensor locations. (a) DS1, (b) DS2, (c) TS1, (d) TS2	137
Figure 6.11: Histograms of RDI_{RWPE}^{UL} in beam1 with different Daubechies orders	139
Figure 6.12: Histograms of RDI_{RWPE}^{UL} in beam 2 with different Daubechies orders	141
Figure 6.13: Histograms of RDI_{RWPE}^{UL} in beam 4 with different Daubechies orders	142
Figure 6.14: Histograms of RDI_{RWPE}^{UL} in (a) beam 1, (b) beam 2, and (c) beam 4 with different Daubechies orders	145
Figure 6.15: The values of RWPE for each depth of damage. (a) DS1, (b) DS2, (c) DS3	147
Figure 6.16: The values of RWPE for each depth of damage. (a) DS4, (b) DS5.....	148

Figure 6.17: RWPE-based reference-free damage identification results for DS1 damage scenario at 10.5mm depth of damage. (a) $RS_{RWPE}(p^\lambda p^\theta)$, (b) comparison of RDI_{RWPE} before and after damage.....	152
Figure 6.18: Result of damage identification by RWPE-based reference-free for 10.5mm damage depth. (a) DS2, (b) DS3, (c) DS4, (d) DS5	154
Figure 6.19: Result of damage identification by RWPE-based reference-free for progressive damage after considered threshold values. (a) DS1, (b) DS2, (c) DS3, (d) DS4, (e) DS5.....	155
Figure 6.20: Histogram of RDI_{RWPE} in DS4 damage scenario with different DB orders after considering the damage threshold	156
Figure 6.21: The relative energy distribution of the acceleration response for the undamaged case.....	159
Figure 6.22: Input and response data at location 5 for undamaged case. (a) Input force, (b) exact acceleration responses, (c) comparison of the exact velocity to the calculated velocity, (d) comparison of the exact displacement to the calculated displacement	161
Figure 6.23: The relative energy distribution of the acceleration response for Case 1.	162
Figure 6.24: Loss of stiffness identification in Case 1	162
Figure 6.25: The relative energy distribution of acceleration response for Case 2.....	163
Figure 6.26: Loss of stiffness identification in Case 2.....	163
Figure 6.27: Input and structural response data at location 3 of Case 1: (a) force; (b) acceleration; (c) velocity; (d) displacement.....	164
Figure 6.28: Frequency domain response of acceleration response signal at location 3	165
Figure 6.29: The relative energy distribution over the wavelet packet components at level 5 for undamaged beam.....	165
Figure 6.30: Loss of stiffness identification in each dominant component in Case 1 ..	166

Figure 6.31: Loss of stiffness identification in each dominant component in Case 2 ..	166
Figure 6.32: Acceleration responses at each floor of the original model along y-direction	168
Figure 6.33: The relative energy distribution of acceleration response at decomposition level 9 for the original model	169
Figure 6.34: Identified results for original numerical model in y-direction	171
Figure 6.35: The difference (error) between the exact and derived displacement responses at the first floor.	172
Figure 6.36: Identified results for original numerical model.....	173
Figure 6.37: Identified results for original numerical model in x-direction	175
Figure 6.38: The proposed auxiliary structure at the first floor in y-direction.....	175
Figure 6.39: Identified results for DC1	176
Figure 6.40: The proposed auxiliary structure at first and second floor in y-direction	177
Figure 6.41: Identified results for DC2.....	178
Figure 6.42: load-deformation rules. (a) Linear model, (b) bilinear model	179
Figure 6.43: Simulated and identified restoring force responses of the structure in which the third floor is soft.	180
Figure 6.44: Simulated and identified restoring force-drift hysteresis curves	181
Figure 6.45: Identified results for original numerical model with noise level of SNR= 2dB	183
Figure 6.46: Identified results for original numerical model with noise level of SNR=5dB	184
Figure 6.47: Identified results for original numerical model with noise level of SNR=10dB	185
Figure 6.48: The identified restoring force-drift hysteresis curves after adding different level of noise. (a) SNR= 2 dB, (b) SNR= 5 dB, (c) SNR= 10 dB	186

Figure 6.49: Measured acceleration responses and input force for original model	187
Figure 6.50: Derived the velocities and displacements from acceleration responses at each floor of the original experimental model in terms of DB 15 scaling function.....	187
Figure 6.51: Identified results for original experimental model.....	189
Figure 6.52: Identified results for Case 1 of experimental model.....	191
Figure 6.53: Identified results for Case 2 of experimental model.....	192
Figure 6.54: Identified stiffness parameters for Case 3 of experimental model	194
Figure 6.55: Identified damping coefficients for case 3 of experimental model.....	195

University of Malaya

LIST OF TABLES

Table 3.1: The coefficients of two-scale relations for DB1, DB2, DB4, and DB5 wavelet functions and scaling functions	52
Table 5.1: Frequency bands of the WPT Components at decomposition level 6 of undamaged Beam	98
Table 5.2: Beam damage scenarios	99
Table 5.3: Dimension and amount of building model components	101
Table 5.4: The detail description of damage scenarios in the building model	102
Table 5.5: Damage scenarios of beam under flexural vibration.....	108
Table 5.6: Structural modal properties of the original mode.....	110
Table 5.7: Damage scenarios in three-story shear-beam building model.....	111
Table 6.1: Considered damage cases in beams	128
Table 6.2: GA set up parameters for beams	128
Table 6.3: The damage severity results obtained by GA	129
Table 6.4: Damage scenarios with different sensor deployments on damaged beams .	133
Table 6.5: GA parameters used in RWPE-based reference-free algorithm.....	134
Table 6.6: GA optimized variables in beams	136
Table 6.7: Daubechies wavelets comparison for each damage depth for beam 1	140
Table 6.8: Daubechies wavelets comparison for multiple damage scenarios	143
Table 6.9: Considered damage cases in double damage scenarios of the building model	149
Table 6.10: Considered damage cases in triple damage scenarios of the building model	149
Table 6.11: Damage severity evaluation results using two damage scenarios	150
Table 6.12: Damage severity evaluation results using three damage scenarios	150
Table 6.13: Damage scenarios of reference-free damage identification.....	151

Table 6.14: Frequency bands of the WPT components at level 6 and modal properties of the undamaged case.....	159
Table 6.15: Estimated values of loss of stiffness in the first convergence region	167
Table 6.16: GA parameters used in wavelet-based system identification algorithm....	168
Table 6.17: Effect of different levels of noise in identified stiffness parameters	182
Table 6.18: Identified stiffness parameters and natural frequencies, ω , of the original model and damage cases 1 and 2. The units of k , ω are N/m and Hz, respectively	193
Table 6.19: The PRE of identified stiffness parameters in damage Case 3	194

University of Malaya

LIST OF SYMBOLS AND ABBREVIATION

WT	Wavelet transform
CWT	Continues wavelet transform
DWT	Discrete wavelet transform
WPT	Wavelet packet transform
MRA	Multiresolution analysis
SHM	Structural health monitoring
GA	Genetic algorithm
NN	Neural network
HT	Hilbert transform
HHT	Hilbert-Huang transform
EMD	Empirical mode decomposition
IMF	Intrinsic mode function
FT	Fourier transform
STFT	Short-Time Fourier Transform
SDOF	Single degree of freedom
MDOF	Multi degrees of freedom
MDLAC	Multiple damage location assurance criterion
MAC	Modal assurance criteria
COMAC	Modal assurance criteria
ULS	Uniform load surface
EMSE	Elemental modal strain energy
MSECR	Modal strain energy change ratio
$\psi(t)$	Mother wavelet
$\phi(t)$	Scaling function
a	Scale parameter
b	Translation parameter
*	Complex conjugate
\langle, \rangle	Inner product
E_ψ	Energy of a wavelet function
$H(\omega)$	Fourier transform of $\psi(t)$
DB	Daubechies wavelet function
V_j	Scale Subspace at scale index j

W_j	Detail Subspace at scale index j
$c(n)$	Daubechies scaling coefficients
$b(n)$	Daubechies wavelet coefficients
E_f	Wavelet packet energy
p	Relative energy
$S(P)$	Entropy
S_{WPE}	Wavelet packet entropy
S_{RWPE}	Relative wavelet packet entropy (RWPE)
DI_{RWPE}	RWPE-based damage index
$\ \cdot\ _2$	Euclidean norm
RS_{RWPE}	RWPE-based reference-free
RDI_{RWPE}	Reference-free damage index
RDI_{RWPE}^{UL}	Reference-free damage index after consider damage threshold
μ	Mean value
σ	Standard deviation
UL	One-side upper confidence limit
$Z_{\bar{\alpha}}$	Standard normal distribution
Fit	Fundamental fitness function
$\ddot{x}(t)$	Acceleration
$\dot{x}(t)$	Velocity
$x(t)$	Displacement
$f(t)$	External force
M	Mass matrix
C	Damping matrix
K	Stiffness matrix
$\mathfrak{I}_1\{\phi_{j,k}(t)\}$	First integral of the scaling function
$\mathfrak{I}_2\{\phi_{j,k}(t)\}$	Second integral of the scaling function
Γ	Connection coefficients for the first integration
Ω	Connection coefficients for the second integration
$U_{i,j}^Y$	i^{th} signal decomposition at the decomposition level j of the signal Y , i.e. acceleration, velocity and displacement
D_c	Dominant component
s_c	Sequence number of the WPT component having the c^{th} highest relative energy

$f_R(\dot{x}(t), x(t))$	Nonlinear restoring force vector
$C(t)$	Piecewise linear damping matrix
$S(t)$	Tangent stiffness matrix
$\Delta\ddot{x}(t)$	Incremental acceleration
$\Delta\dot{x}(t)$	Incremental velocity
$\Delta x(t)$	Incremental displacement
$\xi_h(j, k)$	Integral coefficients of the scaling functions
λ_i	Estimated error evaluation of structural states
Θ_h	Unknown vector
RF	Restoring force response
\widehat{RF}	Unbiased estimation of restoring force response
AF_j	Average of the relative energies at decomposition level j
\tilde{D}	Number of dominant energies of AF_j
t^d	Damage depth
α	Damage severity
DL	Damage location
SNR	Signal-to-noise ratio
RMS	Root-mean-square
A_S	The RMS value of the acceleration signal
A_N	The RMS value of the noise
SS	Single damage scenario
DS	Double damage scenario
TS	Triple damage scenario
ρ	Mass density
ν	Poisson's ratio
E	Elasticity modulus
DC	Damage case
PRE	Percent relative error
VSD	Variable stiffness device
HCP	Hydraulic cylinder-piston
K_{hi}	Effective stiffness of the VSD
K_{fi}	Horizontal stiffness of HCP
K_{bi}	Horizontal stiffness of bracing system
P_0	Initial gas pressure

A	piston area
v_0	Initial volume of piston
γ	Ratio of specific heats

University of Malaya

CHAPTER 1: INTRODUCTION

1.1 Background

During the service life of various civil, mechanical and aerospace structures, damage can accumulate, nucleate and propagate leading to out-of-service conditions, and, sometimes, leading to failure. In order to raise the level of public safety and to improve the maintainability of new and existing structures, the knowledge of structural health monitoring (SHM) plays an increasingly important role and has become an efficient, reliable and economical method which is capable of monitoring the structural performance and making accurate maintenance decisions by localizing damage and evaluating the structural integrity and serviceability. Therefore, detection of damage and its location are the main tasks of SHM. Rytter (1993) distinguishes four levels of damage identification in the structure, as follows:

Level 1 (Damage Detection): Determination of the presence of damage in the structure;

Level 2 (Damage Localization): Level 1 plus determination of the damage location;

Level 3 (Damage Quantification): Level 2 plus quantification of severity of the damage;

Level 4 (Life Prediction): Level 3 plus prediction of the remaining service life of the structure.

The four-level damage identification method provides a sequence to evaluate the structural damage. Since prediction in Level 4 requires knowledge of other fields such as structural design, fracture mechanics, materials aging studies, and damage mechanism, it is therefore not included in this research.

Most non-destructive damage detection methods can be divided into two categories of either local or global, depending on the scale level at which they operate. Local damage detection methods refer to non-destructive methods, such as the ultrasonic or acoustic,

radiographic, eddy-current, magnetic-field, and thermal-field methods, where the existence and location of local damage can be detected. One of the major advantages of these methods is that they do not require information drawn from the intact/healthy structures. Nevertheless, these methods are just useful on simple and small structures. Some information of damage location is needed when one is evaluating complicated and large structures to avoid a time-consuming and expensive process.

Global damage detection methods, such as vibration-based damage detection methods, have been applied to identify damage across the entire structure by using dynamic characteristics of the structures (e.g., mode shapes, natural frequencies and modal damping). The fundamental idea for global damage detection methods is that damage-causes change in some structural parameters (e.g., mass, damping and stiffness), and that change will accordingly alters structural dynamic properties. Therefore, structural state can be evaluated globally, by examining the changes in dynamic properties of a structure. Hence, these methods are known as optimal methods. In the past few decades, these vibration-based damage detection methods have attracted considerable attention from members of the civil, aerospace, and mechanical engineering communities and that interest in turn has prompted the extensive research carried out by Carden and Fanning (2004), Sohn et al. (2004), Yan et al. (2007) and Fan and Qiao (2011). Although vibration-based damage detection methods have demonstrated various degree of success, nevertheless, detection of damage in large-scale civil infrastructures is still a challenging task.

Toward successful damage detection, system identification is a profound stage. System identification deals with the problem of developing or improving mathematical models of dynamic systems based on input-output measurements. System identification methods can be applied to: (i) determination of structural system's properties such as damping ratios, stiffness, natural frequencies and so on; (ii) nondestructive damage evaluations,

where input-output measurements are applied to nondestructively assess the damage location and severity in an existing structure; (iii) health monitoring of the global or local conditions of structures; and (iv) vibrational control for minimizing the risk of structural failure and improving the integral performance of structural systems. In the last few decades, the interest in the general topics of system identification has increased greatly (Loh et al., 2000; Hung et al., 2003; Kijewski & Kareem, 2003; Farrar & Worden, 2007; Wang et al., 2013).

Generally, system identification methods can be classified into either parametric or nonparametric, depending on the basis of their search space. Parametric methods seek to determine the value of the structural parameters (such as mass, damping, and stiffness) for an assumed model of the system to be identified. In other words, they search the suitable value in a more or less structural parameter space, while nonparametric methods produce the best functional representation for structural elements of the system without making any former assumptions about the system model. In short, they search the functional space; e.g., the Chebyshev polynomial series, Volterra series, and so on.

Widely utilized system identification methods for linear structural systems are built on the platform of parametric methods (Lingener & Doege, 1988; Agbabian et al., 1991). The mathematical model for linear structural systems is usually represented by the second-order differential equations using mass, stiffness, and damping matrices. The identification problem aims at determining these matrices by utilizing system responses, natural frequencies and corresponding mode shapes measured from experiments. An optimization approach targets the problem associated with the identification method to minimize the errors between the simulated (estimated) values and the measured values of system responses obtained from the tests. Another way to formulate the problem is to minimize the error in the estimated and known eigenvalues and/or eigenvectors.

The nonparametric methods present the best functional representations for the unknown properties of structural elements of the system without a priori assumptions about the system model. In contrast to the parametric methods, the equation of motion for a structural system is defined by a function which contains the displacement and velocity dependent restoring forces implicitly. This function can be expressed by several types of polynomials such as the power series (Yang & Ibrahim, 1985), the Volterra series (Distéfano & Todeschini, 1973), and the Chebyshev polynomials (Masri & Caughey, 1979).

In addition, one significant subject facing the SHM field is that damage in the structure is usually a time-varying behavior and the structure will normally respond into nonlinear behavior when subjected to large excitations. To understand the system during its lifetime in more detail, nonlinear identification is required for early detection, localization and assessment of possible damages. After a proper characterization of nonlinear phenomenon, some properties of these systems can be taken for a better system design, better control performance, and other useful applications which linear systems cannot provide. However, such identification of nonlinear behavior is a very challenging task.

The main purpose of this research is to develop a hybrid damage detection and system identification method as an effective SHM tool which can provide precise and reliable vibration-based SHM technique.

1.2 Motivation of research

Recently, SHM-related technologies for civil infrastructure have increasingly developed by applications of model updating technologies, advanced system identification, signal processing algorithms for diagnosis and hardware for high speed data processing. However, there are still challenges to overcome until state-of-the-art vibration-based SHM technologies can be applied to actual large-scale civil infrastructure.

Complexity of large-scale civil infrastructures including buildings, dams, power plants and bridges involves structural configuration, details and materials. In detail, these complexities encompass issues such as different types of connection like welding, anchoring, bolts, rivets or different types of members including beams, links, struts, slabs, bearings and anchored foundation or different structural materials like steel, prestressed concrete, reinforced concrete, structural plastics, FRP composites, wood and glasses. Due to the fact that modal properties could be insensitive to early damage in local regions, to resolve the complexity of civil structures, more information of structural response beyond modal properties is required.

Uncertainty of monitoring in-situ structures leads to false alarm in SHM system. Ambient environment such as traffic loading, changes of temperature and humidity, and measurement noise and errors are sources of uncertainties that negatively affects reliability of the vibration-based damage detection. Hence, in order to keep track of life-time structural conditions and successful statistical analysis of monitored data, there is an urgent need for long-term monitoring.

Early damage detection in civil infrastructure has been considered critical for preventing catastrophic major disasters. Notably, most of large-scale civil infrastructure consists of a number of structural members and joints with different materials. In the past several decades numerous modal-based damage detection methods have presented promising results, however, early development of damage only based on structural dynamic modal properties is still a challenge. In order to tackle this difficulty, local diagnosis methods have been applied to compensate limitations of vibration-based damage detection methods. This solution suffered a problem which was expensive costs of dense array of sensors for local diagnosis of ordinary structures with less importance. Nevertheless, developing damage signatures with high sensitivity for early damage detection in large-scale structures will be a strategic approach for future SHM systems.

Moreover, one of the main challenges of current damage detection applications has always been availability of reference data taken from pristine undamaged states of structure. Absence of such data for most of infield structures has given rise to development and applications of reference-free damage detection approaches.

More challenges go to the realization of real-time SHM system. This is because of computational burdens associated with current damage detection logics and algorithms. Higher possibility of detecting damage at early stages, while operations are going on, has caused the real-time SHM system to gain more attention, since more time is provided for evacuation of users and for timely maintenance. Such apparent advantages of real-time SHM of structures ensure both serviceability and safety before any catastrophic disaster takes place.

In the realm of SHM research and practices, fast or real-time monitoring have always gained attention, thanks to advances in information technology for overcoming the disadvantage of updating-based SHM system and for rendering the real-time SHM. This system would overload due to intensive computations associated with large number of model parameters and theoretical rationales employed. In most damage detection techniques and vibration based SHM, changes in model properties and structural stiffness and damping are directly related and this yields tremendous computational time for such model-based diagnosis methods. Hence, model-based diagnosis methods are not applicable to real-time monitoring of large-scale structures. Taking into account all of the aforementioned aspects, the current dissertation is designated and carried out to address and overcome the common challenges in SHM practices.

1.3 Objectives of research

In order to improve present SHM technologies and practices, current research aims to develop a damage detection method along with a system identification, based on the

wavelet theory. With these developed methods, it is possible to investigate the occurrence, location, and severity of damage. Thus the main objectives of this study are outlined below:

- i) To propose an advanced hybrid wavelet-based damage detection algorithm for localization and severity evaluation of damage.
- ii) To propose and improve the robust and viable wavelet-based real-time reference-free damage detection algorithm.
- iii) To develop the wavelet-based system identification algorithm for identifying the structural parameters of beam structure and three-story building model in linear and nonlinear conditions.

1.4 Scope of research

Scope of this thesis is devoted to the development of a deterministic damage detection and a system identification algorithm in beam structures and a three-story building model. To accomplish such developments, the following activities are planned:

Proposing of a hybrid approach will be accomplished using the wavelet multiresolution analysis and GA to determine the location and severity of damage. This approach contains two parts; first part combines the WPT with entropy analysis to determine an effective damage index, RWPE, for investigating the location of damage. Then, damage severities at the identified locations will be assessed in the second step using GA. The WPT component energies for each damage depth used in the first step and the severity evaluation database required for the second step will reveal the relationships between the energies and damage severities.

To make real-time monitoring possible in SHM systems, a reference-free damage detection algorithm will be developed by applying an effective damage index and GA. The RWPE measurements of different sensor-to-sensor pair are utilized for defining

reference-free damage index, *RDI*, for each sensor location. To ameliorate the algorithm, GA will be applied to optimize the algorithm so as to determine the best values for mother wavelet function and decomposition level of the signals by means of the fundamental fitness function. This will result in high accuracy of the damage identification algorithm. The proposed wavelet-based system identification algorithm will be developed for identification of structural parameters of linear and nonlinear systems. Initially, the velocity and displacement will be derived from measured acceleration responses, since response signals from a structure are measured in the form of accelerations. This procedure will be performed by connection coefficients for the scaling function of the proper selection of Daubechies wavelet function. In the next step, the dominant components will be defined based on the distribution of relative energies of the WPT components of the acceleration responses to make the data size smaller along with saving important features of the system. This will be carried out by extracting discriminatory features of the signal and eliminating redundancy in the signal to enhance length-reduction of the data. Finally, the structural parameters can be identified by implementing the least square error minimization method over the dominant components. Moreover, wavelet multiresolution analysis will be utilized for identification of both the tangent stiffness matrix and the hysteresis-restoring force of nonlinear structural systems. Such process will be independent of any prior assumptions regarding the nonlinear characteristics of the systems.

CHAPTER 2: LITERATURE REVIEW

2.1 Introduction

This chapter presents a review of the literature on damage assessment and system identification. Section 2.2, presents the comprehensive review on vibration-based damage detection methods by the classification using the features extracted for damage detection. Section 2.3 studies advanced damage detection methods on the basis of the wavelet theory only and on combinations of that theory with other methodologies (e.g., Hilbert-Hang transform and neural networks). Section 2.4, reviews different types of wavelet transforms, e.g., continuous wavelet transform and discrete wavelet transform and the way they have been utilized in the identification of linear time-invariant, time-varying systems and nonlinear systems.

2.2 Vibration-based damage detection techniques

2.2.1 Frequency change

Reliability of structural damage detection has been attributed only to alteration of structure frequency due to immature mode identification techniques. Those researches addressing frequency-change based damage detections are so many (Salawu, 1997). In general, there are two types of methods. In the first type of methods, the damage detection problem is treated as forward problem, where the patterns of the measured frequency changes for all possible damage cases and then the damage case which produces the best match to the measured frequency changes is regarded as the suspected one. The advantage of this type is that some patterns of measured frequency alteration are directly related to the damage location only. Liang et al. (1992) studied the frequency sensitivity for simply supported and cantilevered beam. The considered damage scenario included one crack. An analytical relationship was developed between the severity and location of the damage

and the first order change in the eigenfrequencies. The frequency sensitivity of a cracked beam was then evaluated by Morassi (1993) explicitly through a general perturbation approach. Ling's and Morassi's approaches were developed according to Bernoulli beam theory and both modeled crack as a massless, infinitesimal rotational spring. All of the earlier mentioned explicit expressions are applicable only to small defects. A cracked symmetric uniform beam case was studied by Kasper et al. (2008) who derived the explicit expressions of wavenumber and frequency shift. Those expressions could only apply to beams with both shallow and deeper cracks, but not for the fundamental beam mode and for a crack spotted in a boundary near field due to dependency of expressions on high frequency approximation.

The second type of methods is the model updating methods, deal with damage detection as an inverse problem and is capable to identify damage magnitude and location. Study on this type dates back to 1978 and started by Adams et al. (1978) who utilized natural frequencies of longitudinal vibrations for damage detection of a one-dimensional component case.

A correlation coefficient namely the multiple damage location assurance criterion (MDLAC) was proposed by Messina et al. (1998). Two methods for estimation of the size of defects in a structure were introduced. This method is function of the sensitivity of the frequency associated with each mode measured from damage in each location. A single damage indicator (SDI) was proposed by Kim and Stubbs (2003) to locate and quantity of a crack in beam type structures with the aid of variation in a few natural frequencies. Two models for a crack location and a crack size were formulated through relating fractional changes in modal energy to changes in natural frequencies due to damage. Zhong et al. (2008) introduced an approach capable of detecting damage by using the output-only time history of beam-like structures. This approach was based on the auxiliary mass spatial probing.

Also, due to the facts that firstly modal frequency is a global property of a structure and secondly frequencies generally cannot provide spatial information about structural changes, there is no assurance that variation of this parameter is a true factor to identify more than the mere existence of damage. In case of a symmetrical structure, natural frequencies alterations caused by damages at two symmetric locations are exactly the same. Therefore, the frequency-based method fails to correctly identify the location of damage. At higher modal frequencies, local modes which are created in part by high modal density are associated and difficult to identify due to insufficient number of frequencies with considerable changes to uniquely determine the damage location because of the practical limitations.

Frequency-based methods have several advantages listed in the following:

- i) independency of frequency information from sensor position,
- ii) not many measuring points are needed,
- iii) lesser contamination of natural frequency due to measurement noise compared to other modal parameters such as low-level energy input originated by normal traffic which causes ambient variation, while continuous structural health monitoring and extraction of the resonant frequencies are still viable through this approach.

2.2.2 Mode shape change

Mode shapes fundamentally encompass the special information associated with structural changes. When it comes to the case of damage identification which is a local change of structure condition, mode shape is a potential factor. With the development of modal testing techniques especially in sensor technology and computing speed, many researches devoted their efforts in detecting damage by applying measured mode shape information. West (1984) first introduced modal assurance criteria (MAC) to identify the level of correlation between the modes obtained from damaged and undamaged structure. Fox (1992) experimentally found that variation measurement associated with single vibration

mode, like MAC, was somehow insensitive to damage in a beam structure caused by saw cut. Therefore he extended MAC and found that a node-line MAC which was based on measurement point close to a node point for a particular mode can be a more sensitive indicator of mode shape variation induced by damage. Mayes (1992) developed a method based on the ratios of relative modal displacement, i.e. rotational and translational error checking, through which structural stiffness difference between two different sets of degrees of freedom could be assessed according to changes in the mode shapes.

The concept of MAC was further extended by Lieven and Ewins (1988) and a coordinate modal assurance criterion (COMAC) was proposed for localizing damage. Later on a method was by Ko et al. (1994) employing MAC, COMAC and sensitivity analysis combined together to detect damage in steel framed structure. By this method, the most relevant DOFs were determined by computing the sensitivities of the analytically derived mode shapes corresponding to particular damage locations. Although results revealed the possibility of damage indication by particular mode pairs, however, in case all mode pairs were used, those were not sensitive to the damage could prevent the damage identification.

The damage localization method was extended by Shi et al. (2000a) based on a multiple damage location assurance criterion; (MDLAC) proposed by Messina et al. (1998), which employed incomplete mode shape instead of modal frequency. Preliminary the damage could be localized by utilizing incomplete measured mode shapes and in the second step the damage site was detected along with its extent by employing measured natural frequencies. Pascual et al. (2005) proposed a general procedure based on an optimized choice which led to satisfactory results.

2.2.3 Mode shape curvature/strain mode shape

As an alternative to mode shapes, mode shape derivatives such as curvatures can be used to detect damage. This is because changes in mode shapes are so small and therefore

difficult to detect. However, the mode shape curvature of a structure can be obtained from the modal displacement or acceleration. For structures such as shells, beams and plates, the relationship between bending strain and curvature is direct, so the practical possibility for calculating the curvature directly from measuring strain has been examined by researches.

Pandey et al. (1991) considered an analytical cantilever and a simply supported beam model and discussed that the absolute changes in the curvature mode shapes are localized in the region of damage and hence can be used to detect damage in a structure. Performance of both curvature and displacement mode shape was studied by Salawu and Williams (1994) and effectiveness of the approach as well as its sensitivity as a damage indicator was confirmed.

On the other hand, the drawbacks of mode shape curvature have been discussed since its sensitivity has been questioned by several researchers. Ratcliffe (2000) experimentally showed that the modal curvature is not sensitive enough by itself to locate small damages. Chance et al. (1994) improved the mode shape curvature result by applying measured strains instead of direct measurement of curvature. Nwosu et al. (1995) measured the variation of strain associated with a crack in a tabular T-joint. Changes were found greater than any frequency shift and measurable at a large distance to the crack. Abdo and Hori (2002) used measurement of mode shapes through a finite element analysis to localize damage in a cantilevered and a simply-supported plate. They concluded that rotation of mode shape had better performance in multiple damage case than displacement mode shape itself.

2.2.4 Modal flexibility change

Another class of damage detection methods uses the dynamically measured flexibility matrix to estimate changes in the static performance of the structure. Typically damage is detected by comparing the synthesized flexibility matrices associated with the modes

of damaged and undamaged structure. It has to be mentioned that in the lower-frequency modes of the structure, flexibility matrix is sensitive to changes because of the inverse relationship to the square of the modal frequencies.

Flexibility matrix technique was applied by Pandey and Biswas (1994) to detect the damage in several numerical examples and to an actual spliced beam. It was shown that estimation of damage location and condition could be achieved by the first two modes of the structure. Zhang and Aktan (1998) used weighted average of mode shapes which is an extension to the modal flexibility and its derivatives namely uniform load surface (ULS). ULS was found less sensitive to noise in compared to mode shapes. Later on ULS was employed by Wu and Law (2004) to localize the damage in plate structure and sensitivity of ULS curvature to local damages even with presence of noisy measurements was reported to be acceptable.

Those damage detection methods which are associated with modal flexibility have the advantage of approximately synthesized matrix from few lower natural frequencies and mode shapes. On the other hand, compared to the stiffness matrix, flexibility matrix is insensitive to mass alteration, (Berman & Flannelly, 1971). The disadvantage however is the need for modal mass or mass normalized mode shapes for estimation of modal flexibility. Therefore, in case of ambient vibration tests out of which the mass-normalized mode shapes cannot be exploited, it is not possible to estimate the modal flexibility through the output-only measurements unless certain assumptions or approximations are considered.

2.2.5 Modal strain energy change

Damage detection method based on the modal strain energy change is one of commonly used methods in the discipline. Some studies revealed that the modal strain energy is the very efficient indicator in structural damage localization. When a particular vibration mode stores a great amount of strain energy in a particular structural load path, the shape

and frequency of that mode are highly sensitive to variations in that load path. This method was developed by Stubbs et al. (1992) for beam type structures and is based on evaluating the reduction in modal strain energy between two structural DOFs. Later, Stubbs and Kim (1996) used this approach to introduce a damage index based on alteration in energy of modal strain to identify the damage location and its size with no baseline modal properties. Shi et al. (1998) introduced the concept of elemental modal strain energy (EMSE) along with the modal strain energy change ratio (MSECR) as a suitable damage indicator. Shi et al. (2000b) and Shi et al. (2002) proposed two damage quantification algorithms on the basis of sensitivity analysis of modal strain energy. Application of both flexibility method and strain energy method for damage detection in a simply supported beam was discussed by Alvandi and Cremona (2006). Random force excitations were utilized to measure modal parameters and discussion concluded that both methods are capable of damage detection. Nevertheless, in case of simultaneous and complex damages, the flexibility method was reported to be less efficient and strain energy method was demonstrated to be stable in the presence of noisy signals.

Despite the fact that damage identification methods on the basis of mode shape changes and their derivatives provide spatial information about location of damage in structure, in practical applications they suffer from some disadvantages listed in the following:

- i) For a complex structure, the required array of measuring points has to be dense.
- ii) Random errors cause more statistical variation compared to resonant frequencies due to sensitivity of mode shape measurements.
- iii) Mode-shape approaches, especially the curvature techniques are not fully applicable for structures with complexity in their configuration.
- iv) Although rotational mode shapes have higher sensitivity to structural changes compared with translational mode shapes, they are still difficult to be measured by current modal test techniques.

2.2.6 Model Updating Methods

Modal updating methods are another class of damage identification approaches and their basic idea is the modification of a structural model in order to reproduce the measured static or dynamic responses obtained from the damaged structure as closely as possible. Modal updating algorithms deal with obtaining the updated matrices on the basis of the original model, the governing equations of structural motion and the measured data. The model is built up on the stiffness, mass and/or damping matrices obtained from finite element theory. Indication of the location and extent of damage is provided through the comparison between updated matrices to the original model correlated to the intact structure.

The aim of model improvement is to seek an accurate model correlated to the actual structure for estimating the response of the structure to disturbances and suggesting the modifications in the structural configuration for performance improvements. In the construction of the original finite element model it is usual to make some simplifying assumptions. Often there are detailed features in the geometric representation of the structure that cannot be modeled by a computationally economical finite element mesh, or the boundary conditions and joints between components are seldom fully understood. In such cases the analyst may, according to experienced engineering judgments, manage to find a compromise with acceptable results.

The damage detection applications aim to recognize variations in mass, damping and stiffness matrices originated by damage. The modal updating methods utilize common basic set of equation, while differences in various damage detections can be classified as follows: i) objective function to be minimized; ii) constraints placed on the problem; iii) numerical scheme applied to perform the optimization. They, either for damage detection application or model improvement, can be categorized into three groups: i) Optimal

matrix updating method; ii) Sensitivity-based updating method; iii) Eigenstructure assignment method.

Optimal matrix update methods utilize a closed-form direct solution to estimate the structural parameter matrices of the damaged structure or the matrix perturbations caused by the damage. Basically, the optimal matrix update problem, as it has been formulated by such researchers as Kabe (1985) and Berman and Nagy (1983), is to minimize the Frobenius norm, a common cost function, of the global parameter matrix perturbations under the constraints of zero modal force error and preservation of the matrix symmetry. Smith (1992) presented an iterative technique to the optimal update problem that enforces the sparsity of the matrix at each iteration step. The sparsity is enforced by multiplying each entry in the stiffness update by either one or zero, depending on the correct sparsity pattern. The minimum rank perturbation theory is also proposed to apply in the matrix updating methods. Doebling (1996) presented a method to compute a minimum-rank update for the elemental parameter vector, rather than for global or elemental stiffness matrices.

Although the optimal matrix update method, with constraints based on structural vibration mechanics and physical connectivity, may be useful in an engineering sense for the model refinement problem, its applicability for damage detection is doubtful. It is because the damage typically causes local changes in the stiffness matrix only at some locations, whereas the optimal matrix update would tend to have the changes throughout the entire stiffness matrix and it could not identify the damage location.

Sensitivity based model update method is based on the solution of first-order Taylor series that minimizes a function of residual errors caused by structural parameter matrices perturbation. In general, the sensitivity matrix is obtained utilizing an analytic model by finding derivatives of the natural frequencies with respect to stiffness perturbations at each potential location of damage. The updating process typically iterates the solution

until the damage variables have satisfactorily converged to the true system perturbations. However, this formulation only works if the structural modification (that is, the amount of damage) is small. Ricles and Kosmatka (1992) utilized a sensitivity-based matrix approach to locate potential damaged regions and evaluate the damage estimation based on the first-order Taylor series. Hemez and Farhat (1995) utilized a sensitivity-based matrix method that formulates the sensitivities at the element level, with the advantage of being calculated more efficiently than the sensitivities at the global matrix level. Lu and Law (2007) proposed a method directly using sensitivity of acceleration response with respect to structural parameters for damage detection. The merits of the method lie in the use of a few sensors in the measurement.

Eigenstructure assignment method is another type of matrix update method which is based on the design of a fictitious controller that minimizes the modal force error. The controller gains are then interpreted as parameter matrix perturbations to the undamaged structural model. Therefore, by inspecting the changes in the matrices of the model, the extent of damage can be estimated. Notable among the researchers who have formulated such procedures based on the eigenstructure assignment theory are Zimmerman and Widengren (1990), Zimmerman and Kaouk (1992), Lim and Kashangaki (1994), and Cobb and Liebst (1997).

2.2.7 Neural network and genetic algorithm

Computational intelligence techniques, such as the neural networks and genetic algorithm, also have been used to deal with the difficulty of damage assessment, because of their excellent capability in pattern recognition. In recent years, many authors have comprehensively explored the optimization problem using neural networks (Tsou & Shen, 1994) and genetic algorithms (Mares & Surace, 1996; Hao & Xia, 2002), by examining the variation of localized damage as a function of modal data. In contrast to the traditional mathematical methods, one of the significant characteristics of

computational intelligence techniques is their robustness and efficiency when it comes to coping with noise, insufficient information, and uncertainty.

Neural networks (NNs) can be used to the damage assessment of structures due to the versatility in dealing with various types of input and output and quick computational capability. Wu et al. (1992) applied the back propagation NNs technique to recognize the locations and the extent of individual member damage of a simple three-story frame. Yun and Bahng (2000) proposed a sub-structural identification method for complex structures using multilayer perceptron. Lee et al. (2002) applied the NN technique utilizing the modal data to health monitoring of bridges. Hadzima-Nyarko et al. (2011) implemented a multilayer perception (MLP) neural network to model the relationship between the structure parameters and the damage ratio coefficient, for examining the damage level of a bridge.

Genetic algorithms (GAs) have been recognized as promising intelligent search techniques for difficult optimization problems. That is why special attention has been given to the design of an effective damage detection procedure. Friswell et al. (1998) applied the GA and eigensensitivity algorithms to identify the location and extent of damage in a structure by optimizing a discrete weighted objective function based on the error between identified and analytical frequencies and mode shapes with a penalty term. Hao and Xia (2002) applied a genetic algorithm with real number encoding to identify the structural damage by minimizing the objective function, which directly compares the changes in the measurements before and after damage. Three different criteria were considered, namely, the frequency changes, the mode shape changes, and a combination of the two. The algorithm did not require an accurate analytical model and provided better damage detection results for the beam than the conventional optimization techniques. Vakil-Baghmisheh et al. (2008) successfully applied the genetic algorithm to predict the

size and location of a crack in a cantilever beam by minimizing the cost function, which was based on the difference of measured and calculated natural frequencies.

2.3 Advanced damage detection methods based on wavelet transform

Although for the majority of damage detection algorithms (Doebbling et al., 1998; Ren & De Roeck, 2002; Pothisiri & Hjelmstad, 2003; Fan & Qiao, 2011), the focus has been on modal analysis of response signals in the time domain by extracting frequency and mode shape information, in recent years, a rapid growth in the application of algorithms based on the wavelet theory to damage assessment has been observed.

The wavelet transform (WT) has emerged as a promising tool for structural health monitoring and damage detection due to its potential characteristics such as singularity detection, good handling of noisy data and being very informative about damage location/time. In particular, wavelets have advantages when structural dynamic responses are complex and non-stationary. It was Newland (Newland, 1993; Newland, 1994) who first observed such potential of the wavelet transform and hence, introduced wavelet functions to vibration analysis. Zeldin and Spanos (1996), then applied the wavelet theory to random field synthesis. Basu and Gupta analyzed the non-stationary seismic responses of dynamical linear (Basu & Gupta, 1997, 1998) and non-linear systems (Basu & Gupta, 1999a; Basu & Gupta, 1999b) by using wavelet functions.

Wavelet functions are included in the family of basis functions that are capable of depicting a signal in a localized frequency (or scale) and time (or space) domain. The main advantage obtained by using wavelets was the capability to execute local analysis of a signal, i.e. zooming in on any interval of space or time. Wavelet analysis is capable of demonstrating some hidden features of the data that conventional Fourier analysis fails to detect. The WT analysis has been widely used in many engineering fields (Taha et al., 2006b; Jiang & Adeli, 2007; Jiang & Mahadevan, 2011).

WT is categorized into continuous wavelet transform (CWT), discrete wavelet transform (DWT) and wavelet packet transform (WPT). Numerous studies have used different types of the wavelet transform for detecting structural damage.

2.3.1 Continuous wavelet transform

A CWT has been employed to divide a continuous-time function into wavelets. A CWT provides a redundant; with more detailed description of a signal. Application of the CWT extends to machinery diagnostics and condition monitoring which considered by many researchers (Staszewski & Tomlinson, 1994; Wang & McFadden, 1995; Staszewski et al., 1999; Peng & Chu, 2004). Staszewski and Tomlinson (1994) presented an application of the WT in detection of a damaged tooth in a spur gear based on a similarity analysis of patterns obtained from the modulus and phase of the wavelet transform. Wang and McFadden (1995) used the WT to analyze actual gearbox vibration signals in the time domain and found their local features. It was shown that the gear damage could be correlated to features in the wavelet domain. Staszewski et al. (1999) used a cross-wavelet analysis to improve the interpretation of Lamb wave data related to defects in a carbon fiber composite plate. Also, Peng and Chu (2004) conducted a systematic survey on wavelet analysis and its applications in mechanical vibration signal analysis, including the topics such as time–frequency analysis via wavelet scalogram, singularity detection and denoising based on wavelet transform.

A relatively recent area of research in structural damage detection and localization is based on the wavelet transform and its application into mode shapes. The wavelet transform acts as a differential operator and can be applied effectively even for noisy signals. Substantial vibrations of wavelet coefficients originated by local abnormalities in a signal obtained from the neighborhood of damage, pave the way for observing the damage which cannot be identified directly from mode shapes. Gentile and Messina (2003) explained the potential of the WT for detecting damage in structures in a more

rational manner. They highlighted the ability of the CWT to identify damage by means of performing an equivalent derivative of the signal. Damage identification was performed by applying the CWT to the mode shapes at certain scales. The Haar and Gaussian mother wavelet were used during the wavelet analysis. Damage detection result was clearly better for mother wavelet with large vanishing moments. Chang and Chen (2005) detected the locations and sizes of multi-cracks in a beam by wavelet analysis. The crack type was open crack and was represented as a rotational spring. The mode shapes of the multi-cracked beam under free vibration were analyzed by WT. The positions of the cracks were observed as a sudden change in the plot of wavelet coefficients. The natural frequencies of the beam were used to predict the depth of the cracks through the characteristic equation. The limitation of this method was that there were two peaks near the boundaries in the wavelet plot and the crack could not be detected when the crack was near the boundaries. Zhong and Oyadiji (2011) proposed a technique for damage detection in beam-like structures with small cracks without baseline modal parameters. The technique was based on the difference of the CWTs of two sets of mode shape data which corresponded to the left half and the right half of the modal data of a cracked simply-supported beam. They analyzed the effect of the sampling distance, and they introduced a spline interpolation to increase the number of input points for the WT. They also proposed a damage parameter based on the addition of the results for all the mode shapes. Jiang et al. (2012) proposed a method for crack detection in beams by using slope of the mode shape to detect cracks. They introduced the angle coefficients of complex CWT. This method detected the exact locations of singularities in an easier way compared with the CWT of the mode shape.

Previous numerical studies have shown high level of accuracy and very good efficiency of the wavelet transform with no consideration of experimental verification while for practical applications of the wavelet damage detection techniques, experimental data is a

necessity. Measurement precision and sampling distance are two vital factors that contribute in applicability of the wavelet detection techniques. Douka et al. (2003) found fundamental vibration modes of a cracked cantilever beam using CWT to estimate the location and size of the crack. Rucka and Wilde (2006) applied CWT to the fundamental mode shape of beam and plate structures by using the reverse biorthogonal wavelet to identify the damage location. The main disadvantage of this method was the need of numerous sensors, which were mounted on the surfaces of the specimens, to obtain the mode shapes of the damaged structures. Location of damage was indicated by a peak in the spatial variation of the transformed response. Gökdağ and Kopmaz (2009) conducted the WT on the experimental mode shapes of a damaged beam to prove the feasibility of their numerical simulation. The undamaged mode shape as an approximation function was extracted from the damaged mode shape by DWT. A damage index was then obtained by calculating the difference between the CWT coefficients of the damaged mode shape and the approximation function. Generally, acquiring modal shapes in practice, involves installing a large number of sensors which is not always straight forward or practical. This not only makes the installation process labour intensive, but can also influence structural/vibrational properties. Such approaches have two common drawbacks: (i) adding sensors can add undesirable damping effects on the structure; altering its modal properties (Quek et al., 2001b); (ii) the total number of sensors deployable are largely limited by the physical form of the accelerometers, this places a bottleneck on the spatial resolution of the acquired modal shapes, which makes damage localization less accurate (Radzieński & Krawczuk, 2009). In addition, if accelerometers are not wireless, a significant amount of cabling must also be laid throughout the structure.

To reduce the quantity of the sensors used for the experiment and to facilitate the operation, another spatial data was used for damage detection based on the dynamic response of structure. Quek et al. (2001a) employed Haar wavelet and Gabor wavelet

functions on static deflection profiles of simply-supported and fixed end beams to examine the sensitivity of the wavelet technique in detection of cracks. Other parameters including crack characteristics as length, orientation, width of slit, and boundary conditions were also investigated. Zhu and Law (2006) proposed a method for damage identification of bridge structures based on CWT. For that purpose, they developed a model for calculating dynamic deflections of a cracked simply supported bridge subjected to a moving load. Damage was detected by applying the CWT to dynamic displacement influence lines calculated at one selected point in the bridge beam. The detection was done using the Gauss 2 mother wavelet from scales one to 512 with unit increments. The larger scales contained the information necessary to perform the damage location identification. Spanos et al. (2006) also applied CWT to damage detection problems in which the difference between the displacement response of the damaged and the undamaged beams under various loading conditions was used. Umesha et al. (2009) applied the CWT and Symlet wavelet to detect the location and also to quantify the damages in model beams by using the deflection response as an input signal. This method emphasized on measuring the deflection at a particular point for various locations since in real application it is often difficult to measure deflection at several points due to a large amount of instrumentation. They utilized a fixed beam with single damage to demonstrate the method. The damage was modeled as a reduced stiffness element in finite element analysis.

As mentioned above, while majority of researches have been conducted on the damage detection of beams by using wavelets, very few studies have been carried out on estimation of the severity of the damage. Hong et al. (2002), however, were able to develop a consistent mathematical framework for the wavelet analysis of damaged beams. They showed that the singularity of the vibration modes can be described in terms of Lipschitz regularity by utilizing the Mexican hat wavelet function. Magnitude of the

Lipschitz exponent was employed as a useful indicator of damage extent. More specifically, they found that the Lipschitz exponent became smaller as the damage got more severe.

A more rational method for calculating the severity of damage was proposed by Douka et al. (2003). In this method, the location of damage was determined by the sudden change in the spatial variation of the CWT with the Symlet mother wavelet with four vanishing moment applied to the mode shapes of a beam. The size of the single open crack was calculated through an intensity factor related to the Lipschitz exponent of the CWT at the crack location. A numerical and experimental model of a cantilever beam was done to test the proposed method. One year later, Loutridis et al. (2004) proposed a similar procedure for numerical and experimental analysis of a cantilever beam with two open vertical cracks. The results were similar to those obtained by Douka et al. (2003).

A common point considered by several researchers is the dependence of the wavelet coefficients to the damage location. Two cracks located in the cantilever beam with the same crack depth can have different wavelet coefficients. This is caused by the slope of the fundamental mode shape which is different for the two crack positions. Such problem can be generalized into cases like evaluation of the damage severity of several cracks present in the beam. Pakrashi et al. (2007) applied the CWT for detecting and locating damage in a beam. As opposed to other studies which also used the CWT to detect damage, they improved the efficiency of this technique by applying a partial windowing to the deflected (static or dynamic) shapes. Moreover, they proposed to measure the severity (crack depth) of the damage using the kurtosis of the transformed wavelet deflected shape. The methodology for damage detection was proved in a simulated and experimental simply supported beam by using Coiflet 4 mother wavelet with 8 vanishing moments.

2.3.2 Discrete wavelet transform

The DWT was invented by the Hungarian mathematician Alfred Haar (Haar, 1910). Like other WTs, DWT can transform discrete time-domain signals into wavelet coefficients in time-frequency domain. The transformation is achieved by decomposing signals into two components through low pass and high pass filter, each of which carries information of the original signals.

Deng and Wang (1998) directly applied the DWT to structural response signals to locate a crack along the length of a beam. Wang and Deng (1999) discussed the feasibility of the DWT of spatially distributed structural response measurements. They found that presence of a crack can be detected by observing sudden changes in the spatial variation of the decomposed response. However, no discussion regarding quantification of damage extent was provided. Al-Khalidy et al. (1997) used the DWT to detect the fatigue damage in structures, modeling damage as a random impulse in the input signal. Hou et al. (2000) examined the potential of the DWT for detecting the precise time of damage occurrence. They proved that damage caused by change of stiffness in structures may be detected by spikes in the first details of the wavelet decomposition of the response data. For that purpose they used a simple numerical model with three parallel breakable springs. In addition, similar results were shown with the data collected from roof of building during 1971 San Fernando earthquake. Lu and Hsu (2002) conducted a research on the wavelet transform for structural damage detection. The DWTs of two sets of vibration signals in the space domain obtained from damage and undamaged structures were compared and occurrence of defects as well as their number and location were detected. It was shown that even a minor localized defect can lead to considerable changes in the wavelet coefficient of the vibration signals. Hera and Hou (2004) applied the DWT approach to the FEM model of the ASCE structural health monitoring benchmark study. They found, similar to (Hou et al., 2000), that the time when the damage occurs can be detected by

looking at the spike of the details at level 1 of the DWT, while the damage location can be identified by looking at patterns in the spatial distribution of spike; in other words, the distribution of spikes in the response signals was found to be related to the distance of response signals to the damage location. Grabowska et al. (2008) used DWT with propagating Lamb waves for identification of the fatigue crack. Beskhyroun et al. (2010) applied DWT for structural damage detection and health monitoring. The method was based on only the output data without the need for measuring the excitation forces, any modal identification or numerical models. The applicability of utilizing piezoelectric actuators for exciting large structures such as steel bridges was also investigated. Several damage scenarios were introduced to the test structure by removing bolts from some stiffeners located on the web of the main girder. Many researchers observed that structural damage or the change in system stiffness could be detected by irregular spikes in details of the wavelet transform of the response data. The most obvious difference was that the DWT uses scale and position values based on powers of two.

Although stand-alone CWT- or DWT-based approaches have been shown to be beneficial for damage assessment, more recently, wavelet analysis has been extended to the WPT-based approaches and to approaches incorporating the WTs with other methodologies, e.g., statistical theory, the Hilbert transform (HT), Hilbert-Huang transform (HHT), empirical mode decomposition (EMD), and neural networks—to obtain a more effective algorithm for damage detection by bringing forth the strengths of each application.

2.3.3 Wavelet packet transform

Nikolaou and Antoniadis (2002) used the WPT, instead of the DWT, to detect faults by analyzing vibration signals coming from bearings having localized defects. Yan et al. (2004) detected the crack in a honeycomb sandwich plate by using two structural vibration damage feature indexes: natural frequency and WPT energy index. Energy of the response of cracked structures, as compared to that of the response of the intact

structure in some special frequency bands, exhibited some remarkable differences, since the structural damage suppressed or enhanced some components of response in special frequency bands. It was found that the energies of the various WPT components yielded ample information on structural damage, and that the energy variation of one or several components can indicate a special status of structural damage; therefore, the index extracted from the WPT component energy can be utilized to reveal the special characteristics of a damage case. Moreover, Law et al. (2005) presented a WPT sensitivity-based method to detect damage in a structure. Measured response signals from a structure were first decomposed into the WPT components. Then components that contained much of the structural system information were identified, and their energy and first-order sensitivity to local damage were computed. In short, the sensitivity of the WPT component energy with respect to local change in the system parameters was derived analytically to detect damage in structures. Ding et al. (2008) developed a procedure for damage alarming of frame structures by introducing a damage alarming index, ERVD, based on energy variations of structural dynamic responses decomposed by WPT. The ASCE structural benchmark data was used to present the practicability of the damage alarming procedure for the frame structure. The damage alarming index ERVD was found sensitive to local damage in presence of actual measurement noise. Efficiency of the proposed index ERVD associated with lower decomposition level and dominant frequency bands, for detection of damage occurrence was illustrated. Amiri and Asadi (2009) compared the wavelet and WPT in processing ground motion records. The signal was expressed as linear combination of time-frequency atoms which were obtained by dilations of the analyzing functions, and were organized into dictionaries as wavelet packets. Mikami et al. (2011) employed a new approach for damage identification in beam-like structure using a wavelet packet-based technique without baseline modal parameters of intact structure. The measured dynamic signals were decomposed into the

wavelet packet decomposition components. Then, the power spectrum density (PSD) of each component was estimated and a damage localization indicator was computed to indicate the structural damage. Also, the effect of damage location and the influence of wavelet type and the decomposition level were investigated. The results demonstrated the efficiency of the proposed method for damage detection.

2.3.4 Combining wavelet transform with other techniques

An effective damage index is a critical factor to detect damage. Many damage indices were studied based on the wavelet transform. In particular, Ren and Sun (2008) suggested the combination of information entropy and discrete wavelet transform, as (Rosso et al., 2006), having a damage-sensitive feature to characterize the level of irregularity in the measured signals to identify the occurrence and location of damage in beam structures. Wavelet entropy, relative wavelet entropy and wavelet-time entropy were employed to identify and locate damage. Two laboratory test cases along with numerically simulated harmonic signals were considered to investigate these features. Wavelet-time entropy was demonstrated as a sensitive damage feature for detection of abnormality in measured successive vibration signals. Occurrence and location of damage, the two parameters to detect from vibration signals, could be measured from the damaged and intact structures. Relative wavelet entropy was a suitable feature to do so; and flexibility of relative wavelet entropy made it a good method for choosing the reference signal obtained from undamaged location of the target structure. Tsai et al. (2009) proposed a complex CWT-based entropy method for damage identification of wind turbine blades and distinguishing the healthy and impaired blades. Feasibility of the method in the blade damage detection was discussed along with computational requirement regarding wavelet entropy of the healthy blades, which is not always available in practical applications. Yun et al. (2011) applied wavelet entropy to detect spatial locations of damage. In order to realize decentralized damage identification, DWT was carried out in Imote2 wireless sensors.

Recently, Lee et al. (2014) proposed a new reference-free damage detection algorithm based on the continuous relative wavelet entropy (CRWE) for truss bridge structures. The damage-sensitive index (DSI) of each sensor's location was defined by CRWE measurements of different sensor-to-sensor pairs. The CRWE was reported to be able to detect damage but with considerably large computation cost for the real time monitoring algorithm.

The feasibility of damage assessment, based on statistical analysis combined with the WPT, was shown by both Sun and Chang (2004) and Han et al. (2005). Sun and Chang (2004) proposed a statistical pattern classification method based on the WPT. The acceleration signals of a structure excited by a pulse load were decomposed into WPT components. The energies of these wavelet packet components were calculated and sorted by their magnitudes. Components having only slight signal energy were discarded, since they were easily contaminated by measurement noise. The remaining dominant energies were defined as constitutive elements of the wavelet packet signature (WPS). Two damage indicators were then formulated, based on the WPS. Basically, these two indicators quantified the deviations of the WPSs from the baseline reference. The statistical control process was used to determine the threshold value for the damage indicators and to monitor any changes in them. Any indicator that exceeded the threshold would set off a damage alarm. Furthermore, Han et al. (2005) proposed a damage detection index, called the wavelet packet energy rate index (WPERI), for detecting damage in beam structures. To establish threshold values for damage indexes, WPERIs, X-bar control charts were constructed, which utilized the probabilistic control limits based on the estimate of the process mean, and one-sided confidence limits were set as thresholds for damage alarming. The proposed approach was applied across three damage scenarios in the laboratory to a simulated simply supported beam and to steel beams. Both the simulated and the experimental studies showed that the WPT-based energy rate index

was a good candidate index, sensitive to local structural damage. Law et al. (2013) developed an approach based on WPT and statistical analysis to describe the damage extent of the structure. The developed method was not dependent on reference baseline measurement and there was no need of model for the damage assessment and monitoring of the structure with alarms at a significant level. Structure was first subjected to an impact load and the corresponding response signal was normalized and decomposed into WPT component, whose energies were then computed to get to the energy distribution. In order to classify the structure from variations in the WPT energy distribution, an F-test based statistical similarity comparison was used along with development of a statistical indicator to describe the damage extent of the structure.

A combination of the WPT and the neural network (NN) approaches to damage diagnosis was utilized by Yen and Lin (2000), Sun and Chang (2002), Yam et al. (2003), and Diao et al. (2006). Sun and Chang (2002) combined the WPT and neural-network models to assess structural damage. First, the energies of the WPT components were calculated, then those that were both significant in value and sensitive to change in structural rigidity were selected as damage indices and were employed as inputs into the NN models. The numerical simulations were conducted by using a three-span continuous bridge under impact excitation. It was concluded that the WPT component energy was a sensitive condition index for structural damage assessment, and that this index was sensitive to changes in structural rigidity but insensitive to measurement noise. Yam et al. (2003) presented an integrated method for damage identification based on the energy variation of the WPT components of the structural vibration response and neural networks. They constructed a non-dimensional damage feature proxy vector to be used in detecting damage in composite structures. The damage feature proxy vector was calculated based on energy variation in the WPT components of the structural response before and after the occurrence of damage, and neural networks were used to establish the mapping

relationship between the damage feature proxy and damage status (i.e., damage location and severity). This approach required accurate model information for both healthy and damaged conditions in order to train the neural networks; that proved to be difficult and challenging in practice, especially for complicated structures. Diao et al. (2006) proposed a two-step structural damage detection approach based on wavelet packet analysis and neural networks. Initially, the location of the damage member was localized by probabilistic neural network according to the wavelet packet node energy change. Then, the damage extent of the damaged member was obtained by back-propagation network according to the wavelet packet node energy.

Prominent among the researchers who have sought to achieve enhanced algorithms for damage assessment by combining the wavelet theory with some other signal processing technique (e.g., the HT, HHT, or EMD) are Shinde and Hou (2005), Hou et al. (2006), and Chen et al. (2007).

Shinde and Hou (2005) incorporated a WPT-based sifting process with the classical HT for structural health monitoring. The original signal was decomposed into its components by a wavelet packet analysis with a symmetrical mother wavelet. Both the energy entropy and the Shannon entropy were utilized as sifting criterion. The dominant components of the WPT of a signal were sifted out based on the percentage contribution of entropy of an individual component, to the total one of the signal. The dominant component of the original signal from the WPT-based sifting process had a quite simple frequency characteristics and was suitable for use with the HT. The transient frequency content or the so-called instantaneous frequency of the component was obtained from the phase curve of the HT of the component. Since, for a healthy structure, the associated instantaneous frequency was time-invariant, any reduction in the instantaneous frequency could be applied as an indicator of structural damage to reflect structural damage. The viability of the proposed sifting process, used both for detecting abrupt loss of structural

stiffness and for monitoring development of progressive stiffness degradation, was demonstrated by two case studies.

In addition, Hou et al. (2006) applied the improved shifting process of Shinde and Hou (2005) to the structural health monitoring of earthquake-excited structures; they applied the concept of the confidence index (CI) to validate the results obtained for normalized mode shapes. A cantilever composite box was considered by Chen et al. (2007) to extract the structural damage information from its response signals through an improved HHT. The WPT was first employed to decompose the signal into sub-signals which were then decomposed again into multiple intrinsic mode function (IMF) components by EMD. In order to eliminate the unrelated IMF components, the IMF selection criterion was employed. The HHT was then applied to transform the retained components to obtain the instantaneous energy of all the sub-signals. These researchers found, by comparing the instantaneous energy corresponding to the IMFs of an intact wingbox with that of a damaged one, that some instantaneous energy was obviously changed. Based on this fact, they defined the variation quantity of instantaneous energy as a feature index vector, and showed that this vector was sensitive to even a very slight damage.

2.4 System identification based on the wavelet transform

A commonly adopted approach to the identification of a structural system is through modal analysis. Identification of the modal characteristics of a structure can be carried out either by time-domain or frequency-domain methods. When it comes to considering a system's properties with respect to time, frequency domain methods are not so adaptable. On the other hand, time domain methods are usually sensitive to noise due to the presence of all the frequency components in the data. To overcome these difficulties, several techniques have been developed in recent years that utilize time-scale or time-frequency domain analysis. Many of these methods are based on wavelet analysis, with

application to linear and non-linear systems, because of the ability to retain information of local frequency content and variation with time, together with the advantage of flexible windowing over short-time Fourier transform (STFT). The use of the wavelet transform is particularly advantageous in problems related to system identification. The properties of frequency localization, for instance, can be useful in detecting and separating individual vibration modes of MDOF linear systems. During the identification process, the property of multi-resolution analysis in discrete wavelet transform can filter out the measurement noise from the structural response without the use of additional filters. Furthermore, the wavelet transform coefficients can be associated directly with the structural parameters (Joo, 2012).

The wavelet-based identification approaches of system parameters can be divided into two groups. Researchers in the first group employed the continuous wavelet transform (CWT)-based approach, whereas those in the second group used the discrete wavelet transform (DWT)-based approach.

2.4.1 Continuous wavelet transform

Initially, it was the CWT-based approaches that were used to identify linear systems. A class of identification method was developed by Ruzzene et al. (1997) and Staszewski (1998) based on the CWT by using the Morlet wavelet function to identify the natural frequencies and damping ratios of a structural system. More specifically, Ruzzene et al. (1997) demonstrated that when high damping was present in a system, the HT-based approach produced more errors in estimating the envelope and the instantaneous frequency. A consistent improvement could be achieved when the CWT-based approach was used, rather than the HT, to approximate the envelope signal and its instantaneous frequency while seeking to identify modal parameters. Staszewski (1997) presented that the CWT approach can be employed to identify the damping ratios and natural frequencies of MDOF systems having either close or well-separated vibrational modes.

This was done by decoupling the impulse response of MDOF systems into the time-scale domain and then identifying each damping ratio for each decoupled signal; such identified damping ratios were shown to be quite accurate.

Lardies and Gouttebroze (2002) developed a CWT approach to identify damping ratios of closely spaced mode systems, an approach that applied a modified Morlet wavelet function and demonstrated better resolution than the CWT approach developed by Staszewski (1997). Slavič et al. (2003) employed a CWT approach based on the Gabor wavelet function to estimate damping ratios.

Staszewski (1998), Lardies and Gouttebroze (2002) and Slavič et al. (2003) applied their identification methods to proportionally damped MDOF systems, but made no attempt to identify the mode shapes. However, Argoul and Le (2003) presented a method based on the Cauchy wavelet function to identify natural frequencies and damping ratios, as well as the mode shapes of viscous damped MDOF systems. Sone et al. (2004) identified the system parameters based on the Mexican hat wavelet using only the acquired acceleration signals. In terms of CWT, the multi-resolution property was utilized to filter out measurement noise, and the localization property was used to separate different modes in the MDOF case. Le and Paultre (2012) proposed a method that directly used the raw ambient response with CWT by modifying the formulation of the CWT of the ambient response. The wavelet analysis of the free responses of a linear mechanical system was used to estimate its natural frequencies, viscous damping ratios, and mode shapes, using either the modulus or the phase of the wavelet transform with ridge and skeleton notions. Staszewski (1998) and Yan and Miyamoto (2006) introduced the CWT to an extended area of application called time-varying or nonlinear systems. To identify the instantaneous characteristics of nonlinear systems out of impulse response, Staszewski (1998) proposed an approach and analyzed two simulated examples with the Morlet wavelet function. These examples were consisted of a SDOF system with cubic stiffness

nonlinearities and coulomb friction and a 2DOF system with cubic stiffness nonlinearities: such nonlinearities were identified but not quantified. In a comparison conducted between CWT approach with Morlet wavelet function and HT or HHT for estimation of the modal parameters, Yan and Miyamoto (2006) reported better performance of the former one.

Further research works that aimed at identifying nonlinear systems by utilizing the CWT were carried out by Garibaldi et al. (1998), Staszewski (2000), Lenaerts et al. (2004), Joseph and Minh-Nghi (2005), Ta and Lardies (2006) and Wang et al. (2013).

Staszewski (2000) summarized the wavelet applications for the analysis and identification of nonlinear systems. The contents include backbone identification based on wavelet ridges and skeletons, damping estimation procedures, wavelet-based frequency response functions, cross-wavelet analysis, solving nonlinear different equations and fractal analysis. Garibaldi et al. (1998) identified only nonlinear damping mechanisms based on the CWT, while Lenaerts et al. (2004) identified a nonlinear system by utilizing two different method: a method based on the CWT and a method using the restoring force surface. Both methods exploited the system free response and results in the estimation of linear and nonlinear structural parameters provided experimental data. Joseph and Minh-Nghi (2005) used the modified Morlet wavelet function to identify and quantify the damping in a non-linear oscillator using its free decay response. For parameter identification, two methods were presented to estimate instantaneous frequency, damping and envelope of the system. The first method was used cross-sections of the CWT and the second method was based on ridges and skeletons. The earlier method was general and gave accurate results in the case of noisy non-linear oscillators.

In another study by Ta and Lardies (2006), the ridges and skeletons of the CWT were used to identify the weak nonlinearities on damping and stiffness. It was assumed that the nonlinear signal can be taken as a linear combination of monocomponents and each

monocomponent was associated with a kind of nonlinearity. The type and order of nonlinearity for each monocomponent were then identified by a least squares estimation using the instantaneous characteristics from wavelet transforms and the predefined class of models. With weak nonlinearity assumption, the effects of nonlinear damping and nonlinear stiffness on the system response were separated, in such a way that the nonlinear damping could only affect the decaying envelope and the nonlinear stiffness could only affect the instantaneous frequency. However, this assumption was not true for strong nonlinearity. Wang et al. (2013) proposed a method based on the wavelet ridges of CWT for the instantaneous frequency identification of time-varying structures. To eliminate noise effect, a penalty function was first imposed, and then the dynamic optimization technique was implemented for wavelet ridge extraction. The instantaneous frequencies were then identified from the extracted wavelet ridges.

2.4.2 Discrete wavelet transform

Another class of identification method which utilized discrete wavelet transform (DWT) for linear time-invariant systems was introduced by Robertson et al. (1998a, 1998b). They used discrete Daubechies (DB) wavelet transform to extract the impulse response functions from input and output data of linear dynamic systems. This approach was then used along with the eigensystem realization method, to obtain the damping parameters and mode shapes of a system subjected to various excitations. Lamarque et al. (2000) proposed a logarithmic decrement formula, having the CWT coefficients, similar to the logarithmic decrement formula for free vibration of a SDOF system. They were able to derive a discrete wavelet-logarithmic decrement formula using the approximation coefficients of the DWT to estimate the damping of MDOF systems. Also, Hans et al. (2000) applied the method presented in Lamarque et al. (2000) to obtain the damping of a building subjected to shock and harmonic excitations. Huang et al. (2005) applied the DWT to discrete equations of motion and determined modal parameters such as natural

frequencies, damping ratios, and mode shapes of structures using either earthquake or free decay responses.

In addition, the DWT-based approaches for identification of linear time-varying and nonlinear systems were further explained by Ghanem and Romeo (2000), Luk and Damper (2006), Chen et al. (2006), Pawlak and Hasiewicz (1998), Xu et al. (2012) and Li et al. (2012). Ghanem and Romeo (2000) proposed a discrete wavelet identification approach to analyze time-varying structures which was associated with a differential equation model that related input and output responses using wavelet Galerkin approach. Chen et al. (2006) developed an approach on the basis of the DWT by utilizing the Haar wavelet function to identify linear time-varying systems. Similarly, Pawlak and Hasiewicz (1998) applied the multiresolution analysis of the Haar wavelet function to the construction of nonparametric identification techniques of nonlinear systems. A wavelet-based state-space method was developed by Xu et al. (2012) to identify dynamic parameters in linear time-varying systems. The method did not require computation of the second connection coefficients, as compared with the linear time-varying identification method presented by Shen and Law (2006). Li et al. (2012) proposed an approach using the extended Kalman filter (EKF) and wavelet multiresolution for identifying the tangent stiffness matrix and the hysteresis curves of structures during strong earthquakes. This method required the structural response from only a limited number of DOFs. The identification could then be divided into two stages. In first stage, the structural responses at all DOFs were estimated utilizing the EKF method based on the structural model at previous step. In second stage, based on the estimated full states, wavelet multiresolution analysis was utilized to identify the tangent stiffness matrix and the hysteresis-restoring force curves of the structure.

2.5 Summary

In this chapter, a comprehensive literature reviews of existing vibration-based damage detection methods, applications of wavelet transform in damage detection and system identification were presented. Vibration-based damage detection methods have shown promising results and still under fast advances in relevant technologies such as sensing, system identification, monitoring systems, algorithms and logics in signal processing, etc. Modal parameters such as natural frequencies and mode shapes are the most commonly used measurements for vibration-based damage detection and model updating methods. For the practically viable damage detection system, real-time and reference-free features in damage detection will upgrade current SHM technology.

In addition, many researchers have reported the benefits and applicability of multiple formulations of the wavelet theory in achieving damage detection and system identification tool for SHM, to overcome the limitations and drawbacks of other signal processing techniques in the framework of structural dynamics. A considerable amount of research carried out over the last three decades and very well demonstrated that the wavelet theory can be utilized to achieve satisfactory damage detection and system identification.

A brief description of each issue was presented to show various ways in which the wavelet theory has been applied to solve the typical problems associated with damage detection and system identification. This review discussed various types of the WTs (e.g., the CWT, and DWT) with the whole range of applications used in damage diagnosis and system identification of structures of different scales ranging from relatively small (e.g., gear boxes) to notably large (e.g., buildings and bridges).

Moreover, this chapter has closely looked into various features of the theory of wavelet and has demonstrated the way researchers and pioneers have employed these features to obtain damage detection and system identification. The performance of the wavelet-based

approaches, as stand-alone methods, has been reported to be efficient in damage detection and system identification, whereas in combination of wavelet theory and other signal processing techniques such as neural networks and statistical theory, better results were obtained. Although much research has been conducted in this area, nevertheless, further study for the wavelet theory as a widespread method of achieving efficient and intelligent SHM is still on demand.

University of Malaya

CHAPTER 3: THE WAVELET THEORY

3.1 Introduction

This chapter aims to provide a general idea of the wavelet theory through presenting the relevant developments. Furthermore, an outline of the properties of wavelets and wavelet transform are discussed. Initially, an investigation over the general characteristics of wavelet functions of continuous wavelet transform will be carried out. In the second step, the DWT will be developed through discretizing the continuous wavelet transform in conformity with the frame theory. Then, the basic features of scaling functions will be presented. The third step will deliver a multi-resolution analysis to describe the roles of the wavelet functions in the analysis of a response signal. The final step will discuss and indicate the WPT as a general form of the DWT.

3.2 Development of wavelet theory

The significant issue in structural dynamics is the identification of certain properties of dynamic systems, such as modal parameters (e.g., mode shapes, natural frequencies, and damping ratios) and structural parameters (e.g., mass, stiffness, etc) obtained from structural response in the time domain. In order to represent the essential characteristics of the response signals in the time domain there are many types of problems faced since integral transforms such as the Fourier transform, STFT and so on, are needed to transfer the response signals in the time domain to other domains.

The commonly used transformation method in signal analysis is the Fourier transform (FT). The basic idea of the FT is to represent a signal by means of an infinite series of trigonometric functions. However, the FT does not provide information about how the frequency contents of the signal vary with respect to time, since trigonometric functions have infinite times. Therefore, the Fourier analysis is not particularly suitable for the

examination of non-linear and non-stationary problems. To overcome such deficiency, the STFT proposed by Gabor can be used. This windowing technique analyzes only a small section of the signal at a time. The STFT maps a signal into a 2-D function of time or space and frequency. The transformation has a disadvantage that the information about time or space and frequency can be obtained with only limited precision determined by the size of the window. A higher resolution in both time and frequency domain cannot be achieved simultaneously since once the window size is fixed, it is the same for all frequencies. This is one of the principal reasons for the creation of the WT. The basic ideas of the wavelet functions are included in the family of basis functions that are capable of depicting a signal in a localized frequency (or scale) and time (or space) domain. The main advantage obtained by using wavelets is the capability to execute local analysis of a signal, i.e. zooming in on any interval of space or time. Wavelet analysis is capable of demonstrating some hidden features of the data that conventional Fourier analysis fails to detect.

3.3 Continuous wavelet transform

In contrast to the frequency-domain methods, the time-frequency methods can be used to analyze any non-stationary event localized in time domain. Physically, a wavelet (function) is a localized small wave centered on a given position in time with a fast decay to zero away from the center. The support of a wavelet function is defined as the interval outside of which wavelet has zero value. In mathematical terms, the wavelet is said to have compact support (i.e., a closed and bounded support). In addition, a wavelet function can be complex or real. A complex wavelet function is preferable for capturing the oscillatory behavior of a signal since a complex wavelet has information about both amplitude and phase, while a real wavelet function is often utilized to isolate peaks or discontinuities.

In wavelet analysis, the mother wavelet $\psi(t)$ localized in both space and frequency domains is used to generate a family of wavelets $\psi_{a,b}(t)$ formulated as

$$\psi_{a,b}(t) = |a|^{-1/2} \psi\left(\frac{t-b}{a}\right), \quad b \in \mathbb{R}, a \in \mathbb{R}, a \neq 0 \quad (3.1)$$

where a and b are the scale and translation parameters, respectively. For a specified pair of a and b , $\psi_{a,b}(t)$ depicts a single wavelet function. The translation parameter b denotes the location of the wavelet function $\psi_{a,b}(t)$ along the time axis. In addition, the scale parameter a controls the width or support of the wavelet function $\psi_{a,b}(t)$.

For time-frequency analysis of a signal, the CWT of a signal $f(t)$ is defined as:

$$\text{CWT}(a,b) = \int_{-\infty}^{+\infty} f(t) \psi_{a,b}^*(t) dt = \int_{-\infty}^{+\infty} f(t) \frac{1}{\sqrt{a}} \psi\left(\frac{t-b}{a}\right) dt = \langle f(t), \psi_{a,b}(t) \rangle \quad (3.2)$$

where the symbols $*$ and \langle, \rangle denote complex conjugate and inner product, respectively. $\text{CWT}(a,b)$ is called the CWT coefficient which is the correlation of $f(t)$ with the corresponding scaled and translated wavelet. The frequency localization is controlled by the scale a which is proportional to the reciprocal of the frequency. Due to the fixity of time-frequency resolution at different frequency ranges, the STFT has a limitation, however, since time resolution becomes arbitrarily good at high frequencies, while the frequency resolution becomes arbitrarily good at low frequencies, therefore, such deficiency is resolved.

In general, the specifications of the CWT are dependent on a given mother wavelet function $\psi(t)$, since the wavelet functions $\psi_{a,b}(t)$ which are utilized in the CWT, are created from their mother wavelet function $\psi(t)$ with the scale and translation parameters. Hence, the features of the mother wavelet function determine the specifications of the corresponding CWT.

Several properties of a wavelet function $\psi(t)$ to become the basis function in wavelet transform (Mallat, 1999) are explained in the following.

First, a wavelet $\psi(t)$ must have zero mean

$$\int_{-\infty}^{+\infty} \psi(t) dt = 0 \quad (3.3)$$

Second, a wavelet $\psi(t)$ must have finite energy:

$$E_{\psi} = \int_{-\infty}^{+\infty} |\psi(t)|^2 dt < \infty \quad (3.4)$$

Here E_{ψ} is the energy of a wavelet function $\psi(t)$. Equation (3.4) indicates that a wavelet function is also square integrable, that is, $\psi(t) \in L^2(\mathbb{R})$. Frequently, the wavelet function $\psi(t)$ is normalized so that it has unit energy:

$$E_{\psi} = \int_{-\infty}^{+\infty} |\psi(t)|^2 dt = 1 \quad (3.5)$$

In the current study, we consider that the wavelet function has unit energy so that the wavelet transform energy of a signal will be identical to the energy of the original signal.

Third, the mother wavelet $\psi(t)$ should satisfy the admissibility condition defined as

$$C_{\psi} = \int_0^{\infty} \frac{|H(\omega)|^2}{\omega} d\omega < \infty \quad (3.6)$$

Here $H(\omega)$ denotes the Fourier transform of $\psi(t)$. The Inverse CWT is defined as:

$$f(t) = \frac{1}{c_{\psi}} \int_{a=-\infty}^{+\infty} \int_{b=-\infty}^{+\infty} \frac{1}{|a|^2} CWT(a, b) \psi_{a,b}(t) da db \quad (3.7)$$

considering that C_{ψ} for a specified wavelet $\psi(t)$ exists. The admissibility condition confirms the existence of the inverse CWT.

The last property is the number of vanishing moments of the wavelet, where the k^{th} moment of $\psi(t)$ is expressed as:

$$m_k = \int_{-\infty}^{+\infty} t^k \psi(t) dt \quad (3.8)$$

A wavelet $\psi(t)$ has n vanishing moments if the following equation is satisfied

$$\int_{-\infty}^{+\infty} t^k \psi(t) dt = 0 \quad \text{for } k=1, 2, \dots, n-1 \quad (3.9)$$

If the support of $\psi_{a,b}(t)$ contains a singularity at a certain point of $f(t)$, that means, it is not differentiable at a point where $f(t)$ changes from one polynomial to another, then the CWT coefficients will have relatively large values.

3.4 Discrete wavelet transform

CWT calculates the wavelet coefficients by continuously shifting a scalable basis function over a signal and calculating the correlation between the two at every possible scale. Its computation may consume significant amount of time and resources, depending on the resolution required. Moreover, the CWT has informational redundancy because the number of the resulting CWT coefficients in the scale-time domain is much larger than the number of time samples in the original signal $f(t)$. In general, redundancy is not desirable since more computations and more computational memory would be necessary to process a signal with redundancy. In order to remove the difficulty in the numerical operation and the redundancy of the resulting coefficients in the CWT, the DWT is introduced by discretizing the continuous scale a and translation b parameters.

A practical way to sample the continuous parameters a and b is to use a logarithmic discretization of the scale parameter a and associate the scale, in turn, with the size of steps taken between b locations. In other words, the scale parameter a is discretized first on a logarithmic grid. The translation parameter b is then discretized with respect to the scale parameter a , i.e., a different sampling rate is used for every scale parameter. Therefore, the form of the wavelet function for the discretization of the CWT is taken from Equation (3.1).

For the discrete WT, the scale and translation parameters become discrete values which form as:

$$a = a_0^j, \quad b = kb_0 a_0^j \quad \text{for } a_0 > 1, \quad b_0 > 1 \quad j, k \in \mathbb{Z} \text{ (set of integers)} \quad (3.10)$$

Therefore, the wavelet function for the discretization of the CWT shown in Equation (3.1) can be written in the following way:

$$\psi_{j,k}(t) = \frac{1}{\sqrt{a_0^j}} \psi\left(\frac{t - kb_0 a_0^j}{a_0^j}\right) \quad (3.11)$$

For practical purposes and computational efficiency, the discrete parameters a_0 and b_0 in Equation (3.11) are generally used to be 2 and 1, respectively. This results in a dyadic translation of $k2^j$ and a binary scaling of 2^j . The dyadic grid wavelet can be obtained by substituting $a_0 = 2$ and $b_0 = 1$ into Equation (3.11), as

$$\psi_{j,k}(t) = \frac{1}{\sqrt{2^j}} \psi\left(\frac{t-k2^j}{2^j}\right) = 2^{-j/2} \psi(2^{-j}t - k) \quad (3.12)$$

where $\psi_{j,k}(t)$ is the k^{th} translation of the wavelet function at scale index j . The DWT is defined by using discrete wavelet functions in Equation (3.11), as:

$$DWT(j, k) = \int_{-\infty}^{+\infty} f(t) \psi_{j,k}^*(t) dt = \langle f(t), \psi_{j,k}(t) \rangle \quad (3.13)$$

Here $DWT(j, k)$ is the DWT coefficient at a scale-translation sampling set j and k . Such a DWT is specified by the choice of a scale and translation parameters through analyzing wavelet $\psi(t)$ in the framework of the frame theory. The frame theory provides a general framework for studying the properties of discrete wavelets (Daubechies, 1992).

3.5 Wavelet multiresolution analysis

The multiresolution analysis (MRA) of wavelet is a significant property in the multilevel approximation of engineering problems (Wang et al., 2010). The concept of MRA for square-integrable signals in the context of wavelet analysis was elaborated further by Mallet (1989). The concept of MRA leads to the reach theory of the scale-based structure of signals by representing a function as a limit of successive approximation, which responds to different level of resolution.

A multiresolution analysis can be defined as a sequence of nested subspaces $\{V_j\}_{j \in \mathbb{Z}}$ in $L^2(\mathbb{R})$ such that the following conditions hold:

- (a) $V_j \subset V_{j-1}$ for all $j \in \mathbb{Z}$
- (b) $\lim_{j \rightarrow -\infty} V_j = \bigcup_{j=-\infty}^{-\infty} V_j = L^2(\mathbb{R})$
- (c) $\bigcap_{j=-\infty}^{-\infty} V_j = \{0\}$

(d) $f(t) \in V_j$ if and only if $f(2t) \in V_{j-1}$ for all $j \in \mathbb{Z}$

(e) There exists a function, called a scaling function $\phi(t)$, such that the subspace V_j is formed by the function:

$$\{\phi_{j,k}(t)\}_{k \in \mathbb{Z}} = \{2^{-j/2} \phi(2^{-j}t - k)\}_{k \in \mathbb{Z}} \quad (3.14)$$

The system of function $\{\phi_{j,k}(t)\}_{k \in \mathbb{Z}}$ forms an orthonormal basis of V_j .

Condition (e) shows that the subspace V_j is the linear span for the set of $\{\phi_{j,k}(t)\}_{k \in \mathbb{Z}}$

$$V_j = \text{Span}\{\phi_{j,k}(t)\} \quad k \in \mathbb{Z} \quad (3.15)$$

scaling function $\phi(t)$ which satisfies the scaling condition, has the following properties

$$\text{Property 1: } \phi(t) = \sum_{k \in \mathbb{Z}} c(k) \phi(2t - k) \quad (3.16)$$

Such a characteristic, represented by Equation (3.16), is called the two-scale relation for the scaling function $\phi(t)$.

$$\text{Property 2: } \int_{-\infty}^{+\infty} \phi(t) dt = 1 \quad (3.17)$$

Property 3: $\{\phi(t - k)\}_{k \in \mathbb{Z}}$ is a Riesz sequence.

Property 4: the Fourier transform $H(\omega)$ of $\phi(t)$ is continuous at zero frequency and not equal to zero at this point.

Equation (3.15) means that for any $f(t) \in V_j$, we have

$$f_j(t) = \sum_{k \in \mathbb{Z}} a(j, k) \phi_{j,k}(t) \quad (3.18)$$

Mathematically, the approximation function of signal $f(t)$ at the scale index j , or $f_j(t)$, can be achieved with the orthogonal projection of a signal $f(t) \in L^2(\mathbb{R})$ onto a scale subspace V_j .

$$f_j(t) = \sum_{k \in \mathbb{Z}} a(j, k) \phi_{j,k}(t) \quad (3.19)$$

where $f_j(t)$ depicts the orthogonal projection of $f(t)$ onto space V_j . In addition, the k^{th} approximation coefficient at the scale index j can be expressed as:

$$a(j, k) = \int_{-\infty}^{+\infty} f(t) \phi_{j,k}(t) dt \quad (3.20)$$

In general, the MRA suggests that the scaling functions play an important role in the piecewise approximation of the continuous function $f(t)$ in $L^2(\mathbb{R})$ and are related to the scale index of the scale subspace that is approximated in. The quality of approximations of the continuous function $f(t)$ can vary. Hence, the MRA is often referred to as a multiresolution approximation.

The nested sequence $\{V_j\}_{j \in \mathbb{Z}}$ of MRA subspaces stimulates the description of the difference space W_j between the two-scale subspaces V_{j-1} and V_j and the creation of the basis that spans such a difference space W_j . The wavelet space W_j is called the detail subspace, such that

$$V_{j-1} = W_j \oplus V_j \quad \text{for } j \in \mathbb{Z} \quad (3.21)$$

where \oplus is the orthogonal summation of spaces. Equation (3.21) indicates that the detail subspace W_j and scale subspace V_j are orthogonal. This leads to an orthogonal decomposition of V_{j-1} , that is

$$V_{j-1} = W_j \oplus W_{j+1} \oplus \dots \oplus W_{j_{max}} \oplus V_{j_{max}} \quad (3.22)$$

where $j_{max} > j$ and also j and j_{max} are integers. In addition, an orthogonal decomposition of $V_{-\infty} = L^2(\mathbb{R})$ is

$$L^2(\mathbb{R}) = \bigoplus_{j=-\infty}^{\infty} W_j \quad (3.23)$$

V_{∞} is equal to zero based on the conditions (a) and (c).

Analogous to condition (e) for the scaling function, there exists a wavelet function $\psi(t) \in W_j$ such that $\{\psi_{j,k}(t)\}_{k \in \mathbb{Z}}$ constitutes an orthonormal basis for W_j . The subspace W_j is spanned by the wavelet functions as

$$W_j = \text{Span} \left\{ \psi_{j,k}(t) \right\}_{k \in \mathbb{Z}} \quad (3.24)$$

Furthermore, owing to the orthonormality of the scale and detail subspaces at the scale index j in Equation (3.21), the wavelet functions are orthonormal to the scaling functions at the scale index j , that is

$$\langle 2^{-j/2}\phi(2^{-j}t - k), 2^{-l/2}\psi(2^{-l}t - l) \rangle = 0 \quad \text{for } j, k, l \in \mathbb{Z} \quad (3.25)$$

Since the wavelet functions are orthogonal to each other at a specified scale index, and as well, W_k and W_l are orthogonal for $k \neq l$ in Equation (3.22), the wavelet functions $\psi_{j,k}(t)$ have the following relation:

$$(2^{-k/2}\psi(2^{-k}t - m), 2^{-l/2}\psi(2^{-l}t - n)) \geq \begin{cases} 1 & k = l \quad \text{and} \quad m = n \\ 0 & \text{otherwise} \end{cases} \quad (3.26)$$

Similar to Equation (3.19), the detail function $g_j(t)$ of a signal $f(t)$ at the scale index j can be achieved with the orthogonal projection of $f(t)$ onto detail subspace W_j .

$$g_j(t) = \sum_{k \in \mathbb{Z}} d(j, k) \psi_{j,k}(t) \quad (3.27)$$

where $g_j(t)$ is the orthogonal projection of $f(t)$ onto the space W_j . Also, the k^{th} detail coefficient at the scale index j is expressed as:

$$d(j, k) = \int_{-\infty}^{+\infty} f(t) \psi_{j,k}(t) dt \quad (3.28)$$

From Equation (3.21), it follows that the relation between the detail subspace and scale subspace can be expressed as

$$W_j \subset V_{j-1} \quad (3.29)$$

This relation suggests that, since $\psi(t)$, one of the basis vectors in detail subspace W_j , resides in scale subspace V_{j-1} , $\psi(t)$ can be expressed in terms of $\{\phi_{j-1,k}(t)\}_{k \in \mathbb{Z}}$, the basis vectors in V_{j-1} : that is,

$$\psi(t) = \sum_{k \in \mathbb{Z}} b(k) \phi(2t - k) \quad (3.30)$$

Equation (3.30) is called the two-scale relation for the wavelet function $\psi(t)$ and $\{b(k)\}_{k \in \mathbb{Z}} \in L^2(\mathbb{Z})$ which are the coefficients for this relation.

From Equations (3.19), (3.21), and (3.27), it can be deduced that the orthogonal projection of $f(t) \in L^2(\mathbb{Z})$ onto V_j is equal to summation of the orthogonal projection of $f(t)$ onto V_{j+1} and the orthogonal projection of $f(t)$ onto W_{j+1} , which is:

$$f_j(t) = f_{j+1}(t) + g_{j+1}(t) \quad (3.31)$$

In addition, $f_{j+1}(t)$ can be decomposed as:

$$f_{j+1}(t) = f_{j+2}(t) + g_{j+2}(t) \quad (3.32)$$

Therefore, Equation (3.31) can be rewritten as:

$$f_j(t) = f_{j+2}(t) + g_{j+2}(t) + g_{j+1}(t) \quad (3.33)$$

Generally, the approximation function $f_j(t)$ can be expressed as:

$$f_j(t) = f_{j_{max}}(t) + \sum_{i=j+1}^{j_{max}} g_i(t) \quad (3.34)$$

or, equivalently

$$f_j(t) = \sum_{k=-\infty}^{\infty} a(j_{max}, k) \phi_{j_{max}, k}(t) + \sum_{i=j+1}^{j_{max}} \sum_{k=-\infty}^{\infty} d(i, k) \psi_{i, k}(t) \quad (3.35)$$

where $j_{max} > j$ and j_{max} and j are integers. On the other hand, $f_j(t)$ can be depicted as the sums of the orthogonal projection of $f(t)$ onto detail subspace W_j for $i = j + 1, j + 2, \dots, j_{max}$ and the scale subspace $V_{j_{max}}$ for the given j_{max} .

3.5.1 The Daubechies wavelets

Among all of the wavelets that have been applied in the multiresolution analysis, the orthonormal Daubechies wavelets are the most commonly used ones for signal analysis and synthesis. This is because it satisfies the two crucial requirements, i.e., the orthogonality of local basis functions and second or higher-order accuracy (Daubechies, 1988, 1992).

Daubechies wavelet includes the Daubechies wavelet functions and scaling functions. The N^{th} order family of Daubechies wavelets, specified by DBN , has no explicit expression with the order N , excluding for $DB1$, which is named the Haar wavelet.

Accordingly, Equations (3.16) and (3.30) become:

$$\phi(t) = \sum_{k=0}^{2N-1} c(k) \phi(2t - k) \quad (3.36)$$

$$\psi(t) = \sum_{k=0}^{2N-1} b(k) \phi(2t - k) = \sum_{k=0}^{2N-1} (-1)^k c_{2N-1-k} \phi(2t - k) \quad (3.37)$$

A Daubechies wavelet of order N always satisfies the following conditions:

- It is compactly supported in the interval $[0, 2N - 1]$,

- $\psi(t)$ has N vanishing moment:

$$\int_{-\infty}^{\infty} t^m \psi(t) dt = 0 \quad m = 0, \dots, N-1 \quad (3.38)$$

With an increasing number of vanishing moments, i.e. with higher order of N , the wavelet function becomes smoother. Figures 3.1 and 3.2 illustrate the DB wavelet and scaling functions with the orders of 1, 2, 4, and 5, respectively.

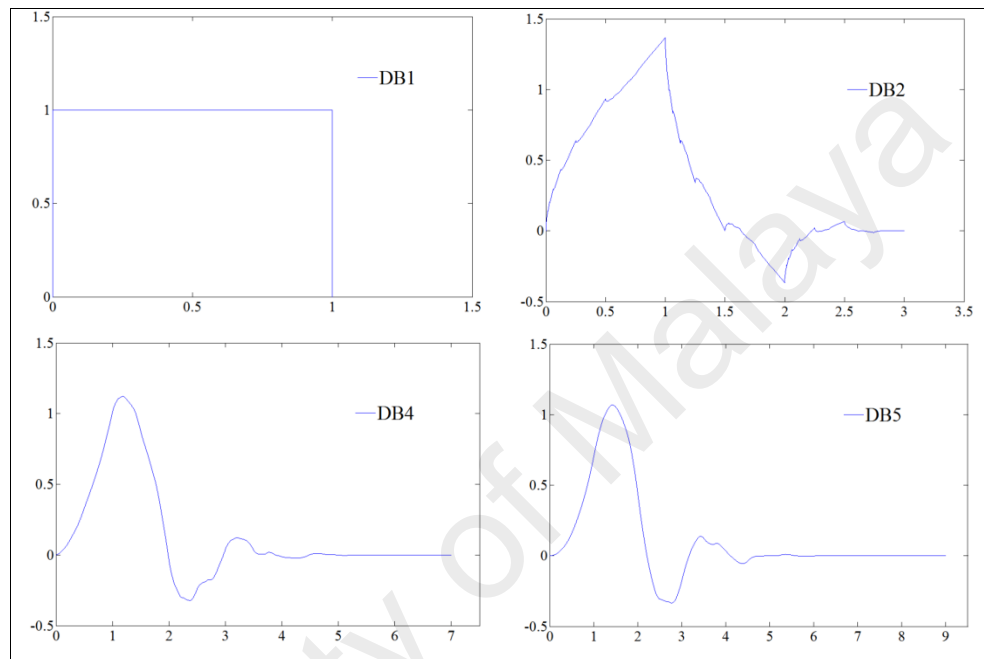


Figure 3.1: The Daubechies wavelet functions for DB1, DB2, DB4 and DB5

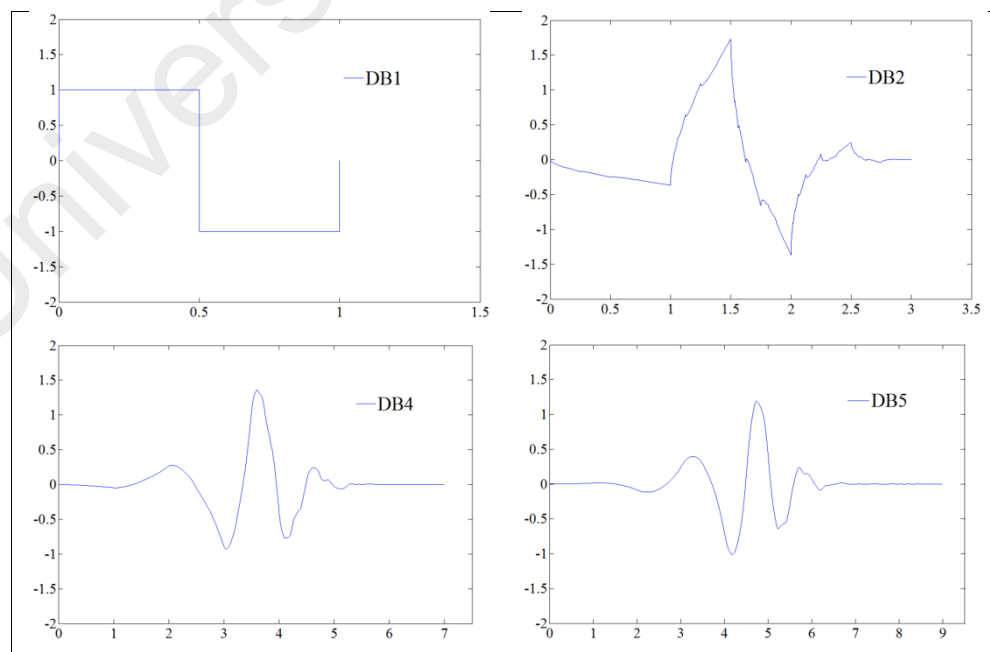


Figure 3.2: The Daubechies scaling functions for DB1, DB2, DB4 and DB5

3.5.2 Fast wavelet transformation

To calculate the scaling function $\phi(t)$ and the corresponding wavelet function $\psi(t)$ of Daubechies wavelets, the two-scale relations introduced by Equations (3.16) and (3.30) should be employed. Therefore, certain conditions or requirements on the sequence $c(n)$ and $b(n)$ beget certain characteristics of the scaling function $\phi(t)$ and of the wavelet function $\psi(t)$. Some of these conditions are summarized as follows:

$$\text{Condition 1: } \sum_{n=0}^{2N-1} c(n) = 2 \quad (3.39)$$

Two additional conditions that must be satisfied by the coefficients $c(k)$ are the condition of accuracy,

$$\text{Condition 2: } \sum_{n=0}^{2N-1} (-1)^n n^m c(n) = 0, \quad m = 0, 1, 2, \dots, N-1 \quad (3.40)$$

and the condition of orthogonality

$$\text{Condition 3: } \sum_{n=0}^{(2N-1-2m)} c(n)c(n+2m) = 0, \quad m = 0, 1, 2, \dots, N-1 \quad (3.41)$$

In addition, the orthogonality of the scaling function results in:

$$\text{Condition 4: } \sum_{n=0}^{2N-1} c(n)^2 = 1 \quad (3.42)$$

The scaling function coefficients $c(n)$ of a Daubechies wavelet of order N can be determined using Equations (3.39) to (3.42). Table 3.1 presents the coefficients $c(n)$ and $b(n)$ for Daubechies orders 1, 2, 4 and 5.

Table 3.1: The coefficients of two-scale relations for DB1, DB2, DB4, and DB5 wavelet functions and scaling functions

	n	$c(n)$	$b(n)$		n	$c(n)$	$b(n)$
DB1	0	1	1	DB5	0	0.226419	0.004717
	1	1	-1		1	0.853944	0.017792
DB2	0	0.68301	-0.18301		2	1.024327	-0.00883
	1	1.18301	-0.31699		3	0.195767	-0.1097
	2	0.31699	1.18301		4	-0.34266	-0.0456
	3	-0.18301	-0.68301		5	-0.0456	0.342657
DB4	0	0.325803	-0.01499		6	0.109703	0.195767
	1	1.010946	-0.0465		7	-0.00883	-1.02433
	2	0.8922	0.043616		8	-0.01779	0.853944
	3	-0.03958	0.264507		9	0.004717	-0.22642
	4	-0.26451	-0.03958				
	5	0.043616	-0.8922				
	6	0.046504	1.010946				
	7	-0.01499	-0.3258				

Replacing $\frac{t}{2^{j+1}} - m$ for t in Equations (3.16) and (3.30), gives the general expressions:

$$\phi_{j,m}(t) = \frac{1}{\sqrt{2}} \sum_{k \in \mathbb{Z}} c(k) \phi_{j-1,2m+k}(t) \quad (3.43)$$

$$\psi_{j,k}(t) = \frac{1}{\sqrt{2}} \sum_{k \in \mathbb{Z}} b(k) \phi_{j-1,2m+k}(t) \quad (3.44)$$

Rewriting Equation (3.20) by substituting the Equation (3.43) into the Equation (3.20), it is expressed as:

$$a(j, m) = \int_{-\infty}^{+\infty} f(t) \frac{1}{\sqrt{2}} \sum_{k \in \mathbb{Z}} c(k) \phi_{j-1,2m+k}(t) dt \quad (3.45)$$

which can be further expanded as:

$$a(j, m) = \frac{1}{\sqrt{2}} \sum_{k \in \mathbb{Z}} c(k) a(j-1, 2m+k) = \frac{1}{\sqrt{2}} \sum_{m \in \mathbb{Z}} c(n-2m) a(j-1, n) \quad (3.46)$$

Equation (3.45) indicates that, by knowing the coefficients $c(n)$, it is feasible to achieve the coefficients $a(j, m)$ at scale index j from the coefficients $a(k, m)$ at scale index k , where $k < j$, by repeating the procedure explained in Equation (3.46).

Similar to Equation (3.46), note that the coefficients $b(n)$ are known, the coefficients $d(j, m)$ can be obtained at scale index j from the coefficients $a(k, m)$ at scale index k , where $k < j$, by the following equation:

$$d(j, m) = \frac{1}{\sqrt{2}} \sum_{k \in \mathbb{Z}} b(k) a(j-1, 2m+k) = \frac{1}{\sqrt{2}} \sum_{m \in \mathbb{Z}} b(n-2m) a(j-1, n) \quad (3.47)$$

In general, while the approximation coefficients have been obtained at a specific scale index j , the approximation and detail coefficients can be achieved at any scale index greater than j , by applying the two-scale relations for the scaling function and the wavelet function in Equations (3.16) and (3.30). This decomposition algorithm is called the fast wavelet transform.

In addition, Equation (3.31) can be expanded by using Equations (3.43) and (3.44):

$$\begin{aligned} f_j(t) &= \sum_{l \in \mathbb{Z}} a(j+1, l) \frac{1}{\sqrt{2}} \sum_{n \in \mathbb{Z}} c(n-2l) \phi_{j,n}(t) \\ &\quad + \sum_{l \in \mathbb{Z}} d(j+1, l) \frac{1}{\sqrt{2}} \sum_{n \in \mathbb{Z}} b(n-2l) \phi_{j,n}(t) \end{aligned} \quad (3.48)$$

Since $f_j(t)$ can be expanded according to $a(j, n)$ and $\phi_{j,n}(t)$ of Equation (3.18).

Accordingly, Equation (3.48) can be rewritten as:

$$a(j, n) = \tilde{a}(j + 1, n) + \tilde{d}(j + 1, n) \quad (3.49)$$

where

$$\tilde{a}(j + 1, n) = \frac{1}{\sqrt{2}} \sum_{l \in \mathbb{Z}} a(j + 1, l) c(n - 2l) \quad (3.50)$$

$$\tilde{d}(j + 1, n) = \frac{1}{\sqrt{2}} \sum_{l \in \mathbb{Z}} d(j + 1, l) b(n - 2l) \quad (3.51)$$

Generally, Equation (3.49) demonstrates that the approximation coefficients at the scale index j can be reconstructed based on the combination of detail and approximation coefficients at the scale index $j + 1$. This reconstruction algorithm is known as the inverse fast wavelet transform.

In order to demonstrate the fast wavelet transform and the inverse fast wavelet transform from a digital filtering point of view, initially $h_0(n)$, $h_1(n)$, $\tilde{h}_0(n)$ and $\tilde{h}_1(n)$ are defined as:

$$h_0(n) = \frac{c(n)}{\sqrt{2}}; h_1(n) = \frac{b(n)}{\sqrt{2}}; \tilde{h}_0(n) = h_0(n); \tilde{h}_1(n) = h_1(n) \quad (3.52)$$

Substituting Equation (3.52) into Equations (3.46) and (3.47), they are rewritten as:

$$a(j, n) = \sum_{m \in \mathbb{Z}} a(j - 1, m) \tilde{h}_0(2n - m) \quad (3.53)$$

$$d(j, n) = \sum_{m \in \mathbb{Z}} a(j - 1, m) \tilde{h}_1(2n - m) \quad (3.54)$$

Equation (3.53) indicates that $a(j, n)$ is achieved from the convolution of $a(j - 1, m)$ with the sequence $\tilde{h}_0(k)$ and by retaining only the even indexed samples. It means passing $a(j - 1, m)$ through a digital filter \tilde{H}_0 with impulse response $\tilde{h}_0(k)$, followed by down-sampling by a factor of 2. Similarly, Equation (3.54) demonstrates that $d(j, n)$ is achieved by the convolution of $a(j - 1, m)$ with a digital filter \tilde{H}_1 with impulse response \tilde{h}_1 and down-sampling by a factor of 2.

Substituting Equation (3.52) into Equations (3.50) and (3.51), they can be rewritten as:

$$\tilde{a}(j + 1, n) = \sum_{l \in \mathbb{Z}} a(j + 1, l) h_0(n - 2l) \quad (3.55)$$

$$\tilde{d}(j + 1, n) = \sum_{l \in \mathbb{Z}} d(j + 1, l) h_1(n - 2l) \quad (3.56)$$

Equations (3.55) and (3.56) can be explicated as embedding zeros among adjacent samples of the sequences $a(j + 1, l)$ and $d(j + 1, l)$, i.e. up-sampling, and filtering the outcoming sequences through the filters H_0 and H_1 with impulse responses $h_0(k)$ and $h_1(k)$, respectively. Consequently, the reconstructed approximation coefficients $a(j, n)$ can be achieved by the sum of two outcoming sequences $\tilde{a}(j + 1, n)$ and $\tilde{d}(j + 1, n)$ in Equations (3.55) and (3.56). Figure 3.3 indicates the performance of the fast wavelet transform and inverse fast wavelet transform.

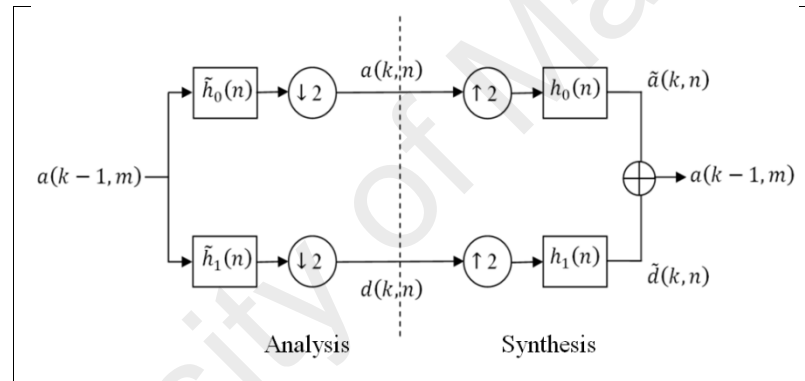


Figure 3.3: The fast and inverse wavelet transform from a digital filter point of view

3.5.3 Wavelet decomposition of signals through filters

The multiresolution analysis always begins with approximation of continuous signals or functions. In real applications, only sampled values of measured signals at a specified time interval Δt are accessible. Otherwise, it is not feasible to correctly calculate such approximation coefficients of discrete signals. In brief, there may be a question on how the set of approximation coefficients is evaluated from the discrete signals, in such a way that it can be applied in the multiresolution analysis.

Practically, because the scaling function operates as the Dirac Delta Function for a lower level of scale index and convolving a continuous function $f(t)$ with the time-delayed

Dirac Delta Function is identical to time-delay $f(t)$ by the same amount. Accordingly, the approximation coefficients at that scale index can be taken into account as a sampling of $f(t)$. If the sampling of $f(t)$ is more than the Nyquist rate, the samples can be considered the approximation coefficients at a specified scale index. This implies that detail coefficients are not required at that scale index. For instance, if a signal is defined and sampled at 2^{-10} in the time interval $0 \leq t < 1$ sec, the samples of this discrete signal can be indicated as approximation coefficients in the expansion of the original signal based on the scaling functions at scale index $j = -10$, i.e., $\{\phi_{-10,k}(t)\}_{k=1,2,3,\dots,2^{10}-1}$.

Hence, the fast wavelet transform can be employed to a discrete signal while the discrete signal can be demonstrated as approximation coefficients at a specific scale index. If the sampling rate of a discrete signal is known, the highest frequency that the signal $X[n]$ can have is determined. The highest frequency of the discrete signal $X[n]$ can be achieved whenever the sampling rate of that signal is known. As depicted in Figure 3.4, the discrete signal $X[n]$ with given sampling rate and the sampling points of 2^n is passed through the half band high-pass filter \tilde{H}_1 and low pass filter \tilde{H}_0 , followed by down-sampling by 2. The outcome of the high-pass filter \tilde{H}_1 has 2^{n-1} samples and only contains the frequencies between $\frac{f_{max}}{2}$ and f_{max} . These samples are called the detail coefficients at level 1, indicated by $D_1[n]$. Similarly, the output of the low-pass filter \tilde{H}_0 has 2^{n-1} samples and includes the frequency range between 0 to $\frac{f_{max}}{2}$, representing the approximation coefficients at level 1, indicated by $A_1[n]$. At the second level, only approximation coefficients, $A_1[n]$, are passed through the high-pass filter \tilde{H}_1 and low-pass filter \tilde{H}_0 , and detail coefficients $D_1[n]$ are transferred to level 2 without any change. The approximation coefficients at level 2 of discrete signal $X[n]$ are represented by $A_2[n]$, with 2^{n-2} samples and the frequency range $[0, \frac{f_{max}}{4}]$ and also, the detail coefficients at level 2, are indicated by $D_2[n]$, with 2^{n-2} samples and the frequency range $[\frac{f_{max}}{4}, \frac{f_{max}}{2}]$.

This process can carry on until approximation coefficients at a specific level disappear. Accordingly, The original discrete signal $X[n]$ at decomposition level Nd , will result in the sets $\{A_{Nd}, D_{Nd}, D_{Nd-1}, \dots, D_2, D_1\}$, where the frequency range of A_{Nd} is $\left[0, \frac{f_{max}}{2^{Nd}}\right]$ and the frequency range of D_j for $1 \leq j \leq Nd$ is $\left[\frac{f_{max}}{2^j}, \frac{f_{max}}{2^{j-1}}\right]$.

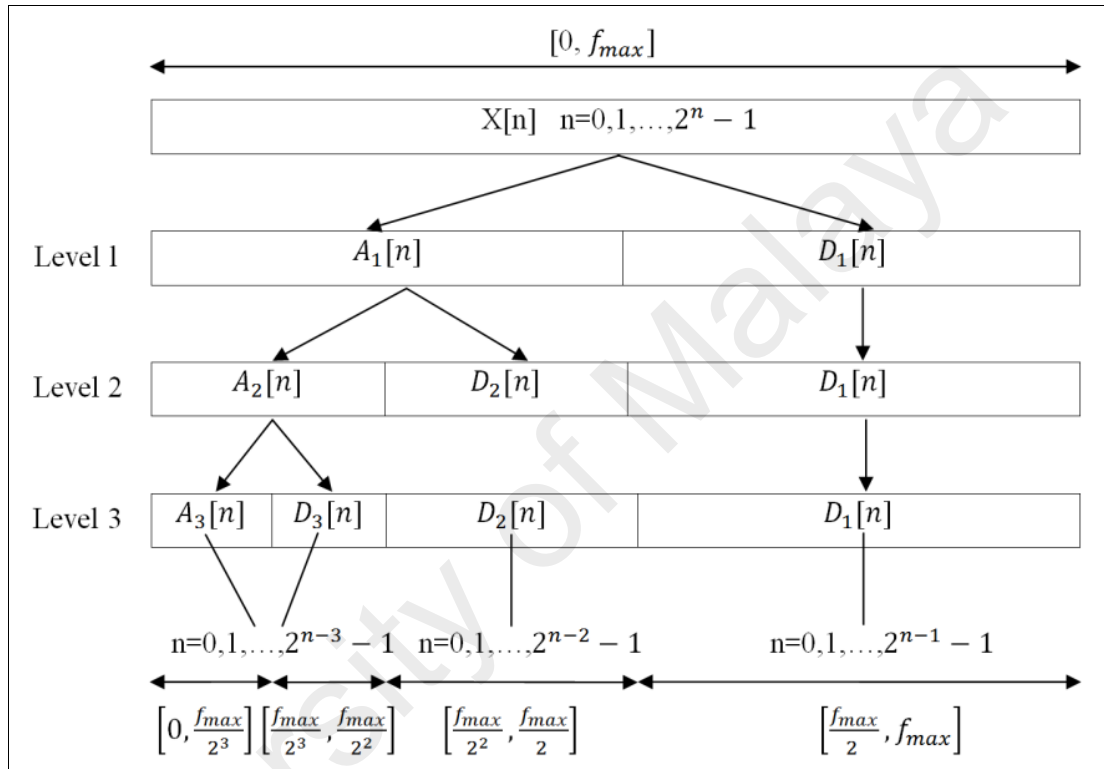


Figure 3.4: A schematic diagram of the DWT at decomposition level 3

3.6 Wavelet packet transform

The WPT can be considered as an extension of the DWT. The difference between WPT and DWT is that, the WPT decomposes not only the approximation but also the detail coefficients at each level of decomposition. This leads to the tree structure of decomposition depicted in Figure 3.5. By comparing this structure with the DWT decomposition, presented in Figure 3.4, it can be seen that at each level of decomposition in the DWT algorithm, the detail coefficients are transferred to the next level without change. However, in the WPT algorithm, all of the coefficients at each level are further

decomposed. Therefore, it is more flexible and has wider base for the analysis of signals. The purpose of separating the signal into packets is to obtain an adaptive partitioning of the time frequency plane depending on the signal.

As shown in Figure 3.4, letters A and D produce the approximation and detail components of the previous set of coefficients through low-pass filtering with \tilde{H}_0 and high-pass filtering with \tilde{H}_1 , followed by down-sampling by 2, respectively. The letter A or D is added to the left of the name of the coefficient to present the most recent filtering process. For instance, the original signal $X[n]$ can be decomposed into the set $\{AAA, DAA, ADA, DDA, AAD, DAD, ADD, DDD\}$, at decomposition level 3 by the WPT. In addition, the decomposed signal $X[n]$ with 2^n samples in terms of the WPT at level Nd have identical samples $\frac{2^n}{2^{Nd}}$ and frequency range of $\left[\frac{(i-1)f_{max}}{2^{Nd}}, \frac{if_{max}}{2^{Nd}}\right]$.

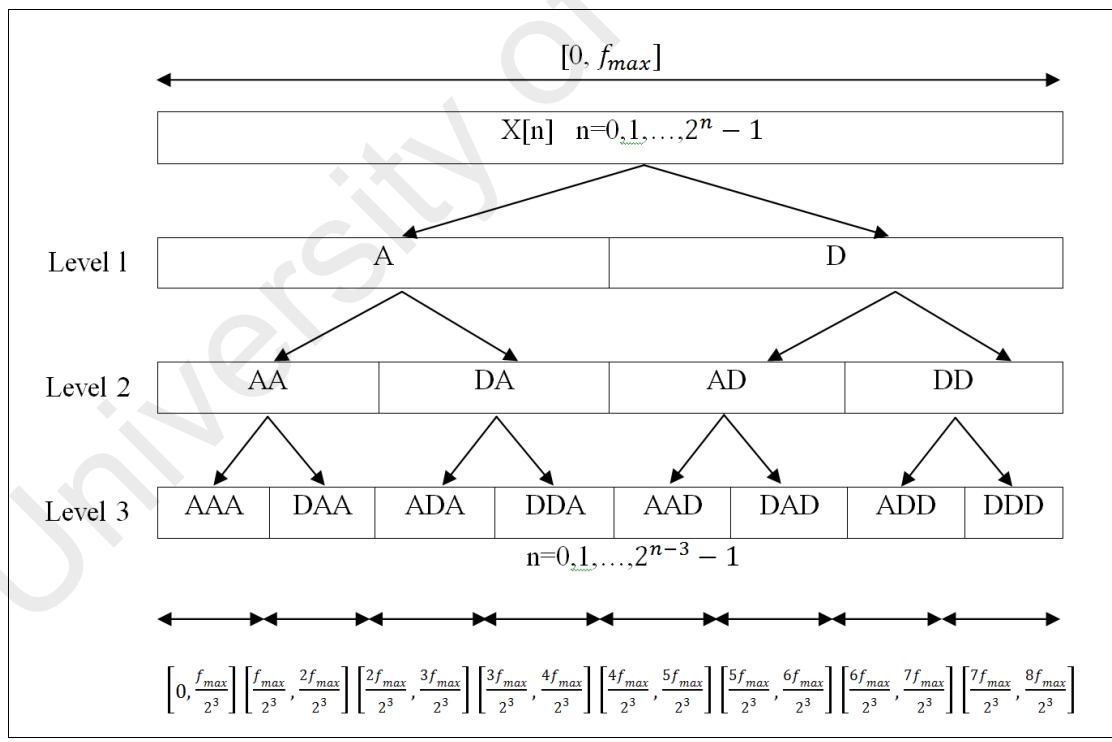


Figure 3.5: A Schematic diagram of the WPT at decomposition level 3

3.7 Summary

In this section, the principal features of the wavelets and the main aspects of the wavelet theory are briefly presented. Due to the localization in time and property of vanishing moments, wavelets are able to represent certain functions, such as piecewise polynomials, in a sparse manner. As the wavelet transform coefficients computed at locations where the function is smooth will be zero, only a few significant coefficients will be sufficient to correctly approximate the function. In addition, their simultaneous localization in frequency and time of wavelets makes them potentially effective building blocks for non-stationary signals whose spectral characteristics evolve over time.

Generally, three various types of the wavelet transform can be specified: the continuous wavelet transform, discrete wavelet transform and wavelet packet transform. The continuous wavelet transform is carried out by the inner product of a signal and wavelet functions. The resulting coefficient of continuous wavelet transform at a given set of specific scale and translation parameter depicts a measure of the similarity among the wavelet function and the signal with a set of the scale and translation parameter. In the discrete wavelet transform, the multiresolution structure inherent to orthogonal wavelets performs two useful objects: (1) it enables the creation of fast decomposition and reconstruction algorithms, and (2) it can analyze the dynamic state of a system simultaneously at several scales chosen to reflect the actual physical processes underlying the observed behavior as closely as possible. The wavelet packet transform indicates the detailed information of a signal in high-frequency range, thus, the deficiency that the discrete wavelet transform suffers from a relative low resolution in the high-frequency range is resolved.

In this chapter, wavelet theory and its utilizations, which are of highest interest for damage detection and system identification, have been presented. Nevertheless, wavelet analysis has an extensive range of applications such as signal analysis, control

applications, numerical analysis and audio applications. Wavelet theory can be used in numerical analysis for solving ordinary and partial differential equations. For signal analysis, the wavelet transform coefficients of signals can be manipulated in various techniques to achieve several consequences, e.g., for feature extraction, classification, compression, and denoising. In addition, wavelet analysis can be applied for modeling and controlling the dynamical systems behavior and separating and partitioning of system responses. Eventually, wavelets are effective tools for the analysis and adaption of audio signals.

University of Malaya

CHAPTER 4: DAMAGE DETECTION AND SYSTEM IDENTIFICATION ALGORITHMS

4.1 Introduction

This chapter describes the formulations of (1) the proposed RWPE-based damage detection algorithms for accurately determining the location and severity of damages, and of (2) the proposed wavelet-based system identification method for identifying the structural parameters of linear and nonlinear systems. In Section 4.2, first deals with the development of a new hybrid approach using wavelet multiresolution analysis and genetic algorithm to accurately determine the location and severity of the damage. This approach contains two steps; first step detects damage locations by defining the damage index called RWPE, and in the next step, genetic algorithm optimization method estimates the damage severities at the identified locations through introducing a database. Secondly, an optimized damage identification algorithm is introduced by using the effective damage index and GA, in a reference-free manner. The RWPE measurements of different sensor-to-sensor pair are utilized for defining reference-free damage index (*RDI*) for each sensor location. In Section 4.3, dealing with parametric system identification, initially the equations of motion of the system in the time domain are converted into the wavelet domain by applying the connection coefficients of the scaling function. Next step is defining the dominant components based on the relative energy of WPT components of the acceleration responses, and creating the equations of motion in the wavelet domain according to the dominant components. Finally, the structural parameters of a linear system, estimated by implementing the least square error minimization method across the dominant components, are demonstrated to converge to the correct values. Moreover, wavelet multiresolution analysis is used to identify the tangent stiffness matrix and the hysteresis-restoring force of nonlinear structural systems. The tangent stiffness of the

structural system can be approximated in terms of the scaling functions at specific scale index.

4.2 Damage detection algorithms based on wavelet multiresolution and GA

Vibration-based structural damage identification aims at comparing structural parameters extracted from measured vibration signals. When structural damage occurs, a corresponding change is produced according to the damage features that evolve from the structural response signals. The key issue in structural damage identification is how to identify and quantify this change. This section deals with the development of a hybrid approach using wavelet multiresolution analysis and GA to accurately determine the location and severity of the damage.

4.2.1 Wavelet packet component energies

In the context of signal processing, the energy of a signal is an important physical factor, since its distribution over time and frequency can reflect the main characteristics of the signal. The theory of wavelet, as regards with the energy concept, can offer noteworthy information as to the distribution of the energy related with the various WPT components. It is stated that the energies of wavelet packet component are sensitive parameters and could be used as damage indices to identify the damage locations (Yen & Lin, 2000; Sun & Chang, 2004; Han et al., 2005; Law et al., 2005). The wavelet packet energy E_f of a signal is defined as:

$$E_f = \int_{-\infty}^{\infty} g^2(t) dt = \sum_{m_1=1}^{2^j} \sum_{m_2=1}^{2^j} \int_{-\infty}^{\infty} g_j^{m_1}(t) g_j^{m_2}(t) dt \quad (4.1)$$

Where $g_j^{m_1}$ and $g_j^{m_2}$ stand for decomposed wavelet components. The total signal energy can be expressed as the summation of wavelet packet component energies when the mother wavelet is orthogonal:

$$E_f = \sum_i^{2^j} E_{g_j^i} = \sum_{i=1}^{2^j} \int_{-\infty}^{\infty} g_j^i(t)^2 dt \quad (4.2)$$

Then, the relative energy of each WPT component can be written as:

$$p_{ij} = \frac{E_{g_j^i}}{E_f} \quad (4.3)$$

The p_{ij} values correspond to a ratio of the energy of a particular coefficient $E_{g_j^i}$ to the total energy. Hence, p_{ij} values sum to one. Furthermore, value of p_{ij} performs as a probability distribution of the energy; it provides information about the relative energy associated with various frequency ranges indicated in the signal and their corresponding degrees of importance.

4.2.2 Relative wavelet packet entropy (RWPE)

The entropy is a quantitative measurement of the amount of disorder in measured signals. The thermodynamic concept of entropy was presented by Shannon (Shannon, 1996) in the field of communication for measuring the estimation error in a signal. While a finite number of N incidents $X = (x_i | i = 1, 2, \dots, N)$ take place with a probability distribution $P = (p_i | i = 1, 2, \dots, N)$, they can be illustrated as

$$\begin{aligned} P &\equiv (p_1, p_2, p_3, \dots, p_N)^T \\ X &\equiv (x_1, x_2, x_3, \dots, x_N)^T \end{aligned} \quad (4.4)$$

The mathematical definition of entropy is expressed by the following equation:

$$S(P) = -k \sum_j^N p_j \ln p_j \quad (4.5)$$

In which $S(P)$ indicates the entropy of P and it is the unique family of functions; k is a positive constant, and \ln denotes the natural logarithmic function. Through Equation (4.5), the general level of disorder in the system can be quantified. Figure 4.1 demonstrates a mapping relationship among entropy i.e., $S = -k \cdot p \cdot \ln(p)$, and the probability distribution related to a finite number of incidents (X).

With increasing the extent of damage, the degree of disorder of the measured structural vibration signals rises. For instance, crack in structural components or missing or

loosening a bolt in connection and welded joints decreases the structural stiffness and increases nonlinearity owing to frictions and gaps. Such changes in a system are due to physical damage and cause uncertainty, increase of the amount of signal disorder because of complex energy dissipation mechanisms and considerable increments in the number of interacting energy dissipation events. As a special case, pure white noises indicate approximately uniform probability distribution while all amplitudes of noisy signals are probably to occur with an identical probability. On the other hand, the structural vibration signals are expected to indicate a certain probability distribution, for instance, adjacent to the normal distribution. As depicted in Figure 4.1, a pure white noise has greater values of entropy compare with those of structural vibrational signals. Hence, if damage takes place at every location, the disorder magnitude of the structural vibrational signals will rise and a greater value of entropy will be also achieved. Thus, the wavelet entropy can efficiently measure variations of the probabilistic distribution of wavelet component energies.

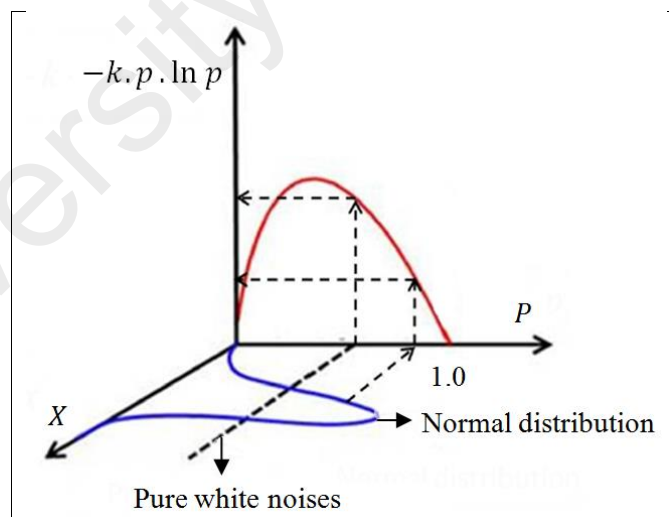


Figure 4.1: Probability distribution and entropy comparison

Wavelet packet entropy is a combination of multiresolution WPT with information entropy to obtain information about the relative energy correlated with various frequency bands presented in structural response segments for investigating damage location. Ren and Sun (2008) applied the concept of the wavelet entropy to structural damage detection

problems. The wavelet entropy spectra represents the level of order/disorder of vibration signals (Rosso et al., 2006). According to the Shannon entropy theory and the wavelet energy ratio defined above, wavelet packet entropy is given as:

$$S_{WPE} = S_{WPE}(p) = - \sum_j \sum_i p_{ij} \cdot \ln p_{ij} \quad (4.6)$$

in which the range of j depends on the selection of decomposition level of a signal and it is a constant value in the case of the WPT. Entropy of the wavelet changes by damage in a structure. Therefore, in order to characterize the location and quantification of damage, such changes in the wavelet packet entropy before and after occurrence of damage can be taken to formulate the damage detection problem. To identify the change of vibration signals of a structure, the relative wavelet packet entropy (RWPE) is defined as:

$$S_{RWPE}(p | q) = \sum_j \sum_i \left| p_{ij} \ln \left(\frac{p_{ij}}{q_{ij}} \right) \right| \quad (4.7)$$

where p and q denote the relative energy of a particular WPT component from damaged and undamaged state, respectively. As can be deduced from the equation, in case of identical quantity for relative wavelet energy ratios p_{ij} and q_{ij} , the RWPE value is zero and when structure is subjected into damage, these values change and, consequently, the RWPE value increases. The RWPE proposed in this study is obtained by slight modification of the relative Kullback-Shanoon entropy (Rosso et al., 2006). It is noteworthy that the measured acceleration responses in the same direction should be employed in calculations of RWPE. Consider the direction of accelerations, RWPE can be rewritten as (Tsai et al., 2009):

$$S_{RWPE}^k(p^k | q^k) = \sum_j \sum_i \left| p_{ij}^k \ln \left(\frac{p_{ij}^k}{q_{ij}^k} \right) \right|, \quad k = x, y, z \quad (4.8)$$

Damage at a location influences the vibration signals in each direction, thus a damage index based on the RWPE is defined as:

$$DI_{RWPE} = \sum_{k=1}^{x,y,z} S_{RWPE}^k(p^k | q^k) \quad (4.9)$$

WPT component energy improves the capability of RWPE-based structural damage identification to extract the irregular information of a signal originated by damage.

Efficiency of the RWPE is significant at analysis of high frequency especially when the related information is important.

4.2.3 Damage severity evaluation using RWPE and GA

4.2.3.1 The genetic algorithm method

GAs are stochastic search algorithms, which are based on the mechanics of natural selection and natural genetics designed to efficiently search large, non-linear, discrete and poorly understood search spaces, where expert knowledge is scarce or it is difficult to model and where traditional optimization techniques fail, (He et al., 2001b). In GA, a population of chromosomes is generated by randomly creating a set of candidate solutions. These solutions are then encoded into binary strings. Each chromosome in the population is then subjected to an evaluation where a fitness value is assigned to each chromosome based on how well the stated objective is satisfied. Generally, a simple GA consists of three operations: (1) selection, (2) crossover, and (3) mutation.

Some basic concepts and operators of a GA are introduced in the following before the description of the suggested algorithm is presented.

4.2.3.1.1 Selection

In order to reproduce the future populations, chromosomes are selected according to their fitness. In case only the most highly fit chromosomes are involved in the selection, due to the lack of diversity, a very limited solution-space may be achieved although the quality of a chromosome is measured by its fitness value. This is why the selection is a key step within GA solution. On the other hand, increase of the future generations' fitness is not guaranteed by arbitrary selection of chromosomes.

Several selection procedures have been applied in GA programs such as roulette wheel, ranking, tournament, and etc. Roulette wheel selection depends on the ratio of fitness

value of a string to the average fitness value of the population. Selection of strings is dependent on their contribution to the mean value of the population, such that those strings which have more contribution are selected for reproduction. Furthermore, strings are linearly ranked in ranking selection according to their fitness and high-ranked strings are chosen for reproduction. In another procedure, namely tournament selection, the strings are usually grouped into pairs of strings in a random manner and the fittest of all groups are selected for mating with each other.

4.2.3.1.2 Crossover

Crossover is the most significant operator in a GA. This operator carries out the mating between two or more parents that are chosen through the selection operator in the previous step. In order to create new pairs of strings (offspring) with an improved performance index, crossover exchanges pieces of information (bits) among promising pairs of string (parents). Fitter children are created by stronger parents. These parent strings exchange portions of their strings at one or n randomly selected bit positions.

Among the crossover operators family, single-point crossover, two-point crossover, uniform crossover and arithmetical crossover are the common ones. Due to the lack of variety in the population of strings, selection and crossover suffer from probable loss of some effective genetic information in the strings and sometimes may even converge to a local optimum, to avoid this and to ensure sufficient variety, the third operator known as mutation is required.

4.2.3.1.3 Mutation

Mutation is a variation in a randomly selected bit of a string; in binary coding this means changing a 0 to 1 and conversely. So, a small probability of mutation should be applied in order to avoid excessive randomness in the search space. This is typically carried out in the range 0.001 and 0.01, while higher values can also be taken, in some cases, to

increase the variety of the population. However, the closer the selected probability of crossover to 1, the higher the exchange of effective information is ensured. Combination of the earlier mentioned operators; selection, crossover, and mutation, originates the global nature of search as opposed to when each operator is used individually.

4.2.3.2 Damage severity assessment

In this section, the GA optimization method is applied to estimate the damage severities at the identified locations through defining a database to reveal the relationships between the energies obtained in the previous steps and damage severities.

For this purpose, a binary GA with tournament selection is used to pick individuals to undergo crossover and mutation. The two-point crossover is employed for every chromosome of the chromosome-pair with a 50% probability of selection; the two parents selected for crossover are in charge of exchanging information that lies between two randomly generated points within the binary string. The chromosomes are the representations of tentative solutions, which can be evaluated by a fitness function. The fitness function determines the fitness of the chromosome. These chromosomes undergo genetic operations to produce next-generation chromosomes. This occurs repeatedly until chromosomes of acceptable solutions are discovered.

The selected chromosome has two kinds of variable: the damage locations, and severities of damage. The GAs use bit strings to represent their chromosomes. Consequently, each gene of the chromosome may be either 0 or 1. Therefore, bit strings may be directly used to encode the candidate solution. In other words, the solution for the true damage configuration is a bit string whose substrings indicate the related parameters. Figure 4.2 depicts the proposed chromosome in a case with two damage locations with different severities.

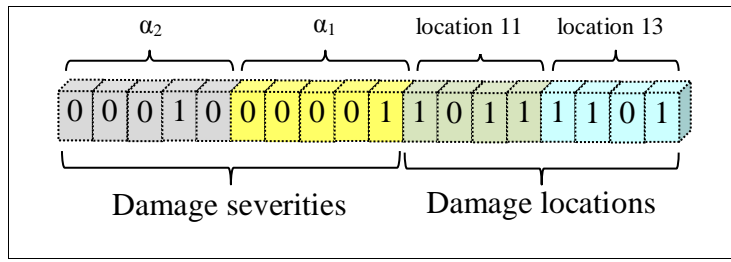


Figure 4.2: Proposed chromosome for GA for two damage location and severities

In order to formulate the damage severity problem as an optimization problem, the following fitness function is applied to search for the “best fit” severities from the evaluation database:

$$\min f = \left\| \frac{\sum_{k=1}^{nd} F_{\alpha_k}^{\beta k} - F_m}{\sum_{k=1}^{nd} F_{\alpha_k}^{\beta k}} \right\|_2 \quad (4.10)$$

Where $\| \cdot \|_2$ is the Euclidean norm, $F = \sum_j \sum_i p_{ij} (\alpha_1, \alpha_2, \dots, \alpha_n)$ is the discrete function of the n damage severities α_n at specified locations (it is reflected by the severity evaluation database). The severity search space is limited to minimum and maximum range of constraint, k is the number of damage locations, β is the sensor locations and F_m is the summation of measured energies in damage locations for each severity of damage. To sum up, GA is used to optimally search for locations and severities of damages, which can be reflected by the values of the energies. Figure 4.3 depicts the whole scheme of the damage identification algorithm.

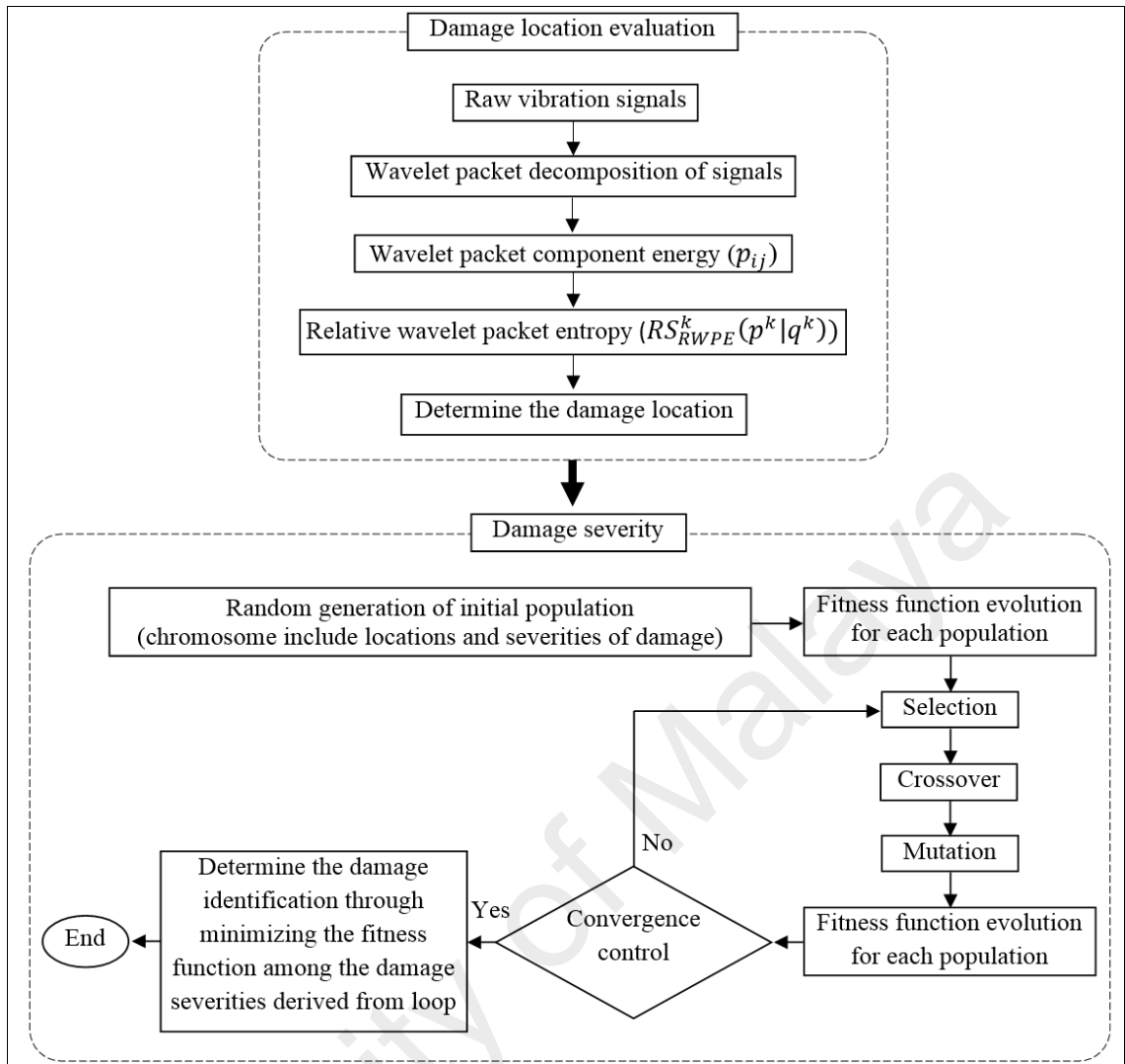


Figure 4.3: Flowchart of the proposed identification algorithm

4.2.4 RWPE-based Reference-free damage identification algorithm

Most of the challenges of existing damage identification methods require reference data which is not always available. There have also been urgent requirements for real-time monitoring to avoid sudden catastrophic disasters. Therefore, application of reference-free damage identification can be vital to most of in-field degraded structures.

Accordingly, a new reference-free wavelet signal processing algorithm, based on the RWPE, has been proposed. The method does not require the reference data from an undamaged beam because of its effective comparative approach of response signals of different locations, which is defined as:

$$RS_{RWPE}^k(p^{\lambda k} | p^{\theta k}) = \sum_j \sum_i \left| p_{ij}^{\lambda k} \ln \left(\frac{p_{ij}^{\lambda k}}{p_{ij}^{\theta k}} \right) \right| \quad k = x, y, z \quad (4.11)$$

where λ and θ indicate location where the data is measured. Since damage at a location affects vibration signals in each direction, the reference-free damage index at a location “ λ ” is defined as:

$$RDI_{RWPE}^\lambda = \sum_{k=1}^{x,y,z} \sum_{\beta=1}^N S_{RWPE}^k(p^{\lambda k} | p^{\theta k}) \quad (4.12)$$

In which N indicates the whole number of locations that correspond to the number of sensors. Based on this equation, the vibration signal at a reference point is compared with signals from other measured points, and thus allows the possibility of damage detection without using data from the undamaged state. In this regard, the proposed RWPE-based reference-free RDI_{RWPE} at various locations $RDI_{RWPE}^1, RDI_{RWPE}^2, \dots, RDI_{RWPE}^n$ are calculated. Suppose that location x is damaged; the RDI_{RWPE}^x becomes a larger value than other values of RDI_{RWPE} which correspond to other locations because all the terms of $RS_{RWPE}(p^x | p^1), RS_{RWPE}(p^x | p^2), \dots, RS_{RWPE}(p^x | p^{n-1})$ and $RS_{RWPE}(p^x | p^n)$ indicate larger amounts, excluding $RS_{RWPE}(p^x | p^x)$ which has the value equal to 0. Figure 4.4, graphically illustrates the calculations of two RWPE-based reference-free RDI_{RWPE} with N sensors. For instance, while only one location of beam, where sensor 3 is placed, is damaged, RDI_{RWPE}^3 has a larger value than other ones, $RDI_{RWPE}^k, k = 1, 2, 4, \dots, N$.

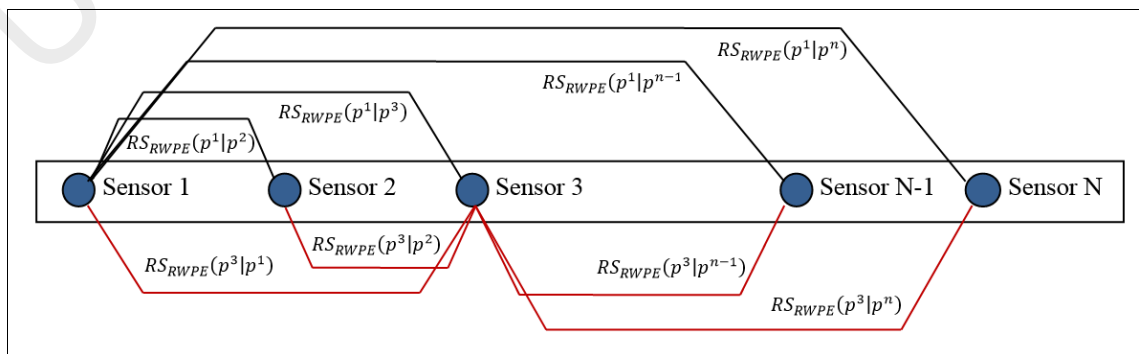


Figure 4.4: Calculation of reference-free damage index (RDI_{RWPE})

In order to determine the location of damage clearly, it is proposed to establish a threshold value for damage indicators through applying statistical properties and the one-side confidence limit of the damage indicators from successive measurements (Han et al., 2005; Xia et al., 2005):

$$UL = \mu + Z_{\bar{\alpha}}\left(\frac{\sigma}{\sqrt{N}}\right) \quad (4.13)$$

in which N stands for the whole number of sensors distributed in a structure where a total of N RDI_{RWPE} values can be achieved. When the mean value and the standard deviation of these RDI_{RWPE} values are represented as μ and σ , UL expresses the one-side $(1 - \bar{\alpha})$ upper confidence limit for these RDI_{RWPE} values, while $Z_{\bar{\alpha}}$ is the value of a standard normal distribution with zero mean and unit variance such that the cumulative probability is $100(1 - \bar{\alpha})\%$. This limit can be considered as a threshold value which is an entrance point of possible abnormality in the damage indicator indicated by the RDI_{RWPE} . The advantage of this damage identification is that setting of the threshold value is according to statistical properties of the damage indicator measured with sensors. The location of sensors whose the RDI_{RWPE} values exceed the threshold will represent where possible damage takes place.

4.2.4.1 Choice of wavelet using GA

The wavelet-based techniques are completely dependent on the mother wavelet function and accurate detection of damage locations can be achieved by choosing a proper mother wavelet function and selecting a suitable resolution level. This is mostly because the correlation between the mother wavelet functions and the signal is calculated as wavelet coefficients. Ingrid Daubechies invented what is called ‘compactly supported orthonormal wavelets’– thus making discrete wavelet analysis practical (Daubechies, 1992). In structural health monitoring, wavelet functions in the Daubechies family are often chosen for signal analysis and synthesis because it satisfies the two crucial

requirements; the orthogonality of local basis functions and second or higher-order accuracy which is generally determined by trial and error methods based on intrinsic characteristics of the data. Apart from the reliance on the mother wavelet function, the wavelet-based methods link up with the decomposition level at which the wavelet analysis must be carried out. Specification of an appropriate level is not known in advance and depends on a wide range of parameters including the characteristics of the structure, the nature of the signal and the type, location and severity of the damage, etc. Several researchers have suggested trying different decomposition levels, (Ovanesova & Suarez, 2004; Shinde & Hou, 2005; Taha et al., 2006a; Sun & Chang, 2007; Ren et al., 2008; Mikami et al., 2011). Basically, there is no computational logic behind the optimum selection of Daubechies order for damage identification. It has to be noted that calculation of the wavelet coefficients is in direct relation with the shape of the mother wavelet; the correlation between mother wavelet and signal is calculated as wavelet coefficients. Hence, in this section, an effectual algorithm is proposed to eliminate the shortcoming arising from the similarity of Daubechies family functions with adjacent order (e.g. DB4 and DB5), as depicted in Figure 4.5.

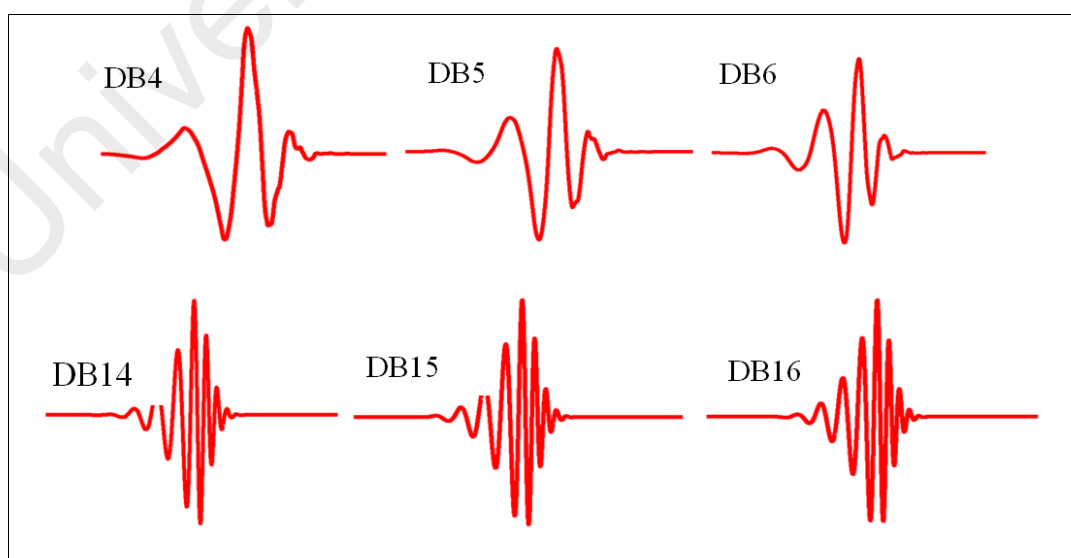


Figure 4.5: Order of Daubechies wavelet function

In the proposed algorithm, the GA is employed in order to search for the optimal Daubechies order and decomposition level of the signals by means of the fundamental fitness function as:

$$\max Fit = \left\| 1 - \frac{mean(RDI_{RWPE}^{\gamma})}{\sum_{k=1}^{nd} RF_k^{\beta}} \right\|_2 \quad (4.14)$$

where $\|\cdot\|_2$ is the Euclidean norm, γ is number of sensor locations ($\gamma = 1, 2, \dots, N$), RF is the RWPE-based reference-free, RDI_{RWPE} , at identified location β , ($\beta = 1, 2, \dots, k$), and k is the number of damage locations.

The procedure of employing GA begins by defining a chromosome, i.e. an array of variables whose values need to be optimized. The proposed chromosomes contain five genes for the Daubechies mother wavelet function and three genes for the decomposition level of signals, as shown in Figure 4.6. The fitness function generates an output from a set of input variables of a chromosome. These chromosomes undertake genetic operations to produce next generation chromosomes. This process is repeated until the convergence condition is reached. The convergence condition is obtained when either the best chromosome has not changed for a number of generations or the number of generations reaches its given maximum value.

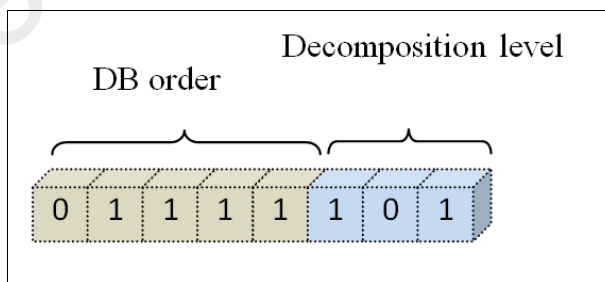


Figure 4.6: Proposed chromosome for GA for the optimal search of DB order and decomposition level

Figure 4.7 depicts the whole scheme of the reference-free damage detection optimization processes.

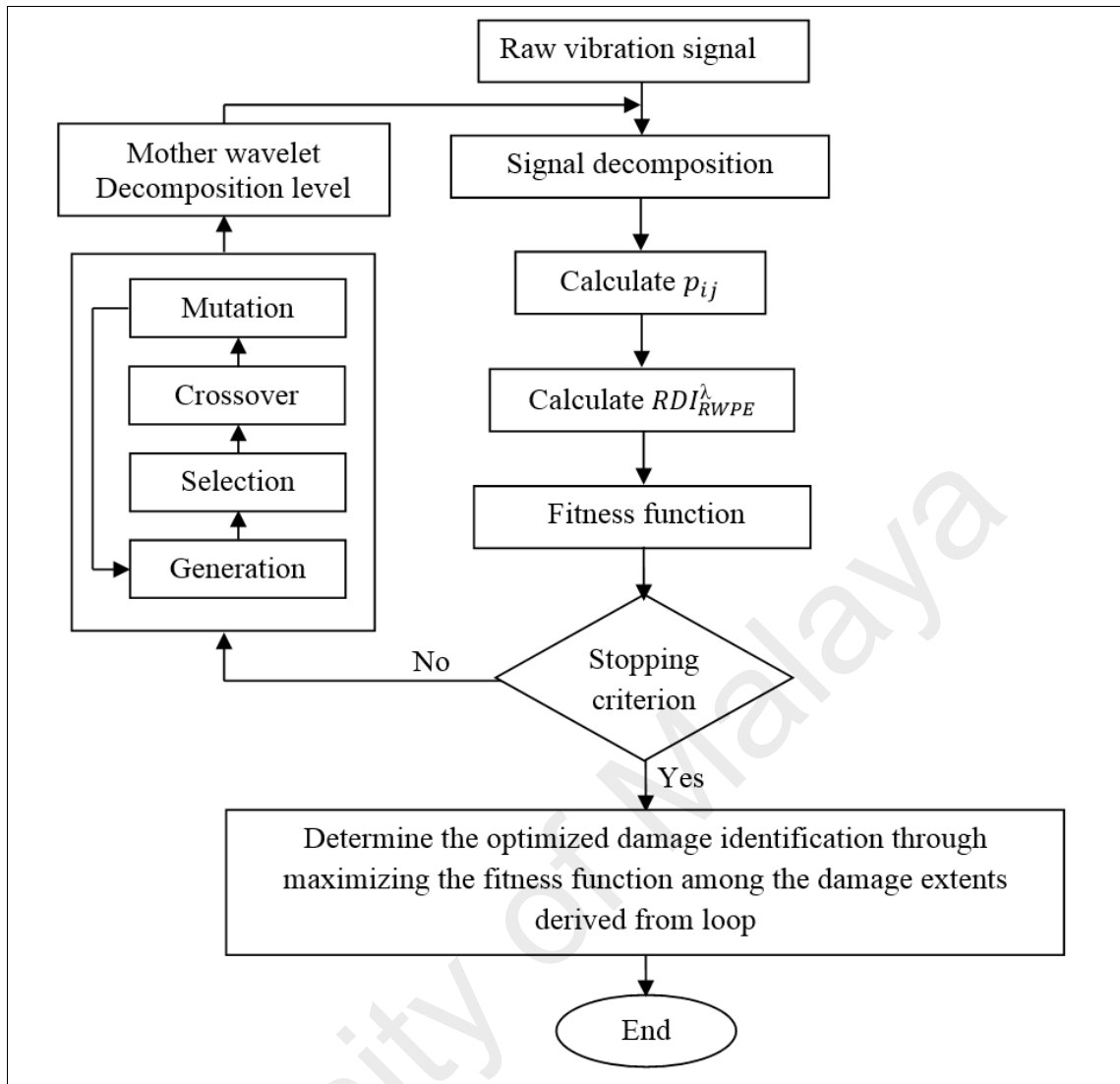


Figure 4.7: Entire proposed reference-free damage identification algorithm

4.3 Parameter identification using wavelet multiresolution analysis

Identification of structural properties is an important task for condition assessment, damage diagnosis, maintenance and repair and life cycle management. In this section, a method for identifying the structural parameters of linear and nonlinear systems is proposed based on the wavelet multiresolution analysis.

4.3.1 Equation of motion according to the scaling function

Generally, two subjects occur when one is identifying structural parameters i.e., stiffness, damping, and mass from the equations of motion of a structural system. One subject is

related with the fact that, in dynamic analyses, measured responses is usually in the form of acceleration response, and consequently the corresponding velocity and displacement is derived from the acceleration by means of integration process. However, retrieving the velocity and displacement from the acceleration response is intricate, while the degree of resolution of the integrated signal relies on several factors such as frequency content, sampling rate, and nature of the signal. The other subject is indicated by the manner that input data (e.g., accelerations, velocities, displacements, and excitations) can be manipulated without missing essential information about the system. This section ascertains how the scaling function plays an important role in deriving the velocity and displacement from the given acceleration.

The force-vibration differential equations of motion of an N -DOF linear system is given as:

$$M\ddot{x}(t) + C\dot{x}(t) + Kx(t) = f(t) \quad (4.15)$$

in which $\ddot{x}(t)$, $\dot{x}(t)$, $x(t)$, and $f(t)$ are the length- N vectors of acceleration, velocity, displacement, and external force vectors, respectively; M , C , and K are $N \times N$ mass, damping, and stiffness matrices, respectively.

In the Daubechies wavelet system with a given scaling function $\phi(t)$ and corresponding wavelet function $\psi(t)$, the acceleration $\ddot{x}_h(t)$ and the excitation $f_h(t)$ with the $n + 1$ data point can be demonstrated in terms of the scaling functions $\phi_{j,k}(t)$ and corresponding coefficients $a_h(j, k)$ and $p_h(j, k)$ (t) at the h^{th} degree-of-freedom ($1 \leq h \leq N$), as follows:

$$\ddot{x}_h(t) = \sum_{k=0}^n a_h(j, k) \phi_{j,k}(t) \quad (4.16)$$

$$f_h(t) = \sum_{k=0}^n p_h(j, k) \phi_{j,k}(t) \quad (4.17)$$

where j indicates the scale index and the approximation coefficients $a_h(j, k)$ and $p_h(j, k)$ can be attained as:

$$a_h(j, k) = \int_{-\infty}^{\infty} \ddot{x}_h(t) \phi_{j,k}(t) dt \quad (4.18)$$

$$p_h(j, k) = \int_{-\infty}^{\infty} f_h(t) \phi_{j,k}(t) dt \quad (4.19)$$

The velocity $\dot{x}_h(t)$ and displacement $x_h(t)$ can be derived using functional integration of the $\ddot{x}_h(t)$ acceleration data:

$$\dot{x}_h(t) = \sum_{k=0}^n a_h(j, k) \int_{-\infty}^t \phi_{j,k}(\tau) d\tau \quad (4.20)$$

$$x_h(t) = \sum_{k=0}^n a_h(j, k) \int_{-\infty}^t \left[\int_{-\infty}^{\tau_1} \phi_{j,k}(\tau) d\tau \right] d\tau_1 \quad (4.21)$$

Differently written as

$$\dot{x}_h(t) = \sum_{k=0}^n a_h(j, k) \mathfrak{b}_1\{\phi_{j,k}(t)\} \quad (4.22)$$

$$x_h(t) = \sum_{k=0}^n a_h(j, k) \mathfrak{b}_2\{\phi_{j,k}(t)\} \quad (4.23)$$

where

$$\mathfrak{b}_1\{\phi_{j,k}(t)\} = \int_{-\infty}^t \phi_{j,k}(\tau) d\tau \quad (4.24)$$

$$\mathfrak{b}_2\{\phi_{j,k}(t)\} = \int_{-\infty}^t \left[\int_{-\infty}^{\tau} \phi_{j,k}(\tau) d\tau \right] d\tau_1 \quad (4.25)$$

$\dot{x}_h(t)$ and $x_h(t)$ can be indicated in the form of $\ddot{x}_h(t)$ by multiplying $\phi_{j,k}(t)$ in Equations (4.22) and (4.23) and taking the integral from $-\infty$ to $+\infty$, respectively, as follows:

$$\dot{x}_h(t) = \sum_{l=0}^n v_h(j, l) \phi_{j,l}(t) \quad (4.26)$$

$$x_h(t) = \sum_{l=0}^n d_h(j, l) \phi_{j,l}(t) \quad (4.27)$$

where

$$v_h(j, l) = \sum_{k=0}^n a_h(j, k) \int_{-\infty}^{\infty} \mathfrak{b}_1\{\phi_{j,k}(t)\} \phi_{j,l}(t) dt \quad (4.28)$$

$$d_h(j, l) = \sum_{k=0}^n a_h(j, k) \int_{-\infty}^{\infty} \mathfrak{b}_2\{\phi_{j,k}(t)\} \phi_{j,l}(t) dt \quad (4.29)$$

Equations (4.16-17) and (4.26-27), show that the equation of motion in the time domain depicted in Equation (4.15) can be converted into those according to the scaling functions $\phi_{j,l}(t)$ and the corresponding coefficients $a_h(j, k)$, $v_h(j, l)$, $d_h(j, l)$ and $p_h(j, k)$. Such a conversion according to the scaling functions at the specific scale index j and the corresponding coefficients can be expressed as follows:

$$M\{\sum_{l=0}^n a_K(j, l) \phi_{j,l}(t)\}_{K=1,2,\dots,h,\dots,N} + C\{\sum_{l=0}^n v_K(0, l) \phi_{0,l}(t)\}_{K=1,2,\dots,h,\dots,N} +$$

$$K\{\sum_{l=0}^n d_K(j, l) \phi_{0,l}(t)\}_{K=1,2,\dots,h,\dots,N} = \{\sum_{l=0}^n p_K(j, l) \phi_{j,l}(t)\}_{K=1,2,\dots,h,\dots,N} \quad (4.30)$$

4.3.2 Wavelet connection coefficients

In previous section, the equations of motion indicated in Equation (4.30) are obtained in terms of the scaling functions $\phi_{j,l}(t)$ as well as the known coefficients $a_h(j, k)$ and $p_h(j, k)$ and unknown coefficients $v_h(j, l)$ and $d_h(j, l)$ ($l = 0, 1, 2, \dots, n$). In Equations (4.28-29) the unknown coefficients $v_h(j, l)$ and $d_h(j, l)$ can be calculated from the first and second integration $I_n\{\phi_{j,k}(t)\}_{n=1,2}$ of the given scaling function $\phi_{j,l}(t)$ and known coefficient $a_h(j, k)$.

By definition, the connection coefficients (CHEN et al., 1996; Restrepo & Leaf, 1997; Romine & Peyton, 1997; Zabel, 2003; Zhou, 2004; Mishra, 2011; Joo, 2012) are integrals, with the integrand being the product of the scaling functions and their integrals or derivatives. The integrals of the product of the scaling function $\phi_{j,l}(t)$ are determined with Γ_j^{l-k} of the first integral $I_1\{\phi_{j,k}(t)\}$ and Ω_j^{l-k} of the second integral $I_2\{\phi_{j,k}(t)\}$, defined as:

$$\Gamma_j^{l-k} = \int_{-\infty}^{+\infty} I_1\{\phi_{j,k}(t)\} \phi_{j,l}(t) dt = \int_{-\infty}^{+\infty} I_1\{\phi_{j,0}(t)\} \phi_{j,l-k}(t) dt \quad (4.31)$$

$$\Omega_j^{l-k} = \int_{-\infty}^{+\infty} I_2\{\phi_{j,k}(t)\} \phi_{j,l}(t) dt = \int_{-\infty}^{+\infty} I_2\{\phi_{j,0}(t)\} \phi_{j,l-k}(t) dt \quad (4.32)$$

For the purpose of simplicity, Equations (4.31-32) are examined in scale index j equal to 0, accordingly:

$$\Gamma_0^{l-k} = \int_{-\infty}^{+\infty} I_1\{\phi_{0,0}(t)\} \phi_{0,l-k}(t) dt \quad (4.33)$$

$$\Omega_0^{l-k} = \int_{-\infty}^{+\infty} I_2\{\phi_{0,0}(t)\} \phi_{0,l-k}(t) dt \quad (4.34)$$

The coefficients Γ_0^q and Ω_0^q are named the fundamental connection coefficients for the first and second integration with regard to the $l - k$, respectively. Supposing that $l - k$ is equal to q in Equations (4.33-34), that is:

$$\Gamma_0^q = \int_{-\infty}^{+\infty} \mathfrak{L}_1\{\phi_{0,0}(t)\}\phi_{0,q}(t)dt \quad (4.35)$$

$$\Omega_0^q = \int_{-\infty}^{+\infty} \mathfrak{L}_2\{\phi_{0,0}(t)\}\phi_{0,q}(t)dt \quad (4.36)$$

Before calculating Γ_0^q and Ω_0^q in Equations (4.35-36), a brief mention of the properties of the Daubechies wavelet is given, as depicted in Section 3.5.1. The Daubechies wavelet with the N^{th} order family referred to DBN, is governed by a set of $L = 2N$ coefficients $b(k), k = 0, 1, 2, \dots, L - 1$, and a set of $c(k), k = 0, 1, 2, \dots, L - 1$. In addition, the two-scale relation for the scaling function $\phi(t)$ and property 2 of the scaling function $\phi(t) = \phi_{0,0}(t)$ in Equations (3.30-31), respectively, can be represented as follow:

$$\phi(t) = \sum_{k=0}^{L-1} c(k) \phi(2t - k) \quad (4.37)$$

$$\int_0^{L-1} \phi(t)dt = 1 \quad (4.38)$$

By inserting the two-scale relation for the scaling function $\phi(t)$, into Equations (4.24-25), and then expand the definition of $\mathfrak{L}_1\{\phi(t)\}$ as follows:

$$\begin{aligned} \mathfrak{L}_1\{\phi(t)\} &= \int_{-\infty}^t \phi(\tau)d\tau \\ &= \int_{-\infty}^t \sum_{j=0}^{L-1} c(j)\{\phi(2\tau - j)\}d\tau \\ &= \frac{1}{2} \sum_{j=0}^{L-1} c(j) \int_{-\infty}^{2t-j} \{\phi(\tau_1)\}d\tau_1 \\ &= \frac{1}{2} \sum_{j=0}^{L-1} c(j) \mathfrak{L}_1\{\phi(2t - j)\} \end{aligned} \quad (4.39)$$

Similar to Equation (4.39), the definition of $\mathfrak{L}_2\{\phi(t)\}$ can also be expressed as

$$\mathfrak{L}_2\{\phi(t)\} = \left(\frac{1}{2}\right)^2 \sum_{j=0}^{L-1} c(j) \mathfrak{L}_2\{\phi(2t - j)\} \quad (4.40)$$

Equations (4.39-40) are called the two-scale relations for $\mathfrak{L}_n\{\phi_{0,0}(t)\}_{n=1,2}$, which are analogous to the two-scale relation for $\phi(t)$ seen in Equation (4.37).

From Equation (4.38), it is possible to indicate the physical meaning of the integrals $\mathfrak{L}_1\{\phi_{0,0}(t)\}$ and $\mathfrak{L}_2\{\phi_{0,0}(t)\}$, as:

$$\mathfrak{b}_1\{\phi_{0,0}(t)\} = \begin{cases} 0 & t \leq 0 \\ \mathfrak{b}_1\{\phi_{0,0}(t)\} & 0 < t < (L-1) \\ 1 & t \geq (L-1) \end{cases} \quad (4.41)$$

$$\mathfrak{b}_2\{\phi_{0,0}(t)\} = \begin{cases} 0 & t \leq 0 \\ \mathfrak{b}_2\{\phi_{0,0}(t)\} & 0 < t < (L-1) \\ \mathfrak{b}_2\{\phi_{0,0}(L-1)\} + t - (L-1) & t \geq (L-1) \end{cases} \quad (4.42)$$

From Equations (4.41-42) can be deduced that $\mathfrak{b}_1\{\phi_{0,0}(t)\}$ and $\mathfrak{b}_2\{\phi_{0,0}(t)\}$ for $t \leq 0$ are zero, while, $\mathfrak{b}_1\{\phi_{0,0}(t)\}$ and $\mathfrak{b}_2\{\phi_{0,0}(t)\}$ for $0 < t < (L-1)$ cannot be explicitly depicted, since the scaling function $\phi(t) = \phi_{0,0}(t)$ for $0 < t < (L-1)$ has no explicit form. In addition, for $t \geq (L-1)$ the value of $\mathfrak{b}_1\{\phi_{0,0}(t)\}$ is equal to one and $\mathfrak{b}_2\{\phi_{0,0}(t)\}$ is a linear function with slope equal to one, as follows:

$$\mathfrak{b}_1\{\phi_{0,0}(t)\} = \overbrace{\int_0^{L-1} \phi_{0,0}(t) dt}^{=1} + \overbrace{\int_{L-1}^t \phi_{0,0}(t) dt}^{=0} = 1 \quad (4.43)$$

$$\begin{aligned} \mathfrak{b}_2\{\phi_{0,0}(t)\} &= \int_{-\infty}^t \overbrace{\left[\int_{-\infty}^t \phi_{0,0}(t) dt \right]}^{=\mathfrak{b}_1\{\phi_{0,0}(t)\}} dt = \overbrace{\int_{-\infty}^{L-1} \mathfrak{b}_1\{\phi_{0,0}(t)\} dt}^{=\mathfrak{b}_2\{\phi_{0,0}(L-1)\}} + \int_{L-1}^t \overbrace{\mathfrak{b}_1\{\phi_{0,0}(t)\}}^{=1} dt \\ &= \mathfrak{b}_2\{\phi_{0,0}(L-1)\} + t - (L-1) \end{aligned} \quad (4.44)$$

From Equations (4.35-36), it can be observed that Γ_0^q and Ω_0^q are functions of q , and $\phi_{0,q}(t)$ is supported from q to shift over time, while the support of $\mathfrak{b}_n\{\phi_{0,0}(t)\}_{n=1,2}$ is constant over time, with support $0 \leq t \leq \infty$.

In general, since the interval of integration $(-\infty, \infty)$ for computing Γ_0^q and Ω_0^q in Equations (4.35-36) can be replaced through the overlapped interval among $\phi_{0,q}(t)$ and $\mathfrak{b}_n\{\phi_{0,0}(t)\}_{n=1,2}$, the value of q , representing the position of $\phi_{0,q}(t)$ in time, with support $q \leq t \leq q + L - 1$, can be considered under the four following cases:

(i) $q \leq -(L-1)$, (ii) $-(L-1) < q < 0$, (iii) $0 \leq q < (L-1)$, and (iv) $q \geq (L-1)$.

In the first case $q \leq -(L - 1)$, as indicated in Figure 4.8, Γ_0^q and Ω_0^q in Equations (4.35-36) are equal to zero, while $\phi_{0,q}(t) = \phi(t - q)$ has no overlap with $\mathfrak{b}_n\{\phi_{0,0}(t)\}_{n=1,2}$.

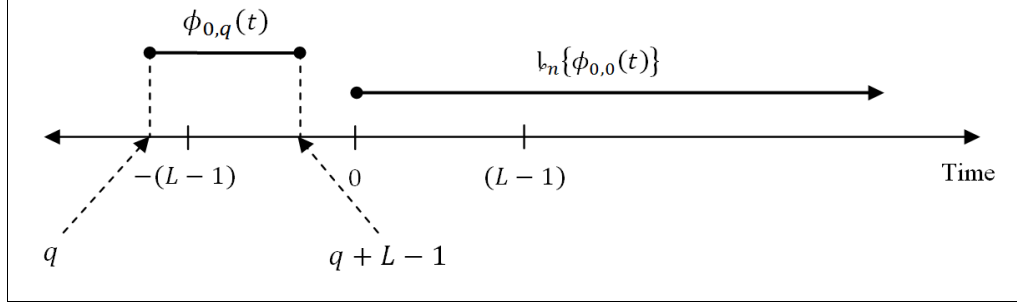


Figure 4.8: The location of $\phi_{0,q}(t)$ in terms of time in the first case, $q \leq -(L - 1)$

In the second case $-(L - 1) < q < 0$, as indicated in Figure 4.9, $\phi_{0,q}(t)$ has partly overlapping $0 \leq t \leq q + L - 1$ with these $\mathfrak{b}_n\{\phi_{0,0}(t)\}_{n=1,2}$, since, it is arduous to modify the integrals in Equations (4.35-36). Accordingly, $\phi_{0,q}(t)$ and $\mathfrak{b}_n\{\phi_{0,0}(t)\}_{n=1,2}$ are unknown functions even in partly overlap. Hence, for now, abandoned Γ_0^q and Ω_0^q are considered as follows:

$$\Gamma_0^q = \Gamma_0^q \Big|_{-(L-1) < q < 0} \quad (4.45)$$

$$\Omega_0^q = \Omega_0^q \Big|_{-(L-1) < q < 0} \quad (4.46)$$

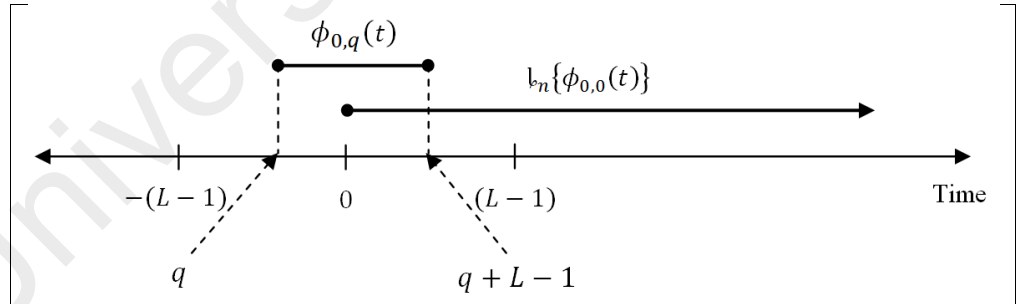


Figure 4.9: The location of $\phi_{0,q}(t)$ in terms of time in the second case, $-(L - 1) < q < 0$

In the third case $0 \leq q < (L - 1)$, as indicated in Figure 4.10, obviously, the overlapped interval can be $q \leq t \leq q + L - 1$, which is the support of $\phi_{0,q}(t)$, hence the supports of $\mathfrak{b}_n\{\phi_{0,0}(t)\}_{n=1,2}$ completely contain the support of $\phi_{0,q}(t)$. Accordingly, Γ_0^q and Ω_0^q can be modified by using Equations (4.41-42), as follows

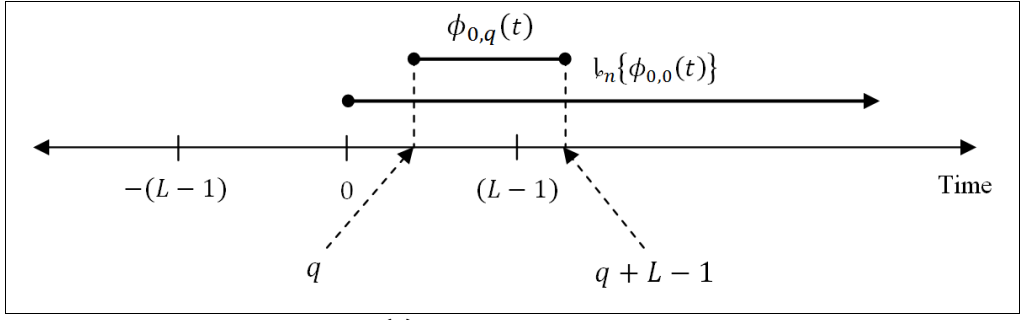


Figure 4.10: The location of $\phi_{0,q}(t)$ in terms of time in the third case, $0 \leq q < (L - 1)$

$$\begin{aligned}
\Gamma_0^q \Big|_{0 \leq q < (L-1)} &= \int_{-\infty}^{+\infty} \mathfrak{b}_1\{\phi(t)\} \phi(t - q) dt \\
&= [\mathfrak{b}_1\{\phi(t)\} \mathfrak{b}_1\{\phi(t - q)\}]_q^{q+L-1} - \int_{-\infty}^{+\infty} \mathfrak{b}_1\{\phi(t - q)\} \phi(t) dt \\
&= \left[\overbrace{\mathfrak{b}_1\{\phi(q + L - 1)\}}^{=1} \overbrace{\mathfrak{b}_1\{\phi(L - 1)\}}^{=1} \right] - \left[\overbrace{\mathfrak{b}_1\{\phi(q)\}}^{=0} \overbrace{\mathfrak{b}_1\{\phi(L - 1)\}}^{=0} \right] \\
&\quad - \int_{-\infty}^{+\infty} \overbrace{\mathfrak{b}_1\{\phi(t')\} \phi(t' + q)}^{=\Gamma_0^{-q}} dt' \\
&= 1 - \Gamma_0^{-q} \Big|_{0 \leq q < (L-1)} \tag{4.47}
\end{aligned}$$

$$\begin{aligned}
\Omega_0^q \Big|_{0 \leq q < (L-1)} &= \int_{-\infty}^{+\infty} \mathfrak{b}_2\{\phi(t)\} \phi(t - q) dt \\
&= [\mathfrak{b}_2\{\phi(t)\} \mathfrak{b}_1\{\phi(t - q)\}]_q^{q+L-1} - \int_{-\infty}^{+\infty} \mathfrak{b}_1\{\phi(t)\} \mathfrak{b}_2\{\phi(t - q)\} dt \\
&= [\mathfrak{b}_2\{\phi(t)\} \mathfrak{b}_1\{\phi(t - q)\}]_q^{q+L-1} - ([\mathfrak{b}_1\{\phi(t)\} \mathfrak{b}_2\{\phi(t - q)\}]_q^{q+L-1} \\
&\quad - \int_{-\infty}^{+\infty} \phi(t) \mathfrak{b}_2\{\phi(t - q)\} dt) \\
&= \mathfrak{b}_2\{\phi(q + L - 1)\} \overbrace{\mathfrak{b}_1\{\phi(L - 1)\}}^{=1} - \mathfrak{b}_2\{\phi(q)\} \overbrace{\mathfrak{b}_1\{\phi(0)\}}^{=0} - \left(\overbrace{\mathfrak{b}_1\{\phi(q + L - 1)\}}^{=1} \mathfrak{b}_2\{\phi(L - 1)\} \right. \\
&\quad \left. - \mathfrak{b}_1\{\phi(L)\} \overbrace{\mathfrak{b}_2\{\phi(0)\}}^{=0} + \int_{-\infty}^{+\infty} \phi(t + q) \mathfrak{b}_2\{\phi(t)\} dt \right) \\
&= \overbrace{\mathfrak{b}_2\{\phi(q + L - 1)\}}^{=q+(L-1)+\mathfrak{b}_2\{\phi(L-1)\}-(L-1)} - \mathfrak{b}_2\{\phi(L - 1)\} + \int_{-\infty}^{+\infty} \phi(t + q) \mathfrak{b}_2\{\phi(t)\} dt \\
&= q + \Omega_0^{-q} \Big|_{0 \leq q < (L-1)} \tag{4.48}
\end{aligned}$$

It is notable that, in Equation (4.48), $\mathfrak{b}_2\{\phi(q + L - 1)\} - \mathfrak{b}_2\{\phi(L - 1)\}$ is identical to q , hence $\mathfrak{b}_2\{\phi(t)\}$ is the linear function with slope identical to one for $t \geq L - 1$. In general,

while the Γ_0^q and the Ω_0^q for $0 < q < (L - 1)$ have been calculated, the Γ_0^q and the Ω_0^q for the second case, i.e., $-(L - 1) < q < 0$, in Equations (4.45-46) can be achieved from Equations (4.47-48).

In the fourth case $q \geq (L - 1)$, as indicated in Figure 4.11, where the overlapped interval is $q \leq t \leq q + L - 1$, Γ_0^q and Ω_0^q can be calculated through inserting $\mathfrak{b}_1\{\phi_{0,0}(t)\} = 1$ and $\mathfrak{b}_2\{\phi_{0,0}(t)\} = t + \mathfrak{b}_2\{\phi_{0,0}(L - 1)\} - (L - 1)$, from Equations (4.41-42), into Γ_0^q and Ω_0^q in Equations (4.35-36), respectively, as follows:

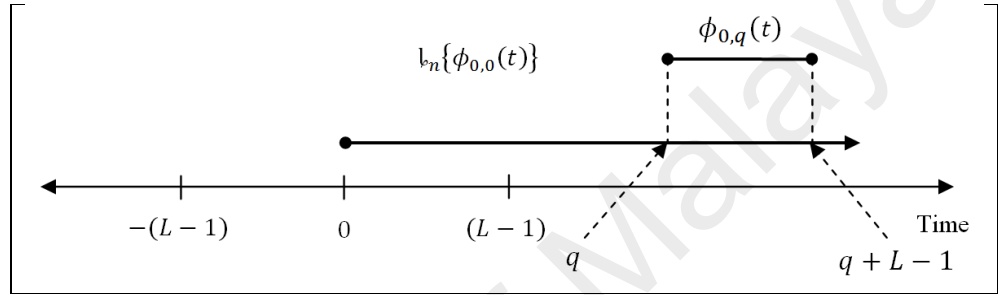


Figure 4.11: The location of $\phi_{0,q}(t)$ in terms of time in the fourth case, $q \geq (L - 1)$

$$\begin{aligned} \Gamma_0^q \Big|_{q \geq (L-1)} &= \int_{-\infty}^{+\infty} \mathfrak{b}_1\{\phi(t)\phi(t-q)\}dt \\ &= \int_q^{q+L-1} \overbrace{\mathfrak{b}_1\{\phi(t)\phi(t-q)\}}^{=1} dt \\ &= 1 \end{aligned} \tag{4.49}$$

$$\begin{aligned} \Omega_0^q \Big|_{q \geq (L-1)} &= \int_{-\infty}^{+\infty} \mathfrak{b}_2\{\phi(t)\phi(t-q)\}dt \\ &= \int_q^{q+L-1} (t + \mathfrak{b}_2\{\phi(L-1)\} - (L-1)) \phi(t-q)dt \\ &= \int_q^{q+L-1} t\phi(t-q)dt + (\mathfrak{b}_2\{\phi(L-1)\} - (L-1)) \int_q^{q+L-1} \phi(t-q)dt \\ &= \overbrace{t[\mathfrak{b}_1\{\phi(t-q)\}]_q^{q+L-1}}^{=(q+L-1)} - \overbrace{\int_q^{q+L-1} \mathfrak{b}_1\phi(t-q)dt}^{=[\mathfrak{b}_2\{\phi(t-q)\}]_q^{q+L-1}} + (\mathfrak{b}_2\{\phi(L-1)\} - (L-1)) \\ &= q \end{aligned} \tag{4.50}$$

The aforementioned results indicate that the following relations of Γ_0^q and Ω_0^q , depending on q , according to the DBN scaling function $\phi(t)$ with the support of $0 \leq t \leq L - 1$:

$$\Gamma_0^q = \begin{cases} 0 & q \leq -(L-1) \\ \Gamma_0^q & -(L-1) < q < 0 \\ 1 - \Gamma_0^{-q} & 0 \leq q < L-1 \\ 1 & q \geq L-1 \end{cases} \quad \Omega_0^q = \begin{cases} 0 & q \leq -(L-1) \\ \Omega_0^q & -(L-1) < q < 0 \\ 1 - \Omega_0^{-q} & 0 \leq q < L-1 \\ q & q \geq L-1 \end{cases} \quad (4.51)$$

From Equation (4.51) is inferred that all the values of Γ_0^q and Ω_0^q for $-\infty < q < \infty$ can be achieved, provided that Γ_0^q and Ω_0^q for $0 \leq q < L-1$ are computed. Hence, in order to ascertain the values of Γ_0^q and Ω_0^q for $0 \leq q < L-1$, the two-scale relations for $\phi(t)$, $I_1\{\phi(t)\}$ and $I_2\{\phi(t)\}$, in Equations (4.37), and (4.39-40) are applied to Equations (4.35-36), as following expressions:

$$\begin{aligned} \Gamma_0^q &= \int_{-\infty}^{\infty} \frac{1}{2} \sum_{j=0}^{L-1} c(j) \mathfrak{b}_1\{\phi(2t-j)\} \sum_{k=0}^{L-1} c(k) \phi(2(t-q)-k) dt \\ &= \frac{1}{2} \sum_{j=0}^{L-1} \sum_{k=0}^{L-1} c(j) c(k) \int_{-\infty}^{\infty} \mathfrak{b}_1\{\phi(2t-j)\} \phi(2t-2q-k) dt \\ &= \frac{1}{2} \sum_{j=0}^{L-1} \sum_{k=0}^{L-1} c(j) c(k) \underbrace{\int_{-\infty}^{\infty} \mathfrak{b}_1\{\phi(t')\} \phi(t'+j-2q-k) dt'}_{= \Gamma_0^{-j+2q+k}} \\ &= \left(\frac{1}{2}\right)^2 \sum_{j=0}^{L-1} \sum_{k=0}^{L-1} c(j) c(k) \Gamma_0^{-j+2q+k} \end{aligned} \quad (4.52)$$

$$\begin{aligned} \Omega_0^q &= \int_{-\infty}^{\infty} \left(\frac{1}{2}\right)^2 \sum_{j=0}^{L-1} c(j) \mathfrak{b}_2\{\phi(2t-j)\} \sum_{k=0}^{L-1} c(k) \phi(2(t-q)-k) dt \\ &= \left(\frac{1}{2}\right)^2 \sum_{j=0}^{L-1} \sum_{k=0}^{L-1} c(j) c(k) \int_{-\infty}^{\infty} \mathfrak{b}_2\{\phi(2t-j)\} \phi(2t-2q-k) dt \\ &= \left(\frac{1}{2}\right)^2 \sum_{j=0}^{L-1} \sum_{k=0}^{L-1} c(j) c(k) \underbrace{\int_{-\infty}^{\infty} \mathfrak{b}_2\{\phi(t')\} \phi(t'+j-2q-k) dt'}_{= \Omega_0^{-j+2q+k}} \\ &= \left(\frac{1}{2}\right)^3 \sum_{j=0}^{L-1} \sum_{k=0}^{L-1} c(j) c(k) \Omega_0^{-j+2q+k} \end{aligned} \quad (4.53)$$

By substituting $q = 0, 1, 2, \dots, L-2$ into Equation (4.52) and considering the Equation (4.51), the following linear system of equations can be obtained for the coefficients Γ_0^q for $0 \leq q < L-1$:

$$\begin{pmatrix} \Gamma_0^0 \\ \Gamma_0^1 \\ \vdots \\ \Gamma_0^n \\ \vdots \\ \Gamma_0^{L-2} \end{pmatrix} = \begin{bmatrix} E_{0,0} & E_{0,1} & \cdots & E_{0,n} & \cdots & E_{0,L-2} \\ E_{1,0} & E_{1,1} & \cdots & E_{1,n} & \cdots & E_{1,L-2} \\ \vdots & \vdots & \vdots & \vdots & \vdots & \vdots \\ E_{m,0} & E_{m,1} & \cdots & E_{m,n} & \cdots & E_{m,L-2} \\ \vdots & \vdots & \vdots & \vdots & \vdots & \vdots \\ E_{L-2,0} & E_{L-2,1} & \cdots & E_{L-2,n} & \cdots & E_{L-2,L-2} \end{bmatrix}^{-1} \begin{pmatrix} c_0 \\ c_1 \\ \vdots \\ c_m \\ \vdots \\ c_{L-2} \end{pmatrix} \quad (4.54)$$

where

$$E_{m,n} = \left(\frac{1}{2}\right)^2 [-\sum_{r \in \mathbb{Z}} c(r)c(r+n+2m) + \sum_{r \in \mathbb{Z}} c(r)c(r+n-2m) - \sum_{r \in \mathbb{Z}} c(r)c(r+2m)\delta_{0,n} - \delta_{m,n}] \quad (4.55)$$

$$c_m = \left(\frac{1}{2}\right)^2 [\delta_{0,m} \sum_{r \in \mathbb{Z}} c(r)c(r+L-1) - \sum_{v=1,2,3,\dots} \sum_{r \in \mathbb{Z}} c(r)c(r+2m+1+v) - \sum_{v=1,2,3,\dots} \sum_{r \in \mathbb{Z}} c(r)c(r-2m+1+(L-2)+v)] \quad (4.56)$$

in which $\delta_{m,n}$ is the Kronecker delta. The vector $\Gamma = \{\Gamma_0^0, \Gamma_0^1, \dots, \Gamma_0^{L-2}\}^{-1}$ can be computed through solving the linear system depicted in Equation (4.54).

In addition, it is feasible to achieve the linear system of equations for the unknown vector Ω from Equation (4.53), by following the same procedure presented for Γ , as follows:

$$\begin{pmatrix} \Omega_0^0 \\ \Omega_0^1 \\ \vdots \\ \Omega_0^n \\ \vdots \\ \Omega_0^{L-2} \end{pmatrix} = \begin{bmatrix} B_{0,0} & B_{0,1} & \cdots & B_{0,n} & \cdots & B_{0,L-2} \\ B_{1,0} & B_{1,1} & \cdots & B_{1,n} & \cdots & B_{1,L-2} \\ \vdots & \vdots & \vdots & \vdots & \vdots & \vdots \\ B_{m,0} & B_{m,1} & \cdots & B_{m,n} & \cdots & B_{m,L-2} \\ \vdots & \vdots & \vdots & \vdots & \vdots & \vdots \\ B_{L-2,0} & B_{L-2,1} & \cdots & B_{L-2,n} & \cdots & B_{L-2,L-2} \end{bmatrix}^{-1} \begin{pmatrix} y_0 \\ y_1 \\ \vdots \\ y_m \\ \vdots \\ y_{L-2} \end{pmatrix} \quad (4.57)$$

where

$$B_{m,n} = \left(\frac{1}{2}\right)^3 [\sum_{r \in \mathbb{Z}} c(r)c(r+n+2m) + \sum_{r \in \mathbb{Z}} c(r)c(r+n-2m) - \sum_{r \in \mathbb{Z}} c(r)c(r+2m)\delta_{0,n} - \delta_{m,n}] \quad (4.58)$$

$$y_m = \left(\frac{1}{2}\right)^3 [-\delta_{0,m} \sum_{r \in \mathbb{Z}} c(r)c(r+L-1) + \sum_{v=1,2,3,\dots} \sum_{r \in \mathbb{Z}} c(r)c(r+2m+1+v) \{v+1\} - \sum_{v=1,2,3,\dots} \sum_{r \in \mathbb{Z}} c(r)c(r-2m+1+(L-2)+v) \{L-1+v\}] \quad (4.59)$$

The vector $\Omega = \{\Omega_0^0, \Omega_0^1, \dots, \Omega_0^{L-2}\}^{-1}$ can be computed by solving the linear system indicated in Equation (4.57).

In general, while the Γ_0^q and the Ω_0^q for $-\infty < q < \infty$ have been acquired from Equations (4.51), (4.54) and (4.57), the velocity $\dot{x}_h(t)$ and displacement $x_h(t)$ can be obtained from the known acceleration $\ddot{x}_h(t)$, as follows:

$$\dot{x}_h(t) = \sum_{l=0}^n \sum_{k=0}^n a_h(0, k) \Gamma_0^{l-k} \phi_{0,l}(t) \quad (4.60)$$

$$x_h(t) = \sum_{l=0}^n \sum_{k=0}^n a_h(0, k) \Omega_0^{l-k} \phi_{0,l}(t) \quad (4.61)$$

4.3.3 Definition of dominant component

This section indicates that the equations of motion depicted in Equations (4.30) can be decomposed by applying the WPT. The dominant component can be defined according to the distribution of the relative energies of the WPT components at a certain level of decomposition of the acceleration response.

One can then convert the equations of motion according to the complete representation set of the WPT components depicted in Equations (4.62-63), into those according to the reduced representation sets, i.e., dominant components, and thereby performs the subsequent step of implementing the least square error minimization method over the dominant components.

4.3.3.1 Equations of motion according to the WPT

The equations of motion according to $a_h(0, l)$, $v_h(0, l)$, $d_h(0, l)$, and $p_h(0, l)$ depicted in Equation (4.30) can be represented in terms of the WPT as follows:

$$M[U_{i,j}^{\ddot{X}}]_D + C[U_{i,j}^{\dot{X}}]_D + K[U_{i,j}^X]_D = [U_{i,j}^F]_D \quad (4.62)$$

Equation (4.62) can be written as:

$$\begin{aligned}
& \begin{bmatrix} m_1 & 0 & \cdots & 0 & \cdots & 0 \\ 0 & m_2 & \cdots & 0 & \cdots & 0 \\ \vdots & \vdots & \vdots & \vdots & \vdots & \vdots \\ 0 & 0 & \cdots & m_h & \cdots & 0 \\ \vdots & \vdots & \vdots & \vdots & \vdots & \vdots \\ 0 & 0 & \cdots & 0 & \cdots & m_N \end{bmatrix} \begin{Bmatrix} \{U_{i,j}^X[\{a_1(0,l)\}_{l=0,1,2,\dots,n}]\}_{i=D} \\ \{U_{i,j}^X[\{a_2(0,l)\}_{l=0,1,2,\dots,n}]\}_{i=D} \\ \vdots \\ \{U_{i,j}^X[\{a_h(0,l)\}_{l=0,1,2,\dots,n}]\}_{i=D} \\ \vdots \\ \{U_{i,j}^X[\{a_N(0,l)\}_{l=0,1,2,\dots,n}]\}_{i=D} \end{Bmatrix} \\
& + \begin{bmatrix} c_1 + c_2 & -c_2 & \cdots & 0 & \cdots & 0 \\ -c_2 & c_2 + c_3 & \cdots & 0 & \cdots & 0 \\ \vdots & \vdots & \vdots & \vdots & \vdots & \vdots \\ 0 & 0 & \cdots & c_h + c_{h+1} & \cdots & 0 \\ \vdots & \vdots & \vdots & \vdots & \vdots & -c_N \\ 0 & 0 & \cdots & -c_N & \cdots & c_N \end{bmatrix} \begin{Bmatrix} \{U_{i,j}^X[\{v_1(0,l)\}_{l=0,1,2,\dots,n}]\}_{i=D} \\ \{U_{i,j}^X[\{v_2(0,l)\}_{l=0,1,2,\dots,n}]\}_{i=D} \\ \vdots \\ \{U_{i,j}^X[\{v_h(0,l)\}_{l=0,1,2,\dots,n}]\}_{i=D} \\ \vdots \\ \{U_{i,j}^X[\{v_N(0,l)\}_{l=0,1,2,\dots,n}]\}_{i=D} \end{Bmatrix} \\
& + \begin{bmatrix} k_1 + k_2 & -k_2 & \cdots & 0 & \cdots & 0 \\ -k_2 & k_1 + k_2 & \cdots & 0 & \cdots & 0 \\ \vdots & \vdots & \vdots & \vdots & \vdots & \vdots \\ 0 & 0 & \cdots & k_h + k_{h+1} & \cdots & 0 \\ \vdots & \vdots & \vdots & \vdots & \vdots & -k_N \\ 0 & 0 & \cdots & -k_N & \cdots & k_N \end{bmatrix} \begin{Bmatrix} \{U_{i,j}^X[\{d_1(0,l)\}_{l=0,1,2,\dots,n}]\}_{i=D} \\ \{U_{i,j}^X[\{d_2(0,l)\}_{l=0,1,2,\dots,n}]\}_{i=D} \\ \vdots \\ \{U_{i,j}^X[\{d_h(0,l)\}_{l=0,1,2,\dots,n}]\}_{i=D} \\ \vdots \\ \{U_{i,j}^X[\{d_N(0,l)\}_{l=0,1,2,\dots,n}]\}_{i=D} \end{Bmatrix} \\
& = \begin{Bmatrix} \{U_{i,j}^X[\{p_1(0,l)\}_{l=0,1,2,\dots,n}]\}_{i=D} \\ \{U_{i,j}^X[\{p_2(0,l)\}_{l=0,1,2,\dots,n}]\}_{i=D} \\ \vdots \\ \{U_{i,j}^X[\{p_h(0,l)\}_{l=0,1,2,\dots,n}]\}_{i=D} \\ \vdots \\ \{U_{i,j}^X[\{p_N(0,l)\}_{l=0,1,2,\dots,n}]\}_{i=D} \end{Bmatrix} \tag{4.63}
\end{aligned}$$

where $U_{i,j}^Y$ is i^{th} signal decomposition at the decomposition level j of the signal Y , i.e. acceleration, velocity and displacement, in terms of WPT and D depicts the set $\{1, 2, \dots, 2^j\}$. Accordingly, Equations (4.62-63) can be considered as the equations of motion decomposed in terms of the WPT.

According to the distribution of relative energies over the WPT components at a specified decomposition level of a signal, the dominant component D_c of the signal are defined as

$$D_c = \{s_1, s_2, \dots, s_c\} \quad (4.64)$$

in which s_c shows the sequence number of the WPT component having the c^{th} highest relative energy. At a certain level of decomposition j , a dominant component D_c can be a subset of the $D = \{1, 2, \dots, 2^j\}$ of the WPT components of the signal. In general, the dominant component D_c is the reduced representation set, by the information with regards to the sequence numbers of the WPT components, in terms of energy.

Technically, while the input and output data are excessively large to be process and are supposed to be redundant, the data are converted into a reduced representation set of features. If the extracted features are accurately selected, the features set will include the relevant information from the input and output data, and make it possible to perform the desired task utilizing this reduced representation instead of the full size of input and output data.

Therefore, the purpose of defining the dominant components is to produce the reduced representation set in order to carry out the least squares error minimization over the dominant components. In structural dynamics, the responses of a linear model consist of a linear combination of modal responses and the coefficients of modal vectors. Sometimes, in the presence of a node in the modal vectors, a response does not have the contribution from the corresponding modal response, which instead can be quite important. Therefore, in defining the dominant components, it is important to consider multiple responses rather than one specific response.

In general, the dominant components can be achieved as follows: first, the relative energies of the WPT components at a certain level of decomposition of acceleration responses at all floors are computed; second, individually, the average of the relative energies of the WPT components of the same direction is computed; third, the dominant components can be defined from the average energy distribution over the WPT components at that specific level.

Based on the fact that the dominant components can be achieved by the average relative energy distribution over the WPT components of the system's acceleration responses, the equations of motion for the system at the certain level j can be transformed into those in terms of the dominant component D_c ,

$$M[U_{i,j}^{\ddot{X}}]_{D_c} + C[U_{i,j}^{\dot{X}}]_{D_c} + K[U_{i,j}^X]_{D_c} = [U_{i,j}^F]_{D_c} \quad (4.65)$$

These equations of motion according to one particular dominant component, D_c , can be observed as the reduced representation of those in terms of the WPT in Equations (4.30). The aim is to carry out the least square error minimization method over the dominant components, as opposed to being forced to apply the complete data.

4.3.4 Least square error minimization procedure

Equations (4.65) can be observed as a linear inverse problem involving the estimation of structural parameters such as the mass, damping, and stiffness components. The determination of such parameters can be obtained by formulating an optimization problem, such as:

$$\|\mathbb{F}_c\| \rightarrow \min \quad (4.66)$$

where

$$\mathbb{F}_c = M[U_{i,j}^{\ddot{X}}]_{D_c} + C[U_{i,j}^{\dot{X}}]_{D_c} + K[U_{i,j}^X]_{D_c} - [U_{i,j}^F]_{D_c} \quad (4.67)$$

in which \mathbb{F}_c is a vector including the unknown components of mass, damping, and stiffness matrices, according to the chosen dominant component D_c .

By utilizing the least square error minimization procedure depicted in Equation (4.66) on $D_1, D_2, \dots, D_{c_j}, \dots, D_c$, the corresponding $\mathbb{F}_1, \mathbb{F}_2, \dots, \mathbb{F}_{c_j}, \dots, \mathbb{F}_c$ can be achieved. The variation among the identified \mathbb{F}_c and \mathbb{F}_{c-1} will be affected directly by the WPT component with c^{th} highest relative WPT component energy. Evidently, as c increases, the variation among \mathbb{F}_c and \mathbb{F}_{c-1} becomes smaller, up to a point where, at a given c_j , such a variation can be considered negligible. This implies that the WPT components

with c_{jj}^{th} highest component energy for $c_{jj} \geq c_j$ cannot be helped in improving the identification results.

By iterating the least square error minimization procedure over the dominant components D_c for $c = 1, 2, 3, \dots$, one can find that F_c converges to the correct values. It can also be observed that the dominant component where F_c starts converging to the correct ones is the most accurate dominant component. Noteworthy that in real application, it is not essential to start implementing the least square error minimization procedure from the first dominant component D_1 . To avoid time-consuming iterative computations for convergence, implementing the least square method can be started from a given dominant component D_{c_s} that includes the WPT components C_s with large relative WPT component energies.

4.3.5 Nonlinear parameter estimation using wavelet multiresolution

When structural damage occurs, nonlinearity usually exists in damaged structures. Hence, in this section, wavelet multiresolution technique is used to identify the nonlinear structural parameters.

4.3.5.1 Procedure for nonlinear system

For the N -DOF nonlinear system, the equation of motion can be expressed as:

$$M\ddot{x}(t) + f_R(\dot{x}(t), x(t)) = f(t) \quad (4.68)$$

where M is the $N \times N$ diagonal mass matrix of mass, $x(t)$ is the length- N vector of structural displacement, $f_R(\dot{x}(t), x(t))$ is nonlinear restoring force vector, and $f(t)$ is the system's external excitation.

Suppose that mass remain constant during the excitation, while damping of the system has piecewise linear characteristics and the stiffness is a function of displacement, once the structure enters a nonlinear stage and require to be identified. If we presume that the

stiffness matrix remain constant within every time step, then Equation (4.68) is easily converted into incremental representation as follows:

$$M\Delta\ddot{x}(t) + C(t)\Delta\dot{x}(t) + S(t)\Delta x(t) = f(t) \quad (4.69)$$

in which $C(t)$ is piecewise linear damping matrix and $S(t)$ is tangent stiffness matrix at the beginning of each time step. Supposing that there is an N -story shear-type building model, Equation (4.69) can be written as:

$$\begin{aligned} & \begin{bmatrix} m_1 & 0 & 0 & \cdots & 0 & 0 \\ 0 & m_2 & 0 & \cdots & 0 & 0 \\ \vdots & \vdots & \vdots & \vdots & \vdots & \vdots \\ 0 & 0 & 0 & \cdots & m_{N-1} & 0 \\ 0 & 0 & 0 & \cdots & 0 & m_N \end{bmatrix} \begin{Bmatrix} \Delta\ddot{x}_1(t) \\ \Delta\ddot{x}_2(t) \\ \vdots \\ \Delta\ddot{x}_{N-1}(t) \\ \Delta\ddot{x}_N(t) \end{Bmatrix} \\ & + \begin{bmatrix} c_1(t) + c_2(t) & -c_2(t) & 0 & \cdots & 0 & 0 & 0 \\ -c_2(t) & c_2(t) + c_3(t) & -c_3(t) & \cdots & 0 & 0 & 0 \\ \vdots & \vdots & \vdots & \vdots & \vdots & \vdots & \vdots \\ 0 & 0 & 0 & \cdots & -c_{N-1}(t) & c_{N-1}(t) + c_N(t) & -c_N(t) \\ 0 & 0 & 0 & \cdots & 0 & -c_N(t) & c_N(t) \end{bmatrix} \begin{Bmatrix} \Delta\dot{x}_1(t) \\ \Delta\dot{x}_2(t) \\ \vdots \\ \Delta\dot{x}_{N-1}(t) \\ \Delta\dot{x}_N(t) \end{Bmatrix} \\ & + \begin{bmatrix} s_1(t) + s_2(t) & -s_2(t) & 0 & \cdots & 0 & 0 & 0 \\ -s_2(t) & s_2(t) + s_3(t) & -s_3(t) & \cdots & 0 & 0 & 0 \\ \vdots & \vdots & \vdots & \vdots & \vdots & \vdots & \vdots \\ 0 & 0 & 0 & \cdots & -s_{N-1}(t) & s_{N-1}(t) + s_N(t) & -s_N(t) \\ 0 & 0 & 0 & \cdots & 0 & -s_N(t) & s_N(t) \end{bmatrix} \begin{Bmatrix} \Delta x_1(t) \\ \Delta x_2(t) \\ \vdots \\ \Delta x_{N-1}(t) \\ \Delta x_N(t) \end{Bmatrix} \\ & = \begin{Bmatrix} \Delta f_1(t) \\ \Delta f_2(t) \\ \vdots \\ \Delta f_{N-1}(t) \\ \Delta f_N(t) \end{Bmatrix} \quad (4.70) \end{aligned}$$

where m_h , $c_h(t)$ and $s_h(t)$ ($h = 1, 2, \dots, N$) are mass, damping and tangent stiffness coefficients at h^{th} story, respectively; and $\Delta\ddot{x}_h(t)$, $\Delta\dot{x}_h(t)$ and $\Delta x_h(t)$ are incremental acceleration, velocity and displacement at h^{th} story, respectively. Matrix Equation (4.70) can be rewritten as:

$$c_h(t)[\Delta\dot{x}_h(t) - \Delta\dot{x}_{h-1}(t)] + s_h(t)[\Delta x_h(t) - \Delta x_{h-1}(t)] = \sum_{\alpha=h}^N [-m_\alpha \Delta\ddot{x}_h(t) + \Delta f_\alpha] \quad (2 \leq h \leq N)$$

$$c_h(t)\Delta\dot{x}_1(t) + s_h(t)\Delta x_1(t) = \sum_{\alpha=1}^N [-m_\alpha \Delta\ddot{x}_h(t) + \Delta f_\alpha] \quad (4.71)$$

where $\Delta x_h(t) = x_h(t) - x_h(t - \Delta t)$ indicates the incremental displacement; $\Delta x_h(t) - \Delta x_{h-1}(t)$ and $\Delta\dot{x}_h(t) - \Delta\dot{x}_{h-1}(t)$ are incremental inter-story drifts and velocity, respectively. The tangent stiffness $s_h(t)$ can be approximated using a scaling function at scale index j , as follow:

$$s_h(t) = \sum_{k=0}^l \mathfrak{K}_h(j, k) \phi_h(2^{-j}t - k) \quad (4.72)$$

where k is translation parameter of scaling function $\phi_h(t)$ and $\mathfrak{K}_h(j, k)$ is the integral coefficients of the scaling functions. With substituting Equation (4.72) into (4.71) creates the incremental governing equation of the h^{th} story:

$$\begin{aligned} c_h(t)[\Delta\dot{x}_h(t) - \Delta\dot{x}_{h-1}(t)] + \sum_{k=0}^l \mathfrak{K}_h(j, k) \phi_h(2^{-j}t - k) [\Delta x_h(t) - \Delta x_{h-1}(t)] \\ = \sum_{\alpha=h}^N [-m_\alpha \Delta\ddot{x}_h(t) + \Delta f_\alpha] \quad (2 \leq h \leq N) \\ c_h(t)\Delta\dot{x}_1(t) + \sum_{k=0}^l \mathfrak{K}_h(j, k) \phi_h(2^{-j}t - k) \Delta x_1(t) \\ = \sum_{\alpha=1}^N [-m_\alpha \Delta\ddot{x}_h(t) + \Delta f_\alpha] \end{aligned} \quad (4.73)$$

For notational convenience, let us set $\Delta\varepsilon_h(t) = \Delta x_h(t) - \Delta x_{h-1}(t)$ and $\Delta\dot{\varepsilon}_h(t) = \Delta\dot{x}_h - \Delta\dot{x}_{h-1}$, Equation (4.73) can be rewritten as:

$$c_h(t)[\Delta\dot{\varepsilon}_h(t)] + \sum_{k=0}^l \mathfrak{K}_h(j, k) \phi_h(2^{-j}t - k) [\Delta\varepsilon_h(t)] = \sum_{\alpha=h}^N [-m_\alpha \Delta\ddot{x}_h(t) + \Delta f_\alpha] \quad (4.74)$$

Substitution of the structural responses at $t = t_1 \sim t_n$ into Equation (4.74) yields

$$V_h = \Theta_h A_h \quad (4.75)$$

where

$$V_{h,n \times (l+e+1)} = \begin{bmatrix} \Delta\dot{\varepsilon}_h(t_1) & 0 & \dots & 0 & \phi_h(2^{-j}t_1)\Delta\varepsilon_h(t_1) & \dots & \phi_h(2^{-j}t_1 - l)\Delta\varepsilon_h(t_1) \\ \vdots & \vdots & \ddots & & & & \\ \Delta\dot{\varepsilon}_h(t_f) & 0 & & & & & \\ & \Delta\dot{\varepsilon}_h(t_{f+1}) & & \vdots & & & \\ & \vdots & \ddots & & \vdots & \ddots & \vdots \\ & \Delta\dot{\varepsilon}_h(t_g) & & & \vdots & & \vdots \\ \vdots & 0 & & 0 & & & \\ & \vdots & \ddots & \Delta\dot{\varepsilon}_h(t_r) & & & \\ & \vdots & & \vdots & & & \\ 0 & 0 & \dots & \Delta\dot{\varepsilon}_h(t_n) & \phi_h(2^{-j}t_n)\Delta\varepsilon_h(t_n) & \dots & \phi_h(2^{-j}t_n - l)\Delta\varepsilon_h(t_n) \end{bmatrix}$$

$$\Theta_{h,(l+e+1) \times 1} = \begin{bmatrix} c_1 \\ c_2 \\ \vdots \\ c_e \\ \kappa_h(j, 0) \\ \vdots \\ \kappa_h(j, l) \end{bmatrix}, A_{h,n \times 1} = \begin{Bmatrix} \sum_{\alpha=h}^N [-m_\alpha \Delta \ddot{x}_h(t_1) + \Delta f_\alpha] \\ \vdots \\ \sum_{\alpha=h}^N [-m_\alpha \Delta \ddot{x}_h(t_n) + \Delta f_\alpha] \end{Bmatrix}$$

in which c_1 for $t_1 \leq t \leq t_f$; c_2 for $t_{f+1} \leq t \leq t_g$; ... c_e for $t_r \leq t \leq t_n$. V_h and A_h are known matrices composed of observations, estimated state, and scaling functions. The unknown parameters, vector Θ_h are obtained by least square method,

$$\Theta_h = (V_h^T V_h)^{-1} V_h^T A_h \quad (4.76)$$

where V_h^T is the transpose of matrix V_h , while Θ_h is the calculated tangent stiffness $s_h(t)$ which can be approximated by substituting $\kappa_h(j, k)$ into Equation (4.72). Accordingly, the time-varying tangent stiffness can be obtained using wavelet multiresolution analysis in every time step. Furthermore, the incremental nonlinear restoring force in every story is computed through multiplying the tangent stiffness by the incremental inter-story drift, and the nonlinear restoring force can be achieved by summing all incremental nonlinear restoring forces. Consequently, the hysteresis curves of every story can be easily obtained. An index λ_i is used to quantitatively evaluate the error between the exact and nonlinear restoring force estimated through the proposed method and is defined as:

$$\lambda_i = \frac{\sum_{r=1}^n (\text{RF}_{ir} - \widehat{\text{RF}}_{ir})^2}{\sum_{r=1}^n (\text{RF}_{ir})^2} \times 100 \quad (4.77)$$

where n is the number of data points; RF_{ir} presents simulated restoring force responses of the i^{th} floor at time t_r and $\widehat{\text{RF}}_{ir}$ stands for unbiased estimation of RF_{ir} .

Furthermore, to obtain accurate estimation and minimize the computational effort in the proposed system identification method, the GA is used for the selection of wavelet type, by introducing a fitness function to search for the optimal Daubechies order

$$\min \left\| \frac{\text{mean}(AF_j)}{\sum_{l_0=1}^D AF_{l_0}} \right\|_2 \quad (4.78)$$

where $\|\cdot\|_2$ is the Euclidean norm, AF_j is average of the relative energies of the WPT components at decomposition level j of the acceleration responses and \tilde{D} is number of dominant energies of AF_j which is related to structural frequencies. The proposed chromosomes contain five genes for the Daubechies mother wavelet function and hence, the Daubechies order search space is limited to DB1 to DB31. The whole scheme of the proposed system identification method is given in the block diagram of Figure 4.12.

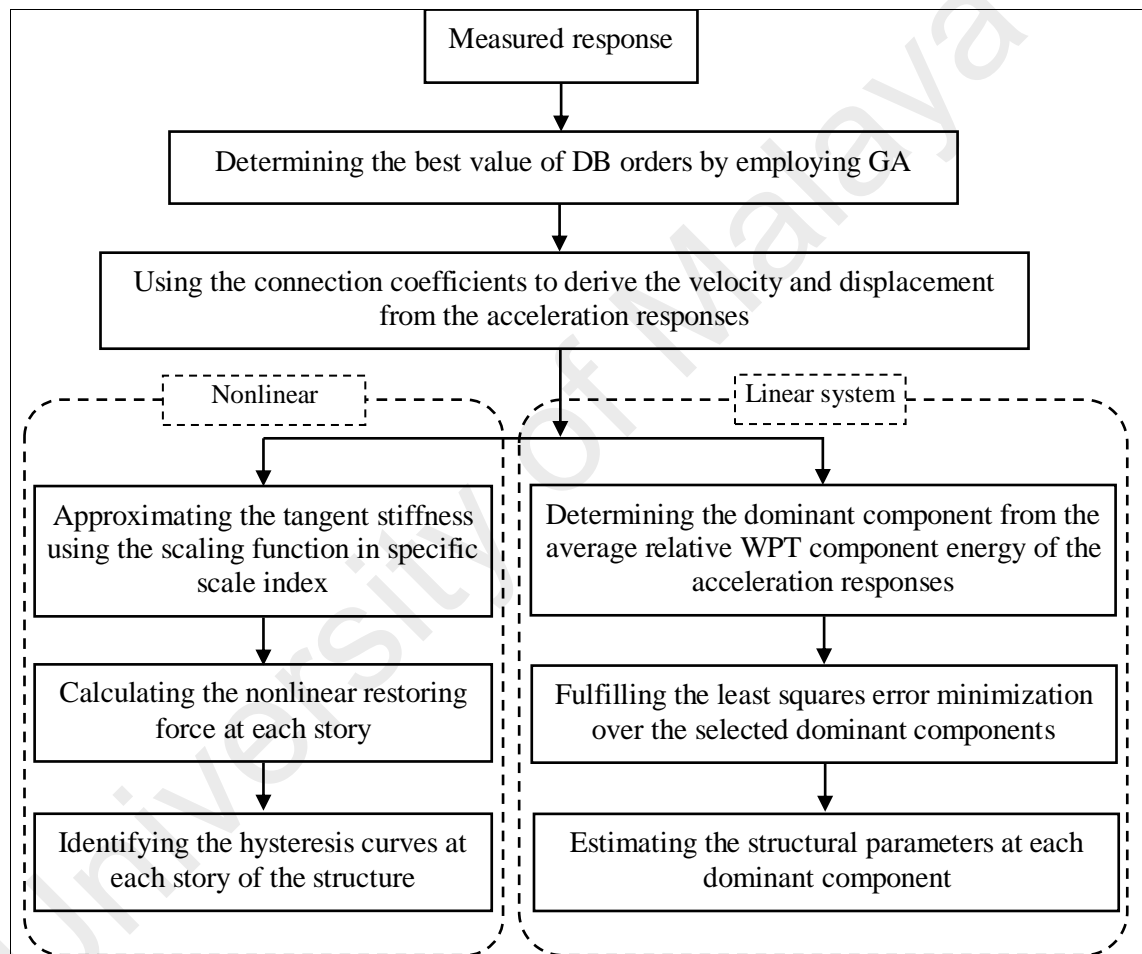


Figure 4.12: Block diagram of the proposed system identification method

4.4 Summary

In this chapter, to examine the structural health condition, at first the multiresolution wavelet packet transform is combined with entropy analysis to determine an effective damage index, RWPE, to obtain the information about the relative energy correlated with various frequency bands presented in structural response segments for investigating the

location of damage. Then, the GA optimization method is applied to estimate the damage severities by defining a database to reveal the relationships between the energies obtained in the previous step and damage severities. However, for most of in-field structures, the monitored data from initial pristine structural states are not available. Therefore, the reference-free damage detection algorithm is proposed based on the RWPE. The procedure does not require vibration signals from an undamaged structure because the proposed method is effectively capable of comparing signals from different locations in the existing state. To ameliorate the algorithm, GA was utilized to identify the best choice for “mother wavelet function” and “decomposition level” of the signals by means of the fundamental fitness function to optimize the algorithm.

Moreover, the wavelet multiresolution analysis is applied for the identification of structural parameters of linear and nonlinear systems. In this way, first, velocity and displacement responses are derived from the acceleration response through applying the connection coefficients. To enhance the accuracy of system identification the best DB order is determined by using GA; Second, defining the dominant components of acceleration responses by introducing the concept of energy to the wavelet components; and next, identifying the accurate structural parameters of the linear system via implementing the least square error minimization over the dominant components. In addition, the scaling function of multiresolution analysis can be used to approximate tangent stiffness matrix and subsequently identified the hysteresis-restoring force curves of the structures. The proposed algorithms will be verified with experimental and numerical structural models.

CHAPTER 5: EXPERIMENTAL WORK

5.1 Introduction

This chapter focuses on the illustration of numerical and experimental setup considered in this research work to evaluate the proposed damaged detection and system identification methods. In the first part, configurations of steel I-beam and three-story building model with various damage scenarios associated with different damage locations and damage severities are presented. In the second part, for the assessment of system identification method, different damage cases with linear and nonlinear conditions have been numerically simulated and tested; beam structure under flexural vibration and three-story building model. Also, to simulate the damage during the experimental test a variable stiffness device is introduced to reduce the stiffness of some stories. Finally, experimental instrumentations such as excitation types and sources, data acquisition, accelerometers and force transducer are explained.

5.2 Illustrative models for damage detection

The numerical and experimental studies of I-section steel beam and three-story building model with various damage scenarios are conducted for assessment of the proposed damage detection methods.

5.2.1 I-Beams

5.2.1.1 Numerical study

In this study, numerical simulations of five 3000 mm-span-length steel-I beams with considered damages are carried out, as shown in Figure 5.1(a). Beams' flange width and section depth is 75 mm and 150 mm, respectively. Thickness of flange and web is 7 mm

and 5 mm, respectively, as shown in Figure 5.1(b). Beam 0 is considered as the reference beam without damage while Beam 1 is the single damage scenario with damage located at point 5. Beam 2 has two points of damage at locations 11 and 13. Beam 3 has three points of damage at locations of 9, 11 and 13, and Beam 4 has three damage points induced at the middle of the beam and at locations 10 and 12. Damage is simulated in the form of a 3mm-width notch. Let t_n^d stands for damage depth in which n is a number assigned to each damage depth case ($n = 1, 2, \dots, 25$). The damage depth is increased gradually for all beams from 3mm up to 75mm, as depicted in Figure 5.1(b). The damage severity is introduced by α_n which is to be calculated by Equation (5.1). The mass density and modulus of elasticity of the beam material are 7850 kg/m^3 and 2.1 GPa, respectively. The Poisson's ratio is 0.33.

$$\alpha_n = \frac{t_n^d}{t} \quad (5.1)$$

The time history acceleration responses of beams are computed by the finite-element based software (ABAQUS) using transient dynamic analysis. To simulate an impulse load, the force-time history is applied at location 14 on the beam. This location is not a node point for the first five flexural mode shapes. If a node point of a mode shape is situated at the excitation point, then this mode cannot be excited and identified. Location 15 is very close to the support and can be affected by the support, thus it cannot be chosen as the excitation point. Also, locations 10, 11 and 13 have node points of modes 5, 3 and 4, respectively. Hence these nodes are not considered as excitation point as well. Therefore, location 14 is chosen against locations 8 and 12 for the following reasons: (i) Mid-span of the beam, labeled as location 8 is the node point for modes 2 and 4; (ii) The damage locations in beam 3 are very close to location 12 and cannot be selected as the excitation point. Thus, to provide a better excitation, location 14 is chosen as an excitation point in this study. The node acceleration responses of the beam subjected to the impulse load are obtained from sixteen locations on the top flange, as shown in Figure 5.1(a) at a

sampling frequency of 2000 Hz to identify the characteristics of damage in beams. Also, the frequency bands of the WPT components at decomposition level 6, as well as the relation between the WPT components and the frequencies of Beam 0 are demonstrated in Table 5.1.

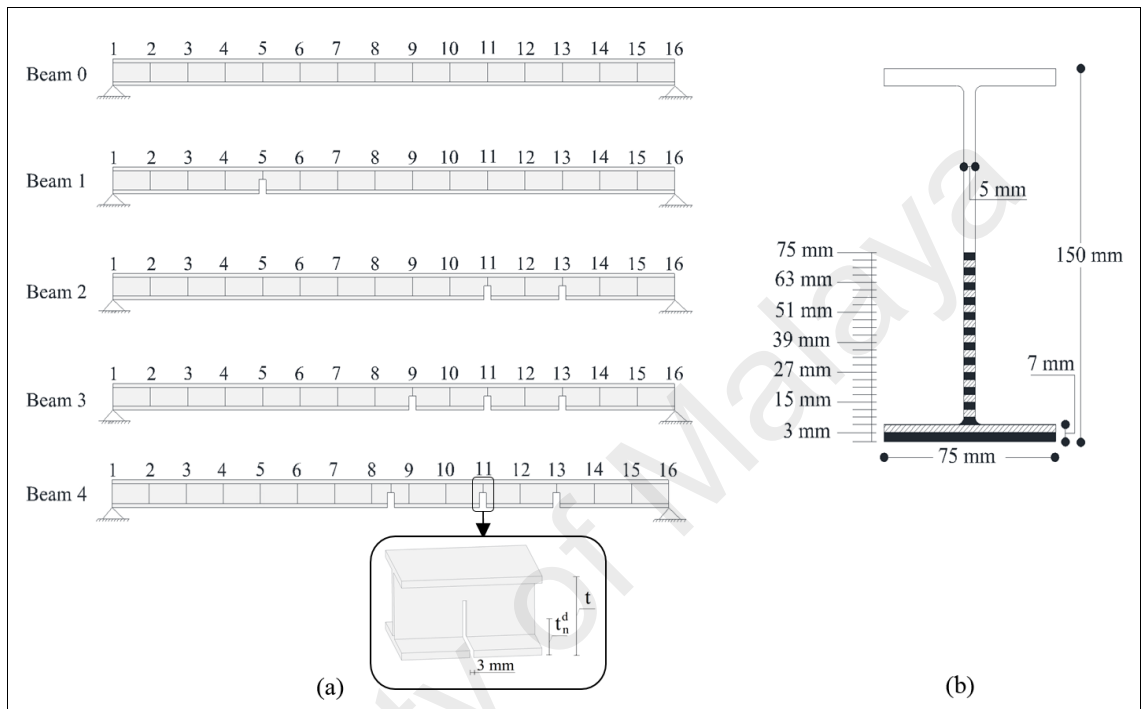


Figure 5.1: I-section specimen. (a) Dimension and damage depth of beams, (b) damage location of beams

Table 5.1: Frequency bands of the WPT Components at decomposition level 6 of undamaged Beam

The sequence of WPT	Frequency bands of WPT components (Hz)	Natural frequencies (Hz)
1	[0-15.625]	12.888
2	[15.625-31.25]	25.784
3	[31.25-46.875]	-----
4	[46.875-62.5]	52.80
⋮	⋮	⋮
15	[187.5-203.125]	201.64
⋮	⋮	⋮
28	[421.875-437.5]	429.67
⋮	⋮	⋮
48	[703.125-718.75]	714.90
⋮	⋮	⋮
64	[984.375-1000]	-----

5.2.1.2 Experimental study

The steel I-beam, with previously described geometry, as the first structure in this study is investigated experimentally. Vibration tests are carried out on four I-section steel beams with a length of 3200 mm including a 100 mm overhang at both end supports ends under undamaged and various damage states, as depicted in Figure 5.2. The damage is induced by introducing a saw cut at the prescribed locations on the beam with varying depths of cut, as described in Table 5.2.

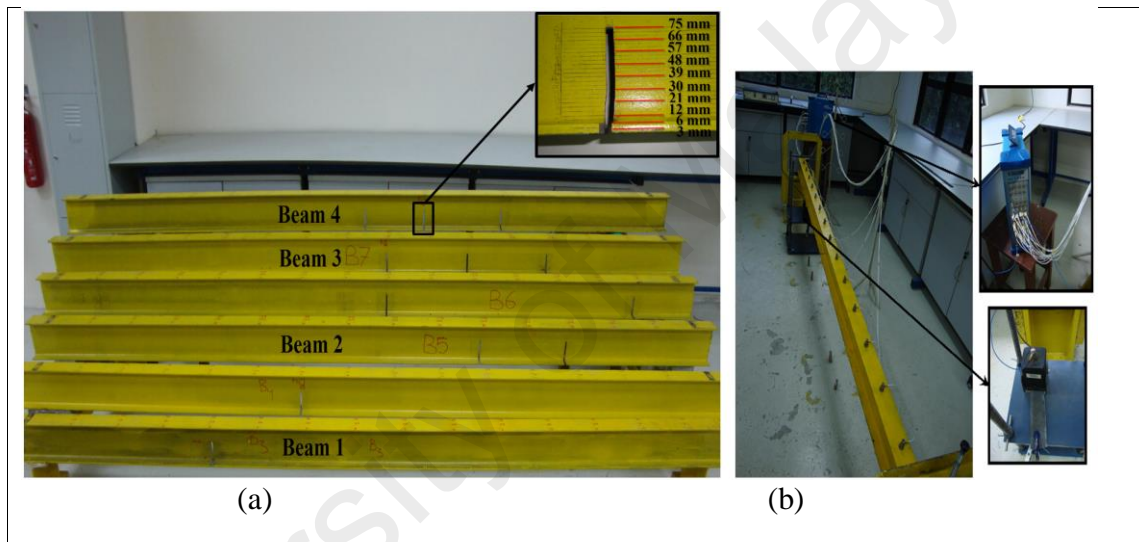


Figure 5.2: Dynamic test in laboratory. (a) Tested beams, (b) experimental setup and data acquisition system

Table 5.2: Beam damage scenarios

Damage case	Damage scenario	Damage location	Width of damage (mm)	Depth of damage (mm)
Beam 0	Undamaged	-	-	-
Beam 1	Single	5	3	3 up to 75
Beam 2	Double	11, 13	3	3 up to 75
Beam 3	Triple	9, 11, 13	3	3 up to 75
Beam 4	Triple	Middle of beam, 10,12	3	3 up to 75

Each of the four beams is tested individually in its datum state to determine the dynamic characteristics of the structure. All the beams are identical, but they are tested one by one as there might be some differences during the manufacturing of the materials, experimental set up and support conditions. The beam is excited at node 14, using a

Labworks ET-132 shaker with a rated force of 22 N. PCB 208C02 force transducer is used to measure the input force with a measurement range of 449 N in both tension and compression and a frequency range of 0.001 Hz to 36 kHz. The analogue data from the sensors is converted via an analysis digital center using the OROS OR35 analyzer. The signal analyzer is capable of generating all the different forms of signals, including white noise, which is used in this test. The acceleration response of the K-shear Kistler accelerometers is measured at sixteen locations on the top flange along the beam. These accelerometers have a frequency range of 0.5 to 10 kHz and a sensitivity of 100 mV/g. The sampling rate is set to 5.12 kS/s to achieve the frequency band width of 2000 Hz.

5.2.2 Three-story building model

5.2.2.1 Model test building

For this experiment, one small building model is designed and constructed. The model contains two theoretical assumptions: 1) the rigid floor; 2) the rigid connections. As shown in Figure 5.3, the model is 120 cm tall and consisted of 3 floors (steel slabs) and 16 columns (steel flat bars). Each floor is supported on four columns. The clear height for each story is 40 cm. Dimensions of steel slabs and flat bars are listed in Table 5.3. To prevent rotation and drift, the foundation slab is fixed to the ground as shown in Figure 5.3.

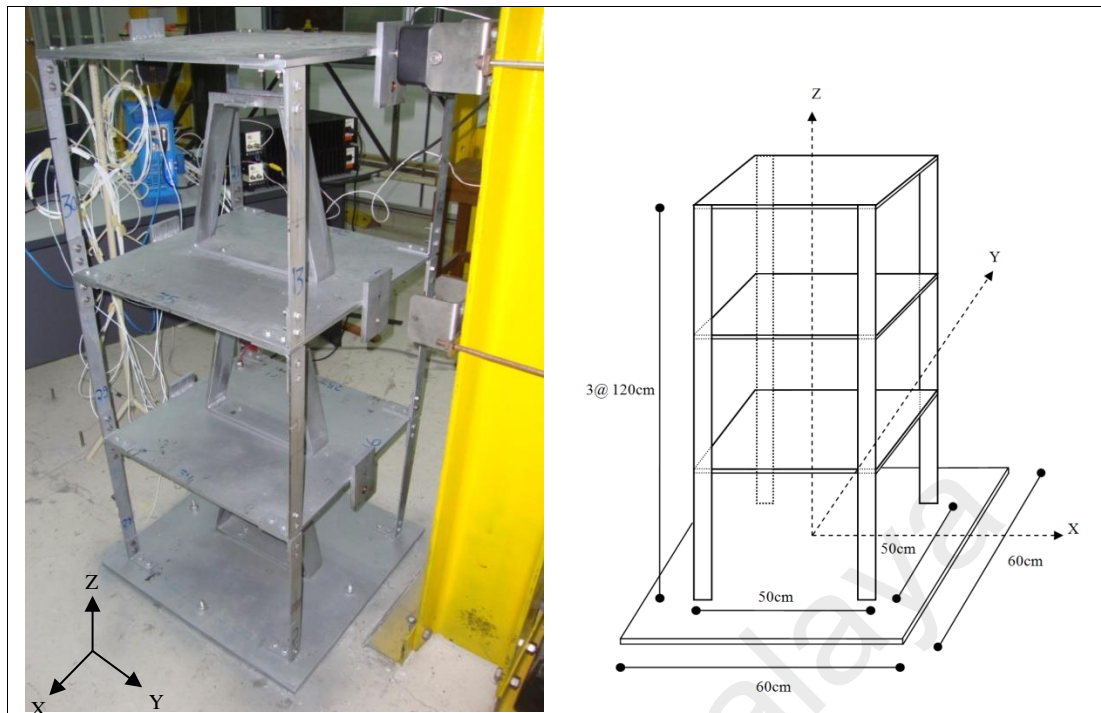


Figure 5.3: Three-story test building model

Table 5.3: Dimension and amount of building model components

Component	Dimension Height × Width (cm × cm)	Thickness (cm)	Amount	Location
Steel slab (Floor)	50 × 50	1	3	1-3 floor
	60 × 60	2	1	foundation
Steel Flat Bar (Column)	40 × 3.5	0.4	12	1-3 floor

For easy removal and replacement of the columns for different damage scenario simulations, bolts are used to connect the steel slab and the steel flat bar. To make a rigid connection between the steel slab and the steel flat column, eight pieces of steel angles (0.4×7×7; length: 3.5 cm) are bolted on each face of the floor plates in the y-direction (see Figure 5.4). A total of twenty four pieces of steel angles are used. To prevent rotation and drift, the foundation slab is fixed to the ground as shown in Figure 5.3.

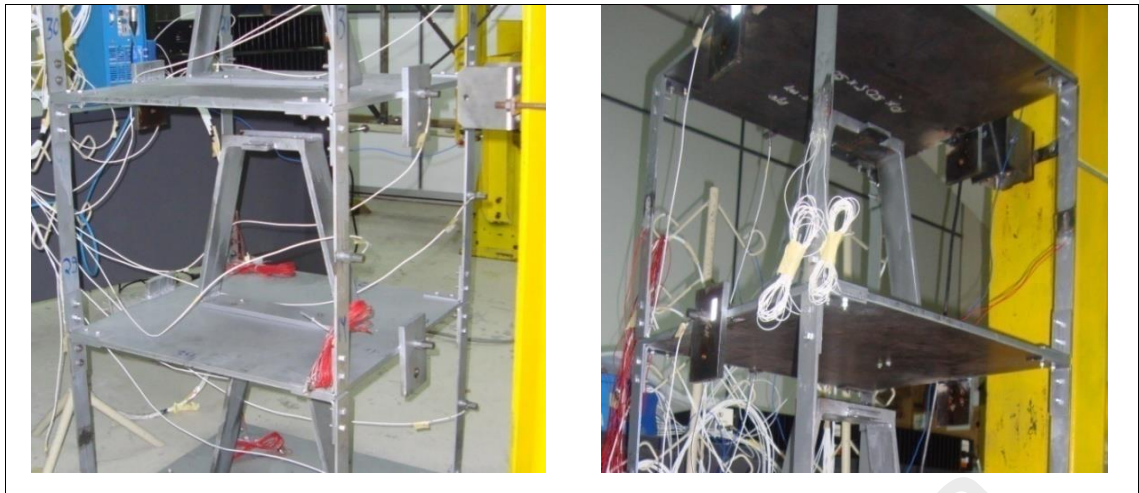


Figure 5.4: Slab and flat bar connection

5.2.2.1.1 Test set up and damage scenarios

The test setup is configured to measure structural vibration response of the building model with different types of damage scenarios under white noise excitation. Figure 5.5 indicates columns and floors identification numbers to distinguish damage and sensor locations. To shake the structure in y-direction, the Labworks ET-132 shaker is attached at point 34. The feasibility and sensitivity of the proposed damage identification algorithms are validated through five different damage scenarios in terms of the number and location of damages in the model. Table 5.4 presents the description of the considered damage scenarios which are more illustrated in the following.

Table 5.4: The detail description of damage scenarios in the building model

Damage type	Damage scenario		Damage location		depth of damage (mm)
			Column number	Point	
Notch cutting	Double	DS1	II	Between points 3 and 4	3.5 up to 17.5
			IV	Between points 8 and 9	3.5 up to 17.5
		DS2	II	Between points 3 and 4	3.5 up to 17.5
			V	Between points 10 and 11	3.5 up to 17.5
		DS3	IV	Between points 8 and 9	3.5 up to 17.5
			VIII	Between points 20 and 21	3.5 up to 17.5
	Triple	DS4	IV	Between points 8 and 9	3.5 up to 17.5
			X	Between points 27 and 28	3.5 up to 17.5
			XI	Between points 30 and 31	3.5 up to 17.5
		DS5	III	Between points 6 and 7,	3.5 up to 17.5
V	Between points 10 and 11		3.5 up to 17.5		
		VI	Between points 13 and 14	3.5 up to 17.5	

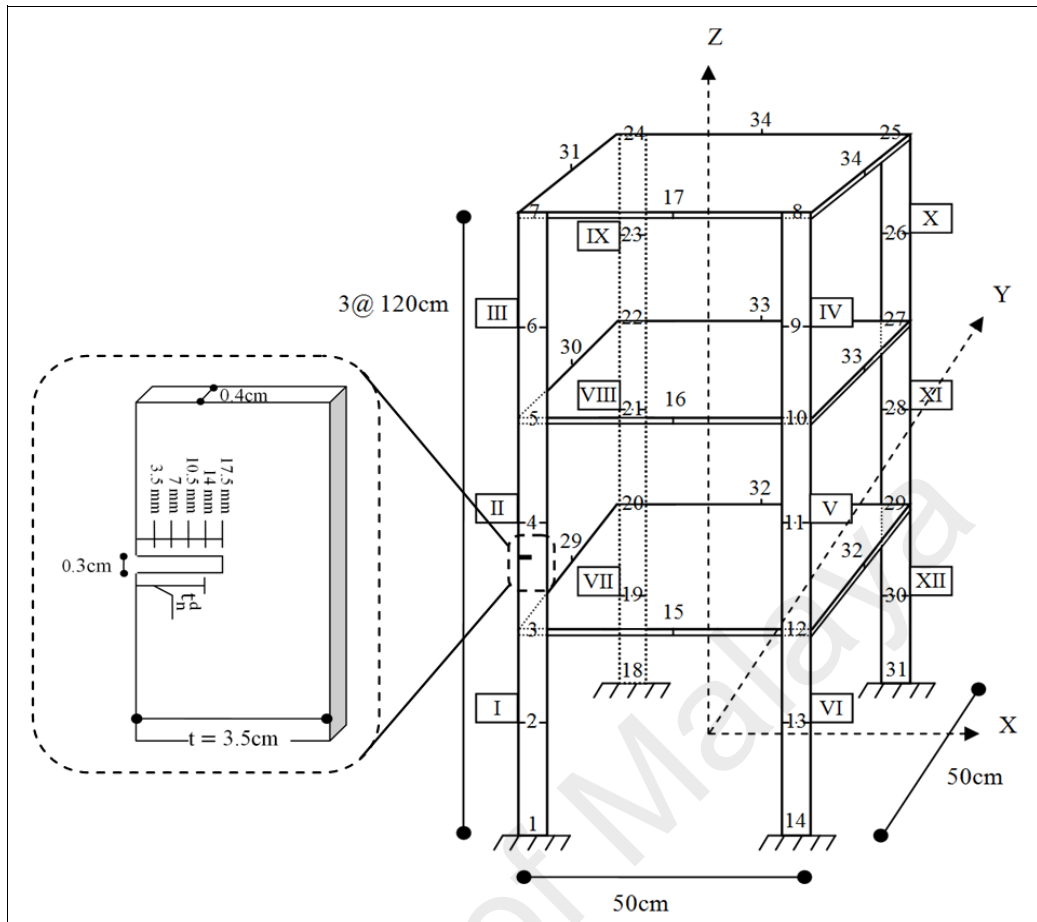


Figure 5.5: Columns and floors numbers of three-story building model

Damage scenario 1 (DS1): two damages are located on the same planar face of the building model at columns II and IV, between points 3-4 and 8-9, respectively (Figure 5.6(a)).

Damage scenario 2 (DS2): two damages are located at the same story at columns II and V, between points 3-4 and 10-11, respectively (Figure 5.6(b)).

Damage scenario 3 (DS3): two damages are located on different planar faces of the building model at columns II and V, between points 8-9 and 20-21, respectively (Figure 5.6(c)).

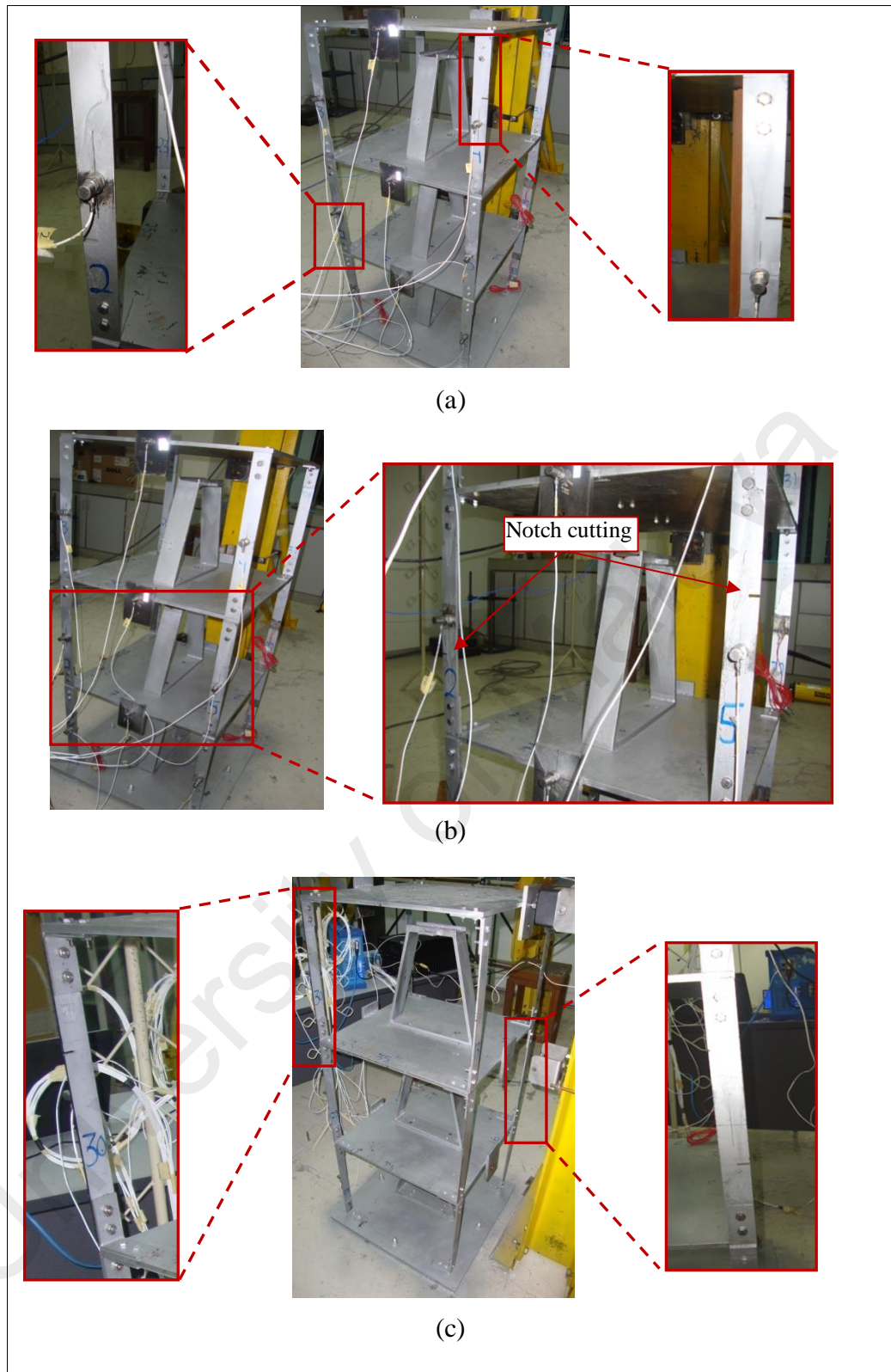


Figure 5.6: Double damage scenarios of three-story building model. (a) DS1, (b) DS2 and (c) DS3

Damage scenario 4 (DS4): three damages are located at different stories on different planar faces of the building model at columns IV, X and XI (Figure 5.7(a)).

Damage scenario 5 (DS5): three damages are located on the same planar face of the building model at columns III, V and VI (Figure 5.7(b)).

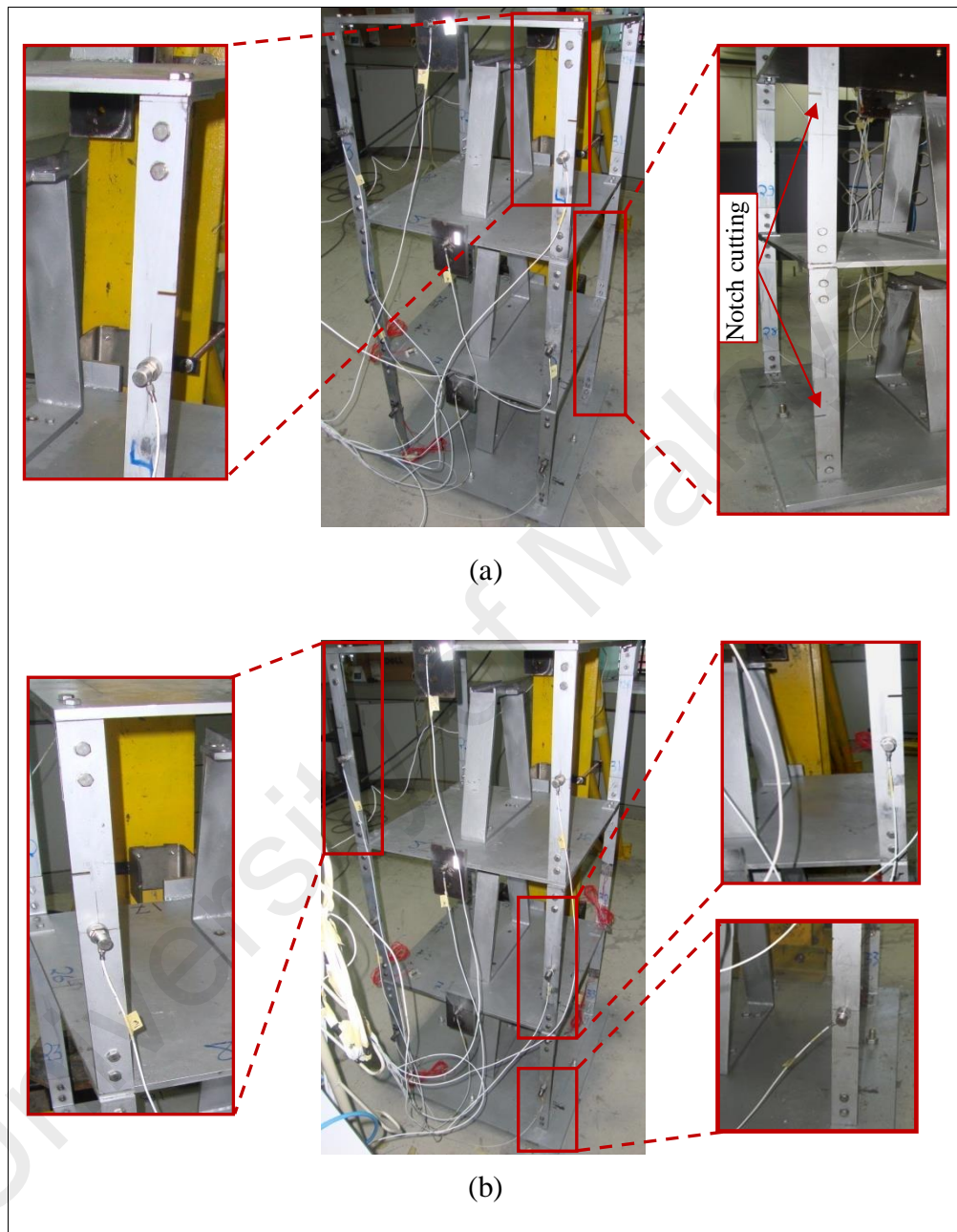


Figure 5.7: Triple damage scenarios of three-story building model. (a) DS4, (b) DS5

A 4mm-thick electrical saw is used to cut pieces of the steel flat bars. All damage scenarios are simulated by notch cuts on one side of steel flat bars as shown in Figure 5.8. Five different levels of cuts are considered for each damage scenario increasing gradually from 3.5 mm up to 17.5 mm with 3.5 mm increment at each step as shown in Figure 5.8.

The simulated damage scenarios are implemented on the structure by replacing damaged columns at designated locations. For this test, twelve shear Kistler accelerometers are installed in building model at locations: 2, 4, 6, 9, 11, 13, 19, 21, 23, 26, 28 and 30, to measure the acceleration responses. The sampling rate is set to 5.24 kS/s to achieve the frequency band width of 2048 Hz.

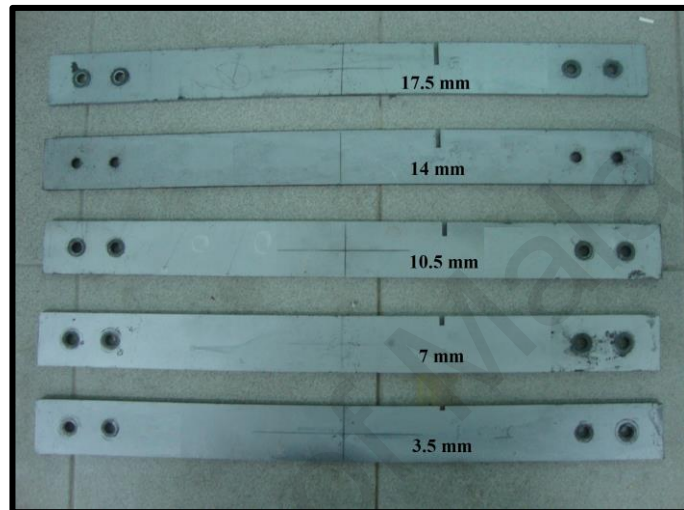


Figure 5.8: Different levels of cuts in steel flat bars

5.3 Illustrative models for system identification

In this section, the numerical and experimental studies of the beam structure under flexural vibration and the three story building model with various damage cases in linear and nonlinear conditions are conducted for assessment of the proposed system identification methods.

5.3.1 Beam structure under flexural vibration

5.3.1.1 Numerical study

In this section, a numerical example of a damaged beam is considered to test the proposed method. For this purpose, the time history acceleration responses of the beam are

computed by the ABAQUS software using a time increment of 4.8828×10^{-4} s, which corresponds to a sampling rate of 2048 Hz.

Consider a fixed supported beam with length $l_x = 1$ m, width $l_y = 0.08$ m, and thickness of $t = 0.005$ m. The node acceleration responses of the beam under loading are obtained from nine locations on the beam, as shown in Figure 5.9. The force-time history is applied at location 5 on the beam. An undamaged case and two different damage cases with varying locations are investigated, as shown in Figure 5.9. Case 1 is the single damage scenario with damage located at point 4 while Case 2 has two points of damage, at locations 4 and 5. The modulus of elasticity of the steel, the Poisson's ratio and the mass density is, 2.1 GPa, 0.33 and 7850 kg/m^3 , respectively.

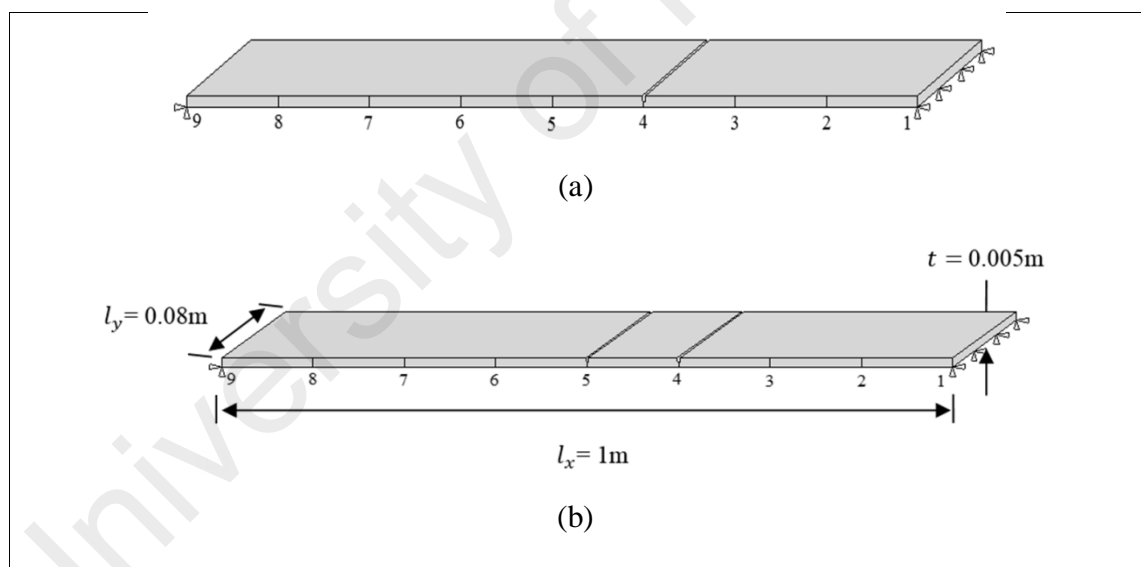


Figure 5.9: Dimensions and damage locations of beams under flexural vibration. (a) Case 1, (b) Case2

5.3.1.2 Experimental study

In this section, an experimental study is carried out on a steel beam with fixed supports, as shown in Figure 5.10. Dimensions of the beam are following the same sizes mentioned in the preceding section. The mass is known and equal to 3.207 kg. Damage is simulated by cutting slots in the beam at the selected locations, as described in Table 5.5.

The model is divided into four intervals along the X axis; each interval is 25 cm long, which produced three nodes in the middle and one node at each support. Acceleration of each node is measured in the Y axis using K-Shear Kistler accelerometer.

Table 5.5: Damage scenarios of beam under flexural vibration

Damage Case	Damage Scenario	Damage Location	Width of Cut (mm)	Depth of Cut (mm)
Case 0	Undamaged	-	-	-
Case 1	Single	Between nodes 2 and 3	2	2
Case 2	Double	Between nodes 2 and 3, node 3	2	2

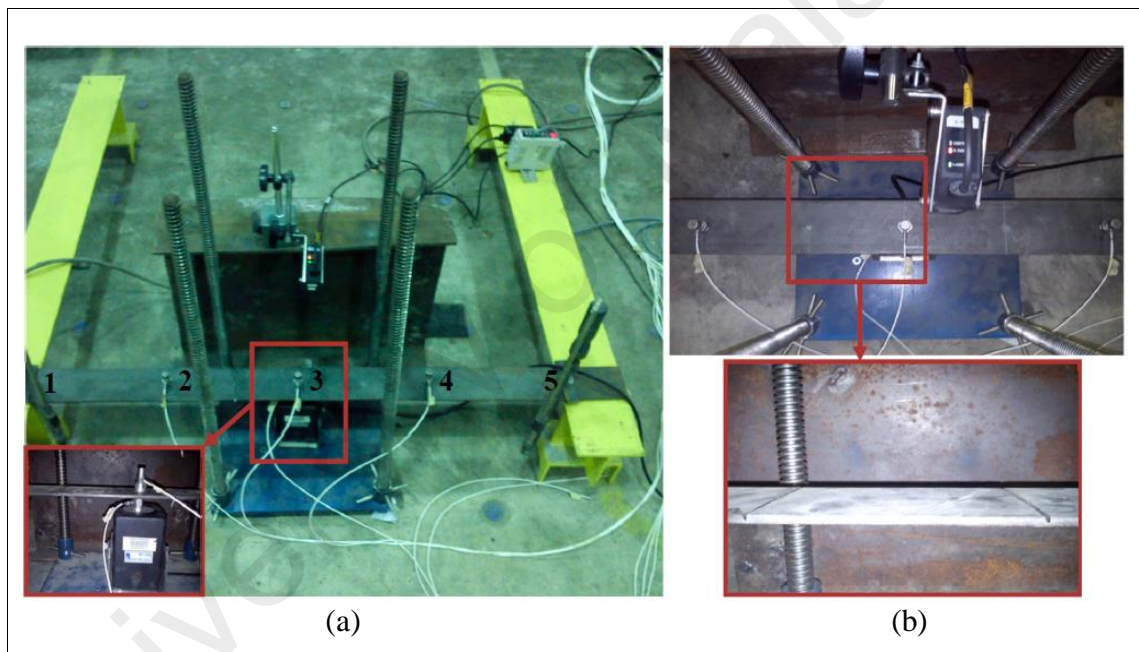


Figure 5.10: Experimental setup using beam under flexural vibration. (a) Data acquisition system, (b) damage locations of tested beam

The beam is excited (white noise) at node three, in the middle of the beam, using a Labworks ET-132 shaker. The analogue data from the sensors is converted and recorded using an OROS-OR35 data logger/analyzer. The sampling rate is set to 5.24 kS/s with frequency band width of 2048 Hz.

5.3.2 Three-story building model

5.3.2.1 Numerical study

The efficiency of the proposed system identification method is demonstrated through a numerical study on a shear beam building model. This building is a three-dimensional three-story frame structure with MDOF, as shown in Figure 5.11. The two degrees of freedom (DOFs) considered in each floor (rigid floor assumption) are two translational displacements in x- and y-directions. Thus, this simplified model has a total of 6 DOFs. The size and dimensions of the building model are in accordance with those of test specimen described in Section 5.2.2. The nominal (undamaged) stiffness coefficient is assumed to be identical for each floor and is 30358.92 N/m along y-direction, and 2134053.31 N/m along x-direction. Thus, the configuration of this model is symmetrical with respect to both x- and y-directions. The lumped mass of all three floors is 27 kg.

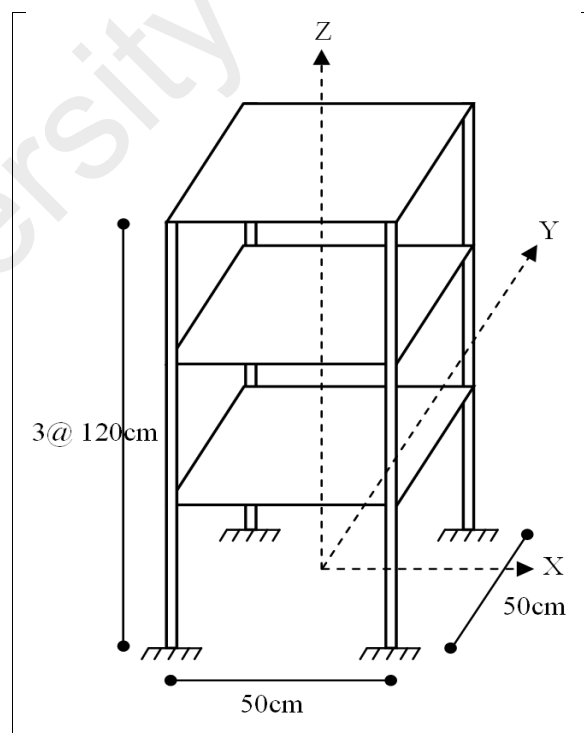


Figure 5.11: The model of a three-story frame structure

The structural damping of the model is assumed to be of the Rayleigh type. The two constants of the Rayleigh damping matrix have been chosen so to have a 1% damping

ratio for the first two vibration modes in the y-direction. The modal properties of the model are listed in Table 5.6.

Table 5.6: Structural modal properties of the original mode

	Mode	Natural frequencies (Hz)	Damping ratios
x	1	19.9335	0.0206
	2	55.4085	0.0548
	3	79.2628	0.0781
y	1	2.6986	0.0100
	2	7.4814	0.0100
	3	10.5813	0.0123

5.3.2.1.1 Basic description of numerical simulation

For this study, a band-limited white-noise excitation force within the frequency range of 0-100 Hz is applied to the top floor of the building model to measure the responses of the model with the sampling rate of 2.048 kHz.

Various combinations of simulation are given in this section to verify the validity and to evaluate the accuracy of the proposed method. In general, the building is subjected to two different types of damage state: linear and nonlinear damage states. In particular, various damage cases are defined including Damage Case 1 (DC1) which is a linear model with a change in stiffness parameter of the first story, Damage Case 2 (DC2) that consists a linear model with a change in stiffness parameter of the first and second stories and Damage Case 3 (DC3) which presents a bilinear model, i.e., a piecewise linear stiffness is used in the third floor to simulate the nonlinearity behavior in the structure.

The proposed method uses acceleration time history of the response output. In the numerical simulations, the mass and the exact structural parameters of the original model are obtained from the explicit dynamic analysis conducted by ABAQUS software.

5.3.2.2 Experimental study

In this section, an experimental study is performed on the three-story shear-beam building model, as shown in Figure 5.12, with identical material properties and test configurations as described in the Section 5.2.2. Mass coefficient of each floor is $m_1=m_2=27.7$ kg and $m_3=25.1$ kg. The first three natural frequencies of the test specimen are 2.875, 7.625 and 10.5 Hz, respectively, as shown in Figure 5.13. The linear stiffness of each story is obtained from experimental static test as $k_1= k_2= 29800$ and $k_3=29500$ N/m. Three damage cases are considered along with the original model, as described in Table 5.7. To simulate structural damage, a variable stiffness device is utilized in this study to change the stiffness of stories.

Table 5.7: Damage scenarios in three-story shear-beam building model

Damage case	Type of damage	Damage location
Case 1	Linear	First story
Case 2	Linear	Second story
Case 3	Piecewise linear	First story

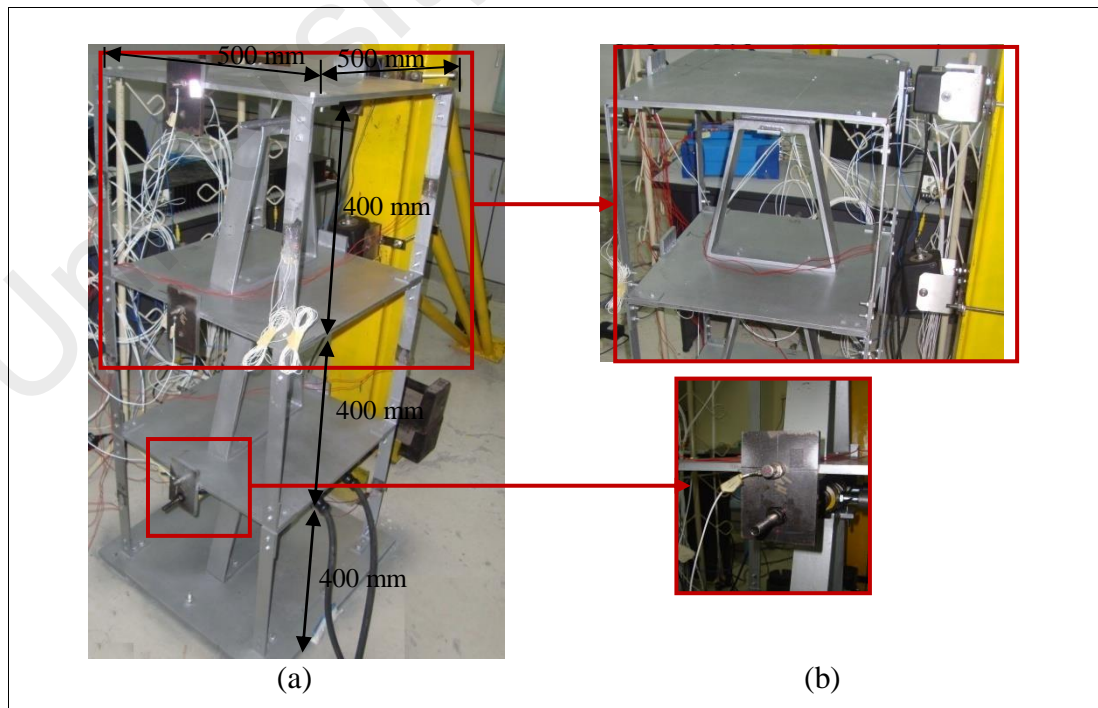


Figure 5.12: (a) Experimental setup of three-story building model, (b) data acquisition system

A random white noise force excitation is applied to the top floor of the building model in a band-limited frequency range of 0-70 Hz, using a Labworks ET-132 shaker as shown in Figure 5.12(b). The input force is measured using a PCB 208C02 force transducer with a frequency range of 0.001Hz to 36 kHz. During the tests, each floor is installed with one K-Shear Kistler accelerometer to measure the floor responses. The analogue data from the sensors is converted and recorded using an OROS-OR35 data logger/analyzer. The sampling rate is set to 5.24 kS/s to achieve the frequency band width of 2048 Hz.

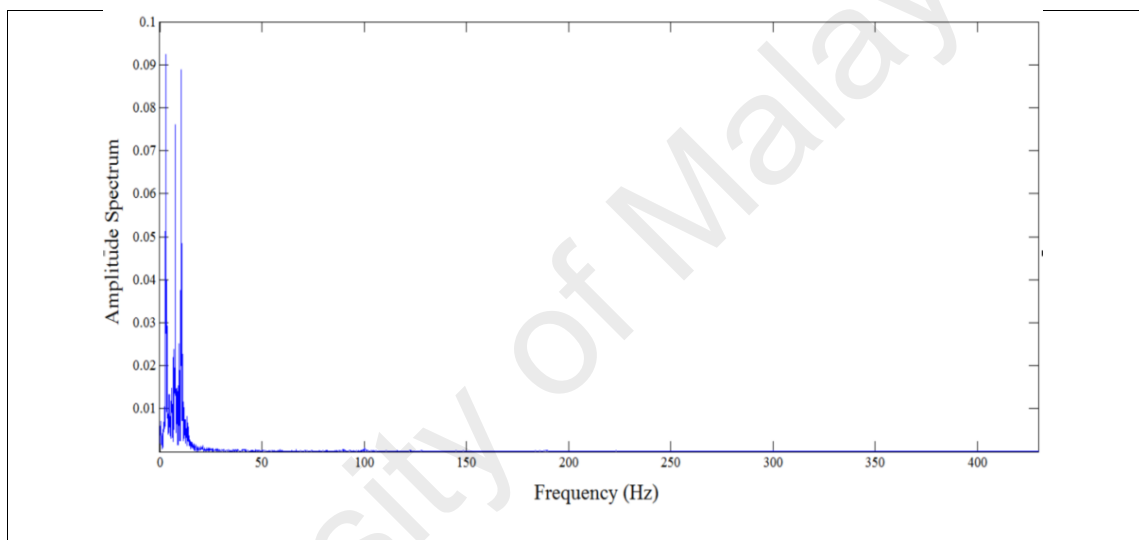


Figure 5.13: Frequency domain response of acceleration response signal in building model

5.3.2.2.1 Variable stiffness device (VSD)

Damage in a story of the shear structure is supposed to be reflected by variation of its stiffness. To simulate the stiffness variations in a selected story, a VSD with an effective stiffness is mounted in the selected story. In the experimental test, the effective stiffness of the VSD is degraded to zero for simulating the reduction of the stiffness caused by damage. The innovative concept for the VSD is motivated by the so-called resettable semi active stiffness dampers, (Yang et al., 2000; He et al., 2001a; Chase et al., 2006; Yang et al., 2007), described in the following.

Consider a device consisting of a hydraulic cylinder-piston (HCP) system with one valve on each side of the piston as shown in Figure 5.14. When both valves are closed, the HCP operates as a stiffness component in which the stiffness is generated by the bulk modulus of the fluid or pressurized gas in the cylinder. When both valves are open, the piston is free to move and the HCP provides only a very small level of damping without stiffness. To simulate the reduction of stiffness in a given story, the HCP is mounted to a bracing system and it is fixed in the given story as shown in Figure 5.15. In this figure, the HCP is installed along with the bracing system and the piston is connected to upper floor. Therefore, the bracing system and the HCP are connected in series. The whole system, including the bracing system and the HCP is referred to as the variable stiffness device.

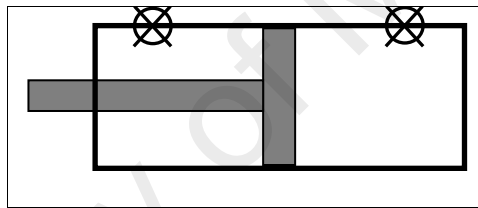


Figure 5.14: Schematic diagram of the hydraulic cylinder-piston system

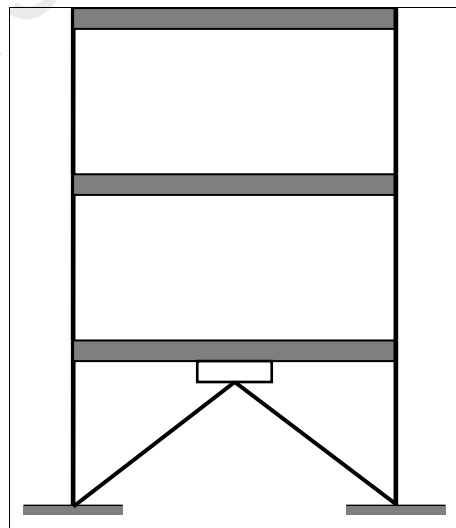


Figure 5.15: A three story building model equipped with VSD

If the horizontal stiffness of the HCP and bracing system in n^{th} story are denoted by K_{fi} and K_{bi} , respectively, since K_{bi} and K_{fi} are connected in series, then the effective stiffness of the entire VSD (Agrawal & Yang, 2000), represented by K_{hi} , is given by

$$K_{hi} = K_{fi} K_{bi} / (K_{fi} + K_{bi}) \quad (5.2)$$

In experimental setup, the stiffness of the HCP is lower than that of the bracing system, i.e., $K_{bi} \gg K_{fi}$, therefore, the effective stiffness of the VSD is almost identical to that of the HCP, i.e., $K_{hi} = K_{fi}$. Installation of the VSD in the first story as depicted in Figure 5.12 increases the stiffness of the first story by K_{hi} .

Stiffness of the HCP depends on the amount of gas pressure in the cylinder, as discussed by Bobrow et al. (2000); Jabbari and Bobrow (2002); Chase et al. (2006); Yang et al. (2007), and that can be expressed as follows:

$$K_{fi} = (2 \cdot A^2 \cdot \gamma \cdot P_0) / v_0 \quad (5.3)$$

where A is the piston area, v_0 stands for the initial volume, P_0 represents the initial pressure and γ is ratio of specific heats. For small motion approximation, it can be assumed that v_0 is identical in both side of the piston. Therefore, stiffness of the HCP is linearly related to the gas pressure P_0 :

$$K_{fi} = C P_0 \quad (5.4)$$

where C is a constant and it depends on the dimension of the cylinder and the property of the fluid or gas. Therefore, the desirable stiffness of the VSD can be obtained by adjusting the P_0 in the cylinder. On the other hand, the selected value of P_0 depends on the amount of the stiffness, K_{hi} , to be decreased in the selected story.

The cylinder applied in this study is capable of peak pressure of 36.36 MPa with a 1.67 cm bore and a 7.3 cm stroke. Area of the piston is 2.2 cm², so the peak force level of about 8 kN can be achieved. During the test, the valves of the VSD are open at the instantaneous time, t_r , thus the K_{hi} becomes zero, consequently the stiffness of the selected story is reduced by an amount of K_{fi} at $t = t_r$.

5.4 Instrumentation

In order to determine real-life dynamic response characteristics of a system, it is necessary to conduct non-destructive experimental tests on the structure concerned. Thus, data acquired from the experimental tests can be used to characterize structural response behavior. In general, experimental testing involves three major components: (i) excitation sources; (ii) data acquisition system; and (iii) measurement sensors.

5.4.1 Excitation

There are three types of excitation, including free vibration, force vibration and ambient vibration. In this study, force vibration is applied to excite the structures. Shakers and impact hammers are commonly used for forced vibration of structures. One advantage of the force vibration test is that the input force is strong enough to dominate other noise disturbance, resulting in a strong signal to noise ratio. In force vibration, by using a known forcing function, many of the uncertainties in data collection and processing can be avoided. In this study, force vibration excitation of structures is implemented through the use of a shaker. Shakers are attractive systems of excitation because they are capable of providing a wide variety of excitation functions, both periodic and random. In this study a Labworks ET-132-2 Electro dynamic transducer permanent magnet shaker with a dimension of 5.5"H x 3.6"W x 3.5L" is used to excite the structure, as shown in Figure 5.16. This shaker is suited for modal analysis and laboratory research.



Figure 5.16: ET-132-2 Electrodynamic shaker

5.4.1.1 Source of excitation

5.4.1.1.1 Power Amplifier

Signals from the excitation sources and the accelerometer give small charges. As a result, the signals need to be amplified by using a charge amplifier. The charge amplifier is used to match the characteristics of the transducer to the input electronics of the digital data acquisition system. In this study, a Power Amplifier type APS 125 with a 500 VA is applied, as depicted in Figure 5.17.



Figure 5.17: APS-125 Power amplifier

5.4.2 Data Acquisition system

In data acquisition, the data is amplified, filtered, converted from analogue to digital format and stored in the computer. In this research, a noise and vibration analyzer called OROS OR38 is used to convert the analogue input signal from the transducer into a digital form (Figure 5.18). This device provides 40 kHz of real-time bandwidth on its 24 bit ICP inputs. The input signals can go up to ± 40 V. It is equipped with a 40 GB internal hard disk and any external device such as laptop or PC can be connected to it via its 100 Mb/s Ethernet port. Its interface program is NVGate. This analyzer is a useful instrument for data acquisition, real-time analysis and post-analysis. The acquired continuous signal is first sampled and then converted into a discrete time series digital signal.

The time interval between two samples is equal to the inverse of the sampling frequency. Once the measured data is converted to a digital signal it may be processed by computer hardware. The signal at this stage is in the time domain and represents the force input to

the structure, and its response is a function of time, but is measured at discrete sampling instants.



Figure 5.18: OROS38 with 32 channels

A NVGate program running on computer controls the Analyzer. This program is used to start data logging, set sampling frequencies, check sample saturation and save the data. NVGate version 8.00 for the OROS OR38 analyzer is used as a release in this research work. NVGate can export results from the recorder to text, UFF and Matlab. Connection of Analyzer (hardware) and NVGate (Software) is shown in Figure 5.19.



Figure 5.19: The setup of analyzer and NVGate

5.4.3 Accelerometers

The accelerometer used in the experimental test is K-shear Kistler type 8702B50M1 as shown in Figure 5.20. This type of accelerometer is very useful for vibration measurement and modal analysis. Some of the important characteristics of this accelerometer contain low impedance voltage mode, low thermal transient response and ground isolated. This

accelerometer is single axis linear, with a mass of 9.7g. Sensitivity is measured in terms of (mV/g) in accelerometers and is 100 mV/g and frequency range is 0.5 to 10k Hz.



Figure 5.20: K-shear accelerometer

In general, the optimum accelerometer has high sensitivity, wide frequency range and small mass.

5.4.4 Force transducer

Transducers convert the physical motion to electrical signals. When a structure is excited, its physical motion is captured by transducers. The piezoelectric type is the most widely used in vibration testing.

Piezoelectric transducers are electromechanical sensors that generate an electrical output when subjected to vibration and have wide frequency and dynamic operational ranges and good linearity. Among the operating specifications to consider are sensitivity, frequency range of operation and resonant frequency. In this research as shown in Figure 5.21 a multi-purpose force transducer PCB 208C02 with sensitivity 11.241 mV/N and measurement range of 449 N in both tension and pressure is used.



Figure 5.21: Force transducer

5.5 Summary

In this chapter, a set of numerical and experimental test was performed to measure the vibration responses of the beam structures and three-story building model at different damage conditions for assessment of the proposed damage detection and system identification methods. In the context of damage detection, firstly, the experimental model of four I-section steel beam and its corresponding numerical simulations with various damage scenarios at different locations were conducted. Damage was induced in the form of notch at designated locations on the beam with varying depth of cut. The acceleration response were measured at sixteen locations on the top flange along the beam. Secondly, the experimental work was conducted on the three-story steel building model. The experimental model was built up by using steel slab (floor) and steel flat bar (column). To create a rigid connection between the steel slab and the steel flat columns at each story, the steel angles were bolted on each face of the floor plates. Various damage scenarios were made by replacing damaged columns at designated locations of the structure. All damage scenarios are simulated by notch cuts on one side of steel flat bars and the twelve accelerometers were installed in building model at specified locations to measure the acceleration responses.

For assessment of the proposed system identification method, initially, a fix support beam with two different damage cases was tested. Local structural damage was simulated by cutting slots in the beam at the selected locations. Then, a numerical study of three-story building with different damage cases in linear and nonlinear conditions were conducted. In addition, to simulate the structural damage in experimental building model, a variable stiffness device was proposed to change the stiffness of stories.

CHAPTER 6: VERIFICATION OF PROPOSED ALGORITHMS

6.1 Introduction

This chapter aims to verify the performance, efficiency, and accuracy of both the proposed damage identification algorithms to determine the location and extent of damage in the structures, and the proposed system identification method based on the wavelet multiresolution analysis for estimating the structural parameters of linear and nonlinear systems. The verification will be conducted on numerical simulations and experimental validations of beam structures and subsequently of three-story building model, with respect to various damage scenarios with different level of severity, noise levels and so on. This chapter consists of five main parts. Section 6.2 verifies a two-step damage identification approach based the effective damage index, RWPE, and GA in beam structures. Section 6.3 verifies RWPE-based reference-free index, RDI_{RWPE} , in beam structures. Section 6.4 the efficiency and practicability of the proposed damage detection algorithms are verified in the experimental three-story building model. Section 6.5 verifies the proposed system identification in beam structures under flexural vibration. Section 6.6 the verification of the proposed system identification algorithm on more challenging examples is conducted of three-story building model with both linear and nonlinear systems.

6.2 Damage identification in beam structures

6.2.1 Two-step damage identification approach

The methodology proposed in this study deals with the development of a hybrid approach using RWPE and GA by defining a database to accurately determine the location and severity of the damage in beam structures. This approach contains two steps, i.e. the first is detecting damage locations and the second is to determine the damage severities at

identified locations. The wavelet packet component energies for each damage depth used in the first step and the severity evaluation database required for the second step to reveal the relationships between the energies and damage severities are obtained using a multiresolution WPT. In addition, to evaluate the influence of changing the wavelet function and level of decomposition on the accuracy of identifying damage location, the wavelet functions DB1 to DB10 are used for beams.

6.2.2 Numerical investigation

6.2.2.1 Damage location identification

To verify the proposed damage identification method, the three simulated simply supported beams (i.e., beams 1, 2 and 3 shown in Section 5.2.1.1) with damage elements are considered. The RWPE at 16 locations are calculated for each damage scenario based on Equation (4.9), as shown in Figure 6.1. According to these figures, the value and distribution of RWPEs changed considerably after damage. In cases with small damage, there is not much frequency difference in signals. This highlights that the type of mother wavelet and decomposition level play a key role in damage identification. Hence, in the single damage scenario, several wavelet functions and different levels of decomposition are investigated. More accurate results for these cases are obtained when the wavelet function DB2 and decomposition level 5 are used for differentiating the damages, as shown in Figure 6.1(a). The damage location can be clearly identified with the significant change in values of RWPE at location 5. However, the peak values of RWPE of the multiple damage scenarios for beam 2, where the damages are located at points 11 and 13, are identified by using the DB5 and decomposition level 6, as shown in Figure 6.1(b). The damage index is noticeably greater at point 11. Furthermore, in beam 3, DB10 with 6 levels of decomposition is found to be the appropriate DB order for damage

identification. Figure 6.1(c) depicts that the peak value of the RWPE at point 9 is larger than that of point 11 and point 13.

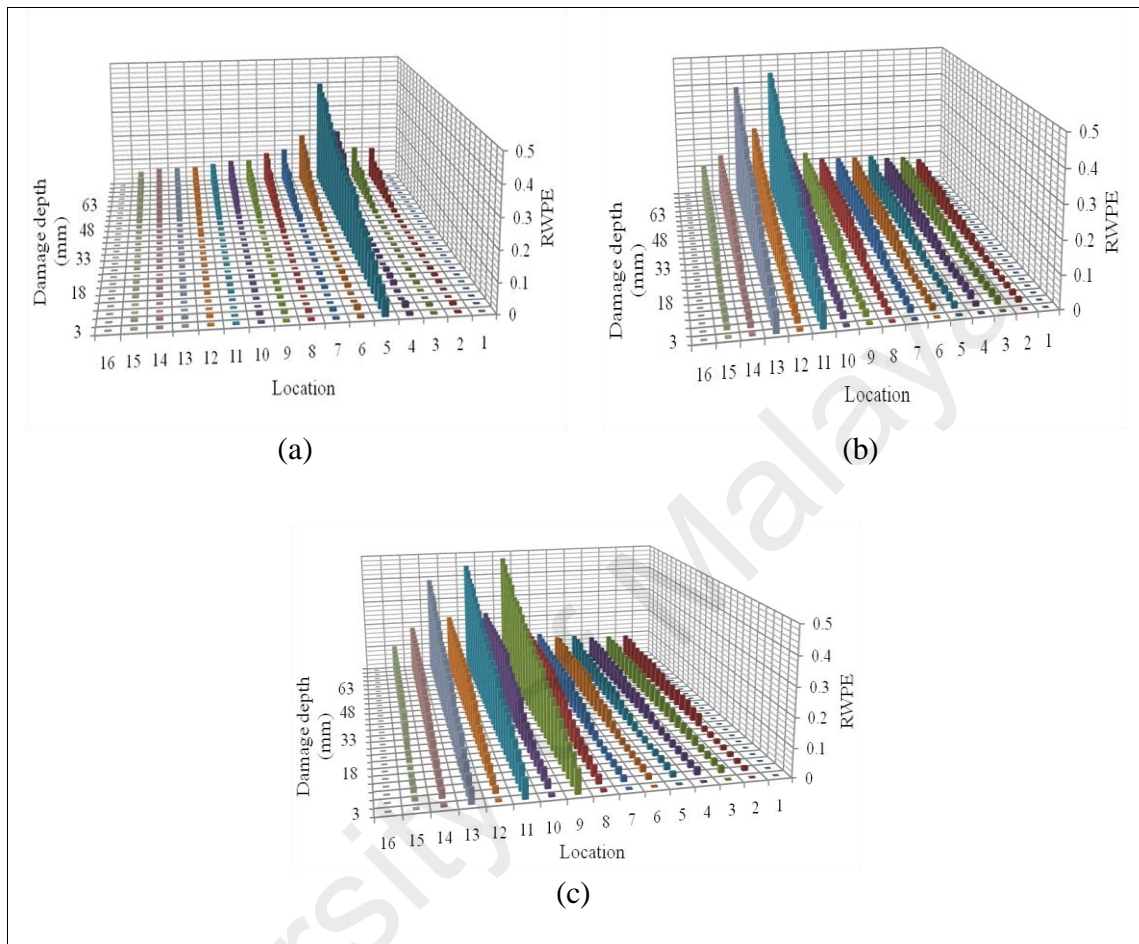


Figure 6.1: The values of RWPE for each depth of damage. (a) Beam1, (b) beam 2, (c) beam3

In order to indicate the influence of changing the wavelet function on the accuracy of identifying the damage location, various wavelet functions DB1 to DB10 are applied for the considered beams. The standard difference percentage of RWPE ($[(\sum_i RDI_{RWPE}^{\max} - \sum RDI_{RWPE}^{\text{ave}}) / \sum RDI_{RWPE}^{\text{ave}}] \times 100$, $i = \text{number of damage scenarios}$) for each damage scenario at every specific depth of damage is calculated, as shown in Figure 6.2. For beam 1, the standard difference percentage is obtained in decomposition level 5, as illustrated in Figure 6.2(a). A comparison of the histograms associated with every depth of damage for all considered DBs indicates that wavelet function DB2 is the suitable wavelet function order. However, in beam 2, as shown in Figure 6.2(b), the values

of DB5 with 6 levels of decomposition are larger than those of the other DBs. The results for beam 3 with multiple damages, as depicted in Figure 6.2(c), reveal that DB10 and the decomposition level of 6 can precisely identify the damage locations along the beam length compared with other Daubechies wavelet functions.

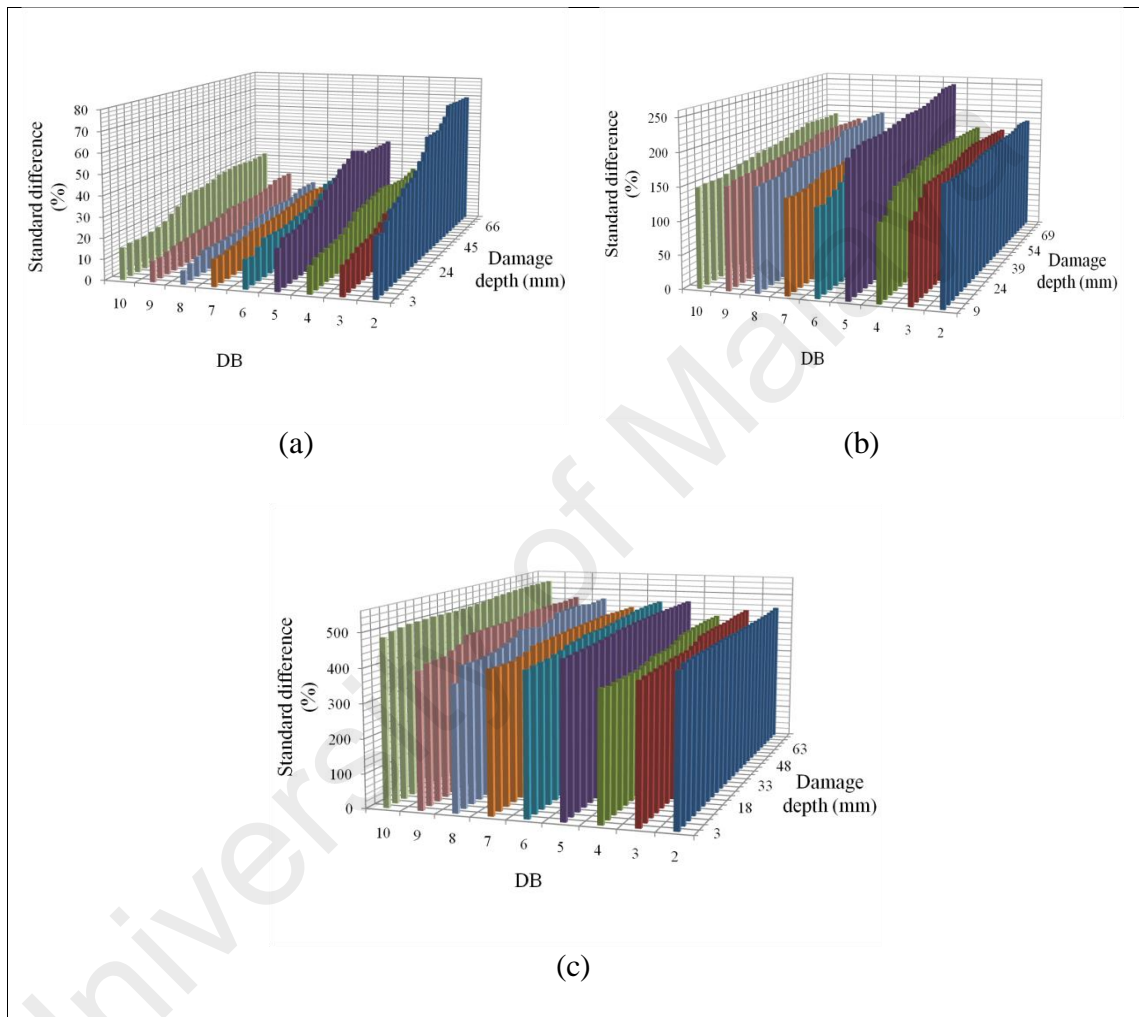


Figure 6.2: Damage identification results using different wavelet function. (a) Beam1, (b) beam2, (c) beam3

In addition, Figure 6.3 depicts the values of RWPE in beam 2 to demonstrate the difference between various orders of Daubechies wavelets in discrimination of damage locations. Evidently, the damage locations are distinguishable in these histograms with RWPE reaching a maximum value at locations 11 and 13, which are the exact damage locations. By comparing the considered Daubechies orders shown in Figure 6.3, it can be observed that the peak of RWPE is not as clearly distinguishable in DB6 even though it

has the identical location and severity of damages. In addition, DB5 shows a significant difference in the values of RWPE relative to the other DBs for each depth of damage. For DB2, the shortcomings are identical to that of DB6 but produced more accurate results. DB10 is not a worthy consideration since it is not able to precisely indicate the damage location. It is considerable to note that the accuracy of differentiating the damage cannot be compared to DB5 for the two damage scenario.

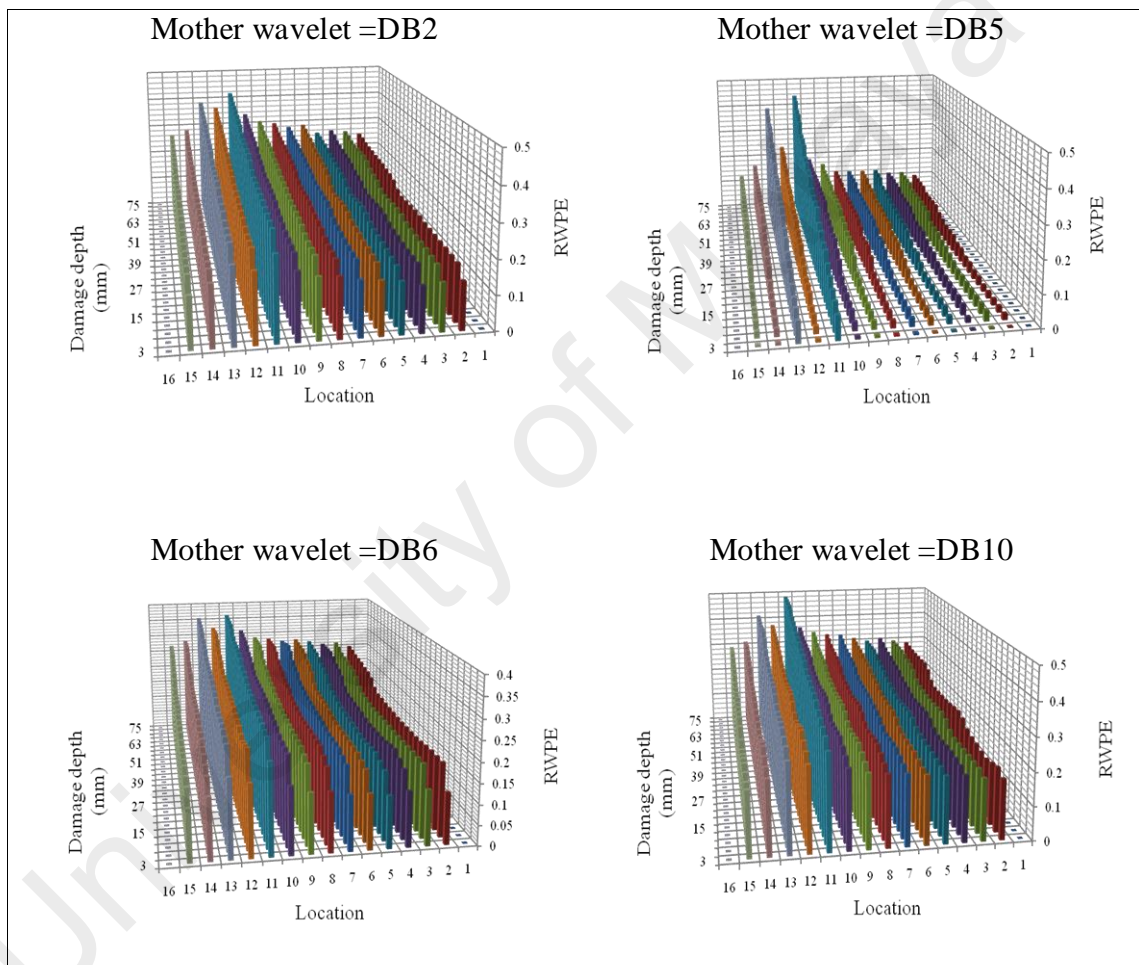


Figure 6.3: Histograms of RWPE in beam 2 with different orders of Daubechies wavelets

From the above observations, it may be construed that an increase in the damage depth of beams influences the vibration response signal, and, consequently, the RWPE values. Comparison of the peak values of RWPEs in the region of damage reveals that larger intensities of the RWPE occurs when the damage is located near the center of the beam since the local perturbations caused by the damage take place at a far distance from the

support. On the other hand, the presence of damage adjacent to the support results in a singularity around the support, which cannot be found with a predetermined DB. The problem with one predetermined DB arises when multiple damages are located on the beam and the proper selection of the mother wavelet function influences the accuracy of damage location identification.

Therefore, the selection of a proper mother wavelet for wavelet-based methods is important, as it can affect the performance improvement of the proposed method in order to achieve accurate results. The type of mother wavelet function plays a key role in reducing the false positives adjacent to the damage locations, as depicted in Figures 6.2 and 6.3. This is mostly because the correlation between the mother wavelet functions and the signal is calculated as a wavelet coefficient.

6.2.2.2 Effect of measurement noise

The presence of noise in the recorded signal is unavoidable in real life applications. Therefore, to investigate the effect of measurement noise on the performance of the proposed method, white Gaussian noise (WGN) is added to the generated acceleration signals of the test cases to simulate the uncertainties of real-life problems such as the environmental conditions during an experimental work. The noise intensity is defined by the signal-to-noise ratio (SNR):

$$\text{SNR(dB)}=20 \log_{10} \frac{A_S}{A_N} \quad (6.1)$$

where A_S and A_N are the root-mean-square (RMS) value of the acceleration signal and the noise, respectively. In present applications, the effect of different levels of noise on damage identification is investigated by applying SNRs 2, 5 and 10 dB. Figure 6.4 shows the noise-contaminated original acceleration signals at location 8 for the undamaged case. Beam 3 with three damage scenarios is analyzed for noise effect, and the identified results in terms of the noise levels are shown in Figure 6.5. It can be observed that the presence

of noise did not have an adverse effect on the histograms regardless of noise level and that the RWPE values are identical to the noiseless case. This could be because the noise is assigned to the different wavelet functions and the noise effect in each bandwidth is reduced. Hence, it can be inferred that the proposed method will work satisfactorily in the presence of measurement noise.

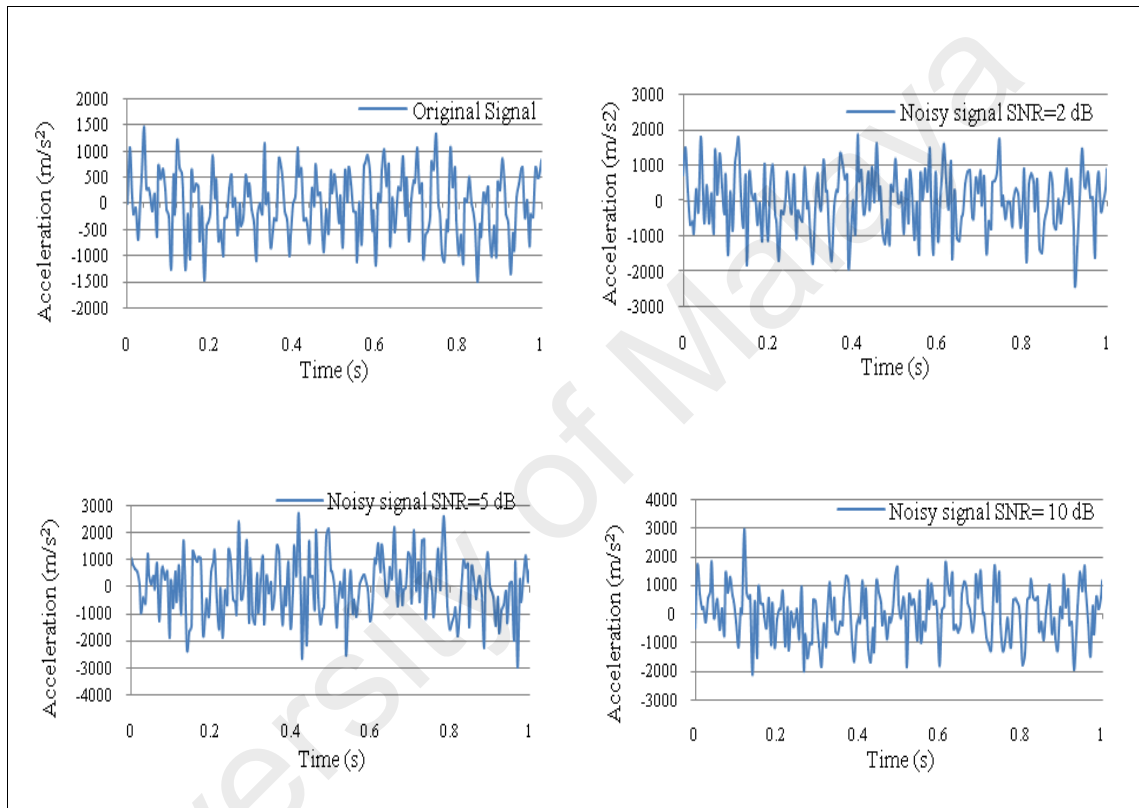


Figure 6.4: Different levels of noise contamination in the measured signal at location 8 for the undamaged case

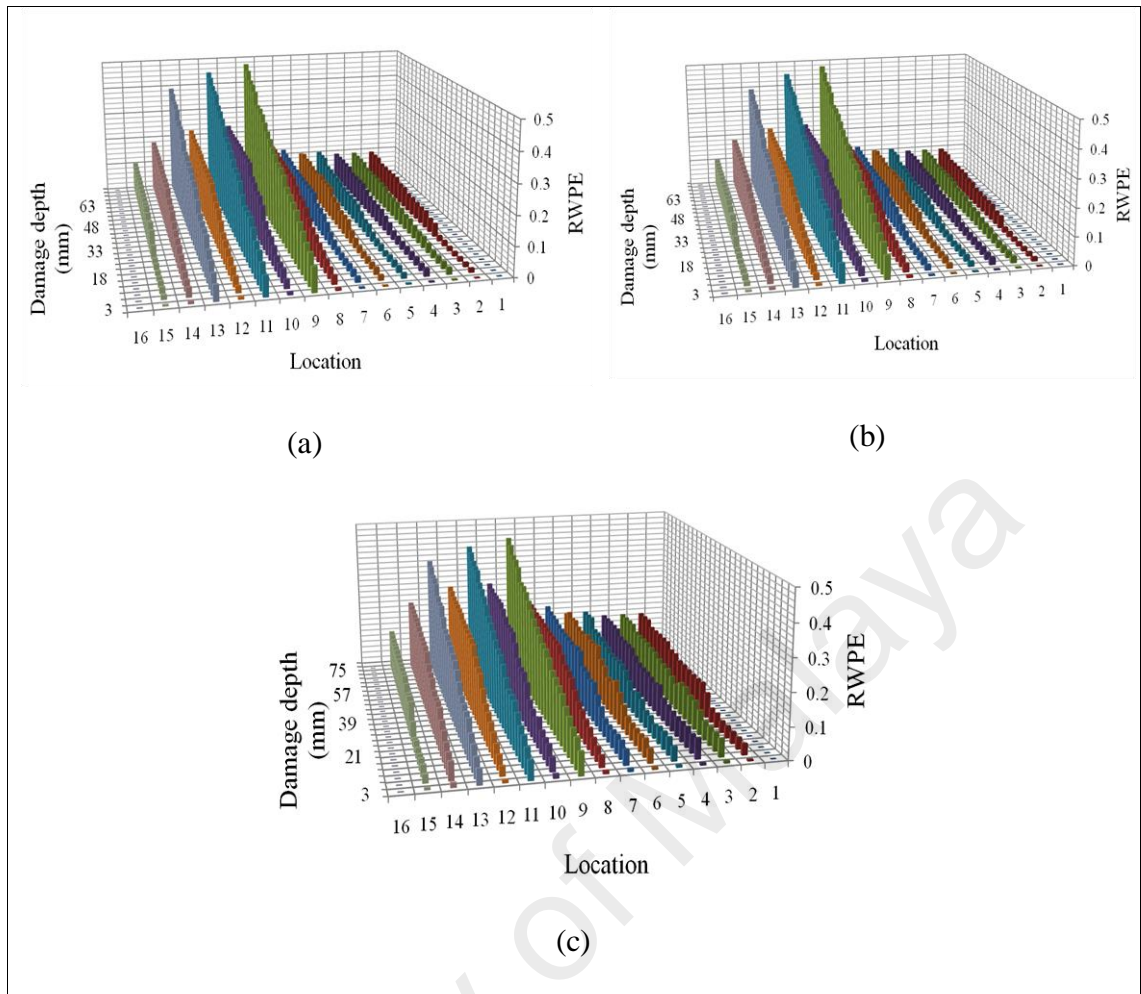


Figure 6.5: Damage identification results in beam 3 after adding different levels of noise. (a) SNR= 2 dB, (b) SNR= 5 dB, (c) SNR= 10 dB

6.2.2.3 Damage severity evaluation

To evaluate the damage severity, the beams with ten different severity combinations specified by various magnitudes of α , presented in Table 6.1, are considered. For the purpose of simulation, only the noise-contaminated signals calculated by Equation (6.1) are employed to obtain energies in each frequency band. The GA is applied with the proposed fitness function to calculate the damage severity. Some preliminary tests are performed to decide the GA set up parameters. The final set up parameters used in this work are shown in Table 6.2.

Table 6.1: Considered damage cases in beams

Case	Damage severity							
	Beam1		Beam 2			Beam 3		
	Damage location (DL)							
	DL ₅		DL ₁₁	DL ₁₃		DL ₉	DL ₁₁	DL ₁₃
1	0.02		0.02	0.02		0.02	0.04	0.02
2	0.04		0.1	0.4		0.08	0.02	0.48
3	0.1		0.06	0.04		0.14	0.14	0.14
4	0.16		0.16	0.16		0.2	0.24	0.28
5	0.22		0.2	0.1		0.26	0.3	0.4
6	0.28		0.12	0.28		0.32	0.16	0.34
7	0.34		0.3	0.3		0.38	0.42	0.38
8	0.4		0.42	0.34		0.44	0.12	0.22
9	0.44		0.48	0.12		0.5	0.18	0.46
10	0.5		0.5	0.5		0.06	0.06	0.36

Table 6.2: GA set up parameters for beams

Number of generation	500
Population	100
Selection function	Tournament
Fitness normalization	Rank
Crossover	Pc=0.7, Two-point, uniform
Mutation	Pm=0.05, Uniform

Figure 6.6 shows the search convergence process for different damage scenarios. The results of the damage severity detection of beam 1 for each damage case are shown in Table 6.3 and Figure 6.6(a). It can be observed from the histograms that the proposed algorithm precisely follows the corresponding specified crack location and severity for the damage cases.

More difficult cases are encountered in multiple damage scenarios with different severities as in beams 2 and 3. Beam 2 relates to two points of damage whose depths are different in each case. Beam 3 has three points of damage, which simulates an even more complicated damage scenario due to the variety of depth values. To show the robustness and sensitivity of the proposed algorithm, the GA is assigned to obtain the damage severity in the specified locations. Table 6.3 presents the predicted value of damage severities. As shown in Figure 6.6 (b) and (c), estimation of the proposed algorithm accurately follows the corresponding values.

The evaluation errors for severities of damages in beams 1 and 2 are in the range of 0% to 6% with mean values of 1.20%, 2.00% and 2.20%. Also, with the increase of damage severities in beam 3, the prediction errors vary in an acceptable range from 0- 8% with mean values of 2.20%, 3.00% and 2.60%. Therefore, the proposed algorithm is effective in evaluating the damage severities and yields reasonably good results when the data contain a certain level of noise.

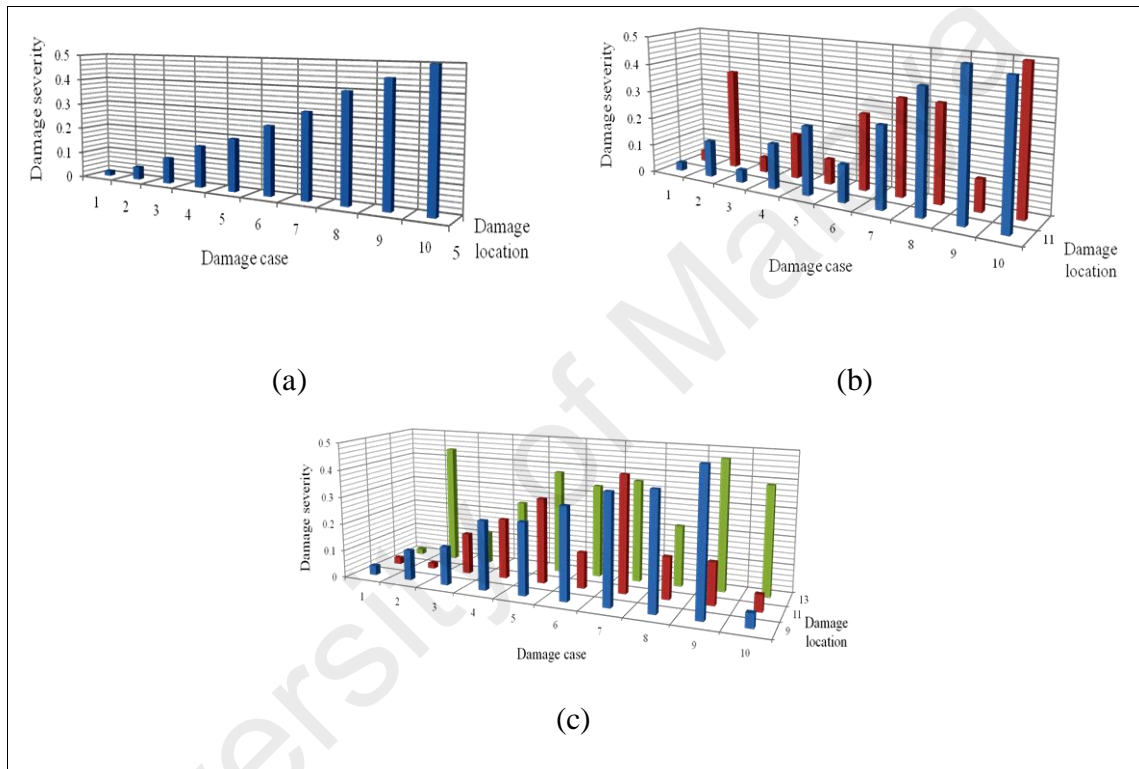


Figure 6.6: The damage severity evaluation results by using GA. (a) Beam1, (b) beam2, (c) beam3

Table 6.3: The damage severity results obtained by GA

Case	Predicted value						Error (%)					
	Beam1		Beam2		Beam 3		Beam1		Beam2		Beam 3	
	DL_5^*	DL_{11}^*	SL_{13}^*	DL_9^*	DL_{11}^*	DL_{13}^*	ϵ_1^a	ϵ_1^a	ϵ_2^a	ϵ_1^a	ϵ_2^a	ϵ_3^a
1	0.02	0.02	0.04	0.04	0.02	0.02	0	0	2	2	2	0
2	0.06	0.14	0.34	0.12	0.02	0.42	2	4	6	4	0	6
3	0.1	0.04	0.06	0.14	0.16	0.1	0	2	2	0	2	4
4	0.16	0.16	0.16	0.26	0.2	0.24	0	0	0	6	4	4
5	0.2	0.26	0.08	0.26	0.32	0.36	2	6	2	0	2	4
6	0.24	0.14	0.26	0.34	0.1	0.34	4	2	2	2	6	0
7	0.32	0.26	0.34	0.4	0.42	0.36	2	4	4	2	0	2
8	0.4	0.42	0.34	0.4	0.2	0.22	0	0	0	4	8	0
9	0.46	0.5	0.1	0.5	0.12	0.48	2	2	2	0	6	2
10	0.5	0.48	0.5	0.04	0.06	0.4	0	2	0	2	0	4
Mean error							1.20	2.20	2.00	2.20	3.00	2.60

^a The detection error, $\epsilon_p = \left| DL_p^* - DL_p \right| \times 100\%$; p =location of damage in each damage scenario.

6.2.3 Experimental investigation

To validate the effectiveness of the proposed method, the experimental study is conducted on the test beam. Most of the vibration-based damage detection techniques obtained from the measured signals requires modal properties, which are sensitive to measurement error and noise. The proposed damage detection technique has to be validated using real measurement data from vibration tests in the presence of measurement errors and noise. Vibration tests are carried out on three I-section beams (i.e., beams 1, 2 and 3), as shown in Section 5.2.1.2,

6.2.3.1 Experimental results

For evaluation of the location of damage through the measured acceleration responses, the RWPE is implemented for each considered beam as shown in Figure 6.7. It is observed that the damage location in beam 1 can be precisely identified with DB2 and decomposition level 6 based on the change of RWPE values shown in Figure 6.7(a). In beam 2, DB 5 with 6 levels of decomposition is chosen for the two-damage scenarios, since the damage locations presented in Figure 6.7(b) are distinguishable in these histograms with RWPE reaching a peak value at locations 11 and 13. Moreover, location 11 has a relatively larger damage index while location 13 has a comparatively lower RWPE. The reason lies in the damage location, which is adjacent to the support. It should be mentioned that selection of a non-suitable type of wavelet may causes a false-negative indication.

A similar trend of damage index, as in beam 2, is observed for beam 3 by using DB10 and decomposition level 6 with three damage locations at points 9, 11 and 13, as shown in Figure 6.7(c). Evaluation of the RWPE associated with beam 3 shows the damage locations precisely with respect to the support, as mentioned earlier for beam 2.

The presented results demonstrate that the proposed damage index (RWPE) can identify the damage location accurately in all damage scenarios from the dynamic measurement.

In addition, varying operational and environmental conditions of the structure raise a discrepancy, i.e., false alarm, which can be reduced by choosing an appropriate mother wavelet function and decomposition level.

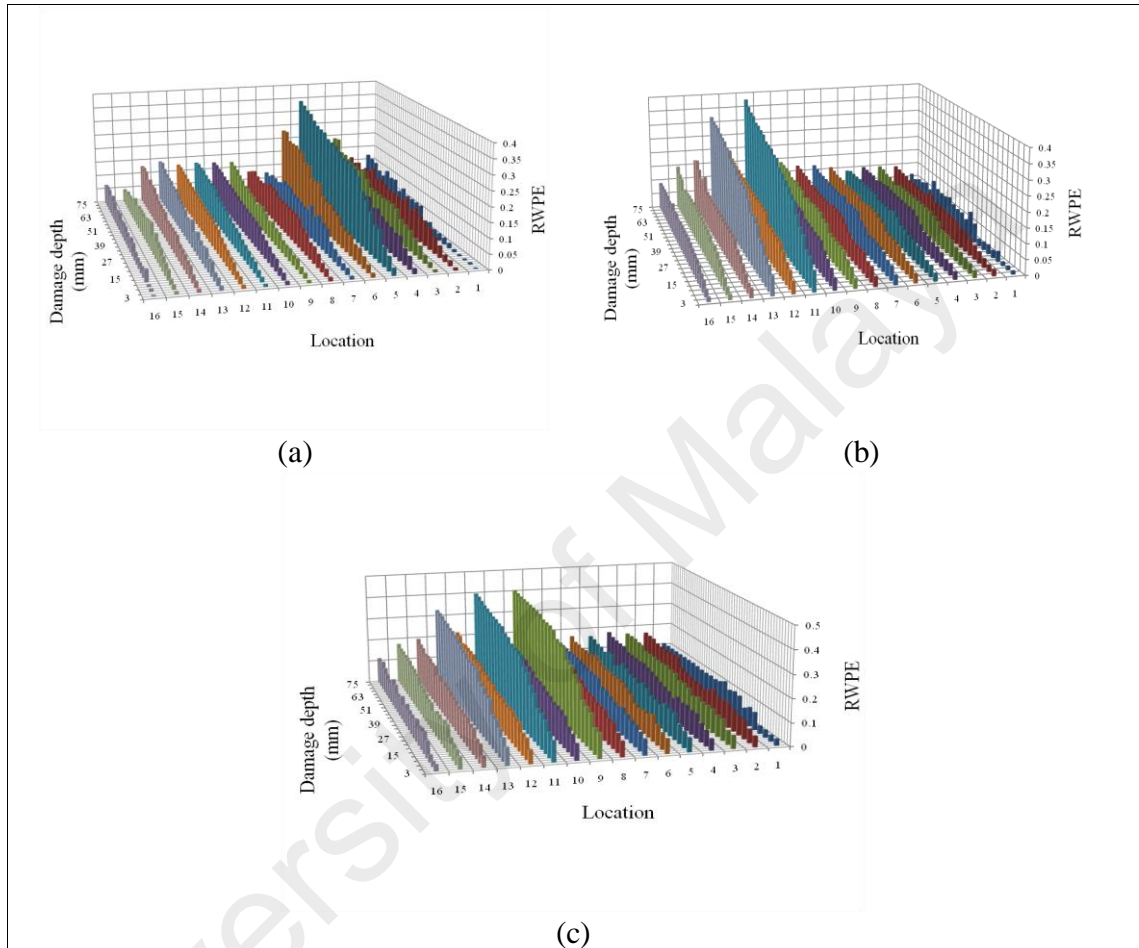


Figure 6.7: RWPE for different damage cases. (a) Beam 1, (b) beam 2, (c) beam 3

After identification of the damage locations, the analysis evaluates the severity of the damage. The optimization algorithm presented in Section 4.3 is employed for detection of the severity of damage. All of the considered beams with different damage scenarios and various levels of severity are subjected to damage severity detection by the proposed algorithm where α is varied from 0.02 to 0.5 with the step length of 0.02. The detection results for each damage scenario of the GA are found to be accurate and identical to the real values of severity. For instance, the results of GA encoded as a binary number

associated with case 3 with three depth ratios of $\alpha_{23}=0.46$, $\alpha_9=0.18$ and $\alpha_{25}=0.5$ are shown in Figure 6.8.

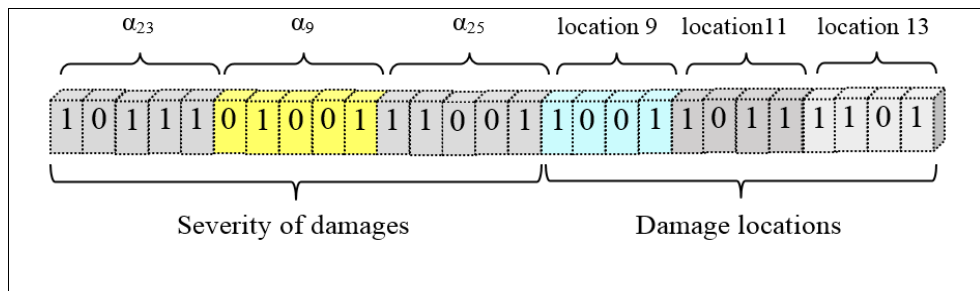


Figure 6.8: Encoded damage severity result for beam3 with different levels of severity

Based on the above results obtained by the proposed algorithm, it can be inferred that the selections of a proper mother wavelet function and decomposition level are crucial to improve the performance of the proposed algorithm. On the other hand, the wavelet-based techniques are absolutely dependent on the mother wavelet function, whose correlation with the signal is influenced by the locations and number of points of damages. It should be highlighted that utilization of a specific mother wavelet and a decomposition level does not necessarily successfully identify various damage scenarios that are located on a beam. Once the damages are located, the severity evaluation database is defined in terms of the relationships between the component energies and the damage severities. The GA optimization is then used to evaluate the damage severities by exploring the database.

6.3 Reference-free damage identification in beam structures

6.3.1 Reference-free damage identification approach

For most of in-field structures, the monitored data from initial pristine structural states are not available. Therefore, this section deals with the proposed reference-free damage detection method in beam structures. The procedure does not require vibration signals from an pristine structure because the RPWE measurements of different sensor-to-sensor pairs are used for defining the reference-free damage index, RDI_{RWPE} , of each sensor

location. To improve the proposed method, GA is utilized to identify the best choice for “mother wavelet function” and “decomposition level” of the signals by means of the fundamental fitness function to optimize the algorithm.

6.3.2 Numerical investigation

6.3.2.1 Tested damage scenarios

To verify the efficiency and accuracy of the proposed reference-free damage identification algorithm, numerical simulations are conducted on three I-section steel beams (i.e., beams 1, 2 and 4), as shown in Section 5.2.1.1. A total of three damage scenarios are tested for small-scale damage, i.e., 3 mm, with different sensor locations, as depicted in Table 6.4. For damage scenarios SS1 (single damage 1), DS1 (double damage 1) and TS1 (triple damage 1) all sensors are located at 16 specified locations. In DS2 scenario, fifteen sensors are distributed at points 1 to 16, except point number 13. The purpose of DS2 is to verify that the proposed algorithm does not indicate any false alarm when the sensor is not located at the damage location. In addition, the TS2 scenario with the fifteen number of sensors is deployed (see Table 6.4), demonstrate the influence of sensor position in identification of damage location.

Table 6.4: Damage scenarios with different sensor deployments on damaged beams

Damage type	Damage scenario		Damage location (point)	Sensor location
Notch cutting	Single	SS1	5	1, 2, 3, 4, 5, 6, 7, 8, 9, 10, 11, 12, 13, 14, 15, 16
	Double	DS1	11,13	1, 2, 3, 4, 5, 6, 7, 8, 9, 10, 11, 12, 13, 14, 15, 16
		DS2	11,13	1, 2, 3, 4, 5, 6, 7, 8, 9, 10, 11, 12, 14, 15, 16
	Triple	TS1	Middle of beam, 10,12	1, 2, 3, 4, 5, 6, 7, 8, 9, 10, 11, 12, 13, 14, 15, 16
		TS2	Middle of beam, 10,12	1, 2, 3, 4, 5, 6, 7, 8, 10, 11, 12, 13, 14, 15, 16

6.3.2.2 Damage location identification

The applicability of the proposed RWPE-based reference-free damage identification algorithm is validated with several considered damage scenarios, shown in Table 6.4. With regard to the identification of damage location in the single damage scenario, SS1, by running the GA with the predefined parameters which are exploited in this study and tabulated in Table 6.5, DB2 and level 5 have been selected as the best values for Daubechies order and decomposition level, respectively, and subsequently the RDI_{RWPE} values for every point are calculated, as depicted in Figure 6.9(a). It can be observed that the magnitude of RDI_{RWPE} at point 5 is greater than those from the other locations corresponding to the exact damage location. To determine the damage location distinctly, the threshold value for damage indices are established through applying the statistical properties and the one-side confidence limit of the RDI_{RWPE} values. With a 98% confidence interval ($\bar{\alpha} = 0.02$), the histogram of RDI_{RWPE} values after considering the damage threshold for SS1 damage scenario is depicted in Figure 6.9(b). It is evident that the RDI_{RWPE}^{UL} arise at sensor location 5, which indicates the actual damage location. In addition, the sensitivity of results are confirmed by comparing of the RDI_{RWPE} values before and after the damage in SS1 damage scenario, as illustrated in Figure 6.9(c). The significant increase in the RDI_{RWPE} can be depicted at the damage location. Thus, the index RDI_{RWPE} is considered an effective measure in the proposed damage detection algorithm.

Table 6.5: GA parameters used in RWPE-based reference-free algorithm

Number of generation	200
Population	30
Selection function	Tournament
Fitness normalization	Rank
Crossover	Pc=0.7, Single-point, uniform
Mutation	Pm=0.2, Uniform

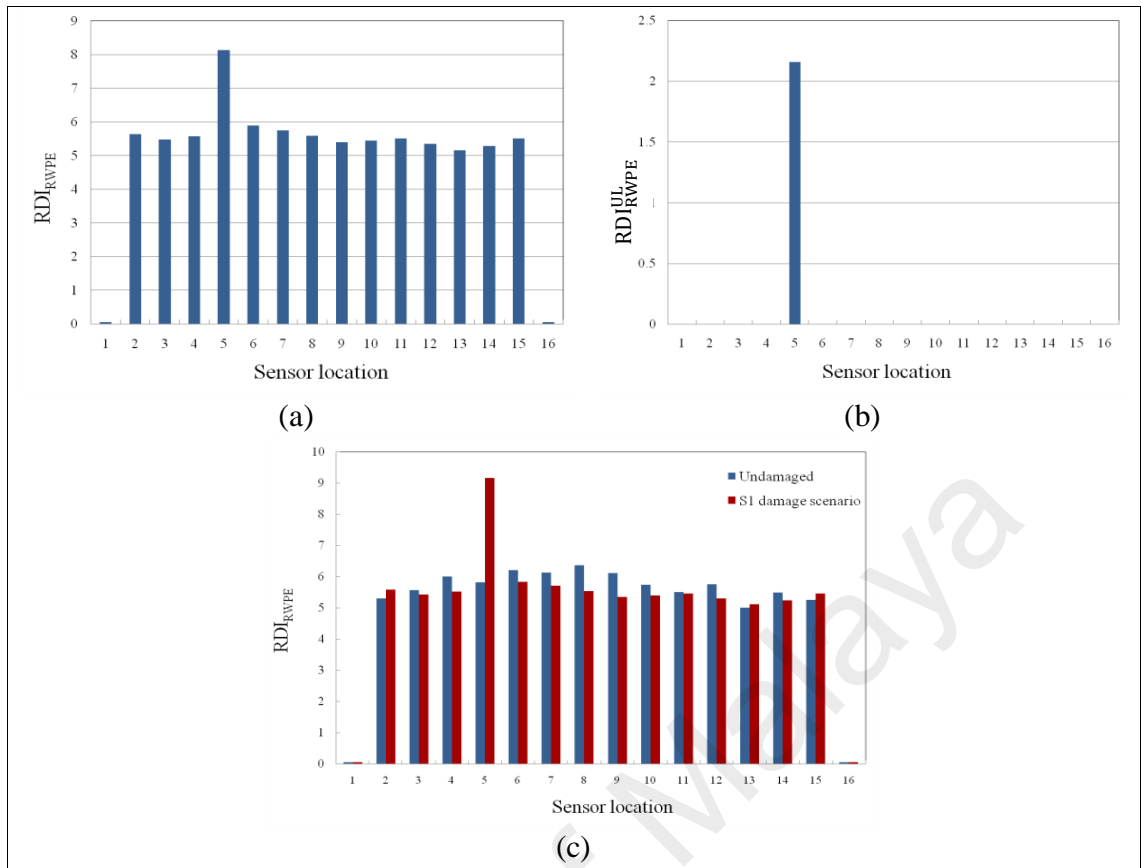


Figure 6.9: Damage identification in beam1. (a) Histogram of RDI_{RWPE} , (b) histogram of RDI_{RWPE}^{UL} after consider damage threshold, (c) comparison of RDI_{RWPE} before and after damage

In the multiple damage cases, the optimal DB order and decomposition level corresponding to each damage scenario have been selected by using GA, as shown in Table 6.6. In addition, the results of double and triple scenarios with various number of sensor locations are presented in Figure 6.10. It can be observed that, in the first damage scenario (DS1), Figure 6.10(a), the RDI_{RWPE}^{UL} arises clearly at sensor locations 11 and 13, which coincide with real damage locations. As indicated in Figure 6.10(b), when the sensor is not located at damage location 13, no peak is observed in RDI_{RWPE} values to indicate the damage location 13. The histogram of RDI_{RWPE}^{UL} with consideration of damage threshold values obtained from statistical analysis is depicted in Figure 6.10(b). From this figure, it can be seen that only the sensor at location 11 is able to successfully identify the location of damage. In addition, comparison of the peak values of RDI_{RWPE}^{UL} in DS1 damage scenario, reveals that higher intensity of the RDI_{RWPE}^{UL} takes place when the damage is situated close to the center of the beam, since the local perturbations caused

by the damage occurs at a far distance from the support. In general, the distance of the damage from the support is a key parameter in damage identification analysis. The farther the distance from the support, the higher the clarity and accuracy of damage identification. On the other hand, the presence of damage adjacent to the support results in a singularity around the support, which can reduce the accuracy of the identification.

Table 6.6: GA optimized variables in beams

Variable name	Range	Optimized value		
		Beam 1	Beam 2	Beam 4
Daubechies order	DB1-DB31	DB2	DB5	DB15
Decomposition level	2-7	5	5	6

The results of triple damage scenarios with different number of sensors are also presented in Figure 6.10(c) and (d), respectively. Based on the result in TS1 damage scenario shown in Figure 6.10(c), it can be seen that the RDI_{RWPE}^{UL} arise at locations 8,9,10 and 12, which coincided with damage locations. In addition, the results indicated that the RDI_{RWPE}^{UL} for sensor locations 8 and 9 have lower intensity and sensitivity relative to the sensor location 10, even though they are located in the middle of the beam span. The reason for such behavior is caused by the influence of damage and signal attenuation, when it is located adjacent to sensor locations the signal attenuates and a part of signal energy decays once it is recorded by the sensor. As shown in Figure 6.10(d), the TS2 damage scenario with fifteen sensor deployment can also successfully identify the damage locations.

By comparing the results, it can be demonstrated that, the RDI_{RWPE}^{UL} value at damaged location for single damage scenario (Figure 6.9) is considerably larger than the one for triple damage scenario (Figure 6.10). It means that as the number of damage locations increases, the number of sensors are also required to increase in order to secure sufficient specificity for identifying multiple damage locations.

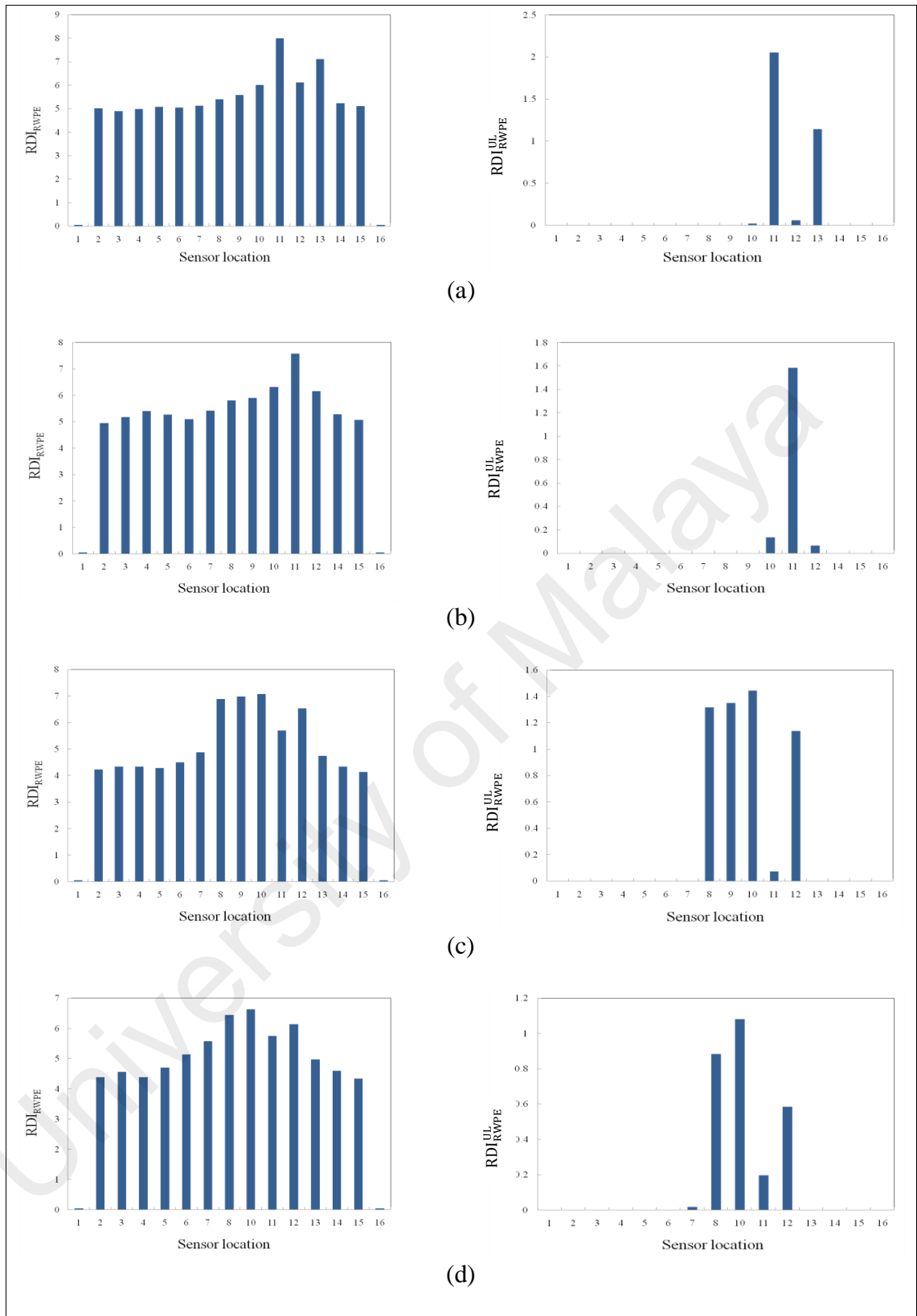


Figure 6.10: Damage identification in multiple damage scenarios with different sensor locations. (a) DS1, (b) DS2, (c) TS1, (d) TS2

6.3.2.3 Identification of progressive damage

Verification of the proposed algorithm is also carried out with progressive damage scenarios, i.e., starting from small scale damage, of the simulated simply-supported beams. Figure 6.11 shows the values of indices RDI_{RWPE}^{UL} for beam 1 with a single damage scenario. By using the GA, DB2 and level 5 are selected as the best values for the Daubechies order and decomposition level, respectively. Figure 6.11 clearly depicts the difference between various orders of Daubechies to discriminate the location and severity of damage. As can be seen, the damage locations are distinguishable in these histograms with RDI_{RWPE}^{UL} reaching a maximum value at location 5 which is the exact damage location. However, the peak of RDI_{RWPE}^{UL} is not as clearly distinguishable in DB15 even though it has the same location and severity of damage. Furthermore, the changes in values of RDI_{RWPE}^{UL} for each depth of damage are not as comparable to DB2. For DB11, the shortcomings are identical to that of DB15 but gave more appropriate results. DB5 is not a worthy consideration since it is not able to precisely indicate the damage location. It is significant to note that the accuracy of differentiating the damage cannot be compared to DB2 for the single damage scenario.

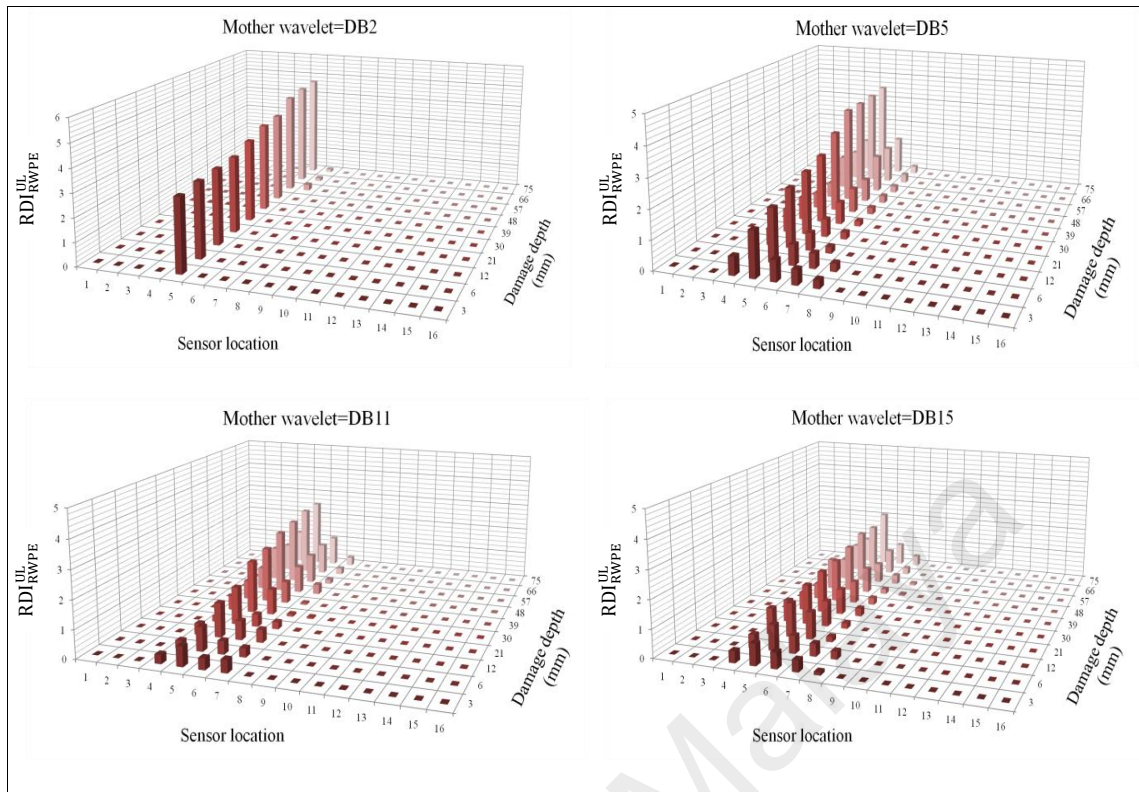


Figure 6.11: Histograms of RDI_{RWPE}^{UL} in beam1 with different Daubechies orders

In order to clarify the estimated values, the performance of the fundamental fitness function at the fifth level of decomposition is also calculated manually through the percentage of standard difference between the RDI_{RWPE} values at damage locations and average of the remaining points $([(\sum_i RDI_{RWPE}^{max} - \sum RDI_{RWPE}^{ave}) / \sum RDI_{RWPE}^{ave}] \times 100; i = \text{number of damage scenarios})$ at every specific depth of damage. The results are tabulated in Table 6.7. Comparison of each column associated with every depth of damage for all the considered DBs indicates that from manual calculations, wavelet function DB2 is the suitable wavelet function order. This coincides with the outcome of GA estimation. For instance, in the case of 30 mm damage depth, the maximum value of standard difference is associated with DB2 by 90.10% compared to other DBs. A similar trend is observed for other considered damage depths.

To extract the relevant information from Table 6.7 for all DBs in each depth of damage, the one-way ANOVA followed by Duncan's multiple-range test are employed. Significant differences between DBs ($F=23.43, p<0.01$) and DB2 are found in the

statistical analysis. The results revealed that the mean of DB2 (M= 50.82) is significantly greater than other DBs.

Table 6.7: Daubechies wavelets comparison for each damage depth for beam 1

Wavelet function order	Standard difference (%)										Mean*
	Damage depth (mm)										
	3	6	12	21	30	39	48	57	66	75	
DB 2	28.74	28.12	36.13	41.41	46.08	59.43	59.54	70.10	69.40	69.34	50.83a
DB 3	14.51	15.11	17.27	18.33	23.81	23.34	27.75	26.79	26.37	27.78	22.11cdef
DB 4	13.09	14.87	15.72	17.16	23.73	25.39	27.49	25.50	24.34	26.64	21.39cdef
DB 5	20.09	30.34	23.64	26.77	34.09	40.68	46.92	42.29	41.83	41.97	34.86b
DB 6	14.08	13.32	18.80	18.31	19.92	20.53	28.24	29.37	28.57	28.94	22.01cdef
DB 7	13.11	13.05	14.17	16.18	16.62	17.35	19.45	19.85	17.70	19.98	16.75fgh
DB 8	6.45	7.96	10.85	10.54	11.15	12.63	14.17	13.06	15.72	15.47	11.8h
DB 9	9.97	9.87	12.01	13.14	14.19	16.69	16.40	17.13	20.06	19.97	14.94gh
DB 10	15.13	15.67	15.42	18.23	27.16	27.26	30.30	31.34	30.39	31.52	24.24cd
DB 11	17.94	19.22	24.37	22.79	30.23	31.82	35.45	31.80	29.61	29.99	27.32c
DB 15	17.45	17.09	20.73	21.90	26.39	26.86	26.67	25.53	24.99	26.59	23.42cde
DB 16	12.99	12.90	13.23	14.35	18.01	18.28	20.82	20.97	19.26	21.58	17.24efgh
DB 17	14.19	13.88	13.97	15.16	19.55	19.72	21.38	23.80	23.07	23.79	18.85defg
DB 18	9.64	11.31	12.19	12.21	12.54	12.46	13.87	12.92	12.94	13.38	12.34h
DB 19	8.36	9.68	11.81	12.37	12.20	13.34	15.73	15.78	15.39	15.84	13.05gh
DB 20	14.50	15.84	15.26	21.73	23.56	23.22	30.22	31.14	29.98	31.36	23.68cd
DB 21	10.29	11.53	12.00	12.00	13.12	13.04	13.80	14.48	13.38	13.89	12.75gh

*Mean values with the same letter are not significantly different.

In beam 2, the GA is utilized to identify the most accurate location and severity of damage by maximizing the fitness function. The outcome of the GA analysis, which is depicted in Figure 6.12, revealed that DB5 with 5 level of decomposition performed better in two damage scenarios compared to other Daubechies orders. Firstly, by comparing the considered Daubechies orders shown in Figure 6.12, it can be seen that for DB11, the damage locations are not easily identified while DB5 clearly identified damage locations 11 and 13 together with appropriate representation by the histograms i.e. values of RDI_{RWPE}^{UL} at damage locations compared to other Daubechies orders. Meanwhile, by scrutinizing the histograms, the damage locations in DB2 and DB15 can be identified. In addition, from the histograms it can be observed that the intensity of RDI_{RWPE}^{UL} at location 11 is relatively larger than location 13 although both have similar damage severity. This is possibly due to location 11 being close to the middle of the beam while location 13 is close to the support.

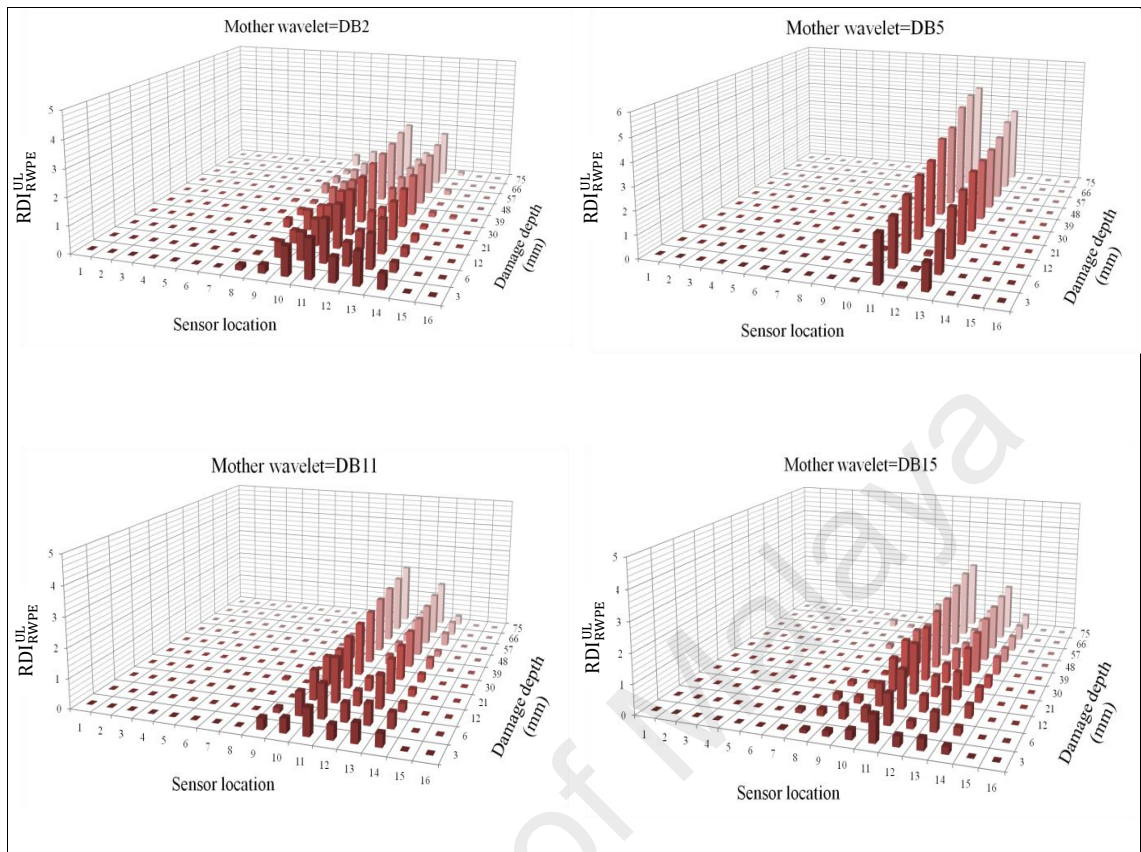


Figure 6.12: Histograms of RDI_{RWPE}^{UL} in beam 2 with different Daubechies orders

For beam 4 with multiple damages, DB15 with 6 level of decomposition is found to be the appropriate DB order for damage identification. The advantage of DB15 compared to other Daubechies orders is that the value of RDI_{RWPE}^{UL} , as shown in Figure 6.13, precisely shows the damage locations along the beam length. The intensity of RDI_{RWPE}^{UL} is influenced by the notch locations as well as the distance from the supports. The corresponding intensity of RDI_{RWPE}^{UL} for the damage located at the middle of the beam is expected to be larger than those closer to the support. However, due to the signal attenuation effect raised by the presence of damage between two sensor locations, the intensity of RDI_{RWPE}^{UL} of the damage between locations 8 and 9 is lower than that of location 10.

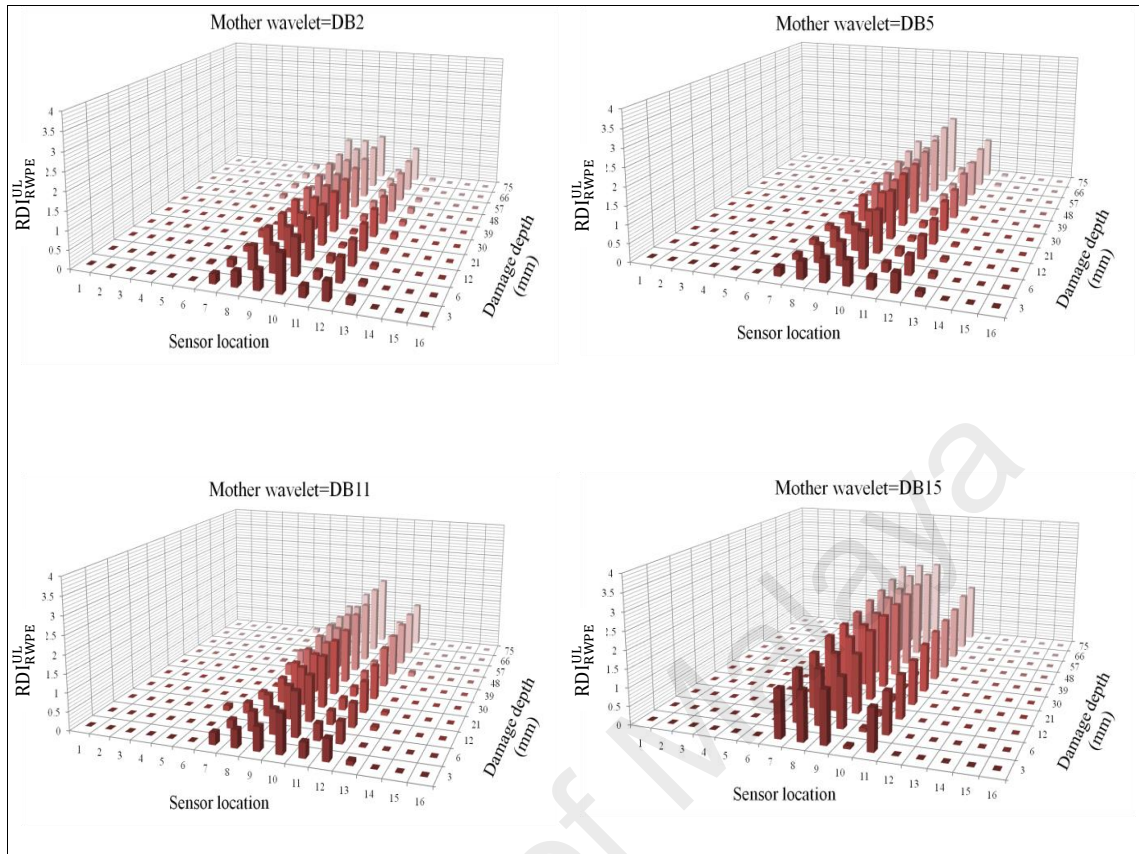


Figure 6.13: Histograms of RDI_{RWPE}^{UL} in beam 4 with different Daubechies orders

To verify the estimated values, Table 6.8 shows the mean values of standard difference percentage of RDI_{RWPE} values for multiple damage scenarios at specified level of decomposition without using GA. Analysis performed by ANOVA indicated the significant differences among the DB5 and DB15 with other DBs in each damage scenario. Comparison of results showed that the mean value of DB5 and DB15 are considerably greater than other DBs in each damage scenario. Hence, it can be inferred that not only does the GA has the potential to verify the proposed algorithm to obtain the optimal solution but also provides evidence for the accuracy of the parameters for adjustment of the algorithm.

Table 6.8: Daubechies wavelets comparison for multiple damage scenarios

Wavelet function order	Mean*	
	Beam 2	Beam 4
DB 2	179.67bc	450.22cde
DB 3	158.36def	426.83ef
DB 4	156.84ef	397.60g
DB 5	223.12a	462.16c
DB 6	166.28cdef	447.53cde
DB 7	153.57f	435.12de
DB 8	173.07bcd	441.83cde
DB 9	168.26cdef	450.44cde
DB 10	167.76cdef	456.26cd
DB 11	169.38bcde	494.83b
DB 15	181.18bc	531.31a
DB 16	163.28def	432.90de
DB 17	162.98def	433.85de
DB 18	158.54def	442.19cde
DB 19	162.21def	407.38fg
DB 20	182.88b	496.71b
DB 21	166.30cdef	457.11cd

*Mean values with the same letter are not significantly different.

Results have demonstrated that the locations of notches can be successfully determined from the measured time history acceleration responses through variation of RDI_{RWPE}^{UL} . In addition, the respective amplitude levels of the histograms can be used as a criterion to identify severity of damage, although not quantitatively. Therefore, selection of a proper mother wavelet for wavelet-based methods is crucial to improve the performance of the proposed method in order to achieve accurate results. The type of mother wavelet function plays a key role in reducing the false positives adjacent to damage locations, as depicted in Figures 6.11, 6.12 and 6.13. This is mostly because the correlation between the mother wavelet functions and the signal is calculated as a wavelet coefficient and this is the significance of the proposed method.

6.3.3 Experimental investigation

To validate the proposed algorithm by experimental data where measurement error and noise are present, vibration tests are conducted on three I-section steel beams (i.e., beams 1, 2 and 4) with different damage scenarios, as shown in Section 5.2.1.2.

6.3.3.1 Experimental results

The following observations are made based on the structural response signal of damaged beams. By running the GA on the first damage case i.e. beam 1 with a single damage as shown in Figure 6.14(a), Daubechies order 2 and decomposition level 6 are chosen as the best parameters for the adjustment of the algorithm for differentiating the damages. The damage location at position 5 can be clearly identified with the significant change in values of RDI_{RWPE}^{UL} . In beam 2 with the double damage scenario as depicted in Figure 6.14(b), the influence of changing the wavelet function as well as level of decomposition on the accuracy of damage identification is investigated by using the GA. As a consequence, Daubechies wavelet function with order of 5 and decomposition level 6 are selected as the best function for identification of damage location and severity. Furthermore, the intensity of RDI_{RWPE}^{UL} at damage location 11 which is located at the middle of the beam are slightly higher than that of damage location 13 which may be due to its close distance to the support. In beam 4 with the multiple damage scenarios as shown in Figure 6.14(c), Daubechies order 20 and decomposition level 6 are selected as the suitable function by GA and both damage locations and severities can be identified. However, for the whole set of data, the maximum value of the RDI_{RWPE}^{UL} is always detected at the exact damage location.

The results have demonstrated that for wavelet-based methods, the choice of the mother wavelet function is of paramount importance to improve the performance of the algorithm. However, as indicated in this study, it is possible to have satisfactory algorithm performance with a particular mother wavelet function. Moreover, from the comparison of histograms in different damage scenarios, the values of RDI_{RWPE}^{UL} are found to be proportional to damage severity. Therefore, this reference-free damage index can be used to quantify the damage severity. Also, by comparing results corresponding to the damage cases, it can be seen that changes in damage location causes a scenario which requires a

different suitable mother wavelet function. Hence, the final outcome obtained from GA is found to have great potential to determine the optimal solution and to investigate the reliability of the parameters for algorithm adjustment.

In addition, varying operational and environmental conditions of the structure raise a discrepancy, i.e., false alarm, which is reduced because of the reference-free nature of the proposed method. Since all sensors are subjected to the same environmental condition and measured the vibration signals at the same time. Thus the vibration signals measured at a location can act as reference signals to other location that has comparable structural feature.

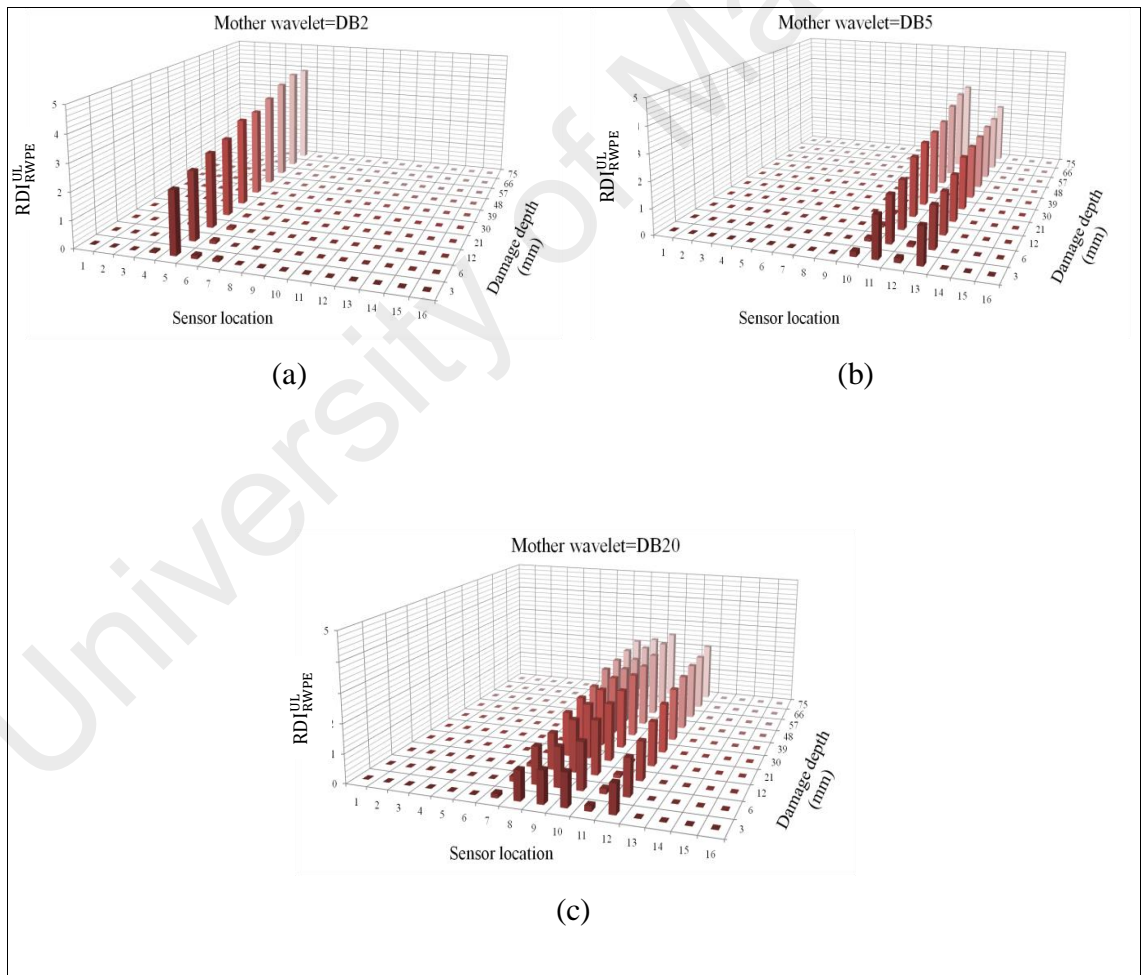


Figure 6.14: Histograms of RDI_{RWPE}^{UL} in (a) beam 1, (b) beam 2, and (c) beam 4 with different Daubechies orders

6.4 Damage identification algorithms for three-story building model

To demonstrate the capability and accuracy of the proposed damage identification algorithms, experimental studies are conducted on the small-scale three-story steel building which is described in Section 5.2.2.

6.4.1 RWPE-based damage identification

In this section, the RWPE-based damage identification algorithm is verified through five different damage scenarios in terms of the number and location of damages in the model, as shown in Section 5.2.2.1.1.

6.4.1.1 Damage location identification

Figures 6.15 and 6.16 shows the calculated values of RWPE at 12 sensor locations for each damage scenario. According to these figures, the value and distribution of RWPEs changed significantly after occurrence of damage. In cases with small damages, type of mother wavelet and decomposition level is important for accurate identification of damage location. Therefore, several wavelet functions, i.e., DB1 to DB10, and different levels of decomposition are investigated. In two-damage cases, more accurate results for DS1 and DS3 scenarios are achieved, when the wavelet function DB2 and decomposition level 8 are used for differentiating the damages, as indicated in Figure 6.15 (a) and (c). The damage locations can be identified with significant variation of RWPE values at designated locations. However, the peak values of RWPE for DS2, where the damages are located at the same story, are clearly identified by using the DB5 and decomposition level 8, as indicated in Figure 6.15(b). By comparing the results, it can be demonstrated that, the accuracy of identification results are affected by location of the damages. On the other hand, the proposed method can provide high-accuracy identification results, when damages are located at different stories.

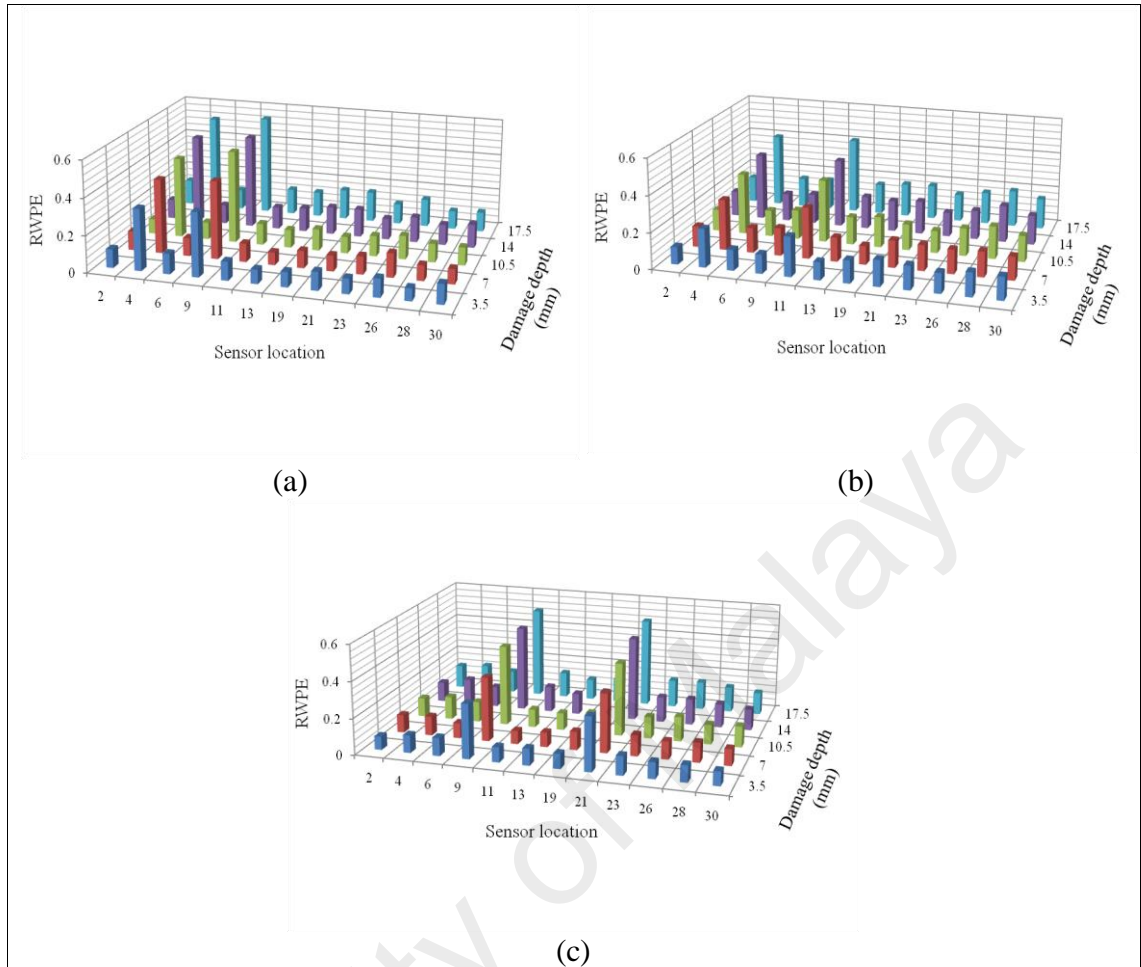


Figure 6.15: The values of RWPE for each depth of damage. (a) DS1, (b) DS2, (c) DS3

Similar trend of RWPE-based damage index, as in double damage scenarios, has been observed for triple damage scenarios by applying DB10 and decomposition level 8 as indicated in Figure 6.16. Evaluation of the RWPE, associated with each damage case, precisely shows the damage locations when RWPE reaches its peak value at damaged points.

From the obtained results, it can be confirmed that the RWPE values show increasing tendency in damage identification as damage extent is progressively increasing. In addition, Comparison of the peak values of RWPEs in the region of the damages indicated that larger values of the RWPE take place when the damage is located at upper stories.

Experimental test results clearly showed consistency and reliability in identifying damaged locations under various damage scenarios in the three-story building model. It

is worth mentioning that, appropriate selection of mother wavelets can effectively help improving accuracy of the results and reducing false alarms.

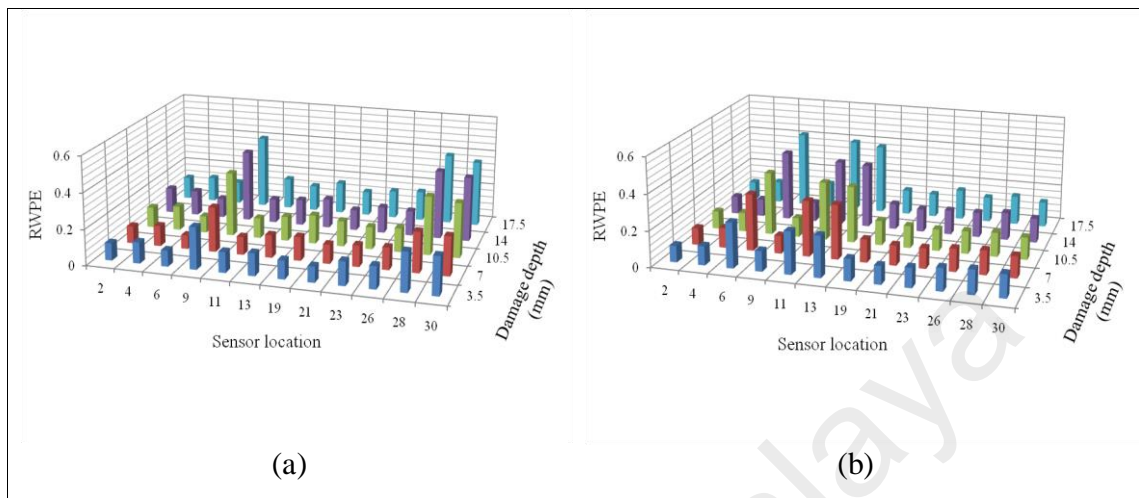


Figure 6.16: The values of RWPE for each depth of damage. (a) DS4, (b) DS5

6.4.1.2 Damage severity evaluation

After identification of damage locations, damage severities of the corresponding damaged elements in the building model can be determined using the GA. Accordingly, to evaluate the damage severities α_n ($n = 1, 2, \dots, 5$) in the model, seven different severity combinations of each damage scenario, indicated in Tables 6.9 and 6.10, are considered. To obtain more accurate severity evaluation database, α_n is varied from the upper and lower bound of severity (depth). Therefore, the constraint α_n limits the severity search space from 0.1 to 0.5. In this investigation, through several test runs the parameters of the GA are setup as follows: population size—40; two-point crossover with crossover probability (Pc)—0.7, mutation probability (Pm)—0.05; and maximum number of generation is 200.

Table 6.9: Considered damage cases in double damage scenarios of the building model

Case	Damage severity					
	DS1		DS2		DS3	
	Damage location (DL)					
	DL ₄	DL ₉	DL ₄	DL ₁₁	DL ₉	DL ₂₁
1	0.1	0.1	0.1	0.1	0.1	0.1
2	0.2	0.2	0.2	0.2	0.2	0.2
3	0.3	0.3	0.3	0.3	0.3	0.3
4	0.4	0.4	0.4	0.4	0.4	0.4
5	0.5	0.5	0.5	0.5	0.5	0.5
6	0.3	0.4	0.3	0.4	0.5	0.3
7	0.2	0.5	0.2	0.5	0.3	0.1

Table 6.10: Considered damage cases in triple damage scenarios of the building model

Case	Damage severity					
	DS4			DS5		
	Damage location (DL)					
	DL ₉	DL ₂₈	DL ₃₀	DL ₆	DL ₁₁	DL ₁₃
1	0.1	0.1	0.1	0.1	0.1	0.1
2	0.2	0.2	0.2	0.2	0.2	0.2
3	0.3	0.3	0.3	0.3	0.3	0.3
4	0.4	0.4	0.4	0.4	0.4	0.4
5	0.5	0.5	0.5	0.5	0.5	0.5
6	0.4	0.3	0.2	0.2	0.2	0.1
7	0.5	0.2	0.1	0.5	0.3	0.1

Tables 6.11 and 6.12 show the damage severity detection results of each damage scenario with different severities combination. As indicated in the tables, evaluation errors for different damage scenarios are within the range of 0% to 20% with the mean values of 7.14% to 12.86%.

To examine the effect of damage location on evaluation of damage severities, evaluation results of double damage scenarios for seven cases are compared (Table 6.11). The results show that when the damages are located at the same floor, i.e., DS2, amount of the mean errors are varied from 11.43% to 12.86%, while in DS1 and DS3, variation range of the mean errors are reduced to the lower range of 7.14% to 10%. These results suggest that if damages are located at different levels better evaluation results are obtained.

Additional analysis is also performed on three damage scenarios for seven cases. The severity detection results are summarized in Table 6.12. As indicated in the table, amount of mean errors for damage scenarios DS4 and DS5 are within the range of 8.57% to

12.86%, which illustrates that variation of mean error is in acceptable range of accuracy even with rise in number of damages.

Table 6.11: Damage severity evaluation results using two damage scenarios

Case	Predicted value						Error (%)					
	DS1		DS2		DS3		DS1		DS2		DS3	
	DL_4^*	DL_9^*	DL_4^*	DL_{11}^*	DL_9^*	DL_{21}^*	ϵ_4^a	ϵ_9^a	ϵ_4^a	ϵ_{11}^a	ϵ_9^a	ϵ_{21}^a
1	0.2	0.1	0.3	0.2	0.2	0.2	10	0	20	10	10	10
2	0.3	0.1	0.3	0.1	0.3	0.1	10	10	10	10	10	10
3	0.4	0.2	0.5	0.1	0.2	0.4	10	10	20	20	10	10
4	0.5	0.3	0.5	0.3	0.4	0.5	10	10	10	10	0	10
5	0.5	0.5	0.5	0.5	0.5	0.5	0	0	0	0	0	0
6	0.4	0.3	0.2	0.5	0.4	0.4	10	10	10	10	10	10
7	0.3	0.4	0.4	0.3	0.1	0.3	10	10	20	20	20	20
Mean error							8.57	7.14	12.86	11.43	8.57	10.0

^a The detection error, $\epsilon_p = \left| DL_p^* - DL_p \right| \times 100\%$; p =location of damage in each damage scenario.

Table 6.12: Damage severity evaluation results using three damage scenarios

Case	Predicted value						Error (%)					
	DS4			DS5			DS4			DS5		
	DL_9^*	DL_{28}^*	DL_{30}^*	DL_6^*	DL_{11}^*	DL_{13}^*	ϵ_9^a	ϵ_{28}^a	ϵ_{30}^a	ϵ_6^a	ϵ_{11}^a	ϵ_{13}^a
1	0.1	0.1	0.2	0.1	0.2	0.2	0	0	10	0	10	10
2	0.1	0.4	0.2	0.3	0.3	0.1	10	20	0	10	10	10
3	0.5	0.4	0.1	0.5	0.4	0.1	20	10	20	20	10	20
4	0.5	0.3	0.2	0.3	0.5	0.3	10	10	20	10	10	10
5	0.5	0.5	0.4	0.5	0.4	0.4	0	0	10	0	10	10
6	0.5	0.1	0.4	0.1	0.4	0.2	10	20	20	10	20	10
7	0.3	0.1	0.2	0.4	0.4	0.3	20	10	10	10	10	20
Mean error							10.0	10.0	12.86	8.57	11.43	12.86

^a The detection error, $\epsilon_p = \left| DL_p^* - DL_p \right| \times 100\%$; p = location of damage in each damage scenario.

Based on the above observations it can be concluded that selection of proper mother wavelet function and decomposition level are crucial to improve the performance of the proposed method in an accurate identification of damage locations. Furthermore, results of the damage severity evaluation demonstrates that the GA is successful in evaluating damage severities by exploring the database and it yields precise estimations even with increasing number of damages.

6.4.2 RWPE-based reference-free damage identification

For demonstration of the proposed RWPE-based reference-free damage identification algorithm of the building model (shown in Section 5.2.2), a total of five damage scenarios with various sensor locations are tested, as depicted in Table 6.13.

Table 6.13: Damage scenarios of reference-free damage identification

Damage type	Damage scenario		Damage location		Sensor location
			Column number	Point	
Notch cutting	Double	DS1	II	Between points 3 and 4	2, 4, 6, 9, 11, 13, 19, 21, 23, 26, 28, 30
			IV	Between points 8 and 9	
		DS2	II	Between points 3 and 4	2, 4, 6, 9, 11, 13, 19, 21, 23, 26, 28, 30
			V	Between points 10 and 11	
		DS3	IV	Between points 8 and 9	2, 4, 6, 11, 13, 19, 21, 23, 26, 28, 30
			VIII	Between points 20 and 21	
	Triple	DS4	IV	Between points 8 and 9	2, 4, 6, 9, 11, 13, 19, 21, 23, 26, 28, 30
			X	Between points 27 and 28	
			XI	Between points 30 and 31	
		DS5	III	Between points 6 and 7,	2, 4, 6, 9, 11, 13, 15, 16, 17, 19, 21, 23, 26, 28, 30, 32, 33, 34
			V	Between points 10 and 11	
			VI	Between points 13 and 14	

For damage scenarios DS1 and DS2, all sensors are located at twelve identical locations namely points 2, 4, 6, 9, 11, 13, 19, 21, 23, 26, 28 and 30. In DS3 scenario, all the sensors are distributed at eleven locations at points 2, 4, 6, 11, 13, 17, 19, 21, 23, 26, 28 and 30, but the damage is located at column number IV which is not one of the sensor locations. The purpose of DS3 is to verify that the proposed algorithm does not indicate any false alarming when all sensors are located at other columns. In addition, tests with triple damage scenarios, i.e., DS4 and DS5, are performed with different numbers of sensors which are randomly distributed at columns, as shown in Table 6.13.

6.4.2.1 Damage location identification

In order to evaluate the feasibility of the proposed reference-free damage identification algorithm, firstly, variation of RDI_{RWPE} before and after damage are confirmed by DS1 damage scenario with 10.5 mm damage depth. By running the GA with the same

parameters given in Table 6.5, DB15 and decomposition level 8 have been selected as the best values. According to the results indicated in Figure 6.17(a), $RS_{RWPE}(p^\lambda|p^\theta)$ values, corresponding to the damaged locations, are higher than those from the other locations. In addition, comparison between the RDI_{RWPE} values before and after the damage, presented in Figure 6.17(b), shows a drastic increase of RDI_{RWPE} at the damage locations.

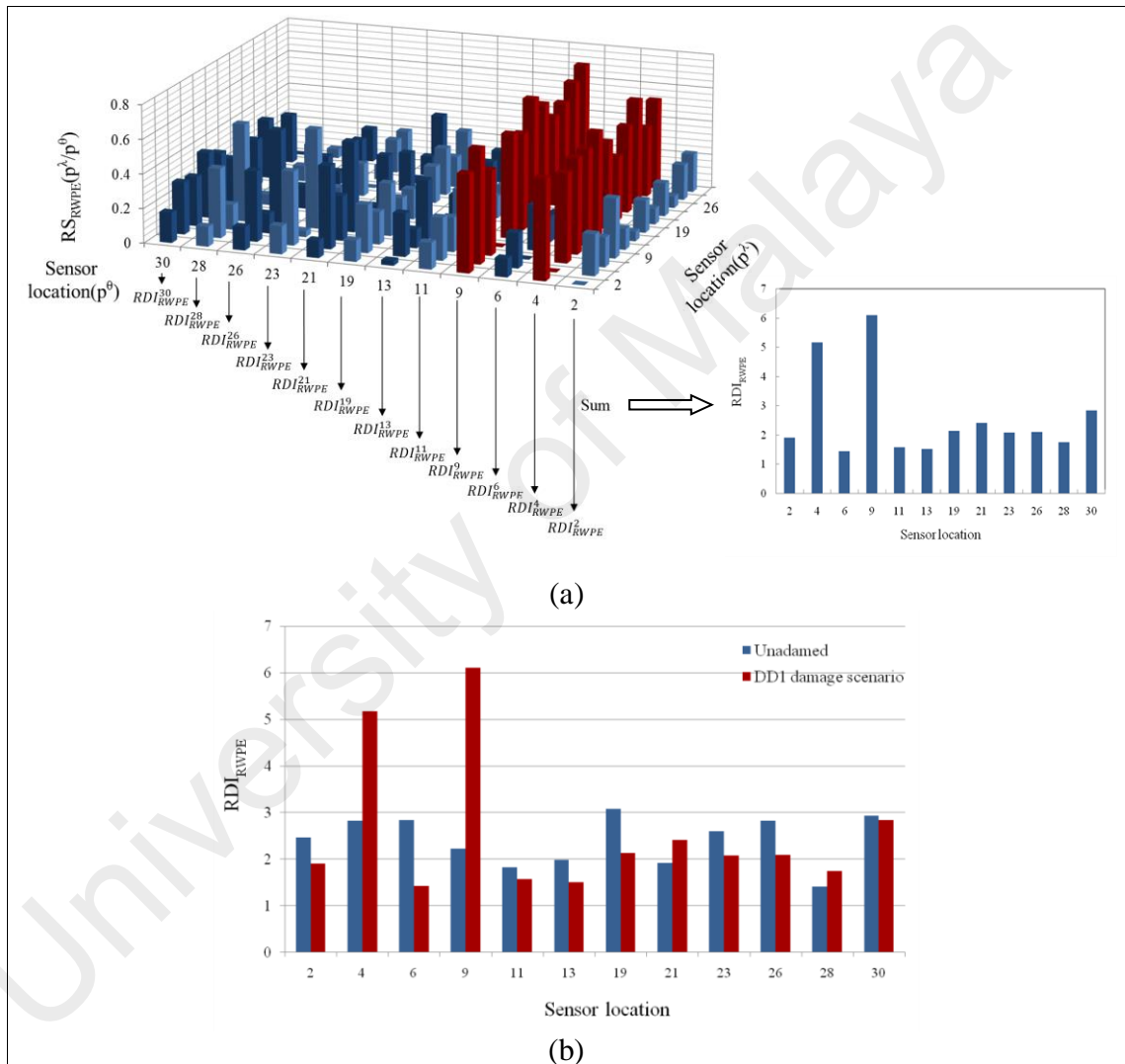


Figure 6.17: RWPE-based reference-free damage identification results for DS1 damage scenario at 10.5mm depth of damage. (a) $RS_{RWPE}(p^\lambda|p^\theta)$, (b) comparison of RDI_{RWPE} before and after damage

The consistency and reliability of the proposed algorithm are investigated with various damage scenarios (Table 6.13) at 10.5 mm depth of damage, as depicted in Figure 6.18. In DS2 damage scenario, by employing the GA, the DB15 and decomposition level 8 are

selected and the corresponding RDI_{RWPE} values are indicated in Figure 6.18(a). In DS3 damage scenario, sensors are not located at the damaged column IV and by running the GA, the DB20 and 8th level of decomposition have been chosen and the corresponding results are shown in Figure 6.18(b). It can be observed that the damage at column VIII can be identified accurately, while no peculiar difference of RDI_{RWPE} values is observed in other sensor locations. In addition, the sensitivity of the proposed reference-free damage identification algorithm is considered for triple damage scenarios with various numbers of sensors. The results of DS4 and DS5 scenarios are obtained from DB20 at 8th level of decomposition, as shown in Figure 6.18(c) and (d), respectively.

By comparing the results of the damage scenarios, it can be observed that the RDI_{RWPE} values of the damaged locations for DS1 and DS2 cases (Figure 6.17(b) and 6.18(a)) are almost two times larger than DS4 case (Figure 6.18(c)), with regard to identical number of sensors. It means that as the number of damage locations increases, the number of sensors also requires to increase in order to secure adequate specificity for identifying multiple damage locations, as shown in Figure 6.18(d). This is an important suggestion for practical application of the proposed algorithm. Moreover, for damage over a large area, some of the sensors are needed to be located over the healthy area.

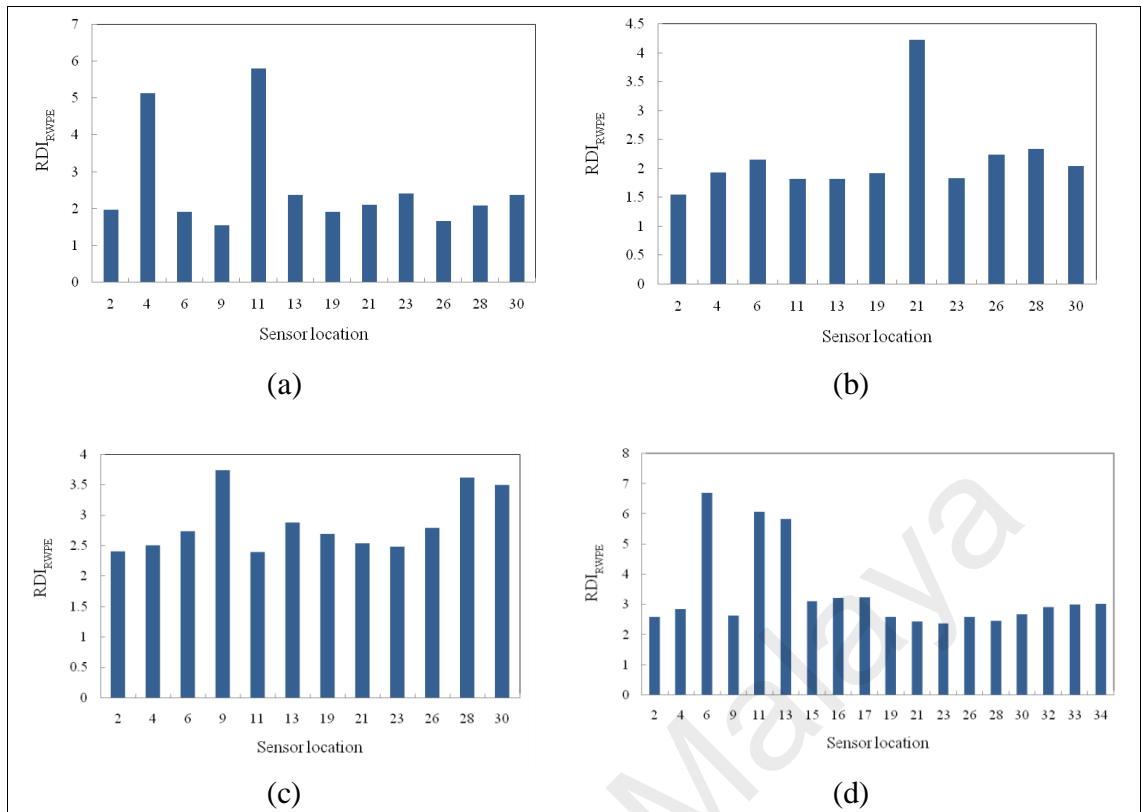


Figure 6.18: Result of damage identification by RWPE-based reference-free for 10.5mm damage depth. (a) DS2, (b) DS3, (c) DS4, (d) DS5

6.4.2.2 Identification of progressive damage

In addition to previous five damage scenarios, the proposed method is also verified through progressive cutting of columns starting from relatively small-scale damage, 3.5mm up to 17.5mm for each damage scenario.

Figure 6.19 shows the results of each progressive damage scenario after considering the damage threshold values obtained by the statistical analysis. Obviously, the proposed method is able to identify the location of damages even for slight extent of damage. It can be observed that by increase of damage extent, the RDI_{RWPE}^{UL} values at the damaged elements increase, although increase of RDI_{RWPE}^{UL} values in small-scale damages is not significant but still are clearly discernible. This is mostly due to the fact that proper estimation of functions by GA, improves the performance of the algorithm. In addition, the farther the distance of damage from the first floor, the higher clarity and accuracy of damage identification can be achieved.

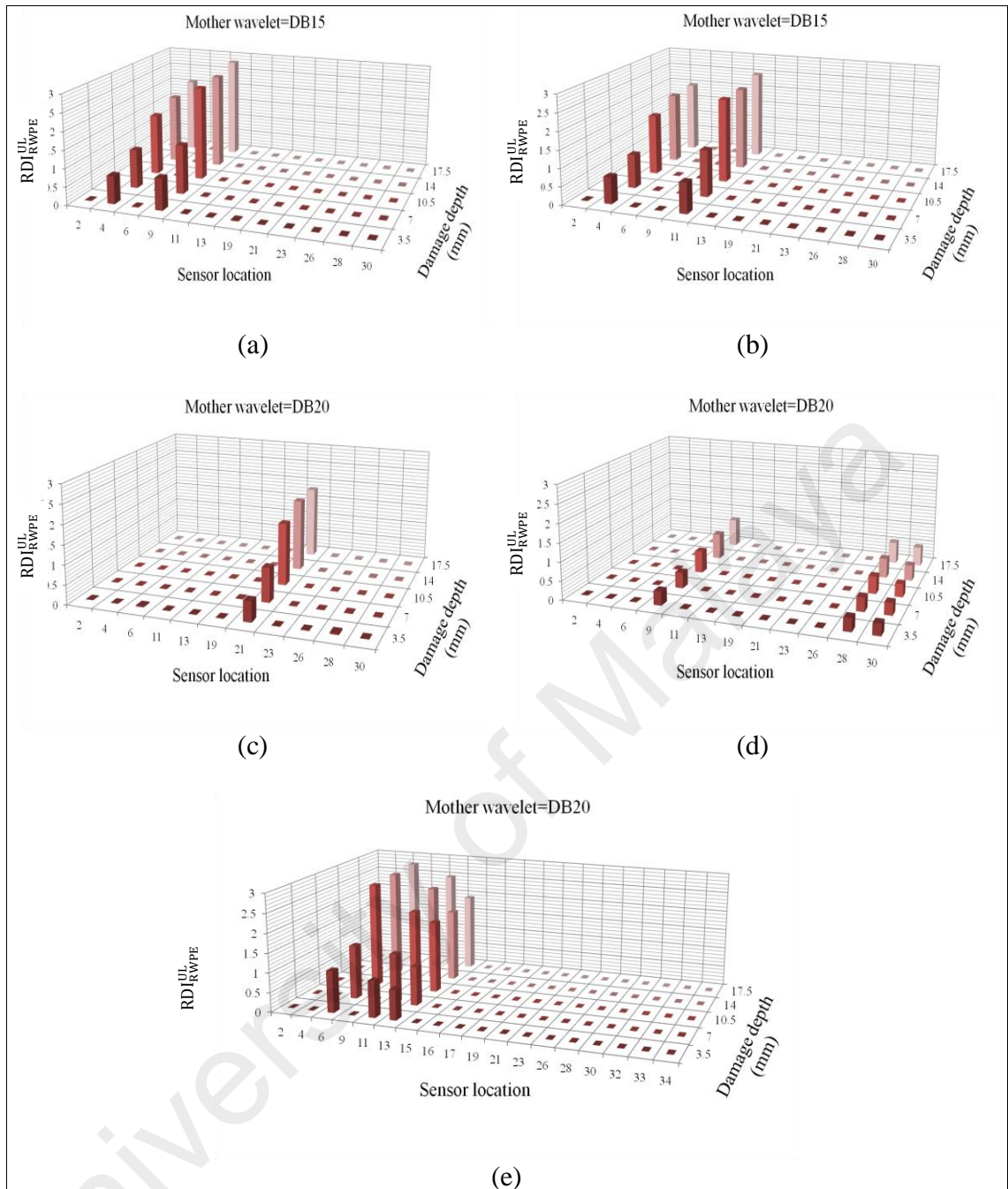


Figure 6.19: Result of damage identification by RWPE-based reference-free for progressive damage after considered threshold values. (a) DS1, (b) DS2, (c) DS3, (d) DS4, (e) DS5

Figure 6.20 obviously indicates the effect of different DB orders to discriminate the small-scale damages, i.e., 3.5mm and 7mm, in DS4 damage scenario after considering the damage threshold. As it can be seen, the damage locations can be clearly discriminated in all of them owing to the appropriate DB order. Nonetheless, the damage at column XI, i.e., sensor location 30, is not as clear as the others in DB2 although there is identical severity in the damage. Besides, the changes in values of RDI_{RWPE}^{UL} at sensor location 30

in each case are not as satisfactory as DB20. In DB11, the drawbacks are the same as DB2 but results are relatively more appropriate. DB15 is not a worthy case for detection of damage locations, but there is still a slight difference between the damage and healthy locations. Most significantly, the preciseness of discriminating the damages cannot be compared with DB20. In DB15, the RDI_{RWPE}^{UL} values for the sensor locations 30 are not distinguished as easily as DB20 especially in incipient stages of the damage. Consequently, Daubechies wavelet function with the order of 20 is selected as the most proper function by GA for damage identification. It means that for wavelet-based methods, the selection of mother wavelet function is mandatory to increase the performance of the algorithm. On the other hand, proper selection of mother wavelet function plays a key role in reducing the false positives and consequently more accurate results can be obtained.

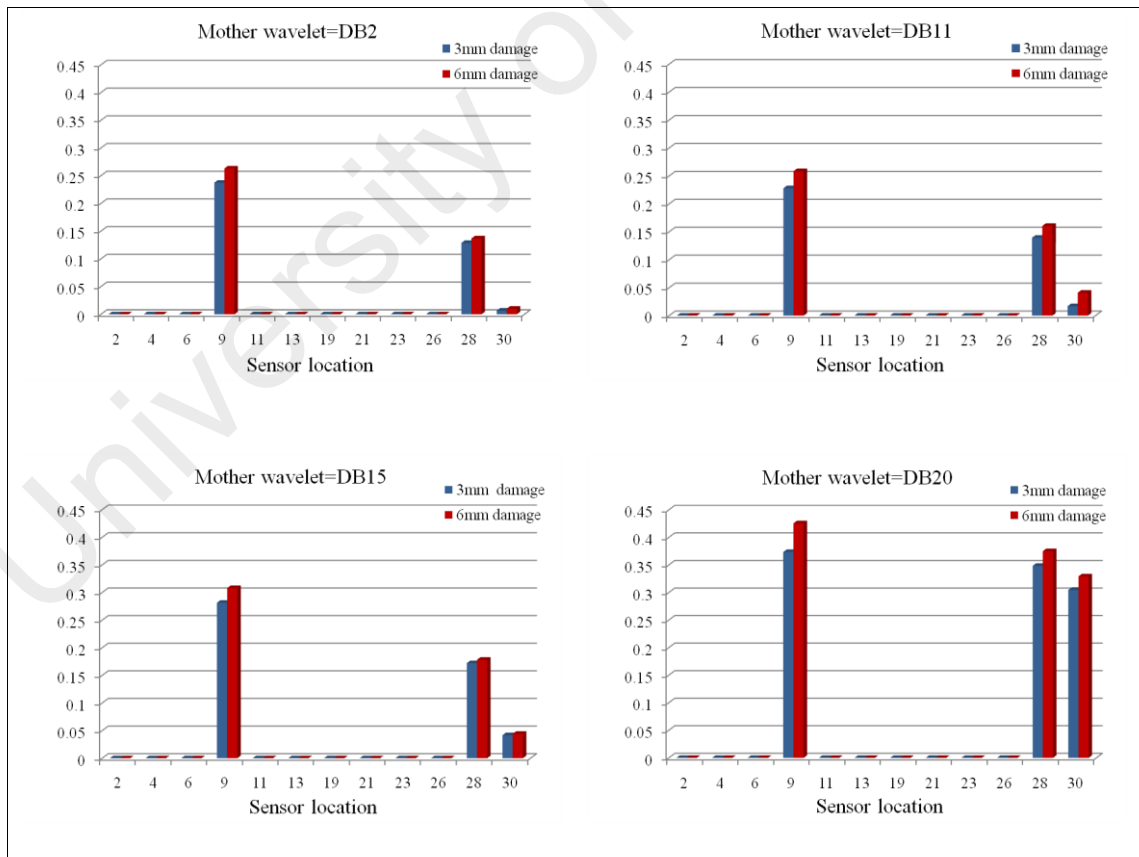


Figure 6.20: Histogram of RDI_{RWPE} in DS4 damage scenario with different DB orders after considering the damage threshold

Based on the results obtained by the proposed algorithm, the following conclusions can be made on the basis of the experimental tests:

(1) the RWPE-based reference-free, RDI_{RWPE} , proved to be damage-sensitive and able to detect damage locations accurately without any reference data from the initially pristine state. In addition, the efficiencies of the proposed algorithm are illustrated for progressive damage, starting from slight damage level to sever level.

(2) another advantage of the proposed algorithm is precise identification of the location of small-scale damages, i.e., 3.5 mm and 7 mm, with appropriate selection of wavelet function and decomposition level by using GA.

(3) under the progressive damage which starts from slight level (~3.5 mm) the RDI_{RWPE} indicated satisfactory sensitivity to the variations of damage level.

(4) with constant number of sensors and increasing number of damage locations, the specificity of RDI_{RWPE} lessens owing to finite wavelet energy. However, increasing the number of sensors is able to resolve this subject in practical applications.

(5) in comparison with another Lamb wave-based technique (Anton et al., 2009; Bagheri et al., 2013), the proposed algorithm does not require the need for identical sensor-to-sensor distance, material properties and spatially uniform structural features among sensors.

6.5 Wavelet-based system identification in a beam structure under flexural vibration

6.5.1 Wavelet-based system identification approach

As in the formulation of the wavelet-based system identification method proposed in Chapter 4 (Section 4.3), the method being proposed includes a three-step procedure: (1) the connection coefficient of the scaling function is used for deriving the responses of displacement and velocity from the acceleration responses; (2) defining the dominant

components based on the relative energies of the WPT components of the acceleration responses; and (3) the least squares error minimization is used iteratively over the dominant components to obtain the best estimation of the stiffness parameters of the model.

6.5.2 Numerical investigation

In this section, the efficiency and accuracy of the wavelet-based system identification method are examined for the beam structure under flexural vibration which is described in Section 5.3.1.1.

6.5.2.1 Evaluation of damage severity in terms of the stiffness parameter

The performance of the algorithm presented in Section 4.3 is illustrated in this section. The proposed method uses the time-history acceleration of the output response. The mass parameters are assumed to be known, since in the numerical simulation, the true structural parameters of the original model are known. The proposed method can be evaluated by studying the accuracy in terms of the percentage loss of stiffness between the identified structural parameters and the true primary values.

To investigate the proposed algorithm based on the WPT, Figure 6.21 depicts the distribution of the relative energies of the acceleration response for the undamaged case by applying DB15 at decomposition level 6. These components provide information about the relative energy associated with the various frequency bands existing in the response signals. Table 6.14 shows the frequency bands of the corresponding WPT components.

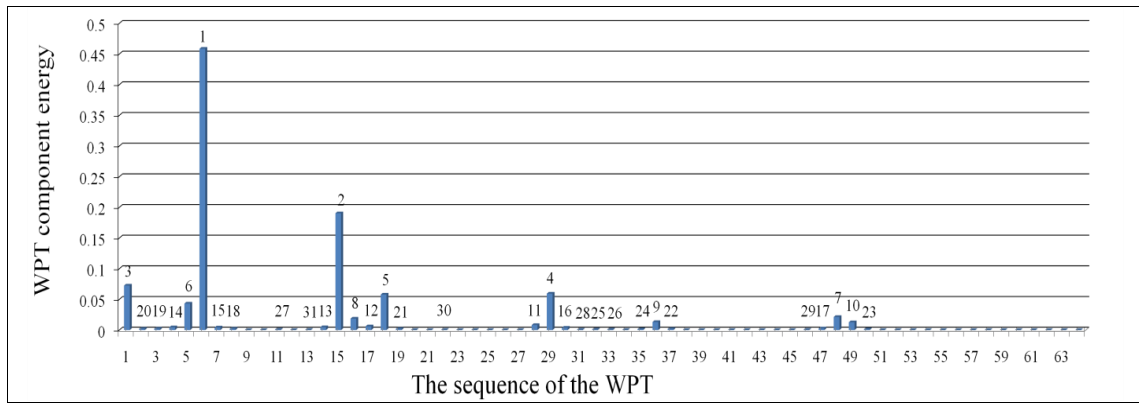


Figure 6.21: The relative energy distribution of the acceleration response for the undamaged case

Table 6.14: Frequency bands of the WPT components at level 6 and modal properties of the undamaged case

The sequence of WPT	1	2	3	...	6	...	15	...	29	...	48	...	64
Frequency bands of WPT components (Hz)	0–16	16–32	32–48	...	80–96	...	224–240	...	448–464	...	752–760	...	1008–1024
Natural frequencies (Hz)	9.29				83.65		232.48		456.03		754.64		
Damping ratios	0.01				0.01		0.025		0.049		0.081		

The Rayleigh model is employed to calculate the damping matrix:

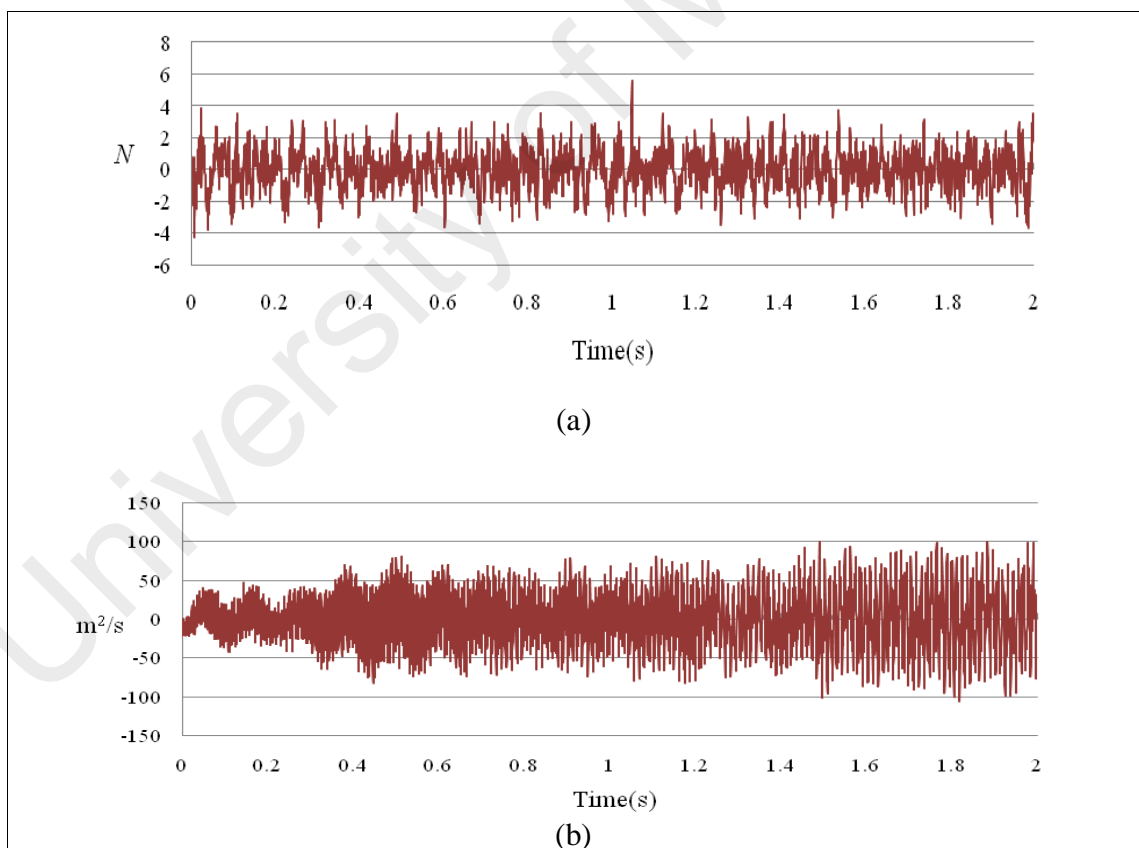
$$C = a_1 K + a_2 M \quad (6.2)$$

where a_1 and a_2 are the mass-proportional and the stiffness-proportional constants, respectively. The two constants of the Rayleigh damping matrix have been chosen so as to have a 1% damping ratio for the frequencies of the first two modes. The modal properties of the model are demonstrated in Table 6.14.

From the distribution of the component energies in Figure 6.21, it can be observed that the sixth WPT component with the frequency band of 80–96 Hz, which includes the natural frequency 83.65 Hz, has the maximum WPT component energy among the others. Consequently, the WPT components that contain the principal frequencies of the signal provide the greatest energy associated with the signal. The dominant components can be obtained by the relative energy distribution over the wavelet components of the system's

acceleration responses, the equations of motion for the system at the given level can be transformed into those in terms of the dominant components.

To identify the stiffness based on the inverse solution of equations of motion of a structural system in the wavelet domain, the input force and response data containing acceleration, velocity, and displacement are required. For this purpose, by using the connection coefficients of the scaling function, as expressed in Chapter 4 (Section 4.3.2), the velocity and displacement are obtained from the measured acceleration responses at location 5 in terms of the DB15. In order to validate the accuracy of the proposed solution method, these velocities and displacements are compared with those obtained from the explicit dynamic analysis conducted using ABAQUS software, as depicted in Figure 6.22.



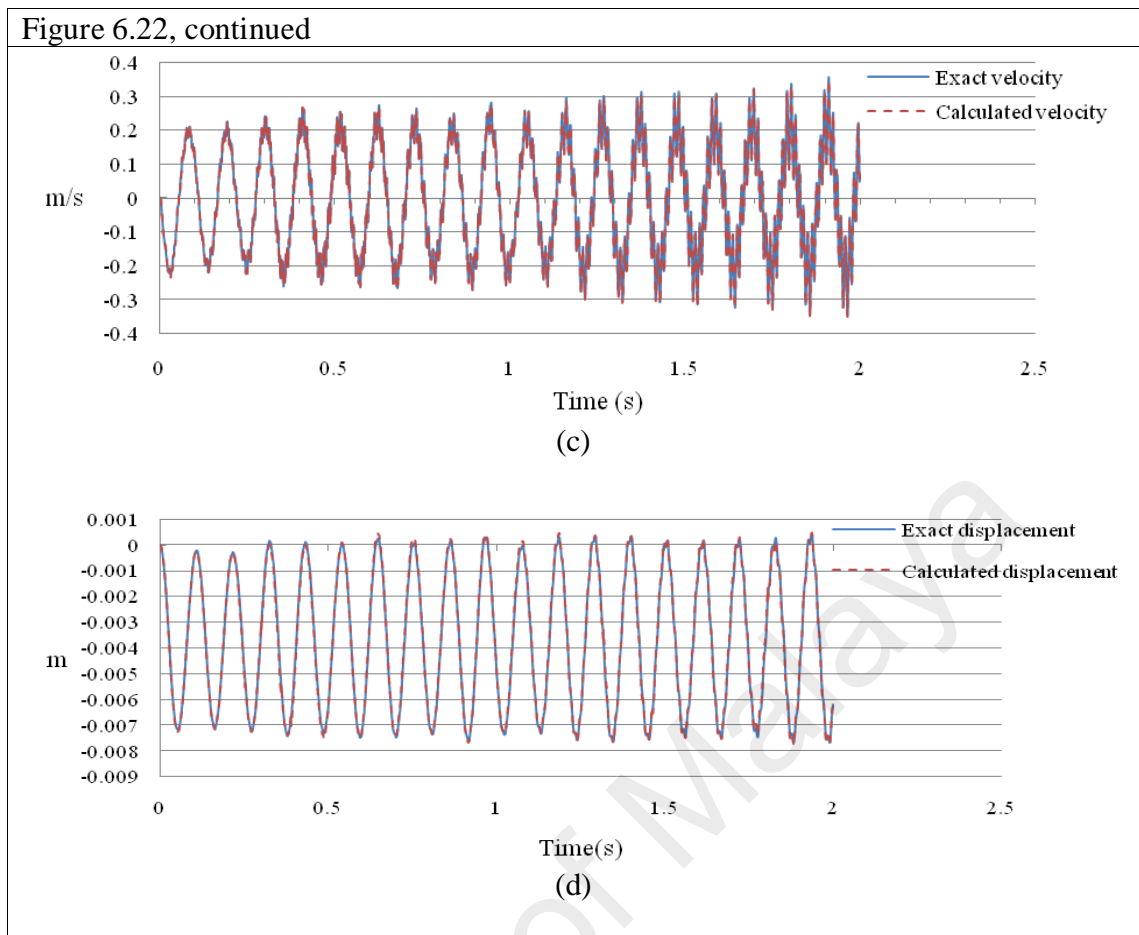


Figure 6.22: Input and response data at location 5 for undamaged case. (a) Input force, (b) exact acceleration responses, (c) comparison of the exact velocity to the calculated velocity, (d) comparison of the exact displacement to the calculated displacement

6.5.2.1.1 Discussion on the Considered Cases

From the above analysis, for Case1 with the single damage scenario, the distribution of relative energy of acceleration responses at decomposition level 6 is demonstrated in Figure 6.23. The best estimation for the structural stiffness at each dominant component, e.g., $D_1=\{6\}$, $D_2=\{6, 15\}$, ..., $D_{10}=\{6, 15, 1, 29, 18, 5, 48, 16, \dots, 36, 49\}$, is obtained by implementing the least squares procedure iteratively over the dominant components. Therefore, the results converge to the exact values. To evaluate the damage severity in terms of the loss of stiffness, as depicted in Figure 6.24, it can be found that the estimated percentage values converge to the exact ones, presented by a red-colored dashed line at each dominant component beginning from D_4 . In addition, the obtained value at dominant component D_{16} in terms of the percentage loss of stiffness is the best and most accurate

among all the dominant components. Moreover, with the increment in dominant components to D_{17} or higher orders, the estimated values degrade, as shown in Figure 6.24. This can be due to the numerical integration error in the derived displacement responses. In addition, the percentages for the loss of stiffness in Case1 between the damaged and undamaged structure, in terms of dominant components D_{15} , D_{16} , and D_{17} , are 0.702977%, 0.702992%, and 0.702577%, respectively. Generally, the accumulation of error in a numerical integration occurs for two reasons. The first source is the local error, which appears at each step of the integration, while the second source is caused by the cumulative effect of previous errors, which stems from many integrations. Since the proposed method depends on the numerical integration procedure, these types of error are unavoidable.

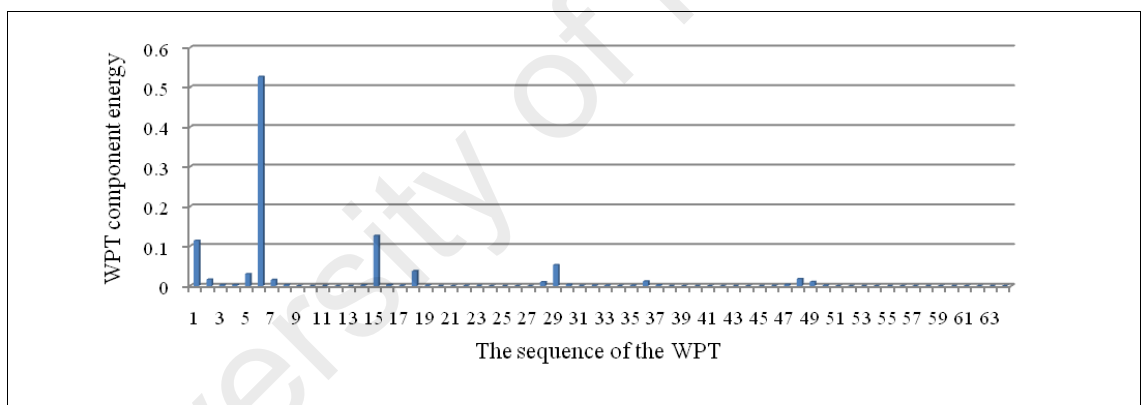


Figure 6.23: The relative energy distribution of the acceleration response for Case 1

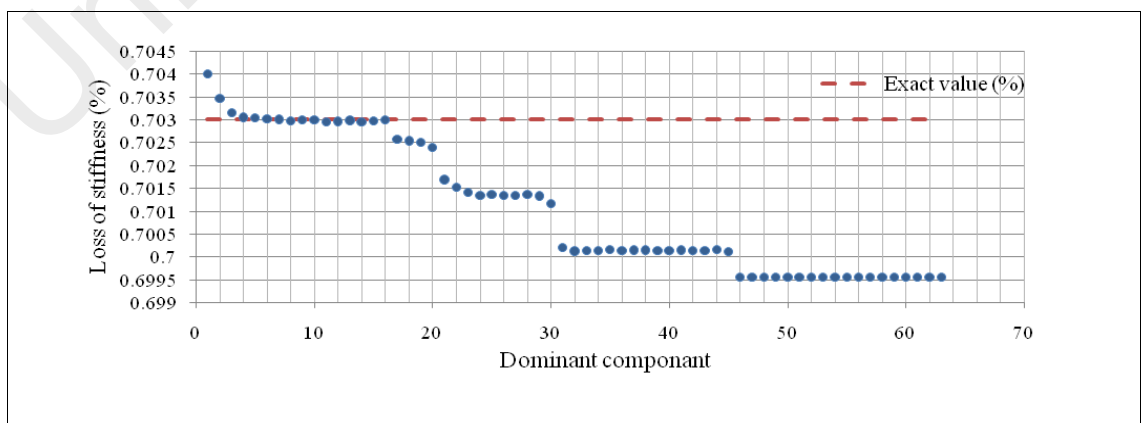


Figure 6.24: Loss of stiffness identification in Case 1

For Case 2, with the two-damage scenario, the relative energy distribution of the acceleration response at decomposition level 6 is depicted in Figure 6.25. To optimize the value of each dominant component, the least squares error minimization is performed. Figure 6.26 shows the convergence of the percentage loss of stiffness for each component together with the exact values. According to Figure 6.26, the onset of convergence takes place around D_4 and the most accurate result is associated with D_{19} , with the appropriate value of 1.4188%. From dominant component D_{20} , with the value of 1.4156% onward, the convergence keeps decreasing.

The above results indicate that the proposed algorithm is effective in evaluating the damage severity in terms of the loss of stiffness. In addition, the results demonstrate that the identification of stiffness parameters can be achieved with less data.

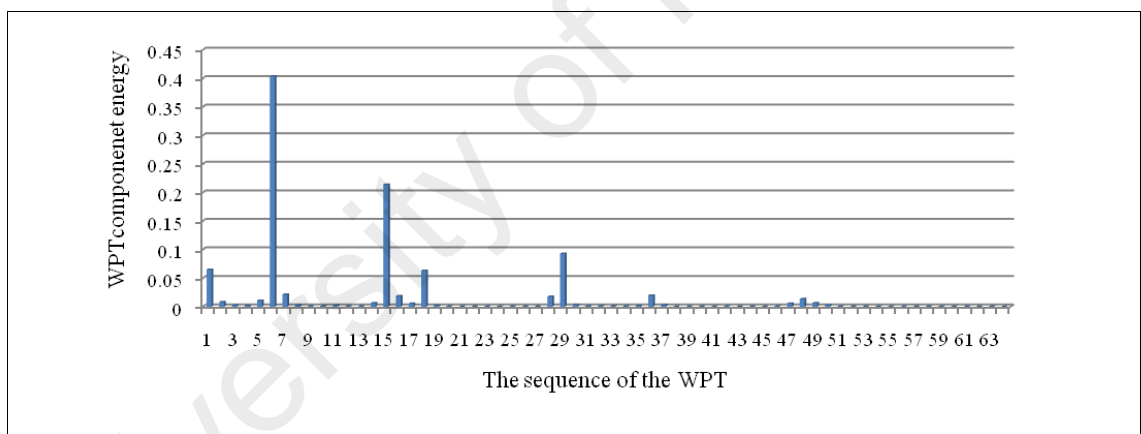


Figure 6.25: The relative energy distribution of acceleration response for Case 2

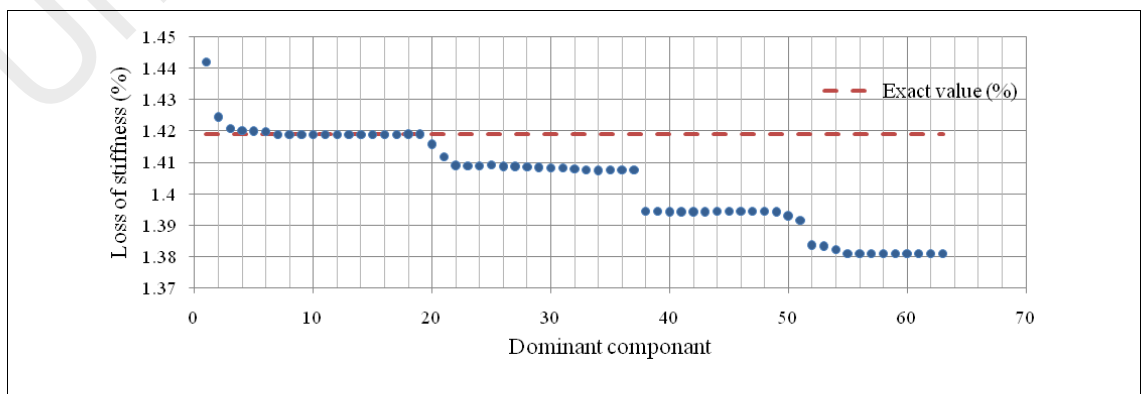


Figure 6.26: Loss of stiffness identification in Case 2

6.5.3 Experimental investigation

To validate the effectiveness of the proposed method, an experimental study is carried out on a steel beam with fixed supports, as described in Section 5.3.1.2. Figure 6.27 shows the input force and output acceleration versus time at location 3 of Case 0 (undamaged). Velocity and displacement are obtained from the acceleration response in terms of DB15 scaling function.

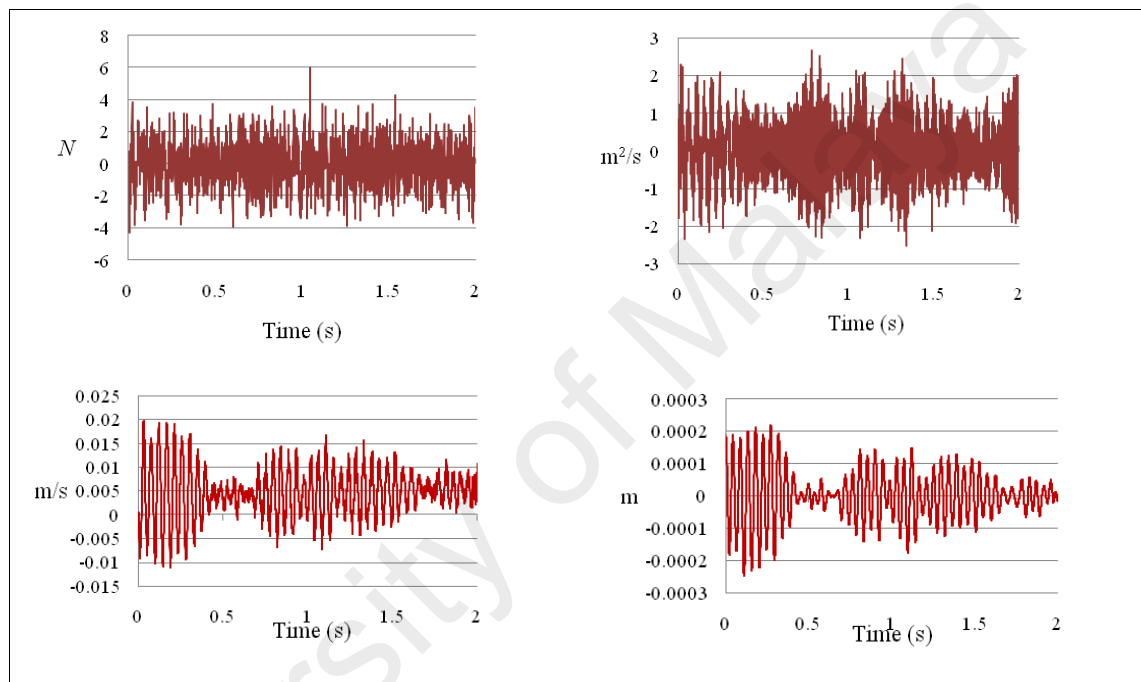


Figure 6.27: Input and structural response data at location 3 of Case 1: (a) force; (b) acceleration; (c) velocity; (d) displacement

6.5.3.1 Experimental Results

The optimization scheme is employed for the identification of damage severity in terms of the loss of stiffness. For this purpose, the relative energy distributions of the acceleration response related to the structural frequencies (Figure 6.28) are achieved by employing DB15 and decomposition level 5 for undamaged beam, as depicted in Figure 6.29. Among these distributions, the WPT component energy of 17 and 1, whose frequency bands are 512–544 Hz and 0–32 Hz, respectively, are larger than the others. Therefore, the dominant components are $D_1 = \{17\}$, $D_2 = \{17, 1\}$, ..., $D_5 = \{17, 1, 16, 10,$

4} and so on. By applying the least squares error minimization in dominant components, the stiffness values corresponding to each dominant component can be obtained.

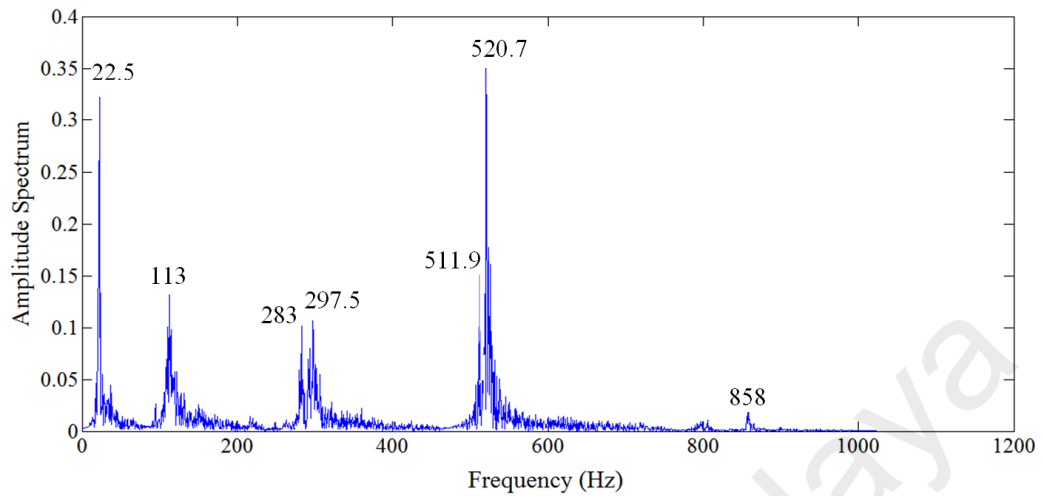


Figure 6.28: Frequency domain response of acceleration response signal at location 3

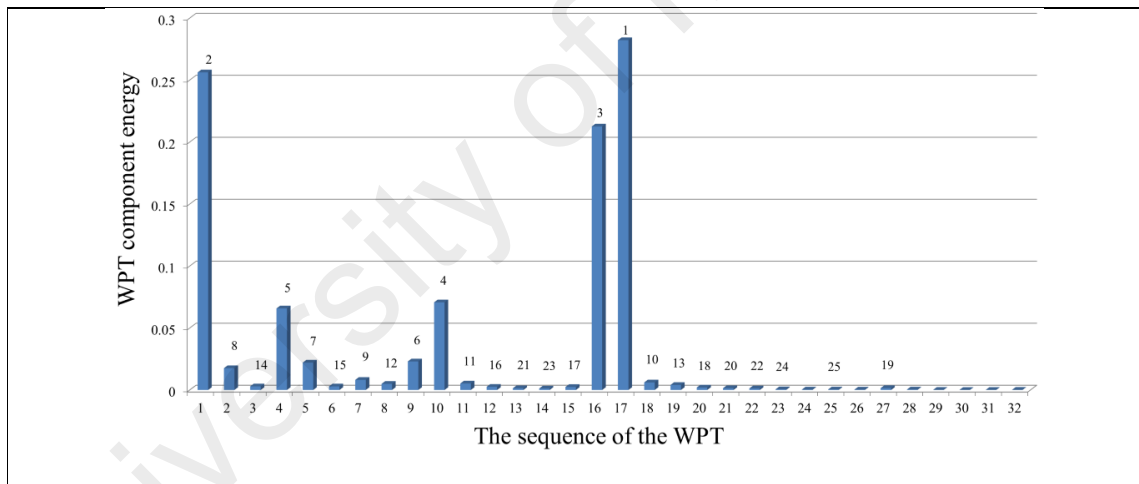


Figure 6.29: The relative energy distribution over the wavelet packet components at level 5 for undamaged beam

With respect to the accuracy of the identification results, Figure 6.30 shows the percentage loss of stiffness in each dominant component for Case 1. It appears that the obtained values have converged at three regions, as illustrated in Figure 6.30. Based on the numerical output, the best and appropriate results can be found in the first converged region, whereas in the second and third regions, more uncertainty is included due to the inclusion of higher-order dominant components. This is because the large input and

output data are considered to be redundant; therefore, it is possible to obtain accurate results by applying the dominant components instead of the full size of data. The percentage loss of stiffness in the first convergence region, in terms of each dominant component, is presented in Table 6.15. In the first region, the estimated values begin to converge at D_5 and deviate from D_{13} onward.

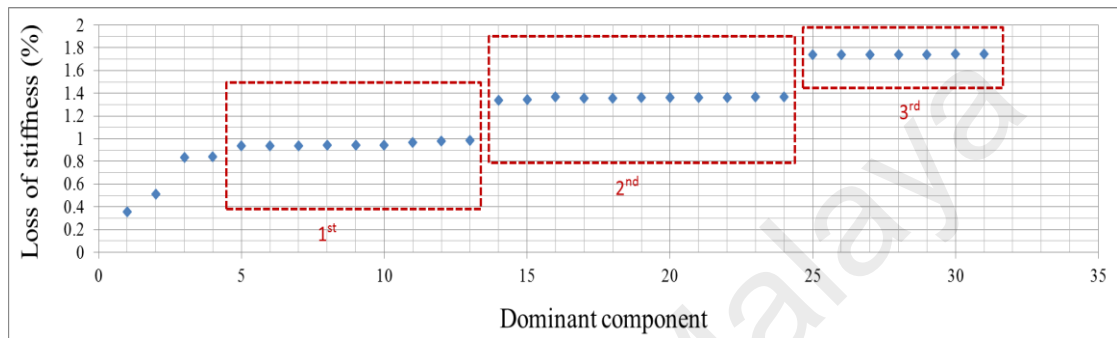


Figure 6.30: Loss of stiffness identification in each dominant component in Case 1

In Case 2, with two damage scenarios, the percentage loss of stiffness in each dominant component is shown in Figure 6.31. The first convergence region with an appropriate result has been specified with respect to the accuracy of the identification parameters. The estimated results start to converge at dominant component D_5 . In addition, the obtained percentage loss of stiffness corresponding to D_{15} is found to be the best result with the highest possible precision in the indicated convergence region, as given in Table 6.15. Other higher-order dominant components, e.g., from D_{16} onward, are reduced.

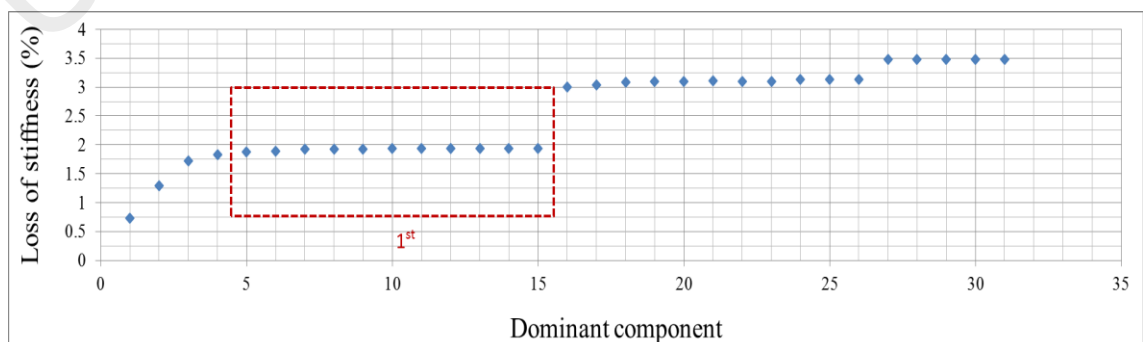


Figure 6.31: Loss of stiffness identification in each dominant component in Case 2

Table 6.15: Estimated values of loss of stiffness in the first convergence region

Dominant Component	Loss of Stiffness (%)	
	Case 1	Case 2
D ₅	0.938	1.883
D ₆	0.939	1.889
D ₇	0.939	1.924
D ₈	0.944	1.924
D ₉	0.942	1.925
D ₁₀	0.945	1.933
D ₁₁	0.966	1.936
D ₁₂	0.978	1.939
D ₁₃	0.986	1.941
D ₁₄	1.336	1.943
D ₁₅	1.342	1.943

Based on the above results obtained by the proposed method it can be deduce that, the proposed system identification based on the wavelet multiresolution analysis can identify the severity of damage by investigating the accuracy of the result in terms of the loss of stiffness in the model between the parameters obtained before and after the damage occurrence. It is noteworthy that in real applications the implementation of the least squares error minimization method is not required from the first dominant component. In addition, to avoid time-consuming iterative computations for convergence and in order to obtain an accurate result with less data, the least squares error minimization can be performed across the dominant components until the first convergence region is achieved.

6.6 Wavelet-based system identification algorithm for three-story building model

6.6.1 Numerical results

The performance and robustness of the proposed method in identifying the structural parameter such as stiffness and damping coefficients is demonstrated via a numerical study on the shear beam building model, as described in Section 5.3.2.1. The proposed method can be evaluated by comparing the accuracy in terms of percent relative error (PRE) between the identified structural parameters and their exact values. Also, the optimal Daubechies wavelets from the orthogonal wavelets family are chosen by GA

through minimizing the fitness function, in the search range of DB1 to DB31. Table 6.16 explore the parameters of the GA exploited in proposed system identification algorithm.

Table 6.16: GA parameters used in wavelet-based system identification algorithm

Number of generation	100
Population	30
Selection function	Tournament
Fitness normalization	Rank
Crossover	Pc=0.7, Single-point, uniform
Mutation	Pm=0.1, Uniform

6.6.1.1 Evaluation of original numerical model

To investigate the proposed algorithm based on the WPT in the original model, Figure 6.32 shows the time histories of the structural acceleration at each floor along y-direction. Distribution of the relative energy is derived from the acceleration response of each floor by using DB15 with 9 levels of decomposition, as indicated in Figure 6.33. These components provide information about the relative energy associated with the various frequency bands existing in the response signals.

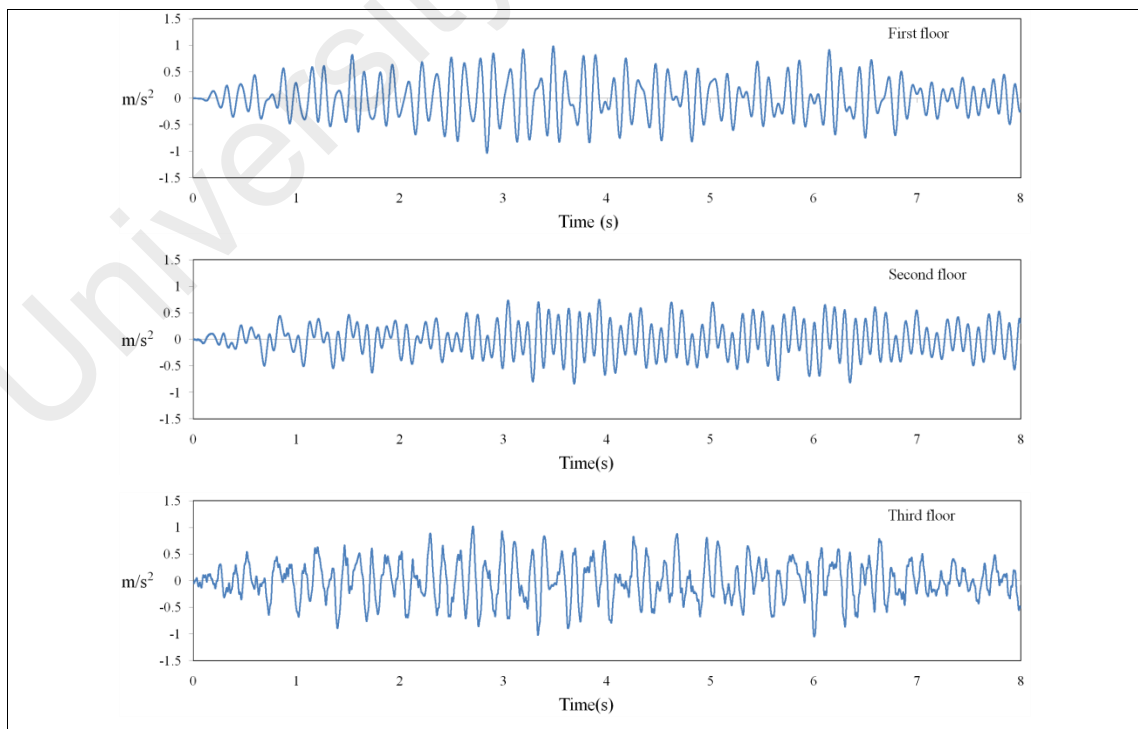


Figure 6.32: Acceleration responses at each floor of the original model along y-direction

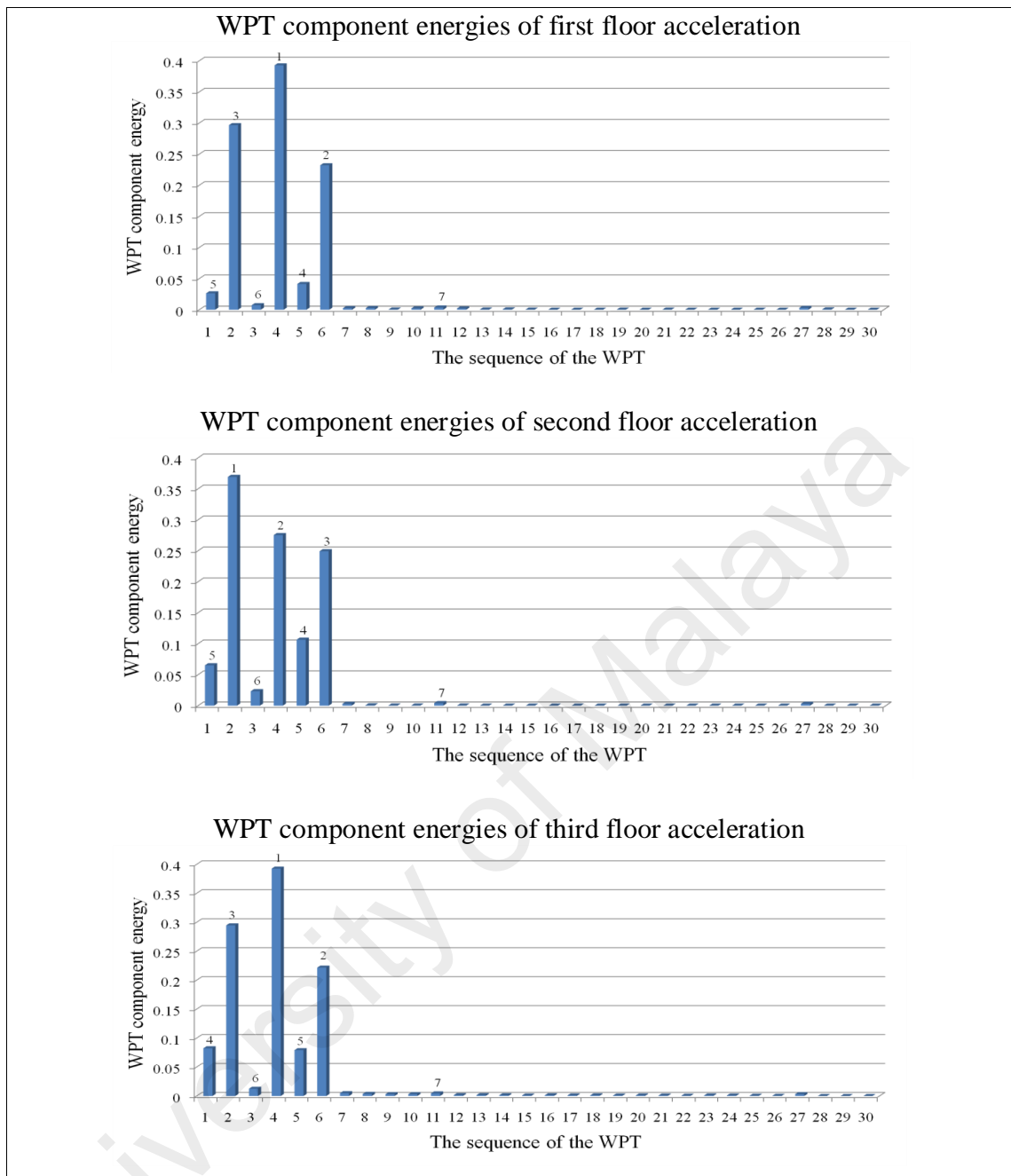


Figure 6.33: The relative energy distribution of acceleration response at decomposition level 9 for the original model

From this distribution of component energies, it can be observed that: (1) for acceleration responses of first and third floor, the relative energy of the fourth WPT component, including the natural frequency (7.4814 Hz), is larger than other WPT components; (2) WPT component energy of the second WPT component at the second floor, encompassing the lowest natural frequency (2.6986 Hz), has a significant increase compared with other floors whereas the WPT component energy of the second WPT

component of the third floor acceleration response is similar to that of the second WPT component of the first floor acceleration response; (3) acceleration responses of all floors associated with the first, third and fifth WPT components, whose frequency bands are [0-2 Hz], [4-6 Hz] and [8-10 Hz], respectively, have some (relative) energy, even though they are not related to the structural frequencies. This stems from the fact that the acceleration responses at all floors are affected by the forces whose dominant frequency components are between 0 and 70 Hz.

As shown in Figure 6.34(a), the average relative energy distribution can be derived from the relative energy distribution of the WPT components of the system's acceleration response at each floor with the sequence numbers of 1 to 30 among the 2^9 WPT components. Therefore, the dominant components can be adjusted based on the average relative energy distribution, e.g., $D_1=\{4\}$, $D_2=\{4, 2\}$, ..., $D_7=\{4, 2, 6, 5, 1, 3, 11\}$, and so on. The best estimation for the structural stiffness at each dominant component is obtained by performing the least squares procedure iteratively over the dominant components, depicted in Figure 6.34(b). It can be observed that for each stiffness parameter, the estimated value at each dominant component converges to the correct value starting from dominant component D_6 , with a very close estimation to the corresponding exact values. In particular, for D_{63} , the identified and the exact stiffness values of the first floor are 30358.92N/m and 30348.29N/m, respectively, and the corresponding PRE is 0.035%. Similarly, the PREs of the identified stiffness values of the second and third floors are 0.02% and 0.01%, respectively.

In addition, based on the identified results for each stiffness parameter, as shown in Figure 6.34(b), the estimated values corresponding to the dominant component D_{63} are the most accurate ones among other dominant components. From dominant component D_{64} onward, the convergence of the estimated values degrades, which is due to the numerical integration error of the derived displacement responses and inclusion of WPT

components of the 64th WPT component energy. This phenomenon happened for the other higher order dominant components accordingly.

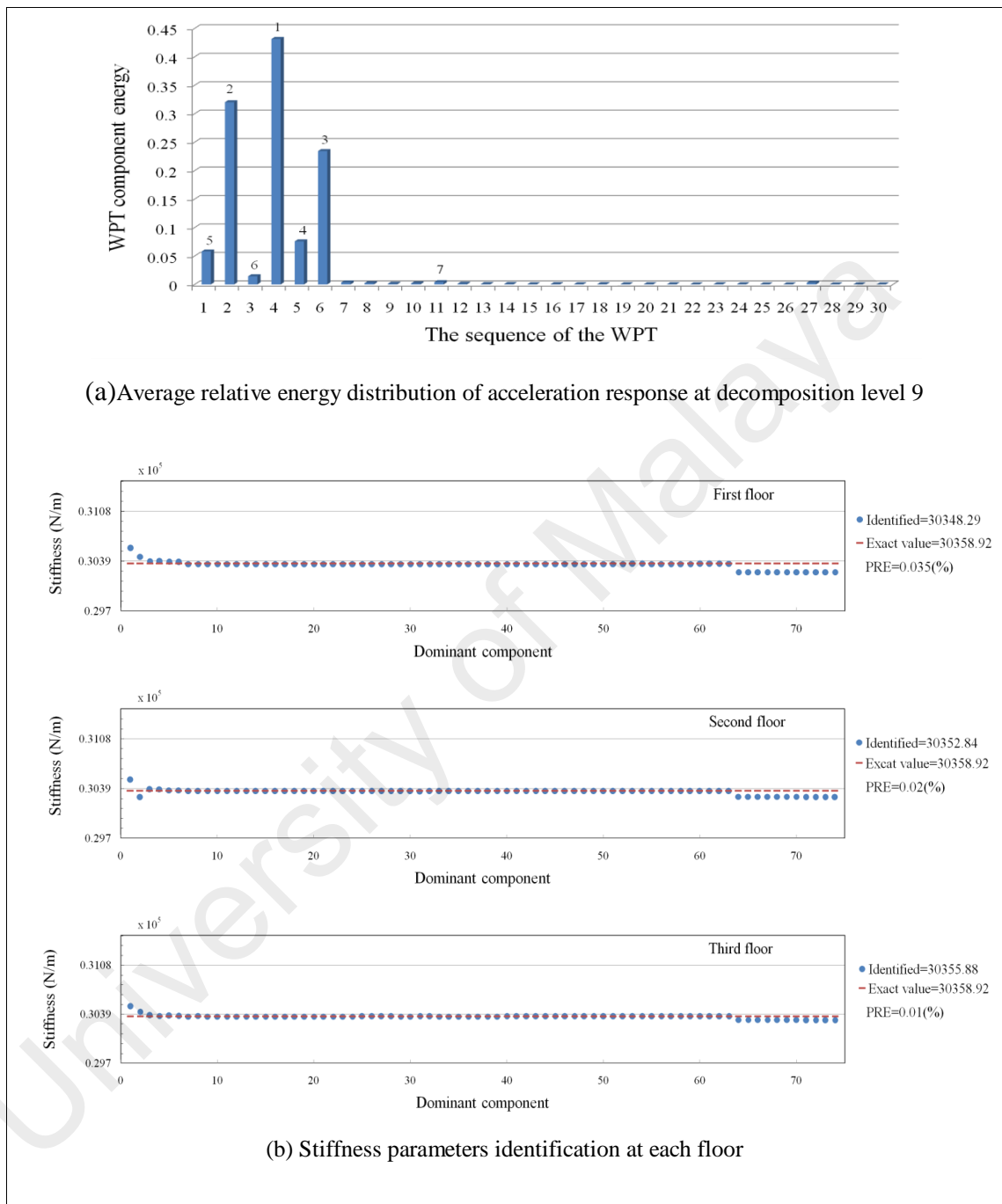


Figure 6.34: Identified results for original numerical model in y-direction

It should be noted that the total error in a numerical integration is a combination of errors which have roots in two causes. The first one is the local error that occurs at the each integration step, while the second cause arises from the cumulative error takes place due to repetition of integration over the past errors. Thus, these kinds of errors are unavoidable

in numerical integration process. For instance, Figure 6.35 shows the difference (error) between the exact and derived displacement responses at the first floor. It can be seen that the difference gets larger as the numerical integration proceeds over time. Note that this deviation is also observed in the derived displacement responses at other floors. For the velocities, such errors are not limited to a specific WPT component.

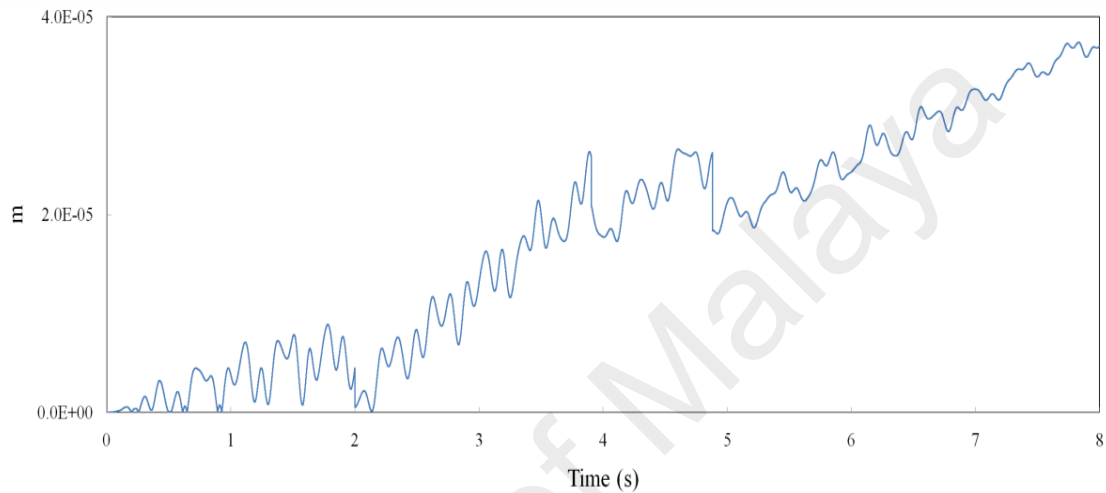


Figure 6.35: The difference (error) between the exact and derived displacement responses at the first floor.

In order to examine the proposed method on more challenging parameters, identification of damping and stiffness parameters is carried out on the original model. Figure 6.36 presents the corresponding PREs of the identified values in terms of damping and stiffness parameters. The PREs of the identified damping and stiffness parameters in the converged line are between 15 to 19% and 11 to 15%, respectively. Estimated values converge to the correct ones at around D_9 while due to inclusion of the components of the first WPT components, deviation at D_{50} and higher orders has taken place.

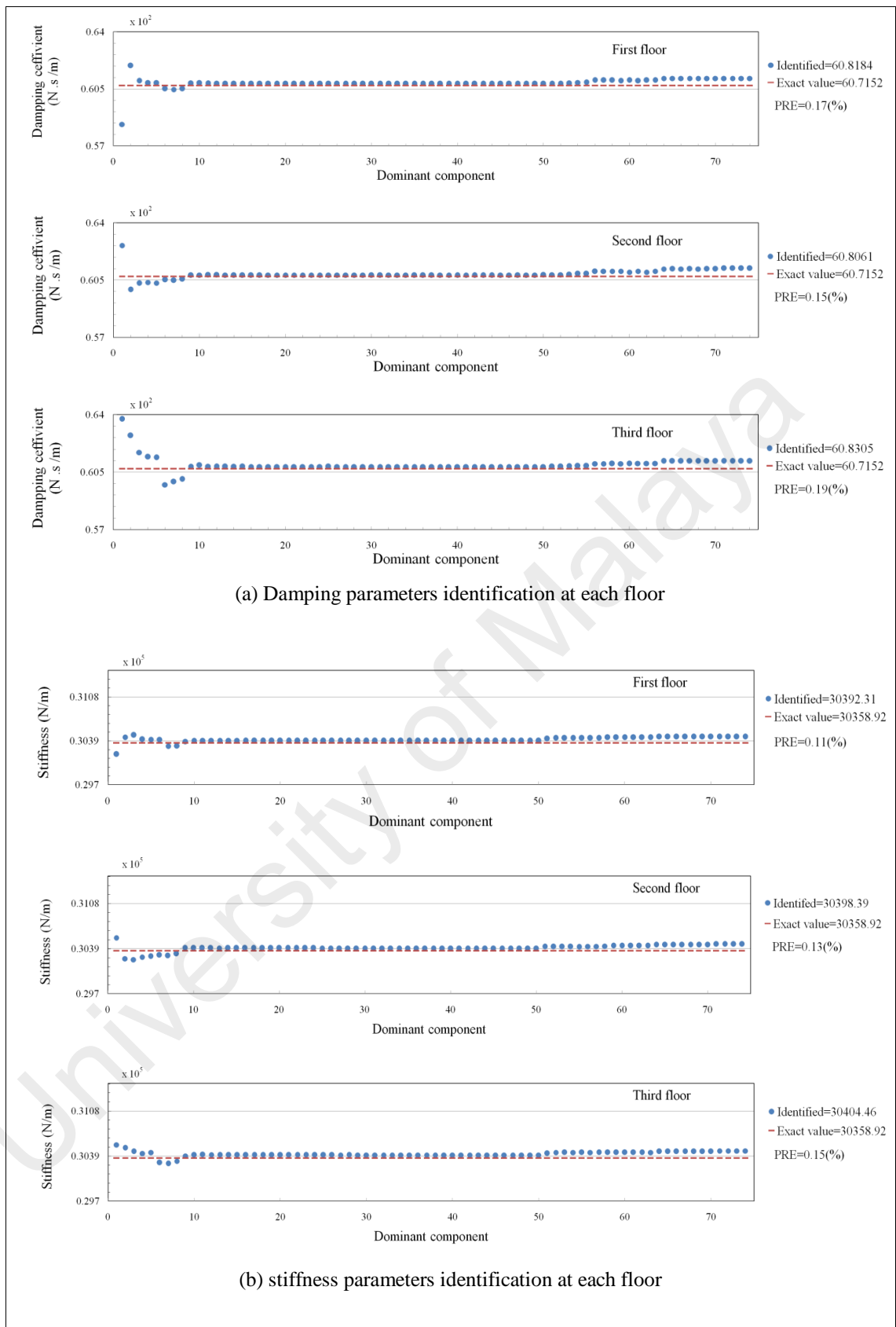
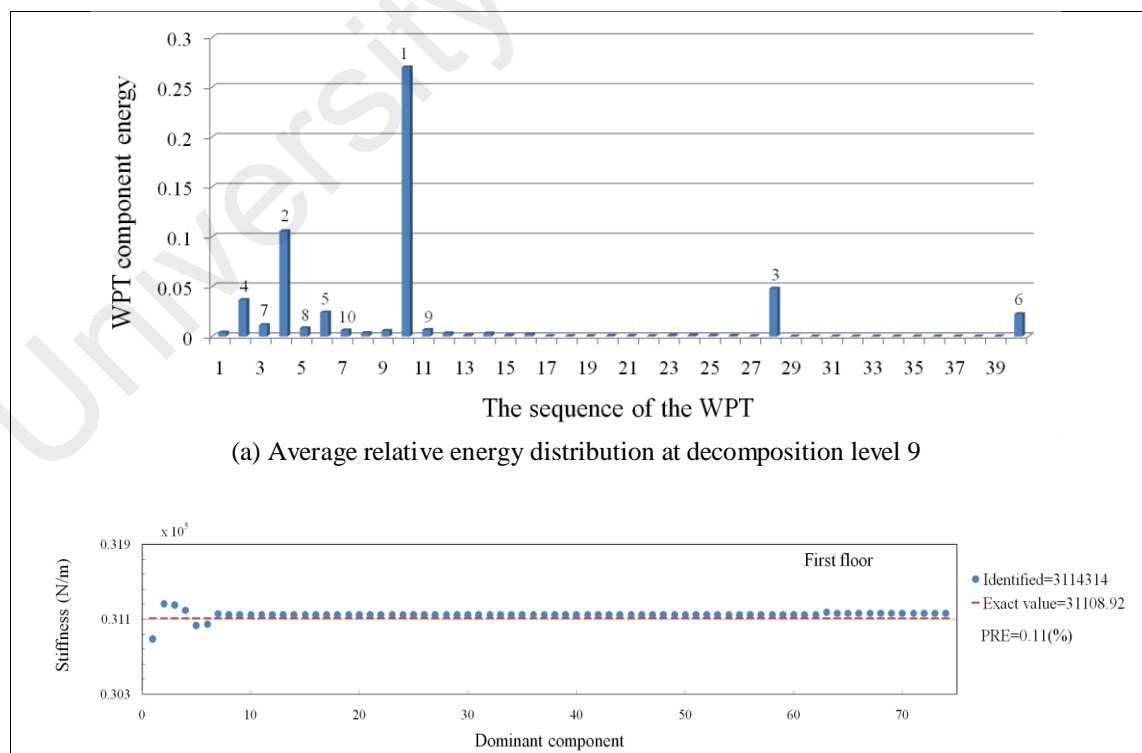


Figure 6.36: Identified results for original numerical model

By Comparing between the identified results, shown in Figures 6.34 and 6.36, reveals that the accuracy of the identified results in terms of damping and stiffness parameters is lower than that in terms of stiffness parameters, but still is very close to exact values.

In order to determine the stiffness parameters of the original model in x-direction, the average relative energy distribution is obtained from the WPT components with sequence numbers of 1 to 40, at decomposition level 9 of the acceleration responses, as depicted in Figure 6.37(a). The stiffness parameters can be estimated at each dominant component by performing the least squares error minimization over the dominant components. As shown in Figure 6.37(b), it seems that the estimated values start to converge at dominant component D₇. The PREs of the identified values, in terms of the stiffness parameter, for the first, second and third story are 0.05%, 0.03% and 0.02%, respectively. Note that similar to the results obtained in Y-direction, the PREs are all under 0.2%, confirming that the proposed method is successful in identifying the unknown structural parameters.



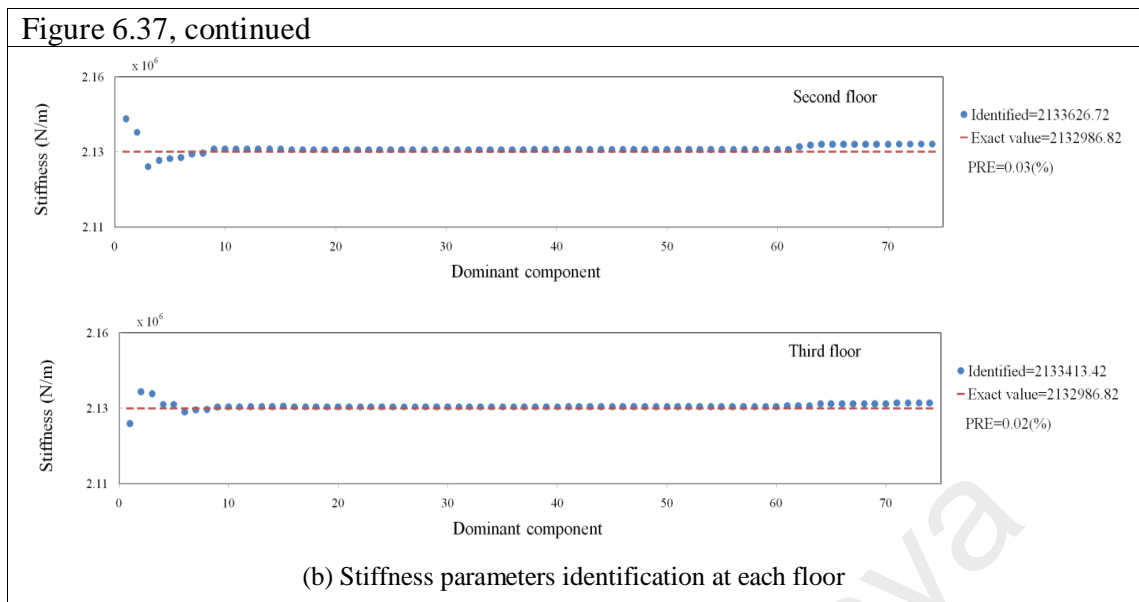


Figure 6.37: Identified results for original numerical model in x-direction

6.6.1.2 Case1: Damage in first story (linear model)

In this section, the shear building structure is subjected to DC1. DC1 is conducted through applying auxiliary structure which is constructed by adding extra spring with stiffness of 750 N/m to the mass center of the first floor of the original model along the y direction, shown in Figure 6.38, Gladwell (2004).

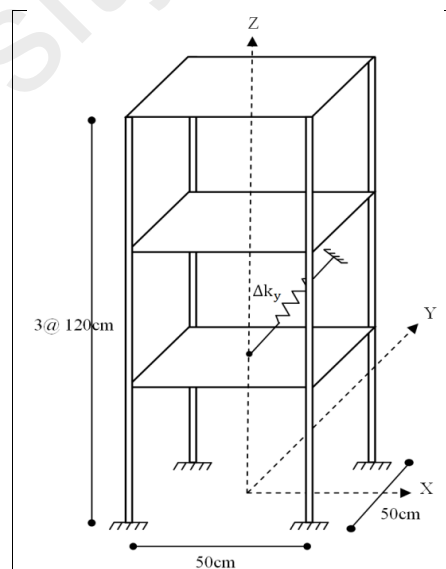


Figure 6.38: The proposed auxiliary structure at the first floor in y-direction

To consider the proposed method for the stiffness identification process, based on the WPT components, by running the GA, DB 15 has been selected as the best value for

Daubichies order. Figure 6.39(a) and (b) show the average relative energy distribution at decomposition level 9 of acceleration responses, and the corresponding PREs for each stiffness parameter, respectively. Except for the first floor, the PREs in other floors, in terms of the stiffness parameters, are less than 0.10%.

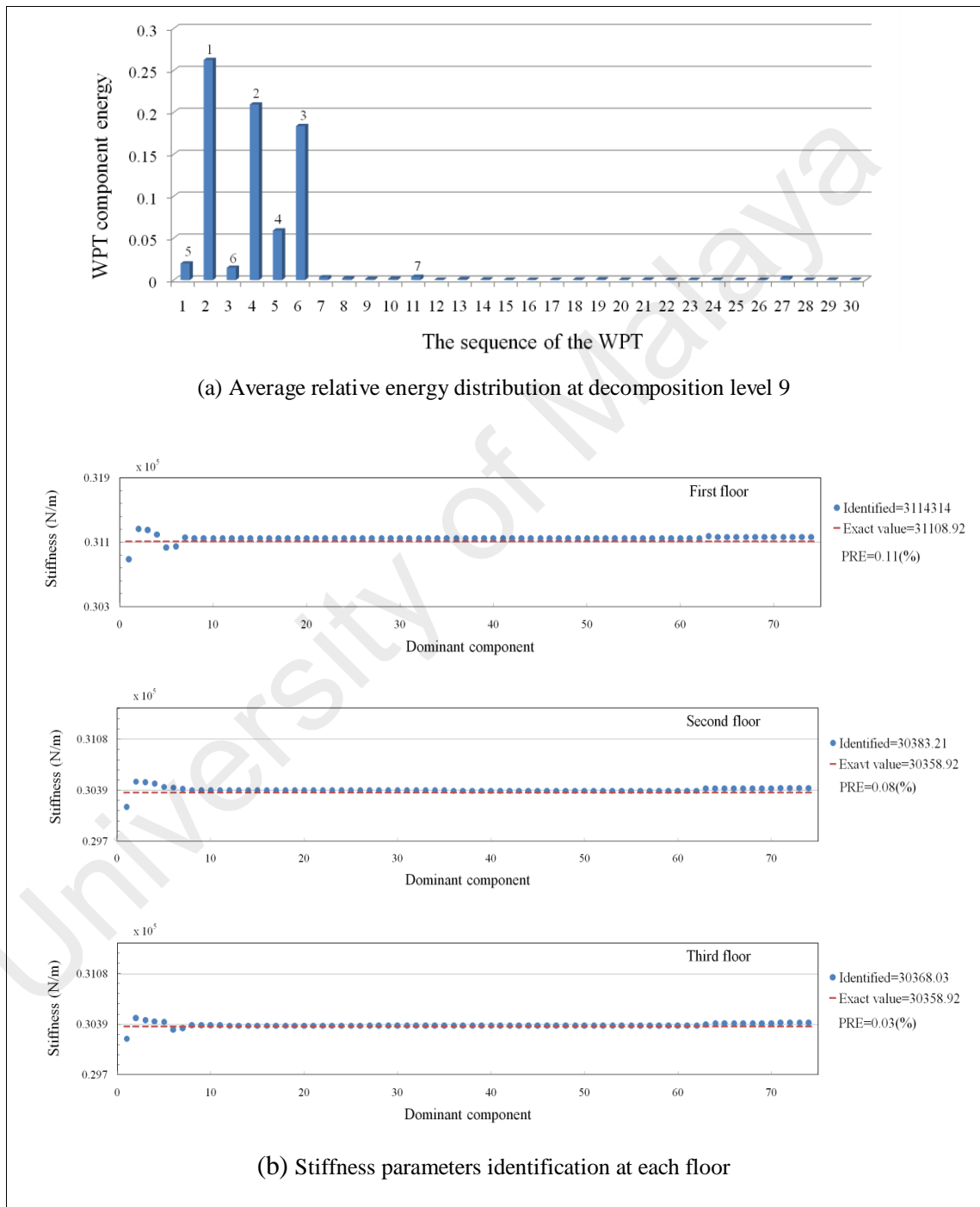


Figure 6.39: Identified results for DC1

6.6.1.3 Case2: Damage in first and second stories (linear model)

In order to examine the proposed method on more challenging examples, two auxiliary structure systems are generated by adding extra springs along the y-direction in first and second floor with stiffness values of 500N/m and 750 N/m, respectively, as shown in Figure 6.40.

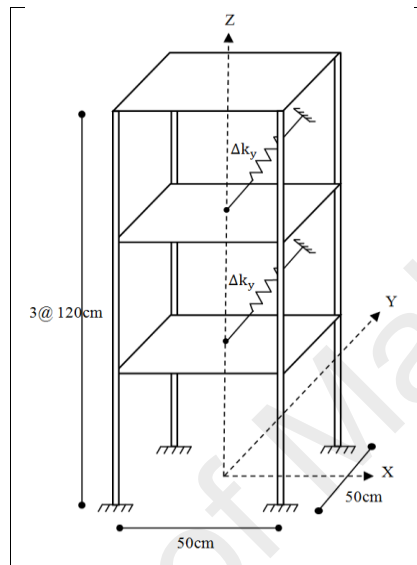
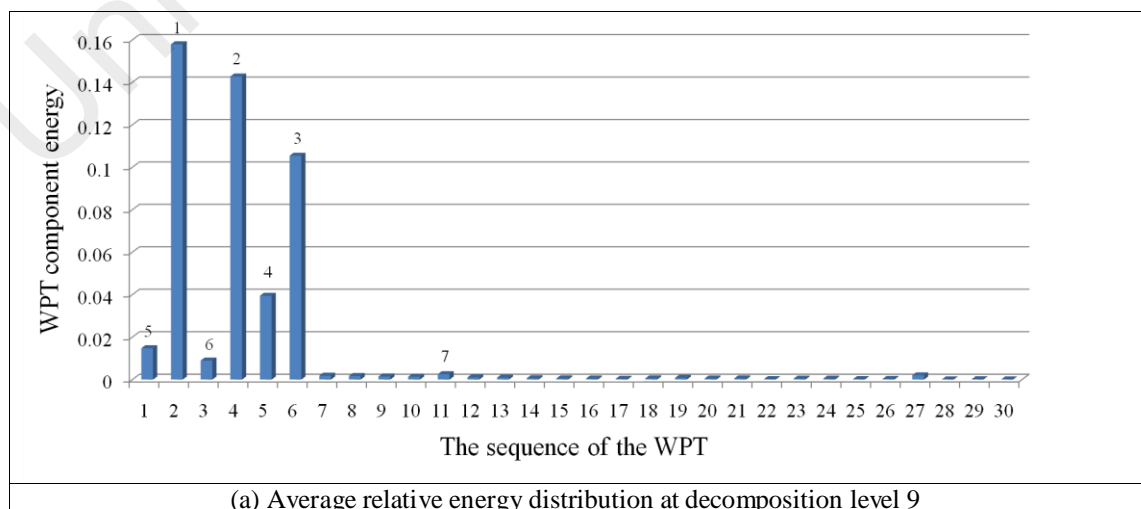


Figure 6.40: The proposed auxiliary structure at first and second floor in y-direction

Figures 6.41(a) and (b) present the average relative energy distribution of the WPT components with Daubechies order 20 at decomposition level 9 for the acceleration responses in y-direction, and the corresponding PREs of the identified values in terms of stiffness parameters, respectively.



(a) Average relative energy distribution at decomposition level 9

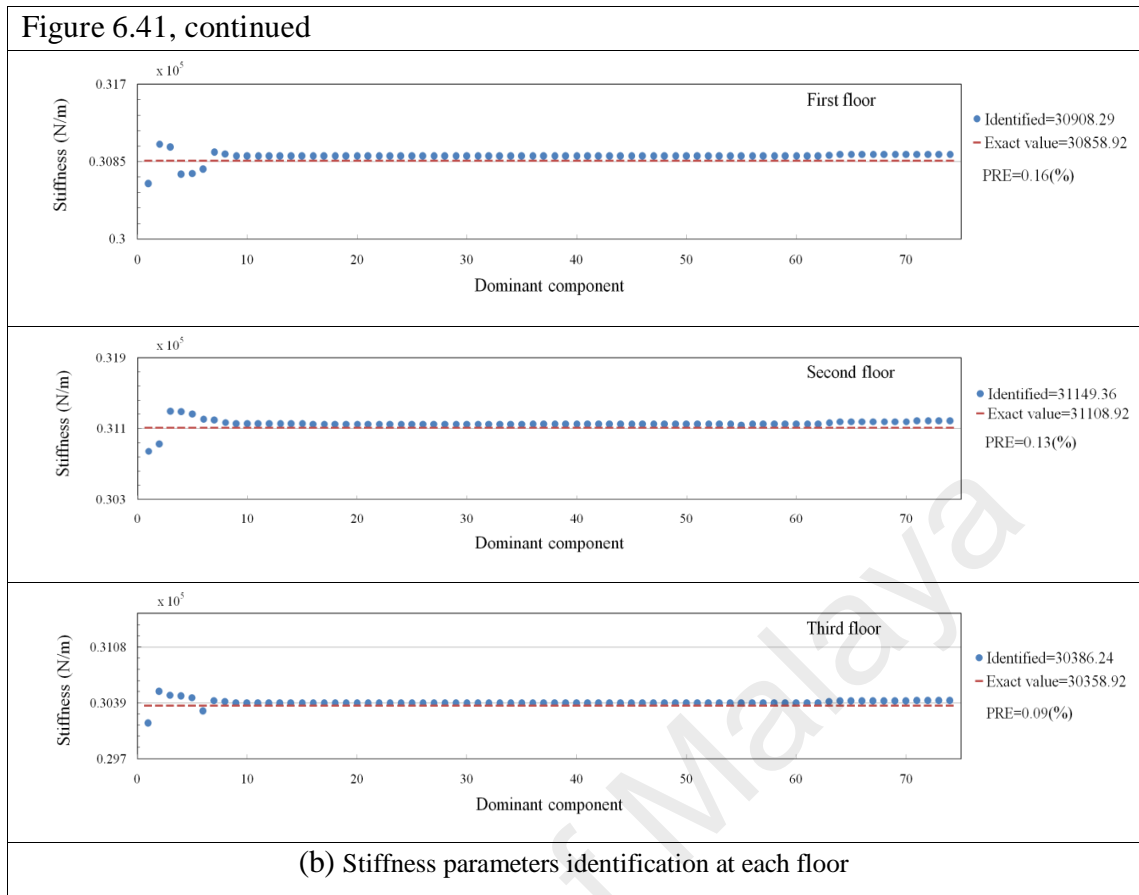


Figure 6.41: Identified results for DC2

A comparison between the obtained results of DC1, shown in Figure 6.39 and DC2, depicted in Figure 6.41, and those gathered from original model, demonstrated in Figure 6.34, reveals that first in terms of accuracy, the PREs of the estimated stiffness value values obtained from the considered DCs are generally slightly higher those of the original model, but still are very low. Second, for the original model, the convergence seems to start at the sixth dominant component D_6 , while for DC1 and DC2, it happens to start at the dominant components D_8 and D_9 , respectively. This is related to the relative energy of the WPT components on the dominant components, required to converge. On the other hand, for the original model, the WPT components on the sixth dominant component D_6 has sufficiently large relative energy (i.e., 56.24%) to converge, while for the DC1 and DC2, the relative energies (i.e., 43.19% and 39.19% , respectively) of the WPT components on the dominant components D_6 are not sufficient. Note that for DC1, the relative energy of the WPT components on D_8 is 53.26% and the relative energy of the

WPT components, in DC2, on D_9 is 51.38%. In short, depending on the stiffness variation, the relative energy of the WPT components on the dominant component needed for convergence is different. Similar procedure can be used when auxiliary structures are placed in other directions.

6.6.1.4 Case3: Damage in third story (bilinear model)

To investigate the efficiency of the proposed method in the state estimation and model identification for the scenario in which the nonlinearity behavior occurs in a frame structure, the third story is assumed to be soft, and the drift of this story exceeds the yield displacement during the excitation, while other stories remain within the elastic stage.

The load-deformation rules of the model are depicted in Figure 6.42.

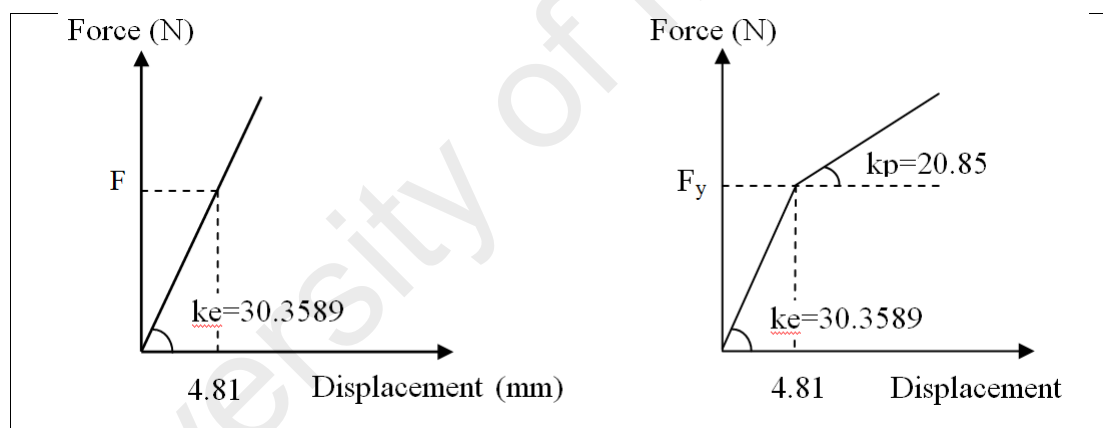


Figure 6.42: load-deformation rules. (a) Linear model, (b) bilinear model

In DC3, the damping coefficient is assumed to be constant during excitation. The wavelet function DB15 is applied in each time step, and the scaling functions belong to the seventh lower-resolution subspaces are employed to approximate the tangent stiffness and the hysteresis-restoring force curves at each story of the structure. The matrix equation $P_i^T P_i \Theta_i = P_i^T A_i$ is solved by the Choleski decomposition to get Θ_i .

Figure 6.43 shows the simulated and identified restoring forces at each story of the structure. The corresponding estimated errors λ_i of identified values for the first, second and third stories are 0.28%, 0.49% and 1.48%, respectively. In addition, Figure 6.44

presents the corresponding simulated and identified restoring force-drift hysteresis curves. It can be seen that restoring force-drift relationship of third floor exhibits hysteresis curves while the response of other stories remain within the elastic range indicating that the proposed approach can estimate the tangent stiffness and hysteresis curves at each story of the structure remarkably well, even in a case where there are considerable material nonlinearities.

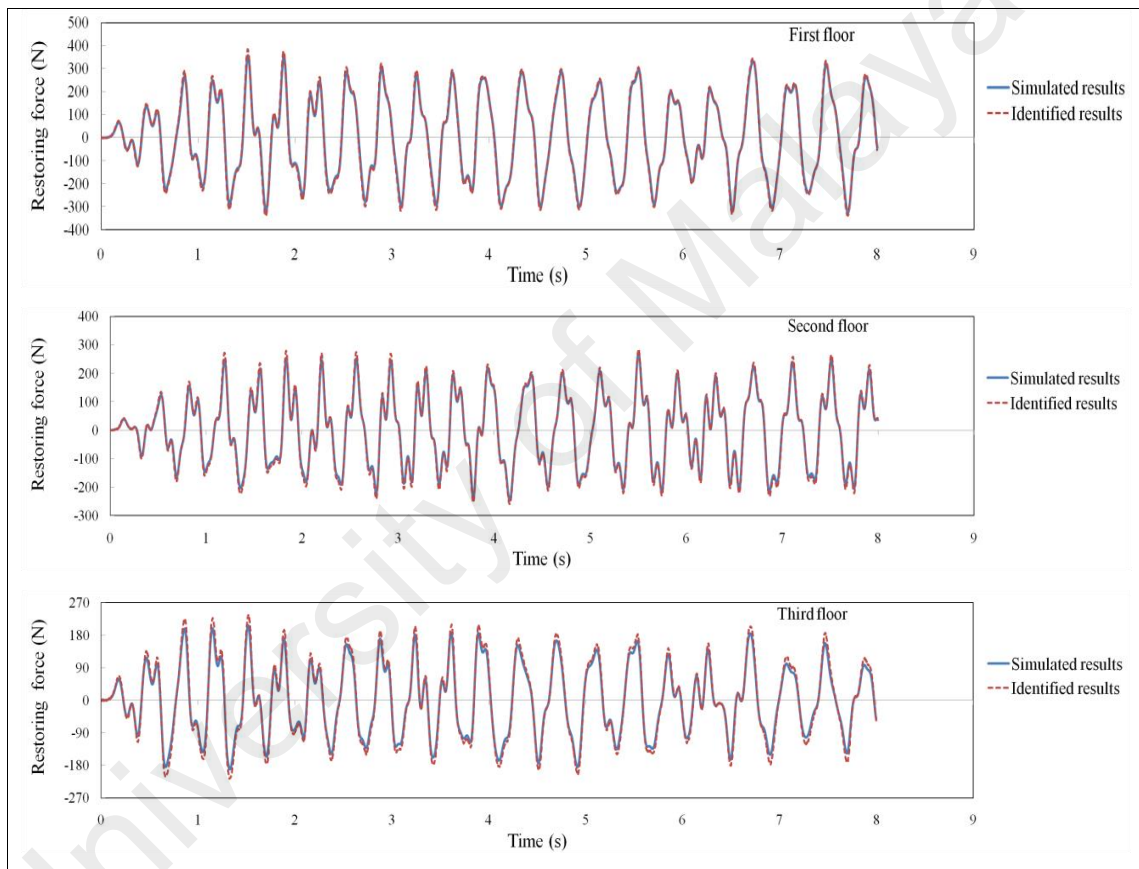


Figure 6.43: Simulated and identified restoring force responses of the structure in which the third floor is soft.

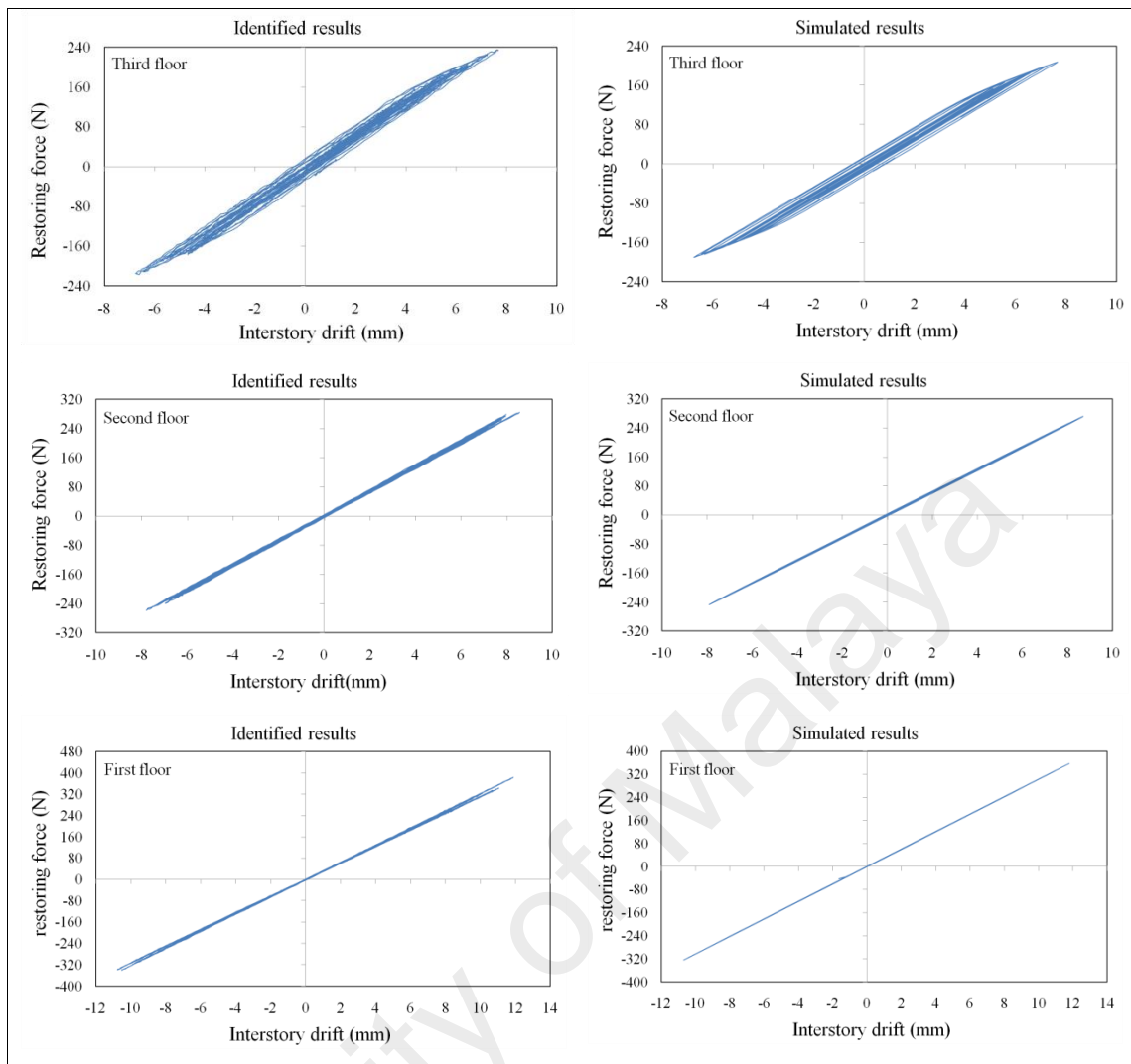


Figure 6.44: Simulated and identified restoring force-drift hysteresis curves

6.6.1.5 Effect of measurement noise

Presence of noise is unavoidable at real measurements, that is why to investigate the effect of measurement noise on performance of the proposed method in the system identification different levels of noise are considered by adding Gaussian white noise signals corresponding to different SNR in the acceleration responses of the original model. In this investigation, values of SNR of the noise signals equal to 2, 5, and 10 dB will be considered.

Figures 6.45-6.47 depict distributions of average relative energy at decomposition level 9, and the corresponding identification results associated with various considered levels

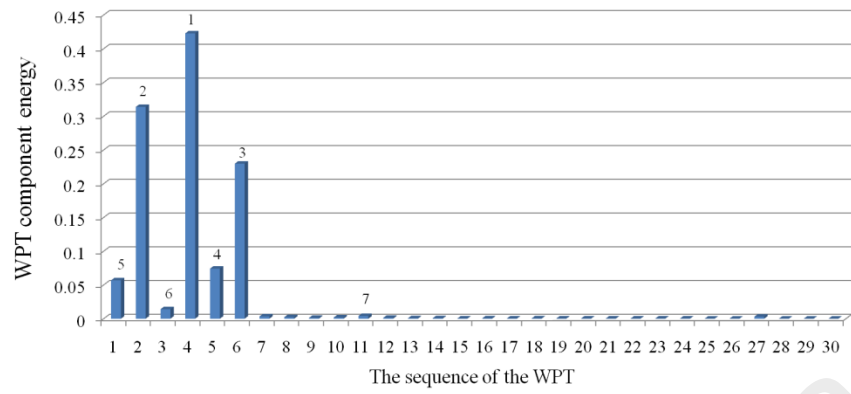
of noise. From Figures 6.34(a) and 6.45(a)-6.47(a), it can be observed that the distribution of average relative energies remain unchanged regardless of the level of noise.

In terms of accuracy of the identification results, as depicted in Figures 6.45-6.47(b), a larger value of PRE is obtained when noise is involved in comparison with the noiseless case shown in Figure 6.34(b). For instance, values of the PREs at the first floor for the noiseless case and for three levels of noise with SNR equal to 2, 5, and 10 dB are 0.035%, 2.68%, 0.91%, and 0.31%, respectively. PRE results of the identified linear stiffness parameters in other cases with different levels of noise are also obtained and summarized in Table 6.17.

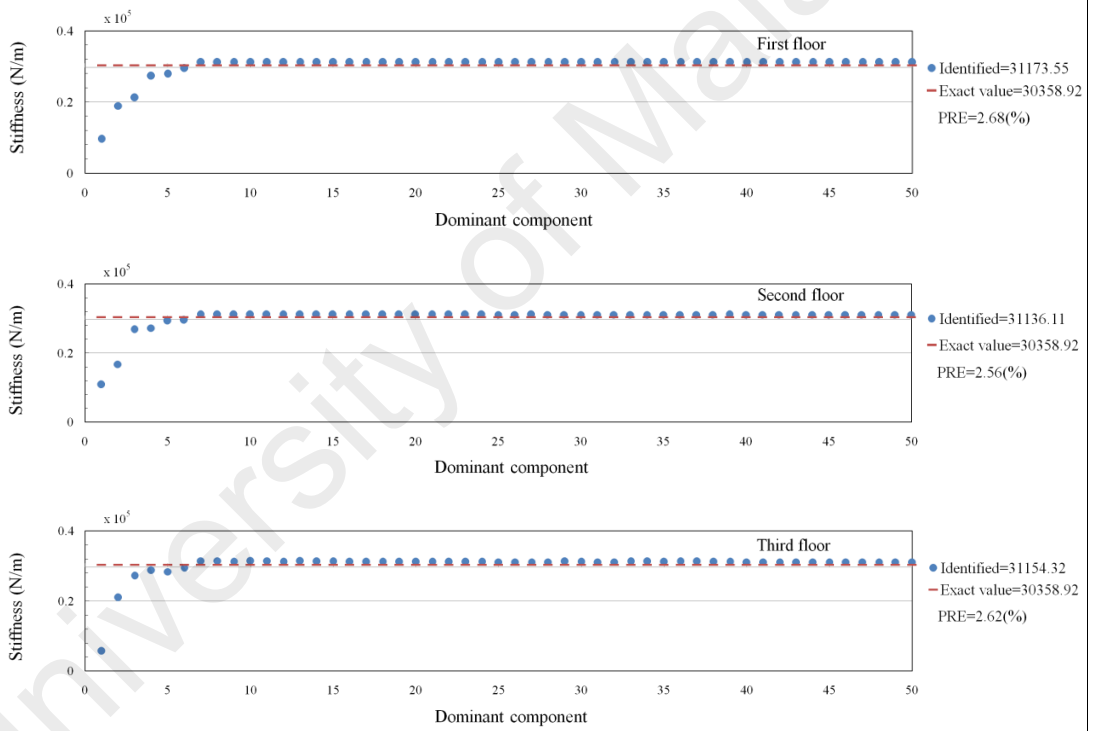
Similarly, In DC3 which demonstrates nonlinear behavior at third floor, the estimated errors λ_i of the identified restoring force values at the third floor for the noiseless case and for three levels of noise are 1.48%, 5.46%, 3.36% and 1.74%, respectively. In addition, a comparison between Figure 6.48, which presents identified restoring force-drift hysteresis curves of the third floor associated with different levels of noise, and Figure 6.44, depicting noiseless cases shows that larger errors occur with rise of noise. Based on the earlier discussion, noise has a negative effect in achieving a precise identification results through the proposed method. Nevertheless, accuracy can still be considered as quite satisfactory even in presence of measurement noise.

Table 6.17: Effect of different levels of noise in identified stiffness parameters

Damage case	Noise level (dB)	PRE (%)		
		Story		
		1	2	3
Original model along with damping	2	3.83	3.79	3.81
	5	1.28	1.35	1.32
	10	0.44	0.32	0.26
DC1	2	7.43	5.12	2.29
	5	2.86	2.08	1.98
	10	0.76	0.5	0.26
DC2	2	10.25	7.95	4.89
	5	3.96	3.18	2.34
	10	1.01	0.93	0.59

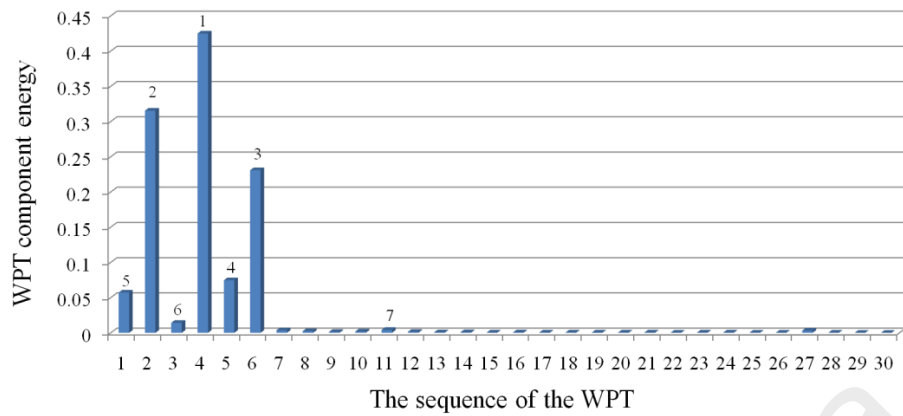


(a) Average relative energy distribution of acceleration response at decomposition level 9

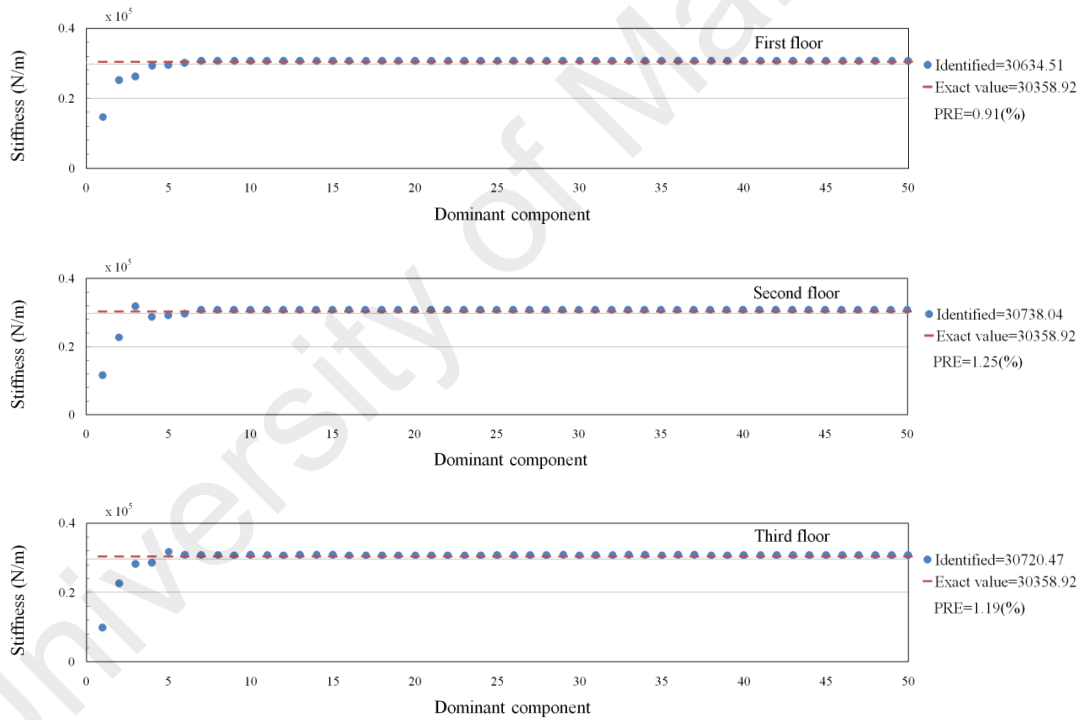


(b) Stiffness parameters identification at each floor

Figure 6.45: Identified results for original numerical model with noise level of SNR=2dB

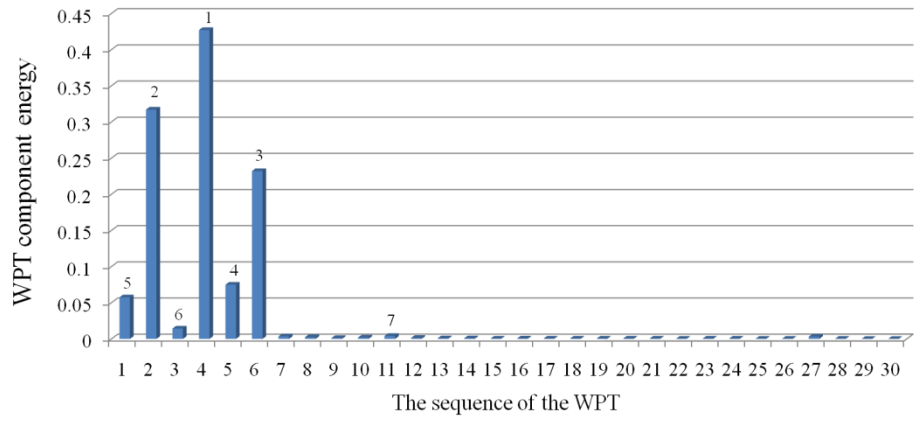


(a) Average relative energy distribution of acceleration response at decomposition level 9

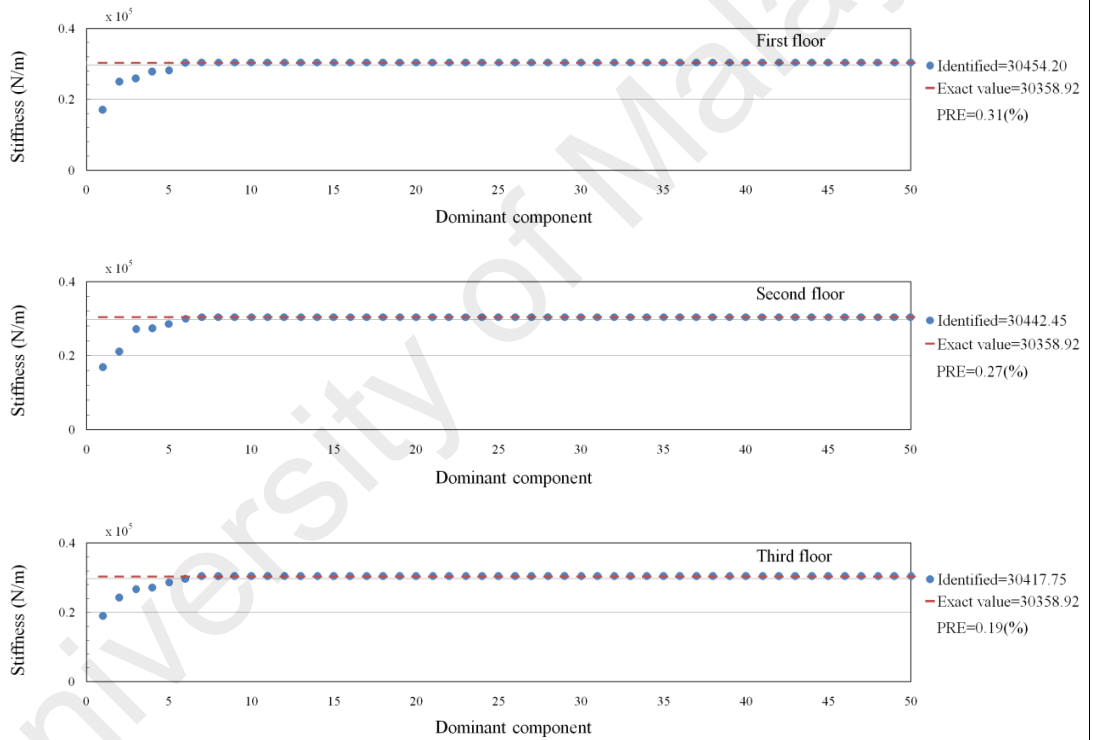


(b) Stiffness parameters identification at each floor

Figure 6.46: Identified results for original numerical model with noise level of SNR=5dB



(a) Average relative energy distribution of acceleration response at decomposition level 9



(b) Stiffness parameters identification at each floor

Figure 6.47: Identified results for original numerical model with noise level of SNR=10dB

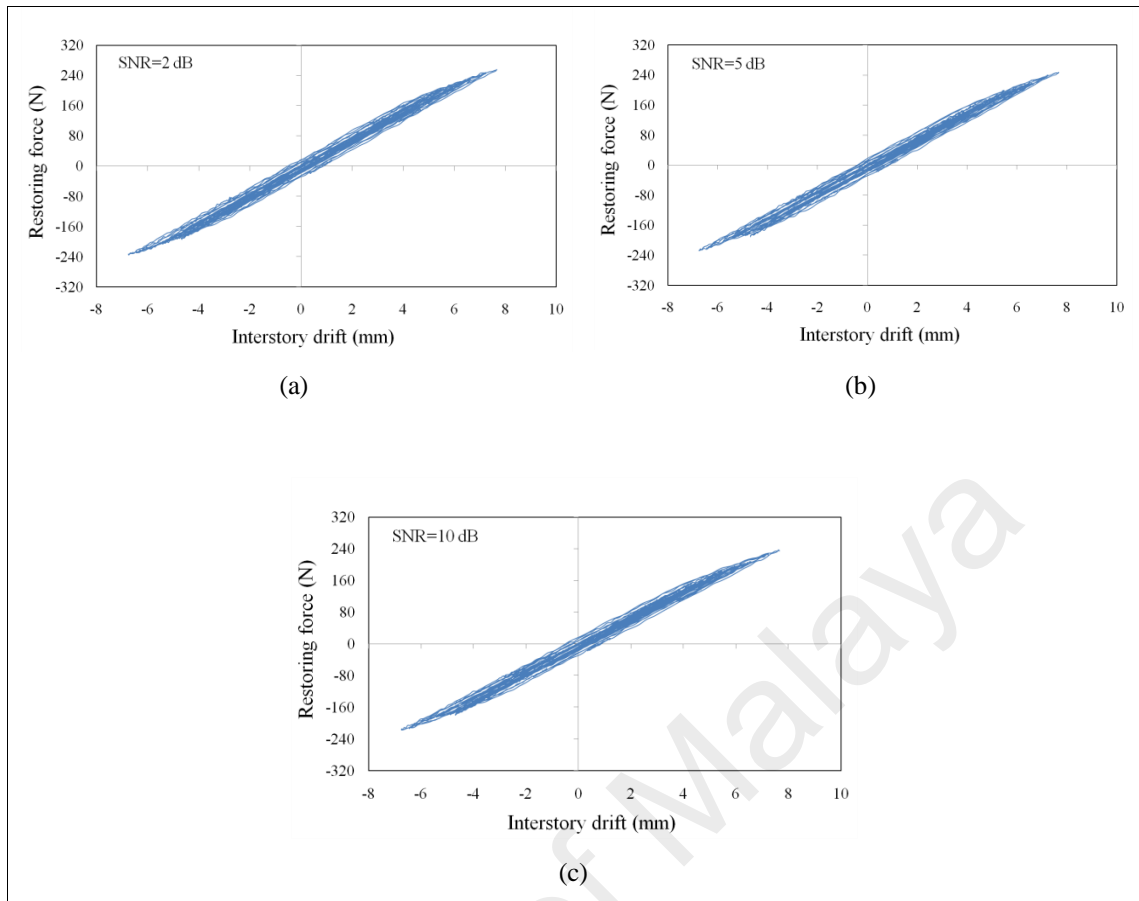


Figure 6.48: The identified restoring force-drift hysteresis curves after adding different level of noise. (a) SNR=2 dB, (b) SNR=5 dB, (c) SNR=10 dB

6.6.2 Experimental results

To validate the applicability of the proposed method, the experimental study is carried out on the three-story shear-beam building model, as described in Section 5.3.2.2.

6.6.2.1 Evaluation of original experimental model

In order to identify the structural parameters of original experimental model, time histories of the applied input force and of the structural acceleration at each floor are measured (Figure 6.49). Subsequently, the corresponding velocities and displacements are derived from the acceleration responses in terms of DB15 scaling function and depicted in Figure 6.50.

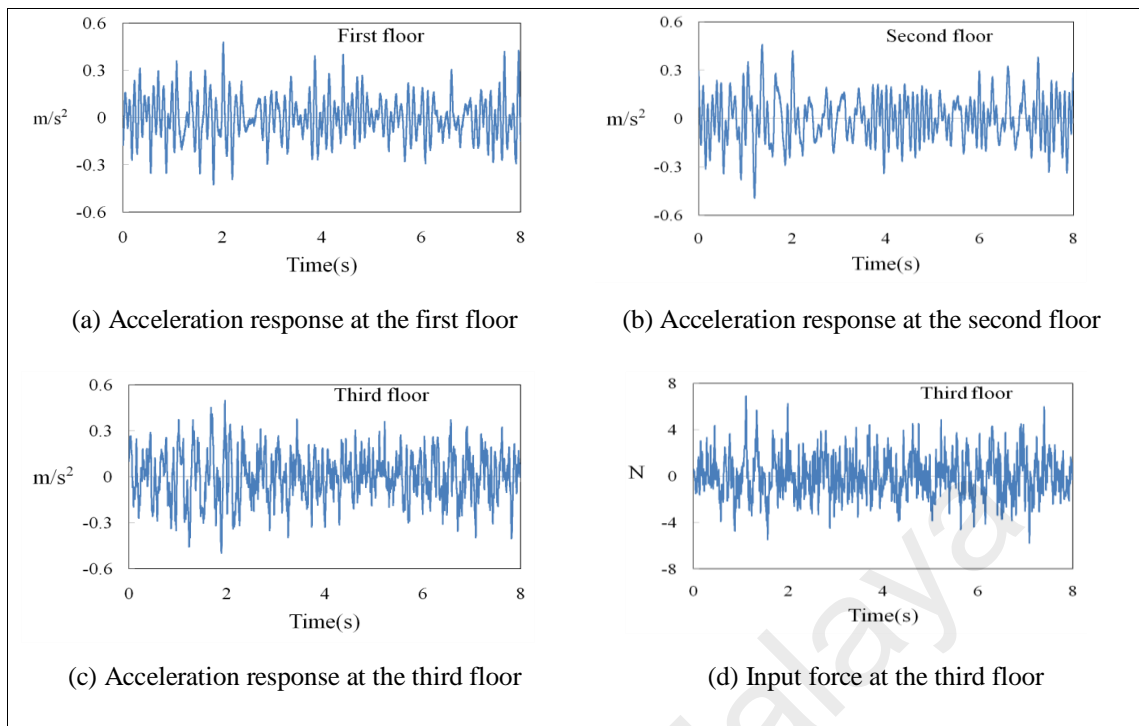


Figure 6.49: Measured acceleration responses and input force for original model

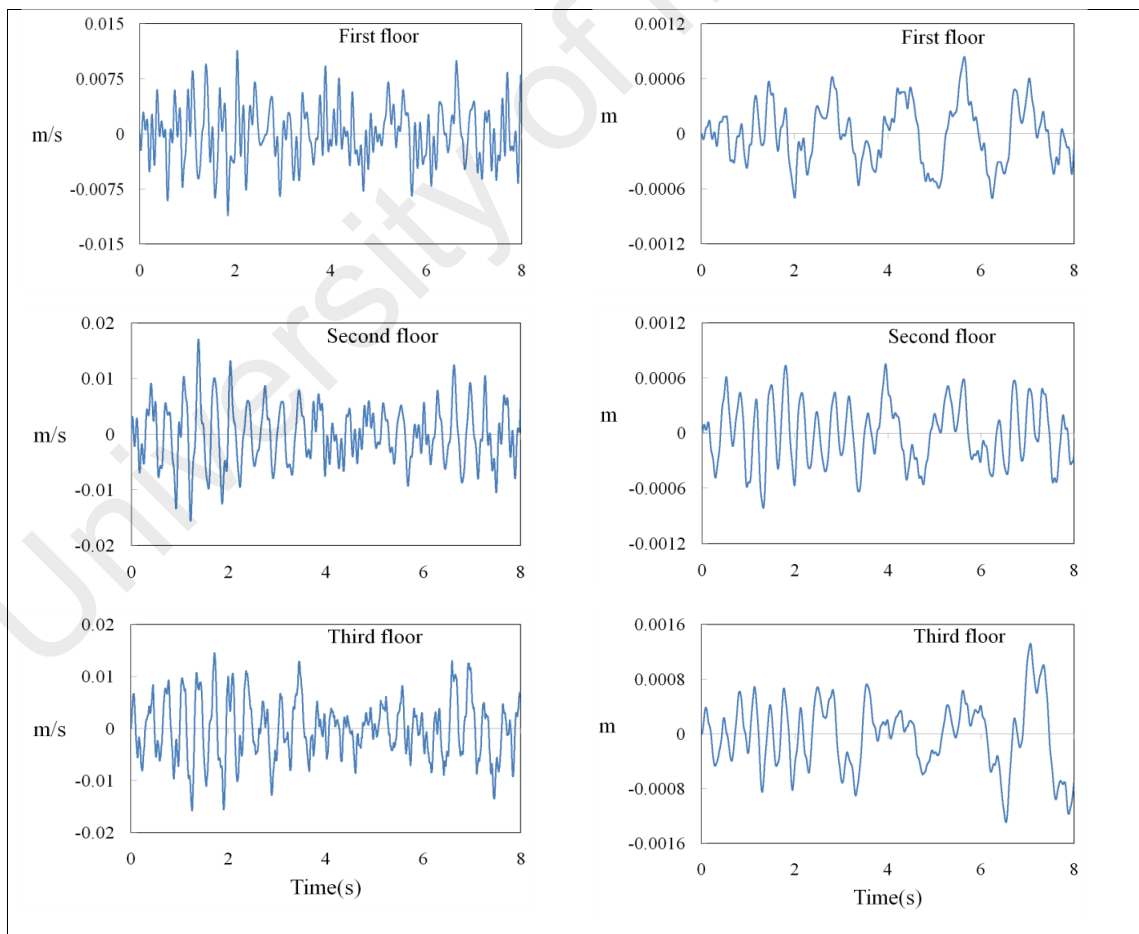


Figure 6.50: Derived the velocities and displacements from acceleration responses at each floor of the original experimental model in terms of DB15 scaling function

Figure 6.51(a) shows the average relative energy distribution of the acceleration responses associated with structural frequencies at decomposition level 9 with the sequence number 1 to 30 among 2^9 WPT components. From these distributions, it can be observed that the second WPT component with the frequency band of [2-4 Hz], including the lowest natural frequency (2.875 Hz), has a great amount of relative energy among other WPT components. Also, the relative WPT component energy of the sixth WPT component, whose frequency band is [6-8 Hz], has a higher energy compared with the fourth WPT component. Therefore, the dominant components can be set as $D_1=\{2\}$, $D_2=\{2, 6\}, \dots$, $D_7=\{2, 6, 4, 5, 1, 3, 7\}$ and so on. By applying the least squares error minimization over those dominant components, the structural parameters corresponding to each dominant component can be estimated.

Figure 6.51(b) demonstrates the identified stiffness parameters in each dominant component. It appears that the obtained values converge to the exact values at around D_7 and deviates from D_{57} onward. The PREs of the obtained values in terms of the stiffness parameters for the first, second and third floor are 4.21%, 4.37% and 4.33%, respectively. In addition, the damping parameters can be accurately identified in the first converged region, based on the numerical output, whereas in the other regions, more uncertainty is included caused by inclusion of higher-order dominant components. The obtained values in terms of damping parameters for the first and second floors are equal to 28.37 N.s/m and for the third floor is 27.76 N.s/m.

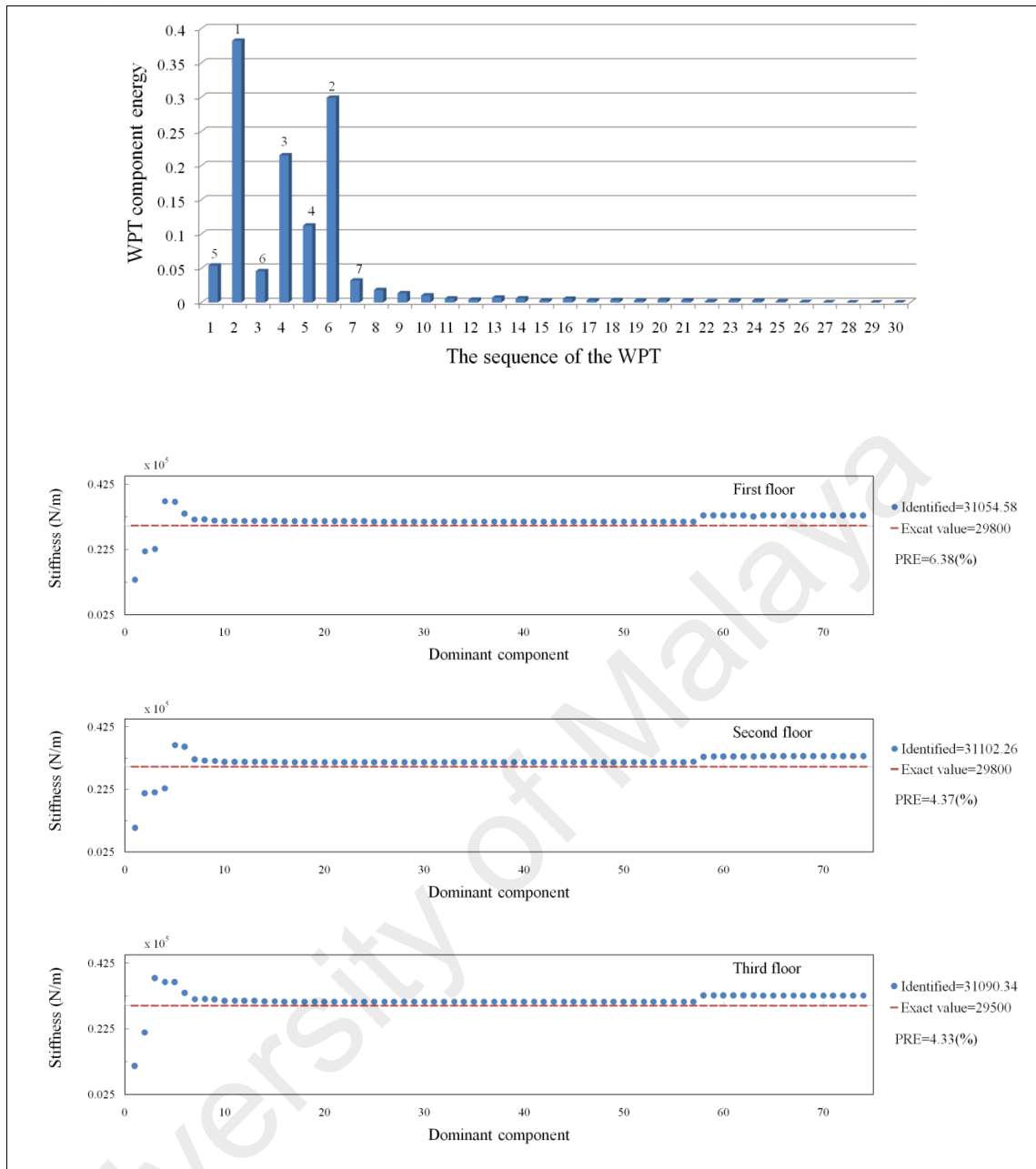


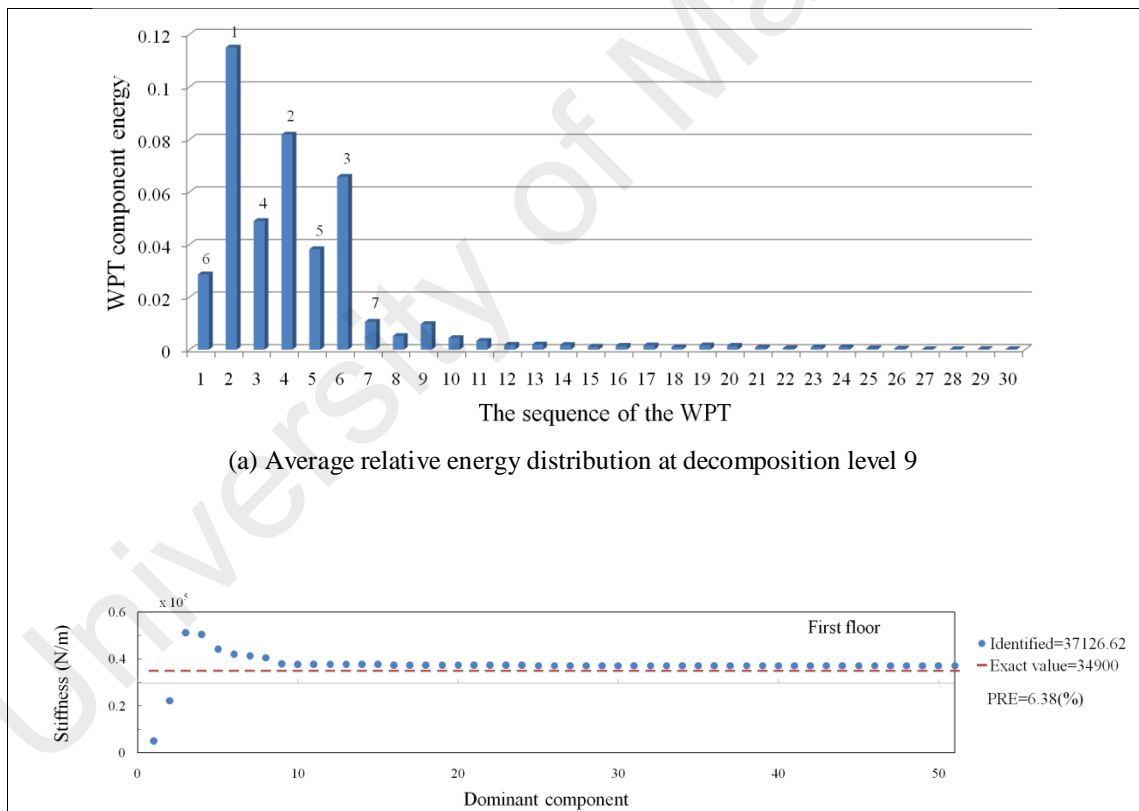
Figure 6.51: Identified results for original experimental model

6.6.2.2 Case1: Damage in first story (linear model)

In this test, a VSD including a bracing system and a HCP system, is mounted in the first story. The cylinder is filled by air with air pressure of $P_0 = 600$ kPa. So that, the effective stiffness of VSD is $K_{hi} = 5.1$ kN/m. Hence, the stiffness of the first story is $k_1 = 34.9$ kN/m, while the stiffness of other stories are $k_2 = 29.8$ kN/m and $k_3 = 29.5$ kN/m.

Figure 6.52 presents the distribution of average relative energy of the acceleration responses at decomposition level 9 and the corresponding PREs for each stiffness

parameter. Looking at results in Figures 6.51 and 6.52, it can be observed that in Figure 6.51(b) the convergence starts at seventh dominant component D_7 , while for case 1, Figure 6.52(b), convergence begins at around D_9 . This is because of the relative energy of the WPT components on dominant component which affects the convergence rate. In addition, in terms of the accuracy of identification results, The PREs of the obtained values for the first, second and third floors are 6.38%, 5.23% and 4.75%, respectively, as shown in Figure 6.52(b). This shows that the proposed method is capable of identifying the stiffness parameter with sufficient accuracy and that leads to detection of structural damages.



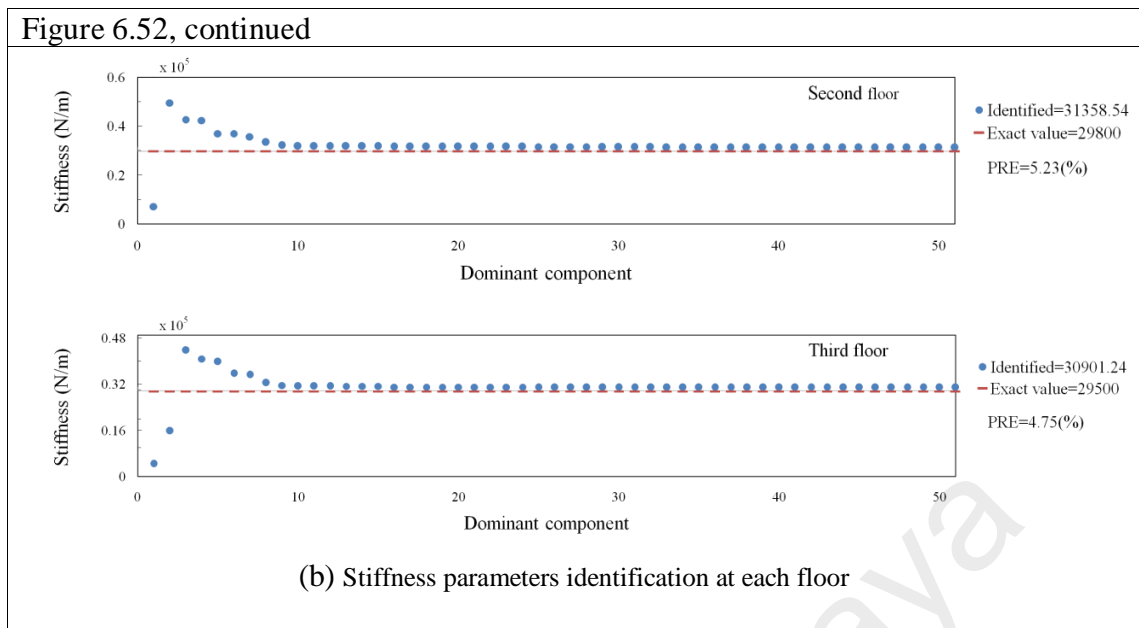


Figure 6.52: Identified results for Case 1 of experimental model

6.6.2.3 Case2: Damage in second story (linear model)

In this test, a VSD with an initial air pressure $P_0=400$ kPa is mounted in the second story of the building model to simulate the damage. The weight of the HCP is 3.6 kg, which should be added to the first floor. Thus, mass of the first floor is $m_1=31.3$ kg and masses of the second and third floor are 27.7 and 25.1, respectively. The effective stiffness of HCP with the air pressure of 400 kPa is 3.4 kN/m, which is added to the stiffness of the second story. Therefore, prior to the test, values of stiffness of stories are $k_1= 29.8$ kN/m, $k_2=33.2$ kN/m and $k_3=29.5$ kN/m.

Figure 6.53 shows the distribution of average relative energy over the WPT components at decomposition level 9, and the corresponding PREs of the identified stiffness values. Also, Table 6.18 demonstrates variation of the identified stiffness parameters for the damage cases. A comparison between the original model and the considered damage cases shows successful detection of the damage. It can be observed that, the damage area for case 1 has occurred in the first floor owing to the large amount of stiffness variation, i.e., 19.55%. Similarly, it can be seen from Table 6.18, for case 2 the maximum change in the stiffness, i.e., 12.20%, has occurred at the second floor, Whereas, variation of the

stiffness parameters of other stories can be neglected, since they are very small and are produced by the process of identification itself.

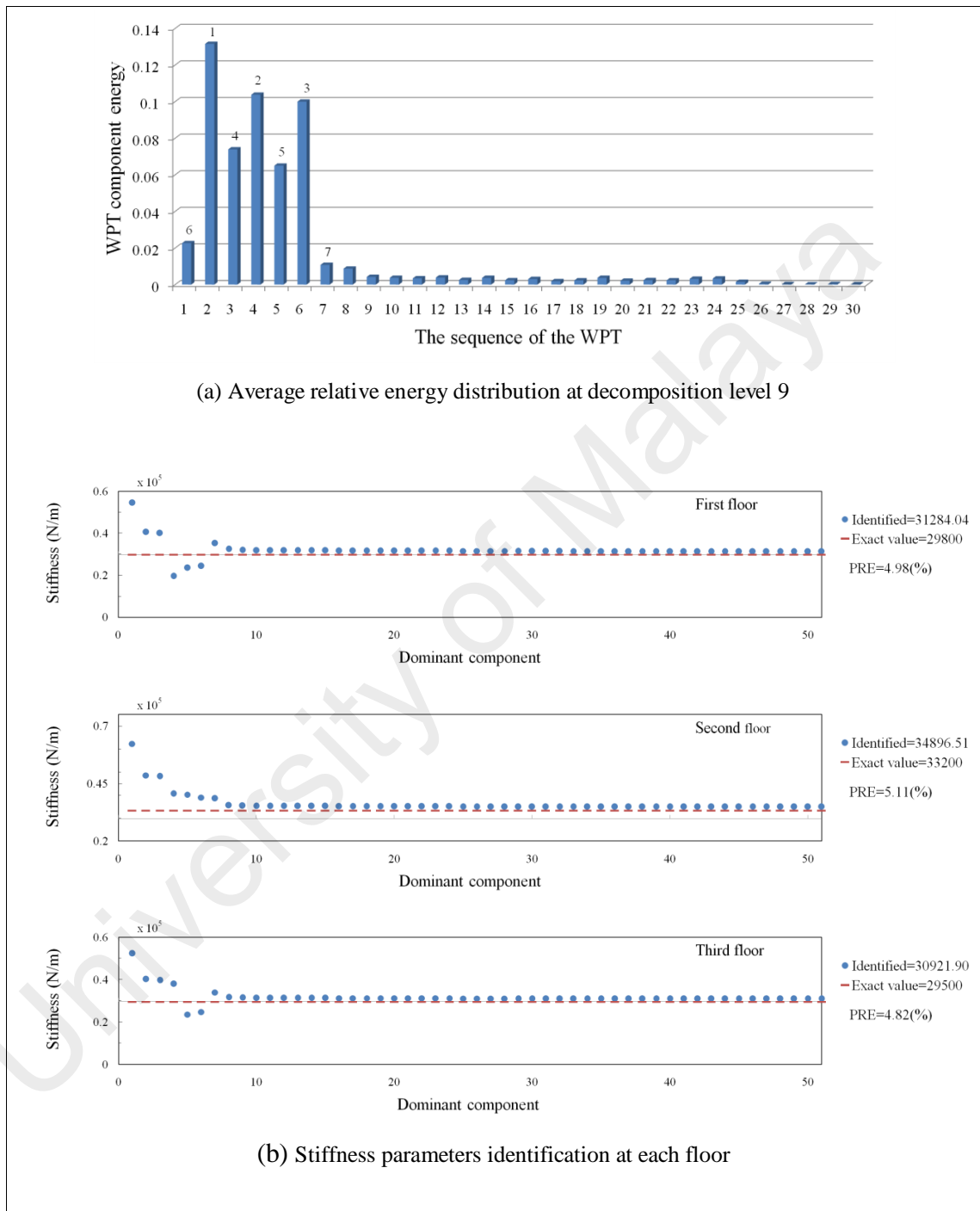


Figure 6.53: Identified results for Case 2 of experimental model

Table 6.18: Identified stiffness parameters and natural frequencies, ω , of the original model and damage cases 1 and 2. The units of k , ω are N/m and Hz, respectively

	Original experimental model	Case 1	Case 2	Variation (%)	
				Case 1	Case 2
k_1	31054.58	37126.62	31284.04	19.55	0.74
k_2	31102.26	31358.54	34896.51	0.82	12.20
k_3	31090.34	30901.24	30921.90	0.61	0.54
ω_1	2.875	3.021	2.929	5.08	1.88
ω_2	7.625	7.866	7.693	3.16	0.89
ω_3	10.5	10.592	10.813	0.87	2.98

6.6.2.4 Case3: Damage in first story (piecewise linear model)

In this test, the experimental configuration is similar to case 1 depicted earlier, except that the air pressure of the VSD mounted in the first story is $P_0 = 400$ kPa and consequently the effective stiffness of the VSD is 3.4 kN/m. Therefore, the stiffness of each story before damage is $k_1 = 33.2$, $k_2 = 29.8$ and $k_3 = 29.5$ kN/m. During the test, valves of VSD are open simultaneously at $t = 4$ s, result in the stiffness of the first story reduced abruptly from 33.2 to 29.8 kN/m.

The wavelet function DB15 is applied in all time steps, and the scaling functions are used to identify the tangent stiffness in each $1/32$ of the total duration. In addition, a piecewise linear damping coefficient is determined for each step. Therefore, the unknown scaling function coefficients and one damping coefficient are identified in each step.

Figure 6.54 presents the identified stiffness parameters for all stories with blue curves, also shown in the same figure by red curves are the results obtained from the static test for comparison. The PREs of the identified stiffness values which are regressed by a straight line are obtained and tabulated in Table 6.19. In addition, the identification of damping coefficients is given in Figure 6.55. It can be observed that the damping coefficients of the first floor is declined at $t = 5$ s compared with those of other floors. There is a trade-off between number of piecewise linear damping coefficients and accuracy of the identification results. Hence, parametric studies are carried out for choosing number of the piecewise linear coefficients, in which accuracy of the

identification process is ameliorated with appropriate selection of the number of the damping coefficients.

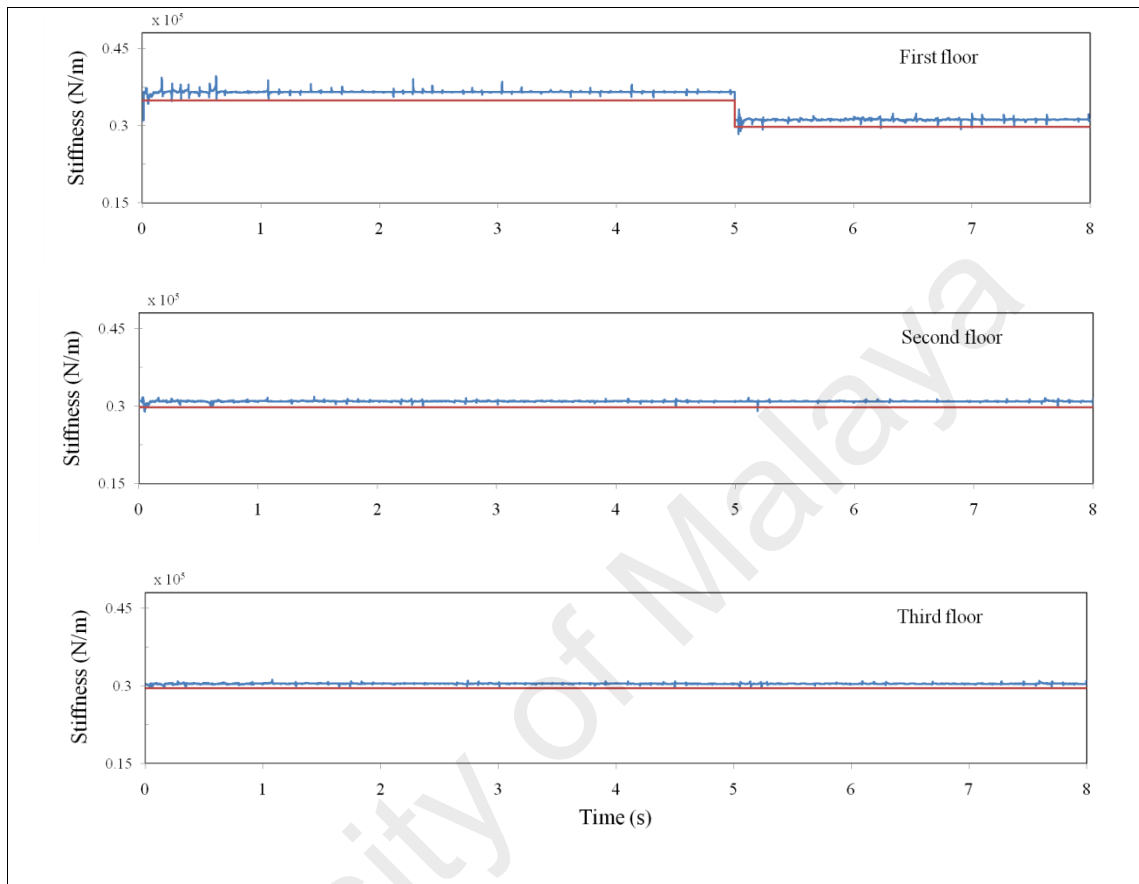


Figure 6.54: Identified stiffness parameters for Case 3 of experimental model

Table 6.19: The PRE of identified stiffness parameters in damage Case 3

Story	PRE(%)	
	Before damage	After damage
First	7.12	6.85
Second	5.84	5.84
Third	4.79	4.79

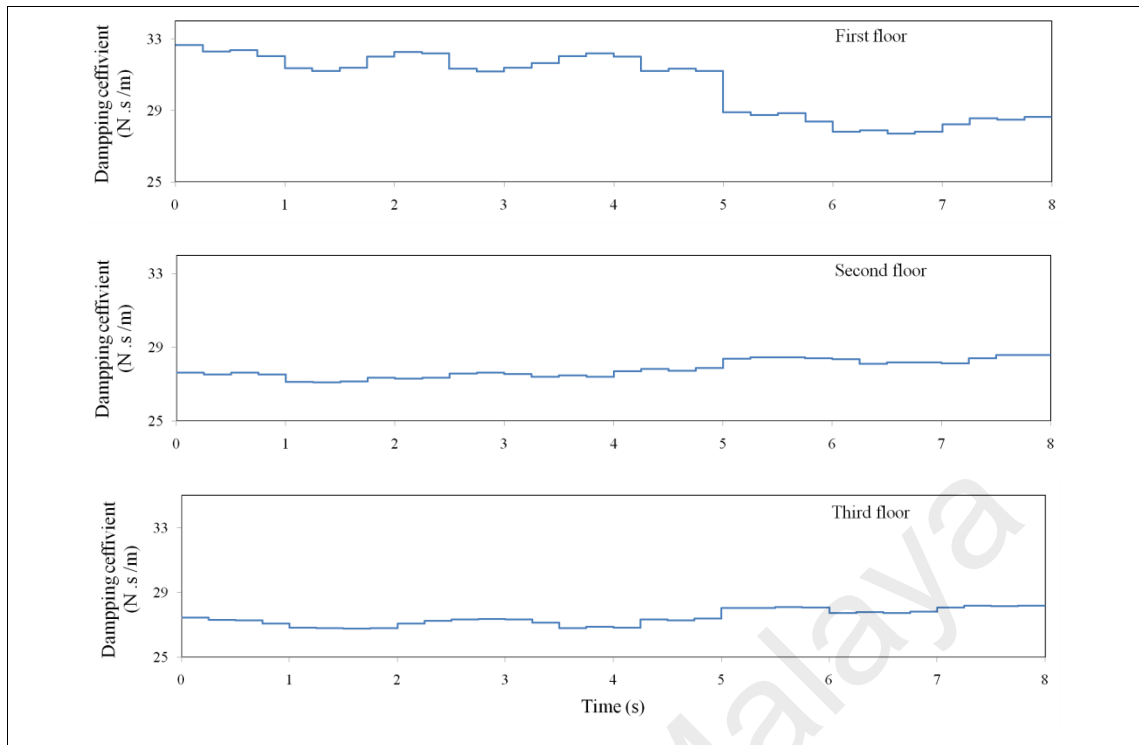


Figure 6.55: Identified damping coefficients for case 3 of experimental model

6.7 Summary

In this chapter, the proposed damage detection and the wavelet-based system identification algorithms are evaluated by using numerical and experimental examples. In first, the RWPE-based damage detection algorithm was tested and verified using beam structures and the three-story building model. The damage locations were accurately identified by using damage index based on the RWPE. The effectiveness of the proposed method was examined by both numerical simulation and experimental tests with different damage scenarios. Based on the results it can be concluded that selection of a proper mother wavelet function and decomposition level has been crucial to improve the performance of the proposed method. Then, the GA optimization was used to evaluate the damage severities by exploring the database. Evaluation of the detected errors of different severity combinations in multiple damage cases demonstrated the sensitivity and accuracy of the proposed algorithm in identification of damage severities. In addition,

evaluation of the severity could reach to a higher level of accuracy in the building model, provided that damage locations were at different stories.

The RWPE-based reference-free damage detection algorithm was also tested and verified with numerical and experimental studies on beam and three-story building model. The feasibility of using the RDI_{RWPE} as damage-sensitive index was studied and verified. In general, the proposed method does not require vibration signals from undamaged structures because of its effective comparison methodology of signals from different locations at current state. Whereas, in the course of this research, accurate detection of damage locations depended on the proper selection of mother wavelet function and decomposition level which was optimally selected by GA. Moreover, performance of the proposed algorithm was demonstrated for progressive damage starting from small-scale level, i.e., 3mm. According to various numerical and experimental demonstrations and verifications, the proposed damage detection algorithm was proven to be very effective in detecting various damage scenarios without reference data from undamaged structures. The physical parameters of three-story building model can be identified by using the proposed wavelet-based system identification algorithm. In numerical simulations, the auxiliary structures are proposed by adding extra spring to the mass center of the considered floors to illustrate the stiffness variations. The precision of the identified parameters was evaluated with PRE of their exact values, conducted by ABAQUS software. Moreover, the numerical tests demonstrated that the proposed method can accurately identify the tangent stiffness parameters and nonlinear hysteresis curves of the building model. In experimental investigations, to simulate the structural damage during the test, a VSD with an effective stiffness was proposed to reduce the stiffness of building stories. Different damage scenarios were simulated and tested. The structural parameters were identified reasonably well based on the proposed algorithm.

CHAPTER 7: CONCLUSION AND RECOMMENDATIONS

7.1 Introduction

In this thesis, current challenges in vibration-based SHM were addressed focusing on damage detection and system identification. The SHM is central to the aim of maintaining civil engineering structures safely and efficiently, and thereby securing people's lives and property. In addition, it plays a crucial role in infrastructure design at a fraction of the capital cost of construction. Therefore, the desire of all those effort in this field to fully exploit the information about the vibration of structures is putting structural responses to good use in the areas of damage detection and system identification. The wavelet-based methods through WPT have been proposed for identification of damage locations and system parameters from data generated in vibration tests of the structures.

This chapter presents the conclusions and recommendations of the current research for the future improvements and higher efficiency of the damage detection and system identification techniques.

7.2 Conclusions

This study initially proposed a two-step vibration-based damage detection algorithm in the framework of the wavelet multiresolution analysis and optimization techniques. This algorithm was then tested and verified with beam-like structures and a three-story building model. In the first step, in order to investigate the damage location, the multiresolution wavelet packet transform was combined with entropy analysis to determine an effective damage index, RWPE, and obtain the information about the relative energy correlated with various frequency bands presented in structural response segments. In the second step, the GA optimization method was applied to estimate the damage severities by defining a database to reveal the relationships between the energies

obtained in the first step and damage severities. Through the numerical and experimental verifications, the results demonstrated that the proposed method and the proposed algorithm can be used to identify the damage locations with different severity combinations for each damage scenario with a high accuracy even in the presence of noise. It has to be mentioned that the appropriate selection of wavelet types affected the performance of the proposed damage identification algorithm.

To make real-time monitoring feasible in SHM systems, a new RWPE- based reference-free damage detection algorithm was developed and verified for beam-like structures and a three-story building model. The RWPE measurements of various sensor-to-sensor pairs were applied for defining the damage index, RDI_{RWPE} , of each sensor location. The RWPE-based reference-free damage identification proved to be damage-sensitive and able to identify the damage locations without signals of intact states of structures with a considerable accuracy, and showed sufficient sensitivity to the changes in damage level. In addition, from the results, it can be concluded that the wavelet-based techniques are absolutely dependent on the mother wavelet function. On the other hand, the most inevitable challenge in wavelet analysis for damage identification, as shown in previous research works, has been the determination of mother wavelet function and decomposition level through trial and error, based on intrinsic characteristics of the data. This has limited earlier researches to use a specific mother wavelet function and decomposition level for various damage scenarios. However, the consistency and accuracy of the proposed method has been verified by using various mother wavelet functions and decomposition levels for every damage scenario at different locations. The mother wavelet and decomposition level were optimally chosen by GA which can resolve the problem of wavelet-based damage detection methods. The reference-free methods suffer from presence of multiple-damage scenario in several locations throughout a beam or in a floor of a building. Therefore, the difficulty in implementation of mother wavelet

function through trial-and-error based methods is eliminated and consequently the proposed RWPE-based reference-free damage identification algorithm can be directly applied to monitor structures continuously in real-time.

With regards to system identification, a new optimization method was presented to identify the structural parameters of linear and nonlinear systems based on the inverse solution of equation of motion in wavelet domains. For the proposed method, the measurements of excitation forces and response data containing displacements, velocities, and accelerations, at each degree of freedom are required. For this purpose, the connection coefficients of the scaling function were applied to derive the velocity and displacement from the output-only measured acceleration responses. This numerical integration process may unavoidably introduce error to the estimated structural parameters. Therefore, by utilizing the GA for proper selection of Daubechies wavelet functions and defining the dominant components based on the relative energies of acceleration responses, the equations of motion in the time domain of the system were transformed to a reduced representation of the equations of motion in terms of the wavelet packet transform. The best estimation of the structural parameters was obtained by using the least square procedure iteratively over each selected dominant component. Also, in cases where there were material nonlinearities in structural building, the tangent stiffness matrix and the hysteresis-restoring force curves of the building model were identified, by applying the wavelet multiresolution analysis based on the structural responses at each degree of freedom. The numerical and experimental results demonstrated that the proposed wavelet-based system algorithm can identify the structural parameters accurately, even in case of material nonlinearity. To simulate the structural damage in the experimental model, a variable stiffness device was proposed to change the stiffness parameter in some building stories. Moreover, the accuracy and reliability of the proposed algorithm was investigated for various damage cases and noise levels.

7.3 Recommendations for future work

The damage detection and system identification in structural dynamics under different damage cases were addressed in this thesis using the wavelet multiresolution analysis. The accuracy of the obtained results from numerical and experimental examples proved the robustness of the proposed methods. However, all the applications were limited to beam structures and small-scale shear-beam building models. It is desirable to verify the reliability of the methods by applying them to a full-scale structure in the field, which will suggest further improvements.

In the future, the proposed RPWE-based reference-free real-time damage detection application can be applied not only in the damage localization application in real structures but also it will be useful to monitor the abnormality of signals caused by sensor failures or local failure of structural components as was demonstrated in this research.

In addition, the proposed wavelet-based system identification algorithm demonstrated a promising potential for parameters identification of a nonlinear system through the numerical simulations. However, investigation of nonlinear behavior of the experimental models was not fully addressed in this research. Hence, the experimental verification of the proposed system identification algorithm for estimation of nonlinear structural parameters can be further pursued.

REFERENCES

- Abdo, M.-B., & Hori, M. (2002). A numerical study of structural damage detection using changes in the rotation of mode shapes. *Journal of Sound and vibration*, 251(2), 227-239.
- Adams, R., Cawley, P., Pye, C., & Stone, B. (1978). A vibration technique for non-destructively assessing the integrity of structures. *Journal of Mechanical Engineering Science*, 20(2), 93-100.
- Agbabian, M., Masri, S., Miller, R., & Caughey, T. (1991). System identification approach to detection of structural changes. *Journal of Engineering Mechanics*, 117(2), 370-390.
- Agrawal, A., & Yang, J. (2000). A semi-active hybrid isolation system for buildings subject to near-field earthquakes. *Advanced technology in structural engineering*, 8-10.
- Al-Khalidy, A., Noori, M., Hou, Z., Carmona, R., Yamamoto, S., Masuda, A., & Sone, A. (1997). A study of health monitoring systems of linear structures using wavelet analysis. In F.-K. Chang (Ed.), *Structural Health Monitoring – Current Status and Perspectives: Proceedings of the International Workshop on Structural Health Monitoring, Stanford University, Stanford, CA, USA* (pp. 164-175). Technomic, Lancaster, Basel.
- Alvandi, A., & Cremona, C. (2006). Assessment of vibration-based damage identification techniques. *Journal of sound and vibration*, 292(1), 179-202.
- Amiri, G. G., & Asadi, A. (2009). Comparison of different methods of wavelet and wavelet packet transform in processing ground motion records. *International Journal of Civil Engineering*, 7(4), 248-257.
- Anton, S. R., Inman, D. J., & Park, G. (2009). Reference-free damage detection using instantaneous baseline measurements. *AIAA journal*, 47(8), 1952-1964.
- Argoul, P., & Le, T.-P. (2003). Instantaneous indicators of structural behaviour based on the continuous Cauchy wavelet analysis. *Mechanical Systems and Signal Processing*, 17(1), 243-250.
- Bagheri, A., Li, K., & Rizzo, P. (2013). Reference-free damage detection by means of wavelet transform and empirical mode decomposition applied to Lamb waves. *Journal of Intelligent Material Systems and Structures*, 24(2), 194-208.
- Basu, B., & Gupta, V. (1999a). On equivalent linearization using wavelet transform. *Journal of Vibration and Acoustics-Transactions of the Asme*, 121(4), 429-432.
- Basu, B., & Gupta, V. (1999b). Wavelet-based analysis of the non-stationary response of a slipping foundation. *Journal of Sound and Vibration*, 222(4), 547-563.

- Basu, B., & Gupta, V. K. (1997). Non-stationary seismic response of MDOF systems by wavelet transform. *Earthquake engineering & structural dynamics*, 26(12), 1243-1258.
- Basu, B., & Gupta, V. K. (1998). Seismic response of SDOF systems by wavelet modeling of nonstationary processes. *Journal of Engineering Mechanics*, 124(10), 1142-1150.
- Berman, A., & Flannelly, W. G. (1971). Theory of incomplete models of dynamic structures. *AIAA journal*, 9(8), 1481-1487.
- Berman, A., & Nagy, E. (1983). Improvement of a large analytical model using test data. *AIAA journal*, 21(8), 1168-1173.
- Beskhyroun, S., Oshima, T., & Mikami, S. (2010). Wavelet-based technique for structural damage detection. *Structural Control and Health Monitoring*, 17(5), 473-494.
- Bobrow, J. E., Jabbari, F., & Thai, K. (2000). A new approach to shock isolation and vibration suppression using a resettable actuator. *Journal of Dynamic Systems Measurement and Control-Transactions of the Asme*, 122(3), 570-573.
- Carden, E. P., & Fanning, P. (2004). Vibration based condition monitoring: a review. *Structural Health Monitoring-an International Journal*, 3(4), 355-377.
- Cawley, P., & Adams, R. (1979). The location of defects in structures from measurements of natural frequencies. *Journal of Strain Analysis for Engineering Design*, 14(2), 49-57.
- Chance, J., Tomlinson, G., & Worden, K. (1994). A simplified approach to the numerical and experimental modelling of the dynamics of a cracked beam. Proceedings of 12th International Modal Analysis Conference, 778-785.
- Chang, C.-C., & Chen, L.-W. (2005). Detection of the location and size of cracks in the multiple cracked beam by spatial wavelet based approach. *Mechanical Systems and Signal Processing*, 19(1), 139-155.
- Chase, J. G., Mulligan, K. J., Gue, A., Alnot, T., Rodgers, G., Mander, J. B., . . . Heaton, D. (2006). Re-shaping hysteretic behaviour using semi-active resettable device dampers. *Engineering Structures* 28(10), 1418-1429.
- Chen, H., Yan, Y., & Jiang, J. (2007). Vibration-based damage detection in composite wingbox structures by HHT. *Mechanical systems and signal processing*, 21(1), 307-321.
- Chen, M. Q., Hwang, C., & Shih, Y. P. (1996). The computation of wavelet-galerkin approximation on a bounded interval. *International Journal for Numerical Methods in Engineering*, 39(17), 2921-2944.
- Chen, S.-L., Lai, H.-C., & Ho, K.-C. (2006). Identification of linear time varying systems by Haar wavelet. *International journal of systems science*, 37(9), 619-628.

- Cobb, R. G., & Liebst, B. S. (1997). Structural damage identification using assigned partial eigenstructure. *AIAA journal*, 35(1), 152-158.
- Daubechies, I. (1988). Orthonormal bases of compactly supported wavelets. *Communications on Pure and Applied Mathematics*, 41(7), 909-996.
- Daubechies, I. (1992). *Ten lectures on wavelets*. Society for Industrial and Applied Mathematics (SIAM), Philadelphia, Pennsylvania.
- Deng, X., & Wang, Q. (1998). Crack detection using spatial measurements and wavelet analysis. *International Journal of Fracture*, 91(2), L23-L28.
- Diao, Y.-S., Li, H.-J., & Wang, Y. (2006). A two-step structural damage detection approach based on wavelet packet analysis and neural network. Proceedings of 5th International Machine Learning and Cybernetics, Dalian, China.
- Ding, Y., Li, A., & Liu, T. (2008). A study on the WPT-based structural damage alarming of the ASCE benchmark experiments. *Advances in Structural Engineering*, 11(1), 121-127.
- Distéfano, N., & Todeschini, R. (1973). Modeling, identification and prediction of a class of nonlinear viscoelastic materials (I). *International Journal of Solids and Structures*, 9(7), 805-818.
- Doebling, S. W. (1996). Damage detection and model refinement using elemental stiffness perturbations with constrained connectivity. Proceedings of the AIAA/ASME/AHS Adaptive Structures Forum, 360-370, AIAA-96-1037.
- Doebling, S. W., Farrar, C. R., & Prime, M. B. (1998). A summary review of vibration-based damage identification methods. *Shock and vibration digest*, 30(2), 91-105.
- Douka, E., Loutridis, S., & Trochidis, A. (2003). Crack identification in beams using wavelet analysis. *International Journal of Solids and Structures*, 40(13), 3557-3569.
- Fan, W., & Qiao, P. (2011). Vibration-based damage identification methods: a review and comparative study. *Structural Health Monitoring-an International Journal*, 10(1), 83-111.
- Farrar, C., & James III, G. (1997). System identification from ambient vibration measurements on a bridge. *Journal of Sound and Vibration*, 205(1), 1-18.
- Farrar, C. R., & Jauregui, D. A. (1998). Comparative study of damage identification algorithms applied to a bridge: II. Numerical study. *Smart materials and structures*, 7(5), 720.
- Farrar, C. R., & Worden, K. (2007). An introduction to structural health monitoring. *Philosophical Transactions of the Royal Society of London A: Mathematical, Physical and Engineering Sciences*, 365(1851), 303-315.

- Fox, C. (1992). The location of defects in structures: a comparison of the use of natural frequency and mode shape data. *Proceedings of 10th International Modal Analysis Conference*, 522-528.
- Friswell, M., Penny, J., & Garvey, S. (1998). A combined genetic and eigensensitivity algorithm for the location of damage in structures. *Computers & Structures*, 69(5), 547-556.
- Garibaldi, L., Ruzzene, M., Fasana, A., & Piombo, B. (1998). Identification of non linear damping mechanisms using the wavelet transform. *Mécanique industrielle et matériaux*, 51(2), 92-94.
- Gentile, A., & Messina, A. (2003). On the continuous wavelet transforms applied to discrete vibrational data for detecting open cracks in damaged beams. *International Journal of Solids and Structures*, 40(2), 295-315.
- Ghanem, R., & Romeo, F. (2000). A wavelet-based approach for the identification of linear time-varying dynamical systems. *Journal of Sound and Vibration*, 234(4), 555-576.
- Gladwell, G. (2004). *Inverse Problems in Vibration*. Second edition. Springer.
- Gökdağ, H., & Kopmaz, O. (2009). A new damage detection approach for beam-type structures based on the combination of continuous and discrete wavelet transforms. *Journal of Sound and Vibration*, 324(3), 1158-1180.
- Grabowska, J., Palacz, M., & Krawczuk, M. (2008). Damage identification by wavelet analysis. *Mechanical systems and signal processing*, 22(7), 1623-1635.
- Haar, A. (1910). Zur theorie der orthogonalen funktionensysteme. *Mathematische Annalen*, 69(3), 331-371.
- Hadzima-Nyarko, M., Nyarko, E. K., & Morić, D. (2011). A neural network based modelling and sensitivity analysis of damage ratio coefficient. *Expert systems with applications*, 38(10), 13405-13413.
- Han, J.-G., Ren, W.-X., & Sun, Z.-S. (2005). Wavelet packet based damage identification of beam structures. *International Journal of Solids and Structures*, 42(26), 6610-6627.
- Hans, S., Ibrahim, E., Pernot, S., Boutin, C., & Lamarque, C.-H. (2000). Damping identification in multi-degree-of-freedom system via a wavelet-logarithmic decrement—part 2: study of a civil engineering building. *Journal of Sound and Vibration*, 235(3), 375-403.
- Hao, H., & Xia, Y. (2002). Vibration-based damage detection of structures by genetic algorithm. *Journal of computing in civil engineering*, 16(3), 222-229.
- He, W., Agrawal, A., & Mahmoud, K. (2001a). Control of seismically excited cable-stayed bridge using resetting semiactive stiffness dampers. *Journal of Bridge Engineering*, 6(6), 376-384.

- He, Y., Guo, D., & Chu, F. (2001b). Using genetic algorithms and finite element methods to detect shaft crack for rotor-bearing system. *Mathematics and computers in simulation*, 57(1), 95-108.
- Hemez, F., & Farhat, C. (1995). Structural damage detection via a finite-element model updating methodology. *Modal Analysis: The International Journal of Analytical and Experimental Modal Analysis*, 10(3), 152-166.
- Hera, A., & Hou, Z. (2004). Application of wavelet approach for ASCE structural health monitoring benchmark studies. *Journal of Engineering Mechanics*, 130(1), 96-104.
- Hong, J.-C., Kim, Y., Lee, H., & Lee, Y. (2002). Damage detection using the Lipschitz exponent estimated by the wavelet transform: applications to vibration modes of a beam. *International journal of solids and structures*, 39(7), 1803-1816.
- Hou, Z., Hera, A., & Shinde, A. (2006). Wavelet-Based Structural Health Monitoring of Earthquake Excited Structures. *Computer-Aided Civil and Infrastructure Engineering*, 21(4), 268-279.
- Hou, Z., Noori, M., & Amand, R. S. (2000). Wavelet-based approach for structural damage detection. *Journal of Engineering Mechanics*, 126(7), 677-683.
- Huang, C., Hung, S., Lin, C., & Su, W. (2005). A Wavelet-Based Approach to Identifying Structural Modal Parameters from Seismic Response and Free Vibration Data. *Computer-Aided Civil and Infrastructure Engineering*, 20(6), 408-423.
- Hung, S. L., Huang, C., Wen, C., & Hsu, Y. (2003). Nonparametric identification of a building structure from experimental data using wavelet neural network. *Computer-Aided Civil and Infrastructure Engineering*, 18(5), 356-368.
- Jabbari, F., & Bobrow, J. E. (2002). Vibration suppression with resettable device. *Journal of Engineering Mechanics*, 128(9), 916-924.
- Jiang, X., & Adeli, H. (2007). Pseudospectra, MUSIC, and dynamic wavelet neural network for damage detection of highrise buildings. *International Journal for Numerical Methods in Engineering*, 71(5), 606-629.
- Jiang, X., Ma, Z. J., & Ren, W. X. (2012). Crack detection from the slope of the mode shape using complex continuous wavelet transform. *Computer-Aided Civil and Infrastructure Engineering*, 27(3), 187-201.
- Jiang, X., & Mahadevan, S. (2011). Wavelet spectrum analysis approach to model validation of dynamic systems. *Mechanical Systems and Signal Processing*, 25(2), 575-590.
- Joo, D. J. (2012). Damage detection and system identification using a wavelet energy based approach. PhD thesis. Columbia University, New York, USA.

- Joseph, L., & Minh-Nghi, T. (2005). A wavelet-based approach for the identification of damping in non-linear oscillators. *International Journal of Mechanical Sciences*, 47(8), 1262-1281.
- Kabe, A. M. (1985). Stiffness matrix adjustment using mode data. *AIAA journal*, 23(9), 1431-1436.
- Kaouk, M. (1993). Finite element model adjustment and damage detection using measured test data. PhD thesis. University of Florida, Gainesville. USA.
- Kasper, D., Swanson, D., & Reichard, K. (2008). Higher-frequency wavenumber shift and frequency shift in a cracked, vibrating beam. *Journal of Sound and Vibration*, 312(1), 1-18.
- Kijewski, T., & Kareem, A. (2003). Wavelet transforms for system identification in civil engineering. *Computer-Aided Civil and Infrastructure Engineering*, 18(5), 339-355.
- Kim, J.-T., & Stubbs, N. (2003). Crack detection in beam-type structures using frequency data. *Journal of Sound and Vibration*, 259(1), 145-160.
- Ko, J., Wong, C., & Lam, H. (1994). Damage detection in steel framed structures by vibration measurement approach. Proceedings of 12th International Modal Analysis Conference, 280-286.
- Lamarque, C.-H., Pernot, S., & Cuer, A. (2000). Damping identification in multi-degree-of-freedom systems via a wavelet-logarithmic decrement—part 1: theory. *Journal of Sound and Vibration*, 235(3), 361-374.
- Lardies, J., & Gouttebroze, S. (2002). Identification of modal parameters using the wavelet transform. *International Journal of Mechanical Sciences* 44(11), 2263-2283.
- Law, S., Li, X., Zhu, X., & Chan, S. (2005). Structural damage detection from wavelet packet sensitivity. *Engineering Structures* 27(9), 1339-1348.
- Law, S., Zhu, X., Tian, Y., Li, X., & Wu, S. (2013). Statistical damage classification method based on wavelet packet analysis. *Structural Engineering and Mechanics*, 46(4), 459-486.
- Le, T.-P., & Paultre, P. (2012). Modal identification based on continuous wavelet transform and ambient excitation tests. *Journal of Sound and Vibration*, 331(9), 2023-2037.
- Lee, J., Kim, J., Yun, C., Yi, J., & Shim, J. (2002). Health-monitoring method for bridges under ordinary traffic loadings. *Journal of Sound and Vibration*, 257(2), 247-264.
- Lee, S. G., Yun, G. J., & Shang, S. (2014). Reference-free damage detection for truss bridge structures by continuous relative wavelet entropy method. *Structural Health Monitoring-an International Journal*, 1475921714522845.

- Lenaerts, V., Kerschen, G., Golinval, J.-C., Ruzzene, M., & Giorcelli, E. (2004). Validation of two nonlinear system identification techniques using an experimental testbed. *Shock and Vibration*, 11(3-4), 365-375.
- Li, H., Mao, C., & Ou, J. (2012). Identification of hysteretic dynamic systems by using hybrid extended Kalman filter and wavelet multiresolution analysis with limited observation. *Journal of Engineering Mechanics*, 139(5), 547-558.
- Liang, R. Y., Hu, J., & Choy, F. (1992). Theoretical study of crack-induced eigenfrequency changes on beam structures. *Journal of Engineering Mechanics*, 118(2), 384-396.
- Lieven, N., & Ewins, D. (1988). Spatial correlation of mode shapes, the coordinate modal assurance criterion (COMAC). Proceedings of 6th International Modal Analysis Conference, 690-695.
- Lim, T. W., & Kashangaki, T. A. (1994). Structural damage detection of space truss structures using best achievable eigenvectors. *AIAA journal*, 32(5), 1049-1057.
- Lingener, A., & Doege, S. (1988). Estimation of dynamic spring and damping parameters of the supports of a nuclear reactor by means of an adaptive method in time domain. In: Natke, H.G. (Ed.): *Application of System Identification in Engineering*, CISM Course, Lecture No. 296, pp. 511–523 New York: Springer.
- Loh, C.-H., Lin, C.-Y., & Huang, C.-C. (2000). Time domain identification of frames under earthquake loadings. *Journal of Engineering Mechanics*, 126(7), 693-703.
- Loutridis, S., Douka, E., & Trochidis, A. (2004). Crack identification in double-cracked beams using wavelet analysis. *Journal of Sound and Vibration*, 277(4), 1025-1039.
- Lu, C.-J., & Hsu, Y.-T. (2002). Vibration analysis of an inhomogeneous string for damage detection by wavelet transform. *International Journal of Mechanical Sciences*, 44(4), 745-754.
- Lu, Z., & Law, S. (2007). Features of dynamic response sensitivity and its application in damage detection. *Journal of Sound and Vibration*, 303(1), 305-329.
- Luk, R.-P., & Damper, R. I. (2006). Non-parametric linear time-invariant system identification by discrete wavelet transforms. *Digital Signal Processing*, 16(3), 303-319.
- Mallat, S. (1999). *A wavelet tour of signal processing*: Academic press, New York.
- Mallet, S. G. (1989). A theory for multiresolution signal decomposition: The wavelet representation. *IEEE Transactions on Pattern Analysis and Machine Intelligence*, 11(7), 674-693.
- Mares, C., & Surace, C. (1996). An application of genetic algorithms to identify damage in elastic structures. *Journal of sound and vibration*, 195(2), 195-215.

- Masri, S., & Caughey, T. (1979). A nonparametric identification technique for nonlinear dynamic problems. *Journal of Applied Mechanics*, 46(2), 433-447.
- Mayes, R. L. (1992). Error localization using mode shapes—an application to a two link robot arm. Proceedings of 4th International Modal Analysis Conference, San Diego, California, USA.
- Messina, A., Williams, E., & Contursi, T. (1998). Structural damage detection by a sensitivity and statistical-based method. *Journal of sound and vibration*, 216(5), 791-808.
- Mikami, S., Beskhyroun, S., & Oshima, T. (2011). Wavelet packet based damage detection in beam-like structures without baseline modal parameters. *Structure and Infrastructure Engineering*, 7(3), 211-227.
- Mishra, V. (2011). Sabina: Wavelet Galerkin solutions of ordinary differential equations. *International Journal of Mathematical Analysis*, 5(9), 407-424.
- Morassi, A. (1993). Crack-induced changes in eigenparameters of beam structures. *Journal of Engineering Mechanics*, 119(9), 1798-1803.
- Mottershead, J., & Friswell, M. (1993). Model updating in structural dynamics: a survey. *Journal of sound and vibration*, 167(2), 347-375.
- Mottershead, J., & Friswell, M. (1998). Special issue on model updating. *Mechanical Systems and Signal Processing*, 12, 1-224.
- Newland, D. (1993). *An Introduction to Random Vibrations, Spectral and Wavelet Analysis* Longman. New York, USA: Harlow and John Wiley.
- Newland, D. E. (1994). Wavelet analysis of vibration: part 1—theory. *Journal of Vibration and Acoustics-Transactions of the Asme*, 116(4), 409-416.
- Ni, Y., Ko, J., & Wong, C. (1999). Nonparametric identification of nonlinear hysteretic systems. *Journal of engineering mechanics*, 125(2), 206-215.
- Nikolaou, N., & Antoniadis, I. (2002). Rolling element bearing fault diagnosis using wavelet packets. *Ndt & E International*, 35(3), 197-205.
- Nwosu, D., Swamidas, A., Guigne, J., & Olowokere, D. (1995). Studies on influence of cracks on the dynamic response of tubular T-joints for nondestructive evaluation. Proceedings of 13th International Modal Analysis Conference, 1122-1128.
- Ovanesoova, A., & Suarez, L. (2004). Applications of wavelet transforms to damage detection in frame structures. *Engineering structures*, 26(1), 39-49.
- Pakrashi, V., O'Connor, A., & Basu, B. (2007). A study on the effects of damage models and wavelet bases for damage identification and calibration in beams. *Computer-Aided Civil and Infrastructure Engineering*, 22(8), 555-569.
- Pandey, A., & Biswas, M. (1994). Damage detection in structures using changes in flexibility. *Journal of sound and vibration*, 169(1), 3-17.

- Pandey, A., & Biswas, M. (1995). Experimental verification of flexibility difference method for locating damage in structures. *Journal of sound and vibration*, 184(2), 311-328.
- Pandey, A., Biswas, M., & Samman, M. (1991). Damage detection from changes in curvature mode shapes. *Journal of sound and vibration*, 145(2), 321-332.
- Pascual, R., Schälchli, R., & Razeto, M. (2005). Improvement of damage-assessment results using high-spatial density measurements. *Mechanical systems and signal processing*, 19(1), 123-138.
- Pawlak, M., & Hasiewicz, Z. (1998). Nonlinear system identification by the Haar multiresolution analysis. *IEEE Transactions on Circuits and Systems I: Fundamental Theory and Applications*, 45(9), 945-961.
- Peng, Z., & Chu, F. (2004). Application of the wavelet transform in machine condition monitoring and fault diagnostics: a review with bibliography. *Mechanical systems and signal processing*, 18(2), 199-221.
- Pothisiri, T., & Hjelmstad, K. (2003). Structural damage detection and assessment from modal response. *Journal of Engineering Mechanics*, 129(2), 135-145.
- Quek, S.-T., Wang, Q., Zhang, L., & Ang, K.-K. (2001a). Sensitivity analysis of crack detection in beams by wavelet technique. *International journal of mechanical sciences*, 43(12), 2899-2910.
- Quek, S., Wang, Q., Zhang, L., & Ong, K. (2001b). Practical issues in the detection of damage in beams using wavelets. *Smart Materials and Structures*, 10(5), 1009.
- Radzieński, M., & Krawczuk, M. (2009). Experimental verification and comparison of mode shape-based damage detection methods. *Journal of Physics: Conference Series*, 181(1), 012067.
- Ratcliffe, C. P. (2000). A frequency and curvature based experimental method for locating damage in structures. *Journal of Vibration and Acoustics-Transactions of the Asme*, 122(3), 324-329.
- Ren, W.-X., & De Roeck, G. (2002). Structural damage identification using modal data. I: Simulation verification. *Journal of Structural Engineering*, 128(1), 87-95.
- Ren, W.-X., & Sun, Z.-S. (2008). Structural damage identification by using wavelet entropy. *Engineering Structures*, 30(10), 2840-2849.
- Ren, W.-X., Sun, Z.-S., Xia, Y., Hao, H., & Deeks, A. (2008). Damage identification of shear connectors with wavelet packet energy: laboratory test study. *Journal of structural engineering*, 134(5), 832-841.
- Restrepo, J. M., & Leaf, G. K. (1997). Inner product computations using periodized Daubechies wavelets. *International Journal for Numerical Methods in Engineering*, 40(19), 3557-3578.

- Ricles, J., & Kosmatka, J. (1992). Damage detection in elastic structures using vibratory residual forces and weighted sensitivity. *AIAA journal*, 30(9), 2310-2316.
- Robertson, A., Park, K., & Alvin, K. (1998a). Extraction of impulse response data via wavelet transform for structural system identification. *Journal of Vibration and Acoustics-Transactions of the Asme*, 120(1), 252-260.
- Robertson, A., Park, K., & Alvin, K. (1998b). Identification of structural dynamics models using wavelet-generated impulse response data. *Journal of Vibration and Acoustics-Transactions of the Asme*, 120(1), 261-266.
- Romine, C., & Peyton, B. (1997). Computing connection coefficients of compactly supported wavelets on bounded intervals. *Computer Science and Mathematics Division, Mathematical Sciences Section, Oak Ridge National Laboratory, Oak Ridge, Technical Report ORNL/TM-13413*.
- Rosso, O., Martin, M., Figliola, A., Keller, K., & Plastino, A. (2006). EEG analysis using wavelet-based information tools. *Journal of Neuroscience Methods*, 153(2), 163-182.
- Rucka, M., & Wilde, K. (2006). Application of continuous wavelet transform in vibration based damage detection method for beams and plates. *Journal of Sound and Vibration*, 297(3), 536-550.
- Ruzzene, M., Fasana, A., Garibaldi, L., & Piombo, B. (1997). Natural frequencies and dampings identification using wavelet transform: application to real data. *Mechanical Systems and Signal Processing*, 11(2), 207-218.
- Rytter, A. (1993). Vibration based inspection of Civil Engineering Structures. PhD Thesis, Department of Building Technology and Structural Engineering, Aalborg University, Denmark.
- Salawu, O. (1997). Detection of structural damage through changes in frequency: a review. *Engineering structures*, 19(9), 718-723.
- Salawu, O., & Williams, C. (1994). Damage location using vibration mode shapes. Proceedings of 12th International Modal Analysis Conference, 933-939.
- Shannon, C. E. (1996). The mathematical theory of communication. *MD computing: computers in medical practice*, 14(4), 306-317.
- Shen, Z. S. L., & Law, S. (2006). Parameter identification of LTV dynamical system based on wavelet method. Proceedings of 4th International Conference on Earthquake Engineering, 202-210.
- Shi, Z., Law, S., & Zhang, L. (1998). Structural damage localization from modal strain energy change. *Journal of Sound and Vibration*, 218(5), 825-844.
- Shi, Z., Law, S., & Zhang, L. (2000a). Damage localization by directly using incomplete mode shapes. *Journal of Engineering Mechanics*, 126(6), 656-660.

- Shi, Z., Law, S., & Zhang, L. (2002). Improved damage quantification from elemental modal strain energy change. *Journal of engineering mechanics*, 128(5), 521-529.
- Shi, Z., Law, S., & Zhang, L. M. (2000b). Structural damage detection from modal strain energy change. *Journal of engineering mechanics*, 126(12), 1216-1223.
- Shinde, A., & Hou, Z. (2005). A wavelet packet based sifting process and its application for structural health monitoring. *Structural Health Monitoring-an International Journal*, 4(2), 153-170.
- Slavič, J., Simonovski, I., & Boltežar, M. (2003). Damping identification using a continuous wavelet transform: application to real data. *Journal of Sound and Vibration*, 262(2), 291-307.
- Smith, S. W. (1992). Iterative use of direct matrix updates: connectivity and convergence. Proceedings of 33rd AIAA Structures, Structural Dynamics and Materials Conference, 1797-1806.
- Sohn, H., Farrar, C. R., Hemez, F. M., Shunk, D. D., Stinemates, D. W., Nadler, B. R., & Czarnecki, J. J. (2004). *A review of structural health monitoring literature: 1996-2001*. Report No. LA-13976-Ms, Los Alamos National Laboratory.
- Sone, A., Hata, H., & Masuda, A. (2004). Identification of structural parameters using the wavelet transform of acceleration measurements. *Journal of Pressure Vessel Technology-Transactions of the Asme*, 126(1), 128-133.
- Spanos, P. D., Failla, G., Santini, A., & Pappatico, M. (2006). Damage detection in Euler-Bernoulli beams via spatial wavelet analysis. *Structural Control and Health Monitoring*, 13(1), 472-487.
- Staszewski, W. (1997). Identification of damping in MDOF systems using time-scale decomposition. *Journal of sound and vibration*, 203(2), 283-305.
- Staszewski, W. (1998). Identification of non-linear systems using multi-scale ridges and skeletons of the wavelet transform. *Journal of Sound and Vibration*, 214(4), 639-658.
- Staszewski, W. (2000). Analysis of non-linear systems using wavelets. Proceedings of the Institution of Mechanical Engineers Part C-Journal of Mechanical Engineering Science, 214(11), 1339-1353.
- Staszewski, W., Pierce, G., Worden, K., & Culshaw, B. (1999). Cross-wavelet analysis for Lamb wave damage detection in composite materials using optical fibres. *Key Engineering Materials*, 167(1), 373-380.
- Staszewski, W., & Tomlinson, G. (1994). Application of the wavelet transform to fault detection in a spur gear. *Mechanical Systems and Signal Processing*, 8(3), 289-307.
- Stubbs, N., & Kim, J.-T. (1996). Damage localization in structures without baseline modal parameters. *AIAA journal*, 34(8), 1644-1649.

- Stubbs, N., Kim, J., & Topole, K. (1992). An efficient and robust algorithm for damage localization in offshore platforms. Proceedings of the ASCE 10th Structures Congress, 543-546.
- Stubbs, N., & Osegueda, R. (1990). Global damage detection in solids- Experimental verification. *Modal Analysis: The International Journal of Analytical and Experimental Modal Analysis*, 5(2), 81-97.
- Sun, Z., & Chang, C.-C. (2007). Vibration based structural health monitoring: Wavelet packet transform based solution. *Structure and Infrastructure Engineering*, 3(4), 313-323.
- Sun, Z., & Chang, C. (2002). Structural damage assessment based on wavelet packet transform. *Journal of structural engineering*, 128(10), 1354-1361.
- Sun, Z., & Chang, C. (2004). Statistical wavelet-based method for structural health monitoring. *Journal of structural engineering*, 130(7), 1055-1062.
- Ta, M.-N., & Lardiès, J. (2006). Identification of weak nonlinearities on damping and stiffness by the continuous wavelet transform. *Journal of sound and vibration*, 293(1), 16-37.
- Taha, M., Noureldin, A., Lucero, J., & Baca, T. (2006a). Wavelet transform for structural health monitoring: a compendium of uses and features. *Structural Health Monitoring-an International Journal*, 5(3), 267-295.
- Taha, M. R., Noureldin, A., Lucero, J., & Baca, T. (2006b). Wavelet transform for structural health monitoring: a compendium of uses and features. *Structural Health Monitoring-an International Journal*, 5(3), 267-295.
- Tsai, C., Hsieh, C., & Lew, K. (2009). Detection of wind turbine blades damage by spectrum-recognition using Gaussian wavelet-entropy. Proceedings of 3rd International Conference on Anti-counterfeiting, Security, and Identification in Communication, 108-113.
- Tsou, P., & Shen, M.-H. (1994). Structural damage detection and identification using neural networks. *AIAA journal*, 32(1), 176-183.
- Udwadia, F., & Kuo, C. P. (1981). Non-parametric identification of a class of non-linear close-coupled dynamic systems. *Earthquake Engineering & Structural Dynamics*, 9(4), 385-409.
- Umesha, P., Ravichandran, R., & Sivasubramanian, K. (2009). Crack detection and quantification in beams using wavelets. *Computer-Aided Civil and Infrastructure Engineering*, 24(8), 593-607.
- Vakil-Baghmisheh, M.-T., Peimani, M., Sadeghi, M., & Ettefagh, M. (2008). Crack detection in beam-like structures using genetic algorithms. *Applied Soft Computing*, 8(2), 1150-1160.

- Wang, C., Ren, W.-X., Wang, Z.-C., & Zhu, H.-P. (2013). Instantaneous frequency identification of time-varying structures by continuous wavelet transform. *Engineering Structures*, 52, 17-25.
- Wang, Q., & Deng, X. (1999). Damage detection with spatial wavelets. *International journal of solids and structures*, 36(23), 3443-3468.
- Wang, W., & McFadden, P. (1995). Application of orthogonal wavelets to early gear damage detection. *Mechanical Systems and Signal Processing*, 9(5), 497-507.
- Wang, Y., Chen, X., He, Y., & He, Z. (2010). New decoupled wavelet bases for multiresolution structural analysis. *Structural Engineering and Mechanics*, 35(2), 175-190.
- West, W. M. (1984). Illustration of the use of modal assurance criterion to detect structural changes in an orbiter test specimen. Proceedings of the Air Force Conference on Aircraft Structural Integrity, 1-6.
- Wu, D., & Law, S. (2004). Damage localization in plate structures from uniform load surface curvature. *Journal of Sound and Vibration*, 276(1), 227-244.
- Wu, X., Ghaboussi, J., & Garrett, J. H. (1992). Use of neural networks in detection of structural damage. *Computers & structures*, 42(4), 649-659.
- Wu, Z., Xu, B., & Yokoyama, K. (2002). Decentralized parametric damage detection based on neural networks. *Computer-Aided Civil and Infrastructure Engineering*, 17(3), 175-184.
- Xia, Y., Hao, H., & Deeks, A. (2005). Vibration-based damage detection of shear connectors in Nickol river bridge and Balla Balla river bridge. Part II: Laboratory study. Australia: School of Civil & Resource Engineering. The University of Western Australia. *Australia: School of Civil & Resource Engineering, The University of Western Australia, Report No. ST-05-02.*
- Xu, B., Wu, Z., Chen, G., & Yokoyama, K. (2004). Direct identification of structural parameters from dynamic responses with neural networks. *Engineering Applications of Artificial Intelligence*, 17(8), 931-943.
- Xu, X., Shi, Z., & You, Q. (2012). Identification of linear time-varying systems using a wavelet-based state-space method. *Mechanical Systems and Signal Processing*, 26, 91-103.
- Yam, L., Yan, Y., & Jiang, J. (2003). Vibration-based damage detection for composite structures using wavelet transform and neural network identification. *Composite Structures*, 60(4), 403-412.
- Yan, B., & Miyamoto, A. (2006). A comparative study of modal parameter identification based on wavelet and Hilbert–Huang transforms. *Computer-Aided Civil and Infrastructure Engineering*, 21(1), 9-23.

- Yan, Y., Cheng, L., Wu, Z., & Yam, L. (2007). Development in vibration-based structural damage detection technique. *Mechanical Systems and Signal Processing*, 21(5), 2198-2211.
- Yan, Y., Hao, H., & Yam, L. (2004). Vibration-based construction and extraction of structural damage feature index. *International journal of solids and structures*, 41(24), 6661-6676.
- Yang, J., Bobrow, J., Jabbari, F., Leavitt, J., Cheng, C., & Lin, P. (2007). Full-scale experimental verification of resettable semi-active stiffness dampers. *Earthquake engineering & structural dynamics*, 36(9), 1255-1273.
- Yang, J. N., Kim, J.-H., & Agrawal, A. K. (2000). Resetting semiactive stiffness damper for seismic response control. *Journal of Structural Engineering*, 126(12), 1427-1433.
- Yang, Y., & Ibrahim, S. (1985). A nonparametric identification technique for a variety of discrete nonlinear vibrating systems. *Journal of Vibration and Acoustics-Transactions of the Asme*, 107(1), 60-66.
- Yen, G. G., & Lin, K.-C. (2000). Wavelet packet feature extraction for vibration monitoring. *IEEE Transactions on Industrial Electronics*, 47(3), 650-667.
- Yun, C.-B., & Bahng, E. Y. (2000). Substructural identification using neural networks. *Computers & Structures*, 77(1), 41-52.
- Yun, G. J., Lee, S.-G., Carletta, J., & Nagayama, T. (2011). Decentralized damage identification using wavelet signal analysis embedded on wireless smart sensors. *Engineering Structures*, 33(7), 2162-2172.
- Zabel, V. (2003). Applications of wavelet analysis in system identification. PhD thesis. Bauhaus-University Weimar, Germany.
- Zeldin, B., & Spanos, P. (1996). Random field representation and synthesis using wavelet bases. *Journal of Applied Mechanics-Transactions of the Asme*, 63(4), 946-952.
- Zhang, Z., & Aktan, A. (1998). Application of modal flexibility and its derivatives in structural identification. *Research in Nondestructive Evaluation*, 10(1), 43-61.
- Zhao, J., & DeWolf, J. T. (1999). Sensitivity study for vibrational parameters used in damage detection. *Journal of structural engineering*, 125(4), 410-416.
- Zhong, S., & Oyadiji, S. (2011). Detection of cracks in simply-supported beams by continuous wavelet transform of reconstructed modal data. *Computers & structures*, 89(1), 127-148.
- Zhong, S., Oyadiji, S. O., & Ding, K. (2008). Response-only method for damage detection of beam-like structures using high accuracy frequencies with auxiliary mass spatial probing. *Journal of Sound and Vibration*, 311(3), 1075-1099.
- Zhou, X. (2004). Wavelets-Galerkin scheme for a Stokes problem. *Numerical Methods for Partial Differential Equations*, 20(2), 193-198.

- Zhu, X., & Law, S. (2006). Wavelet-based crack identification of bridge beam from operational deflection time history. *International Journal of Solids and Structures*, 43(7), 2299-2317.
- Zimmerman, D., & Widengren, M. (1990). Correcting finite element models using a symmetric eigenstructure assignment technique. *AIAA journal*, 28(9), 1670-1676.
- Zimmerman, D. C., & Kaouk, M. (1992). Eigenstructure assignment approach for structural damage detection. *AIAA journal*, 30(7), 1848-1855.
- Zimmerman, D. C., & Smith, S. W. (1992). Model refinement and damage location for intelligent structures. *Intelligent Structural Systems*, Kluwer Academic Publishers. (pp. 403-452): Springer.
- Zimmerman, D. C., & Smith, S. W. (1992). Model refinement and damage location for intelligent structures. In H.S. Tzou & G.L. Anderson (Eds.), *Intelligent Structural Systems* (pp. 403-452). Boston: Kluwer Academic Publishers.

List of Publications and Papers Presented

(i) Journals:

Ravanfar, S.A., Razak, H. A., Ismail, Z., & Hakim, S. (2016). A Hybrid Wavelet Based– Approach and Genetic Algorithm to Detect Damage in Beam-Like Structures without Baseline Data. *Experimental Mechanics*, 56(8), 1411-1426.

Ravanfar, S. A., Razak, H. A., Ismail, Z., & Hakim, S. (2016). A two-step damage identification approach for beam structures based on wavelet transform and genetic algorithm. *Meccanica*, 51(3), 635-653.

Ravanfar, S. A., Razak, H. A., Ismail, Z., & Monajemi, H. (2015). An improved method of parameter identification and damage detection in beam structures under flexural vibration using wavelet multi-resolution analysis. *Sensors*, 15(9), 22750-22775.

Ravanfar, S. A., Razak, H. A., Ismail, Z., & Hakim, S. (2015). A Hybrid Procedure for Structural Damage Identification in Beam-Like Structures Using Wavelet Analysis. *Advances in Structural Engineering*, 18(11), 1901-1913.

Hakim, S., Razak, H. A., & **Ravanfar, S. A.** (2015). Fault diagnosis on beam-like structures from modal parameters using artificial neural networks. *Measurement*, 76, 45-61.

Hakim, S., Razak, H. A., & **Ravanfar, S. A.** (2016). Ensemble neural networks for structural damage identification using modal data. *International Journal of Damage Mechanics*, 25(3), 400-430.

(ii) International Conferences

Ravanfar, S.A., Razak, H. A., Ismail, Z., & Hakim, S. (2016). Damage Detection Optimization Using Wavelet Multiresolution Analysis and Genetic Algorithm. *Proceedings of the 34th IMAC, A Conference and Exposition on Structural Dynamics. Volume 2 (pp. 43-48): Springer.*

Ravanfar, S.A., Razak, H. A., Ismail, Z., & Hakim, S. (2014). Damage Detection Based on Wavelet Packet Transform and Information Entropy. Proceedings of the 32nd IMAC, A Conference and Exposition on Structural Dynamics. Volume 5 (pp. 223-229): Springer.

Hakim, S., Razak, H. A., **Ravanfar, S.A.,** & Mohammadhassani, M. (2014). Structural Damage Detection Using Soft Computing Method. Proceedings of the 32nd IMAC, A Conference and Exposition on Structural Dynamics., Volume 5 (pp. 143-151): Springer.

Hakim, S., Razak, H. A., & **Ravanfar, S. A.**(2014). Structural damage identification using Artificial Neural Networks (ANNs) and Adaptive Neuro Fuzzy Interface System (ANFIS). Proceedings of the 9th International Conference on Structural Dynamics, EUROODYN 2014,Porto, Portugal.

Hakim, S., Abdul Razak, H., & **Ravanfar, S.A.** (2014). Vibration-based structural damage identification using ensemble neural networks. Proceedings of 23rd Australasian Conference on the Mechanics of Structures and Materials.